CLUSTER DEVICES/ INTERCONNECTS FOR NANO-TECHNOLOGY

A thesis submitted in partial fulfilment of the requirements

for the Degree of

Doctor of Philosophy in Electrical Engineering

in the University of Canterbury

by Kheng Chok Tee

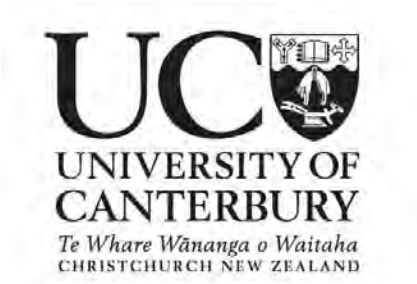

Department of Electrical and Computer Engineering

2008

Abstract

Integrated circuit (IC) technology has evolved rapidly but the continual development of transistors and interconnects (the connection between the transistors) is facing greater and greater challenges, which require new materials and new processes. Research in nano-particles (or nanoscale clusters) creates possibilities for both new materials and new processes. This thesis explores the electrical properties of amorphous antimony clusters and develops a new copper cluster deposition technique for application to transistors and interconnects respectively.

For amorphous antimony clusters, an electron diffraction technique was applied to identify the phase of the clusters prior to deposition on electrically contacted samples. The deposition process produced uniform cluster films suitable for electrical measurements. A consistent percolation exponent for conduction (t=1.85) was obtained. After deposition, the resistance of the films continued to increase because of coalescence. Although it was previously reported that amorphous antimony films were semiconducting, from linear $I(V)$ curves, a low temperature coefficient of resistance (10^{-4} K^{-1}) and no observable gate effect, it was found that the antimony cluster films in this study were not semiconducting, possibly due to the effect of coalescence.

The development of the copper clusters for the interconnects application was very successful. Trenches of sub-200 nm widths, with different diffusion barriers and seed layers, and up to 5:1 aspect ratios have been completely filled with copper clusters. Due to the propensity for reflection of clusters from the planar surfaces between trenches, the process results in selective deposition into the trenches and bottom up filling is demonstrated. After annealing in hydrogen or in vacuum, the clusters sinter into a copper seed layer. The resistivity measured by a thin film four-point probe (1.6 - 2.3×10^{-8} Ωm) meets the requirement by industry (2.2×10^{-8} Ωm). The process is therefore promising for industrial application, but further testing and investigation of integration issues is required.

Table of Contents

“Anyone who has never made a mistake
has never tried anything new.”
- Albert Einstein

"The real voyage of discovery consists not in
seeking new landscapes but in having new eyes."
- Marcel Proust

"For a successful technology, reality must
take precedence over public relations,
for nature cannot be fooled."
- Richard Feynman

Chapter 1

Introduction

In 1959, Richard Feynman gave a famous lecture, "*There's plenty of room at the bottom*", at Caltech [1]. He predicted that the future of manipulating and controlling matter on an atomic scale would not be far away. One of the examples he quoted was the miniaturisation of the computer. In order to make computers small, the elements such as transistors and the metal connections have to be sub-microscopic. The technology that controls matter in a 0.5 to 100 nanometre range (one nanometre is one billionth of a metre, or 10^{-9} m) or the fabrication of devices with such dimensions is called "nanotechnology".

One of the interesting fields in nanotechnology is the use of nano-particles or nanoscale clusters as building blocks for device applications. Because of finite size effects, large surface to volume ratios, and quantum confinement, nanoscale particles which bridge the gap between atom/molecules and condensed matter, exhibit a range of unique structural, electronic and optical properties [2-4]. For example, the light emission at the particle plasmon frequency observed in gold nano-particles is different from that in metal films [4].

This thesis focuses on two different types of clusters for electronic devices and interconnect applications: amorphous antimony clusters and copper clusters. In this chapter, some general cluster properties, the previous studies at the University of Canterbury, the motivation and objectives, followed by the outline of the thesis are presented.

1.1 General cluster properties

This section describes some general cluster properties. First, the surface/volume ratio of a nanoscale cluster is discussed. Then, different atomic structures of clusters are illustrated. Although the melting point of clusters reduces as the cluster diameter reduces and the surface/volume ratio increases, there are some abnormalities for the melting temperature of a cluster in relation with the so-called “magic numbers”. A brief discussion of magic numbers is presented. Lastly, the metal to semiconductor transition of clusters is described.

1.1.1 Surface/Volume ratio

When a particle is made smaller, the ratio of the number of atoms on its surface to the total number of atoms of the particle increases. Table 1-1 shows a simple calculation of surface/volume ratios assuming a spherical particle having a diameter, *R* (nm). There are between 40 % and 4 % of the atoms on the surface for particles with diameter between 3 and 30 nm. Thus, the properties of the particle can be dominated by the properties of the surface atoms rather than the bulk properties. Many applications use the catalytic and surface properties of the clusters and so to make new sensors [5-8].

Table 1-1: **A simple of calculation of the ratio of the numbers of surface atoms to volume atoms of a spherical particle of radius *R* nm. N and $N_{surface}$ denote the total number of atoms and the number of atoms on the surface. Ref. [9].**

R (nm)	N	$N_{surface}$	$N_{surface}/N$
0.3	1	-	-
0.6	12	all	100 %
1.1	55	42	76 %
2	300	180	60 %
3	1000	400	40 %
30	10^6	40 000	4 %
1 mm	10^{20}	10^{13}	10^{-7}

1.1.2 Atomic structures

In order to reduce the total surface free energy of a particle, the atoms re-arrange themselves until a stable structure is formed (see Chapter 1 in Ref. [10]). For materials which are FCC in the bulk, three common cluster structures - icosahedra, decahedra and FCC cuboctahedra – are observed depending on size, as illustrated in Figure 1-1. When the cluster is large, a cluster has the same FCC arrangement of atoms as the bulk structure. For small clusters, the icosahedra and decahedra are more energetically favourable [11]. In some cases, clusters with amorphous phase can be made, for example through super-cooling in an inert gas aggregation process [10]. Therefore, different structures of clusters could be made and possibly be applied to different applications by making use of their electronic properties. In this thesis, the amorphous phase of antimony clusters is one of the main focuses of the study.

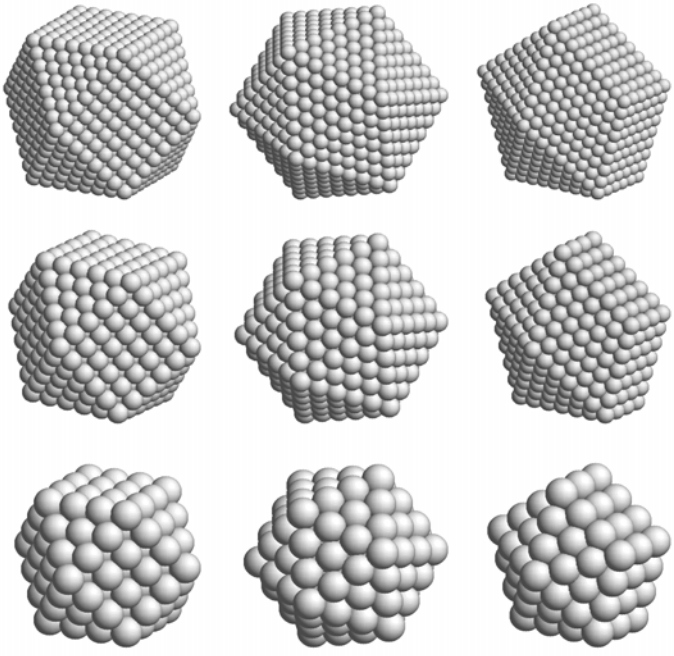

Figure 1-1: **Examples of three types of cluster structures: FCC cuboctahedra, icosahedra and decahedra. The cuboctahedra (first column, N=1415; 561, 147 atoms, from top to bottom) have the same FCC arrangement of atoms as the bulk structure, and are typically observed for large particle sizes. The icosahedral (second column; N=1415, 561, 147 atoms also) and decahedral (third column; N=1514, 605, 116 atoms) structures are believed to be energetically favoured only for very small clusters. After Wurl [12].**

1.1.3 Melting temperature

As the atoms at the surfaces are less bound than the atoms in the bulk, the high surface to volume ratios of nano-particles facilitate the rearrangement of atoms, and hence reduce the melting point of the clusters. In 1977, Couchman *et al.* proposed a thermodynamic size effect - melting is initiated at the surface and that the solid-liquid interface sweeps rapidly through the solid at the melting temperature [13]. Since then, many experiments and simulations have demonstrated the reduction of the melting point as the cluster size reduces [3, 14-18]. Figure 1-2 shows that as the size of tin clusters decreases the melting temperature drops rapidly [18].

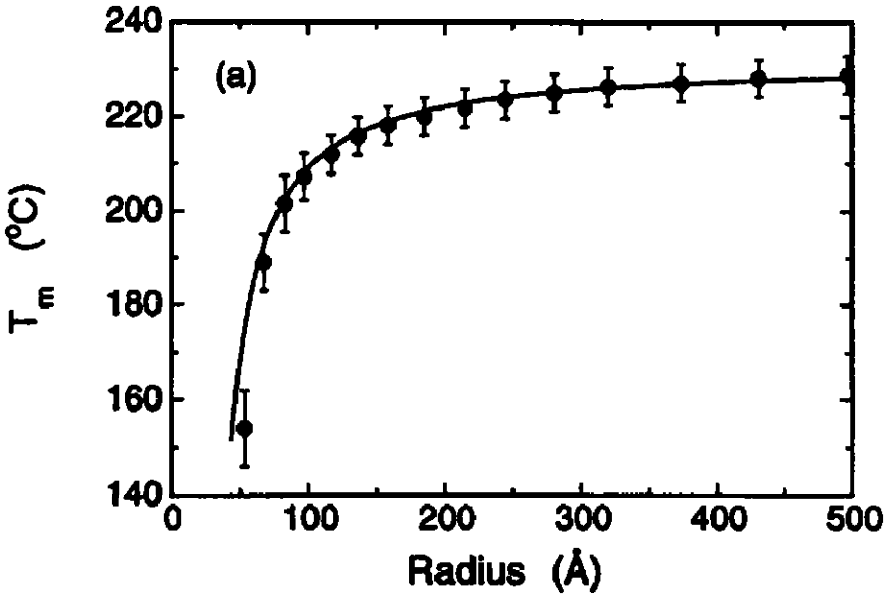

Figure 1-2: Melting temperature of tin particles as a function of radius. After Ref. [18].

1.1.4 Magic numbers

Atomic nuclei and simple metal clusters exhibit several surprising similarities, as described by Haberland [14]. Clusters of certain sizes of *N*, known as magic numbers, can take on unusually stable geometric structures. There are two factors contributing to the magic numbers: (a) closing of geometrical shells and (b) closing of electronic shells. When a complete structure, as described in Section 1.1.2, is formed, the nano-particle is in a stable state (geometrical factors); for closed electronic shells, one calculates a

spherical shape for the cluster and a maximum for the binding energies, both for electrons and atoms, as described by Haberland *et al.*[14, 19]. As shown in Figure 1-3, the binding energy of supported silver clusters was higher than its normal value at cluster sizes n = 4, 6 and 9 [20]. For the deposition of clusters, an abnormally high yield was observed for clusters with the size of magic numbers. For example, Yamada *et al.* demonstrated the magic number by using a time-of-flight mass spectrometer [21].

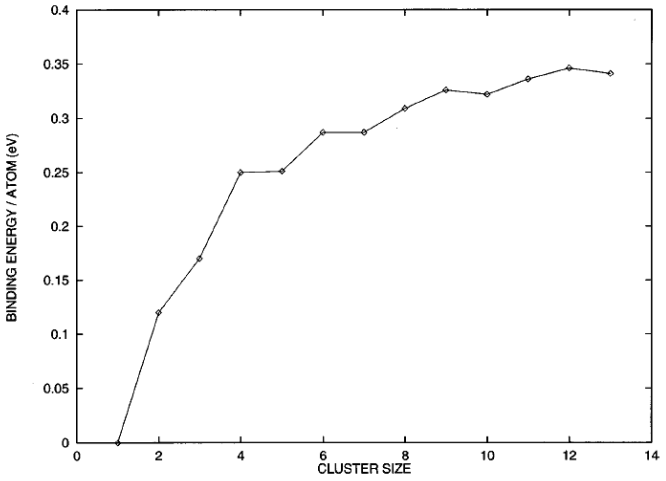

Figure 1-3: **Result from a numerical experiment showing the effect of magic numbers on the binding energy for supported silver clusters. After Ref. [20].**

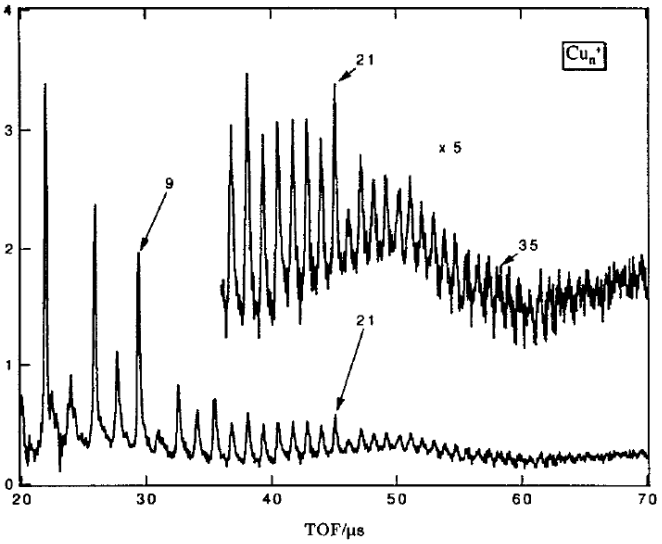

Figure 1-4: **Time-of-flight mass spectra of pure Cu clusters. Indicated numbers correspond to cluster size (n). The magic numbers are observed at n=9 and 21. After Ref. [21].**

1.1.5 Effects of magic numbers on melting

Although the melting point reduces as a function of the cluster size, it has been reported that the melting temperature of a nano-particle increases abnormally at certain cluster sizes [16, 22]. As shown in Figure 1-5, the melting point of size-selected sodium clusters changes dramatically at certain cluster sizes with magic numbers of atoms [22]. A complete closed shell of a particle (see Section 1.1.4) is believed to have a more stable state. However, there were still some discrepancies between the experimental and theoretical values, thus the mechanism was not fully understood. The same phenomenon was also observed in gallium clusters [16]. As the magic number only exists for small clusters (~ a few nm), the increase in the melting point of the clusters does not concern the clusters produced in this study.

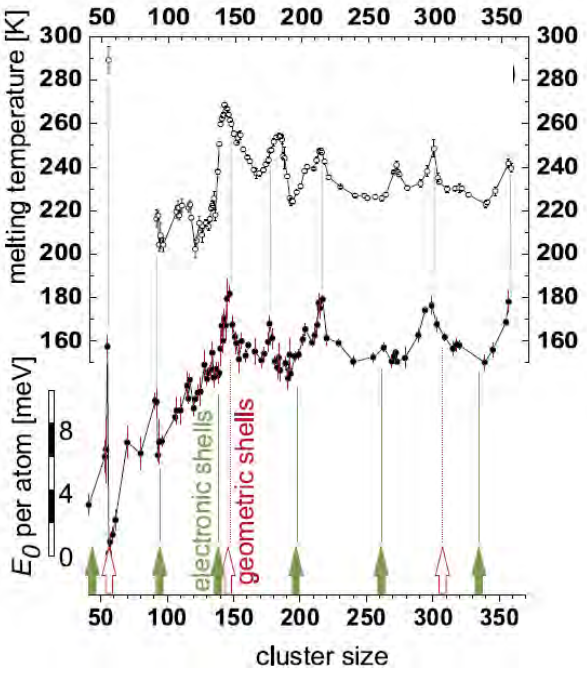

Figure 1-5: **(Top) Melting temperature as a function of Na cluster size. (Bottom) Energy differences E_0 between solid sodium and liquid sodium as a function of cluster size. The changes E_0 between the cluster sizes can be extracted by using the relative scale on the left. The arrows mark the electronic and geometric shell closings which cannot sufficiently explain the observed features in the melting point. After Ref. [22].**

1.1.6 Metal to semiconductor transition

An interesting behaviour observed in nanoscale clusters is the transition from metals to semiconductors. The valence band and conduction band of a metal can be separated as the size of the clusters reduces [23]. In this case, metallic clusters such as mercury clusters can be transformed into semiconductors, as shown in Figure 1-6 [24]. In some of the previous bismuth studies in University of Canterbury, attempts to make Bi clusters as semiconducting devices were made [25, 26].

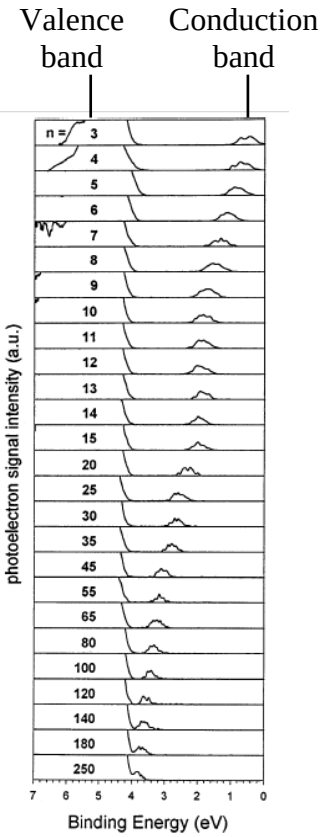

Figure 1-6: Photoelectron spectra of mercury clusters. The cluster size varies between 3 and 250 atoms. After [24].

This section only illustrates a few examples of the cluster properties. More examples can be found in the reviews in Ref. [2, 3, 23, 27]. There are many deposition techniques and many ways of analysing clusters [19]. Different deposition techniques will be discussed in Section 3.2. The next section describes the analytical studies conducted at the University of Canterbury.

1.2 Previous Studies at the UC

This section describes the previous studies at the University of Canterbury. For these studies, two cluster deposition systems were used, namely a high-vacuum compatible system and an ultra-high vacuum compatible system (see Chapter 2 for details). With these two systems, the research focused on the clusters from different materials, such as bismuth (Bi) [12, 25, 26], antimony (Sb) [10], lead (Pb) [28], zinc (Zn) [28], silver (Ag), tin/tin oxide (Sn/SnO_2) [6] and palladium (Pd) [26]. The experiments performed at the University of Canterbury can generally be grouped into three main fields: (a) electron diffraction studies of unsupported clusters [10, 12, 28]; (b) electrical characterisation of the cluster films [25, 26, 29, 30]; (c) development of cluster deposition system [31] and (d) the measurements of the mass distribution either by time of flight (TOF) [10], or mass filter [26].

Previously, the structure of unsupported clusters was identified by electron diffraction at the University of Canterbury. Kaufmann showed distinct electron diffraction patterns between the crystalline antimony clusters and amorphous antimony clusters [10]. Since the electronic properties of antimony depends on the structures of the clusters (or the arrangement of atoms), it is important to produce the clusters which have the amorphous phase for it to be semiconducting.

As shown in Figure 1-7, one way of building a device is to have the clusters randomly occupying the space between a pair of contacts. Percolation theory is a powerful tool for analysing such a system with a random nature. It was demonstrated by Dunbar *et al.*, that depositions with bismuth and silver could be explained by percolation theory [32] (as will be discussed in greater details in Section 3.5). Schmelzer *et al.* demonstrated the finite size effects in 2D bismuth cluster films, which were in agreement with percolation theory [29, 33, 34]. The finite size effects were observed by reducing the spacing of the electrodes for the percolating films.

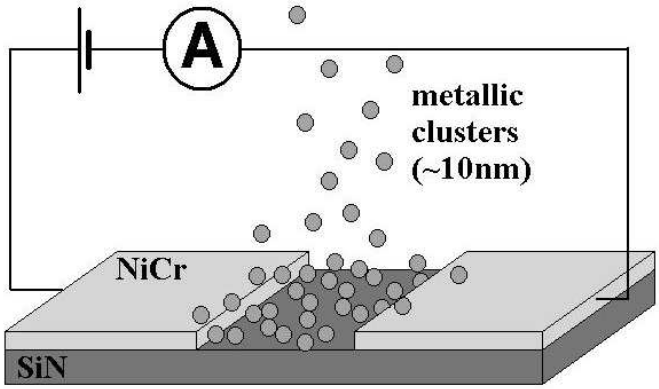

Figure 1-7: A typical percolation experiment using clusters. After Ref. [35].

Instead of depositing clusters on a flat surface, self-assembly of clusters was demonstrated in V-groove templates by Partridge *et al.* [36-38]. The self-assembly was achieved by using the bouncing properties of clusters. In this case, the clusters bounced off the flat plateau, and slid along the sidewall of the V-grooves, and finally resulted in a wire connected between two electrodes. The bouncing properties of clusters have a great potential to be applied to other templates. In this thesis, the bouncing properties are used for the trench-filling of the copper interconnects application.

1.3 Motivation and Objectives

In the past, amorphous antimony films were mostly deposited by molecular beam deposition (MBD) either for a very thin layer or at cryogenic substrate temperatures. Recently, there were some reports on amorphous antimony films produced by low energy cluster beam deposition (LECBD) [27, 39-41]. Although amorphous antimony films produced by MBD have been demonstrated to be semiconducting, the semiconductor behaviour has not been shown for amorphous films produced by cluster deposition. At the University of Canterbury, electron diffraction of unsupported antimony clusters was previously developed [10]. Thus, by identifying the phase of the clusters from the electron diffraction, amorphous clusters were deposited on electrically contacted samples for further analysis. The objective of the antimony experiments is to

electrically characterise the amorphous antimony cluster films. If the semiconducting behaviour is observed, a useful device could be made.

According to the Semiconductor Industry Association (SIA), world wide semiconductor sales reached ~ US$ 248 billion in 2006 [42, 43]. It was forecasted that the sales would reach US$ 273 billion in 2007 [44]. With such an enormous amount of revenue, it is certainly lucrative to align research to the needs of the semiconductor industry. In particular, the development of interconnects attracts many groups. The Damascene process (in Section 5.2) is used for copper interconnects. There are still many challenges faced by the industry. One solution that the industry would like to have is a process that is able to fill deep trenches with a high purity of copper. Up to date, the existing processes do not have both high aspect ratio filling capability and the high purity of deposits.

For the copper development, the support from the industry is critical. This study is a joint project between University of Canterbury and Nano Cluster Devices Ltd. (NCD), under the sponsorship of the Technology for Industry Fellowship (TIF). With the support of technology partners of NCD (Novellus Systems Inc. and Texas Instruments Inc.), processed silicon wafers could be obtained. The wafers were coated with thin films using state-of-the-art processing. With the supply of the silicon wafers and the suggestion from two semiconductor manufacturers, the development of the technology could be more tailored to the industry requirements. In this study, the focus is on the development of trench-filling with high purity copper clusters.

The objectives of the thesis are therefore: a) to study the semiconducting behaviour of amorphous antimony films and b) to develop a trench filling technology with pure copper for copper interconnect application.

1.4 Outline of the thesis

The remainder of the thesis is organised as follows:

Chapter 2 describes the experimental equipment used to fabricate and analyse the nanoscale clusters. Firstly, the background of cluster formation is discussed. Then, a high-vacuum compatible (HV) system and an ultra-high-vacuum (UHV) compatible system are illustrated. An inert gas aggregation source is used in the HV system and the UHV system at the University of Canterbury while a magnetron sputtering source is used in the UHV system in the NCD laboratory. A “von Issendorff and Palmer” mass filter and a deflector are used for the analysis of ionised clusters from the magnetron sputtering source. An annealing stage is used for sintering the copper clusters. In order to anneal samples in a hydrogen environment, a hydrogen transfer chamber is required for safety purposes.

Chapter 3 reviews the molecular beam deposition (MBD) and cluster deposition. As the MBD films have different properties depending on the substrate temperature during deposition, the conventional evaporations and the evaporations with substrate cooling are reviewed separately. As for the cluster films, the general cluster depositions are described. The electronic transport properties of the amorphous antimony films prepared by MBD and cluster deposition are compared with the electronic transport properties of antimony nanowires. Then a previous study at the University of Canterbury using electron diffraction as well as the concept of percolation theory is described.

Chapter 4 presents the results of amorphous antimony deposition and characterisations. The phase of the antimony clusters is identified by electron diffraction. The preparation of two types of samples is described. Next, the parameters such as source pressure, the spot size of the cluster beam and deposition rate are studied. The initial depositions follow the conditions used in previous research at the University of Canterbury. Then different source configurations are used to produce uniform cluster films. The cluster diameter, film morphology and the electrical characteristics of the films are analysed

separately. The electrical characteristics include the percolation exponent, $I(V)$, $R(T)$ and gate effect measurements.

Chapter 5 gives an overview of the copper interconnects in ultra-large-scale technology (ULSI). First, a brief history of the interconnects is described. Then, the copper damascene process is presented. The potential problems of the damascene process are discussed, highlighting the need for a new technology. Some advanced copper filling and copper reflow technologies are reviewed. The chapter concludes by providing some studies of literature regarding cluster deposition and sintering.

Chapter 6 presents the results of the trench filling by copper clusters. First, the sample structures and the deposition conditions of two sources are described. Second, the cluster properties such as cluster diameter and cluster velocity are discussed. As the bouncing of clusters depends on the substrate used, the reflection of clusters on different surfaces is analysed and the self-assembly of wires in V-grooves is demonstrated. Lastly, the chapter highlights the trench filling and sintering of copper clusters in the nanoscale trenches.

Chapter 7 presents the resistivity calculated for the annealed copper cluster films. The sample preparations, the cluster deposition and annealing condition are briefly described. Then, the equipment setup and the methodology are also illustrated. Finally, the film morphology and the resistivity are presented.

In Chapter 8, the conclusions of the previous chapters are reviewed, including a summary of the future and outlook for further studies.

References

[1] http://www.its.caltech.edu/~feynman/plenty.html.

[2] H. Haberland, *Clusters of atoms and molecules: theory, experiment, and clusters of atoms*. Berlin: Springer-Verlag, 1994.

[3] P. Jensen, "Growth of nanostructures by cluster deposition: Experiments and simple models," *Reviews of Modern Physics*, vol. 71, p. 1695, 1999.

[4] E. Dulkeith, T. Niedereichholz, T. A. Klar, J. Feldmann, G. von Plessen, D. I. Gittins, K. S. Mayya, and F. Caruso, "Plasmon emission in photoexcited gold nanoparticles," *Physical Review B (Condensed Matter and Materials Physics)*, vol. 70, pp. 205424-1, 2004.

[5] *Clusters and Nano-assemblies: Physical and biological systems.* Richmond, Virginia, USA: World Scientific Publishing Co., 2005.

[6] A. Lassesson, M. Schulze, J. Van Lith, and S. A. Brown, "Tin oxide nanocluster hydrogen and ammonia sensors," *Nanotechnology*, vol. 19, p. 015502, 2008.

[7] J. van Lith, A. Lassesson, S. A. Brown, M. Schulze, J. G. Partridge, and A. Ayesh, "A hydrogen sensor based on tunneling between palladium clusters," *Applied Physics Letters*, vol. 91, Oct 2007.

[8] J. T. Zhang, J. F. Liu, Q. Peng, X. Wang, and Y. D. Li, "Nearly monodisperse Cu_2O and CuO nanospheres: Preparation and applications for sensitive gas sensors," *Chemistry of Materials*, vol. 18, pp. 867-871, Feb 2006.

[9] *Hellmut Haberland's cluster lecture at the University of Canterbury. Feb 2006.*

[10] M. Kaufmann, "Electron diffraction studies of unsupported antimony clusters," *PhD thesis, University of Canterbury*, 2006.

[11] D. Reinhard, B. D. Hall, P. Berthoud, S. Valkealahti, and R. Monot, "Unsupported nanometer-sized copper clusters studied by electron diffraction and molecular dynamics," *Physical Review B*, vol. 58, p. 4917, 1998.

[12] A. Wurl, "Electron diffraction studies of unsupported bismuth clusters," *PhD thesis, University of Canterbury*, 2003.

[13] P. R. Couchman and W. A. Jesser, "Thermodynamic theory of size dependence of melting temperature in metals," *Nature*, vol. 269, pp. 481-3, 1977.

[14] H. Haberland, "Metal clusters and nuclei: some similarities and differences," *Nuclear Physics A*, vol. 649, pp. 415C-422C, Mar 1999.

[15] L. C. A. van den Oetelaar, A. Partridge, S. L. G. Toussaint, C. F. J. Flipse, and H. H. Brongersma, "A surface science study of model catalysts. 2. Metal-support interactions in Cu/SiO2 model catalysts," *Journal of Physical Chemistry B*, vol. 102, pp. 9541-9549, Nov 1998.

[16] G. A. Breaux, D. A. Hillman, C. M. Neal, R. C. Benirschke, and M. F. Jarrold, "Gallium cluster "magic melters"," *Journal of the American Chemical Society*, vol. 126, pp. 8628-8629, 2004.

[17] I. Shyjumon, M. Gopinadhan, O. Ivanova, M. Quaasz, H. Wulff, C. A. Helm, and R. Hippler, "Structural deformation, melting point and lattice parameter studies of size selected silver clusters," *European Physical Journal D*, vol. 37, pp. 409-415, Mar 2006.

[18] S. L. Lai, J. Y. Guo, V. Petrova, G. Ramanath, and L. H. Allen, "Size-dependent melting properties of small tin particles: nanocalorimetric measurements," *Physical Review Letters*, vol. 77, pp. 99-102, 1996.

[19] *Clusters of atoms and molecules: theory, experiment, and clusters of atoms*. Berlin: Springer-Verlag, 1994.
[20] S. K. Nayak, P. Jena, V. S. Stepanyuk, W. Hergert, and K. Wildberger, "Magic numbers in supported metal clusters," *Physical Review B (Condensed Matter)*, vol. 56, pp. 6952-7, 1997.
[21] Y. Yamada and A. W. Castleman, Jr., "The magic numbers of metal and metal alloy clusters," *Journal of Chemical Physics*, vol. 97, pp. 4543-8, 1992.
[22] M. Schmidt, J. Donges, T. Hippler, and H. Haberland, "Influence of energy and entropy on the melting of sodium clusters," *Physical Review Letters*, vol. 90, pp. 103401-1, 2003.
[23] B. V. Issendorff and O. Cheshnovsky, "Metal to insulator transitions in clusters," *Annual Review of Physical Chemistry*, vol. 56, pp. 549-580, 2005.
[24] R. Busani, M. Folkers, and O. Cheshnovsky, "Direct observation of band-gap closure in mercury clusters," *Physical Review Letters*, vol. 81, p. 3836, 1998.
[25] R. Reichel, "Nano Scale Cluster Devices," *PhD thesis, University of Canterbury*, 2007.
[26] A. Ayesh, "Device fabrication using Bi nanoclusters," *PhD thesis, University of Canterbury*, 2007.
[27] G. Fuchs, M. Treilleux, F. Santos Aires, B. Cabaud, P. Melinon, and A. Hoareau, "Cluster-beam deposition for high-quality thin films," *Physical Review A (General Physics)*, vol. 40, pp. 6128-9, 1989.
[28] M. Hyslop, "Electron Diffraction Studies of Unsupported Clusters," *PhD thesis, University of Canterbury*, 2002.
[29] J. Schmelzer Jr, S. A. Brown, M. Schulze, A. Dunbar, J. Partridge, S. Gourley, B. Ramsay, A. Wurl, M. Hyslop, and R. Blaikie, "Formation of Nanowires at the Percolation Threshold in Rectangular 2D Systems," San Diego, CA, United States, 2003, pp. 189-203.
[30] J. Schmelzer Jr, S. A. Brown, A. Wurl, M. Hyslop, and R. J. Blaikie, "Finite-size effects in the conductivity of cluster assembled nanostructures," *Physical Review Letters*, vol. 88, pp. 226802-1, 2002.
[31] R. Reichel, J. G. Partridge, A. D. F. Dunbar, S. A. Brown, O. Caughley, and A. Ayesh, "Construction and application of a UHV compatible cluster deposition system," *Journal of Nanoparticle Research*, vol. 8, pp. 405-416, 2006.
[32] A. D. F. Dunbar, J. G. Partridge, M. Schulze, and S. A. Brown, "Morphological differences between Bi, Ag and Sb nano-particles and how they affect the percolation of current through nano-particle networks," *European Physical Journal D*, vol. 39, pp. 415-422, 2006.
[33] J. Schmelzer, "Finite-size effects in cluster films," *Msc thesis, University of Canterbury*, 2001.
[34] J. Schmelzer, S. A. Brown, A. Wurl, M. Hyslop, and R. J. Blaikie, "Finite-size effects in the conductivity of cluster assembled nanostructures," *Physical Review Letters*, vol. 88, Jun 2002.
[35] *www.phys.canterbury.ac.nz/research/nano*.
[36] J. G. Partridge, S. A. Brown, A. D. F. Dunbar, R. Reichel, M. Kaufmann, C. Siegert, S. Scott, and R. J. Blaikie, "Templated-assembly of conducting antimony cluster wires," *Nanotechnology*, vol. 15, pp. 1382-1387, 2004.
[37] A. Awasthi, S. C. Hendy, P. Zoontjens, and S. A. Brown, "Reentrant Adhesion Behavior in Nanocluster Deposition," *Physical Review Letters*, vol. 97, p. 186103, 2006.
[38] R. Reichel, J. G. Partridge, F. Natali, T. Matthewson, S. A. Brown, and A.

Lassesson, "From the adhesion of atomic clusters to the fabrication of nanodevices," *Applied Physics Letters*, vol. 89, Nov 2006.

[39] G. Fuchs, P. Melinon, F. S. Aires, M. Treilleux, B. Cabaud, and A. Hoareau, "Cluster-beam deposition of thin metallic antimony films - Cluster-size and Deposition-rate effects," *Physical Review B*, vol. 44, pp. 3926-3933, Aug 1991.

[40] G. Fuchs, P. Melinon, Y. Yan, B. Cabaud, A. Hoareau, M. Treilleux, and V. Paillard, "Films of controlled nanosize grains deposited by low-energy cluster beam," *Zeitschrift Fur Physik D-Atoms Molecules and Clusters*, vol. 26, pp. S249-S251, May 1993.

[41] G. Fuchs, M. Treilleux, F. S. Aires, P. Melinon, B. Cabaud, and A. Hoareau, "Crystallization of thin antimony deposits on amorphous-carbon," *Thin Solid Films*, vol. 204, pp. 107-114, Sep 1991.

[42] *http://www.edn.com/article/CA6412897.html*.

[43] *http://www.sia-online.org/home.cfm*.

[44] *http://www.sia-online.org/downloads/Summary_November2004.pdf*.

Chapter 2

Experimental Equipment

This chapter describes the equipment used for cluster deposition and characterisation. In this work, three cluster deposition systems were used. The deposition systems are: a high-vacuum compatible (HV) system with an inert gas aggregation (IGA) source and an electron gun column; an ultra-high vacuum compatible (UHV) system with an inert gas aggregation source; and an ultra-high vacuum compatible (UHV) system with a magnetron sputtering source. The components of these systems are described in Section 2.1. Other than the deposition systems, the auxiliary components such as the mass filter, deflector, annealing stage and hydrogen chamber are also described.

2.1 Cluster deposition system

The section begins with a description of cluster formation in Section 2.1.1, followed by a description of the cluster systems used in this work. The HV system is described in Section 2.1.2, and the UHV system is described in Section 2.1.3. The magnetron sputtering source is described separately in Section 2.1.4.

2.1.1 Cluster formation

In an inert-gas aggregation source, a heated crucible is used. By heating the metal in the crucible, metal vapour is formed. The metal vapour then mixes with an inert gas flow which cools down the vapour and leads to a region with supersaturated metal vapour. In this region, the clusters nucleate by homogeneous nucleation and grow by an adsorption from the vapour and coalescence with other clusters. Homogeneous nucleation theory [1] describes the formation of a liquid droplet by condensation from the vapour.

The most relevant part of the nucleation theory for the present work is the equation relating the nucleation rate I to the temperature of the vapour T [1]:

$$I = s\frac{n^2}{\rho}\sqrt{\frac{2\gamma m}{\pi}}e^{\frac{-\Delta F^*}{k_B T}} = s\frac{P}{\rho k_B T}\sqrt{\frac{2\gamma m}{\pi}}n^* \qquad (Eq.2\text{-}1)$$

where s is the condensation coefficient, n is the number of monomers per unit volume, ρ is the density of a droplet, γ is the surface tension, m is the mass, ΔF^* is the maximum free energy, k_B is the Boltzmann constant, P is the pressure of the supersaturated vapour, and n^* is the density of critically-sized droplets.

The nucleation rate is directly proportional to the vapour pressure of the metal at a certain evaporation temperature. It is well known that the vapour pressure of the metal increases exponentially with temperature. Therefore, the higher the temperature of the heated metal, the higher the nucleation rate.

Once the nucleation has taken place the growth stage begins. As suggested in Ref. [2], increasing the inert gas pressure limits the vapour diffusion and provides better cooling. This results in a more effective condensation, a higher n^* and a higher nucleation rate. The increased number of clusters results in more coalescence and larger clusters. Increasing the flow rate of the inert gas reduces the time clusters spend in vapour rich regions, provided the source pressure remains constant. An increased flow rate will also tend to dilute the concentration of clusters resulting in less coalescence. Thus, both effects from the flow rate reduce the size of the clusters produced [3]. The details of the physics of cluster deposition can be found in Ref. [4-8].

2.1.2 High-vacuum compatible system

Figure 2-1 shows an overview schematic of a HV compatible cluster deposition system. The HV system consists of a cluster source, a high energy electron gun, an electron detector, and the beam sampling devices. The clusters are generated in an IGA source. The mixture of clusters and inert gas is pumped through two pumping stages into the diffraction chamber where it is probed by a high energy electron beam.

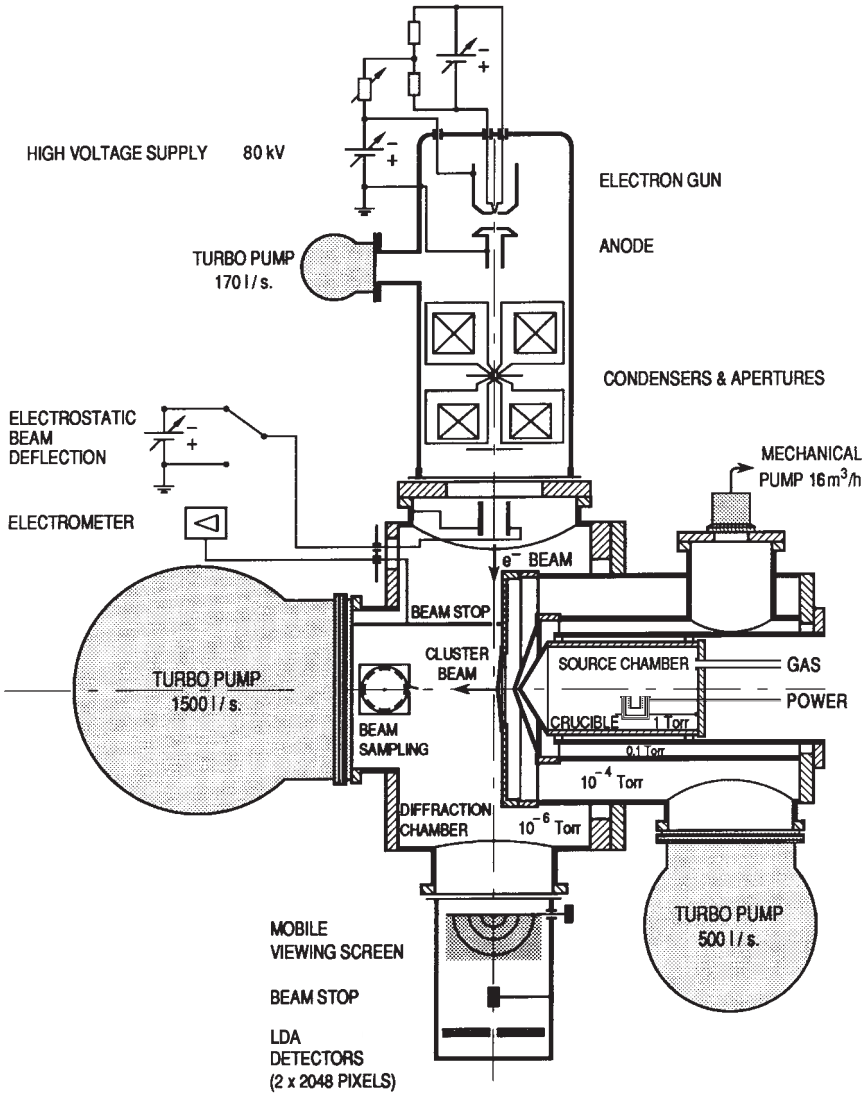

Figure 2-1 : An overview of the HV system. After Wurl [4] and Kaufmann [5].

Figure 2-2 shows the schematic of an evaporation inert-gas aggregation source and the pumping stages, with labels for various components which will be referred to in the text. The source chamber has an internal diameter of 87 mm and length of 110 mm. The flange fitted into the source chamber holds the crucible arrangement and has feedthroughs for an inert gas inlet, a K-type thermocouple, power feedthroughs and source pressure gauge. The flange and the source chamber are water-cooled to keep the source chamber walls at approximately room temperature during an experiment. A tantalum plate can be inserted into the source for process tuning. The plate is basically a copper plate wrapped by tantalum sheet.

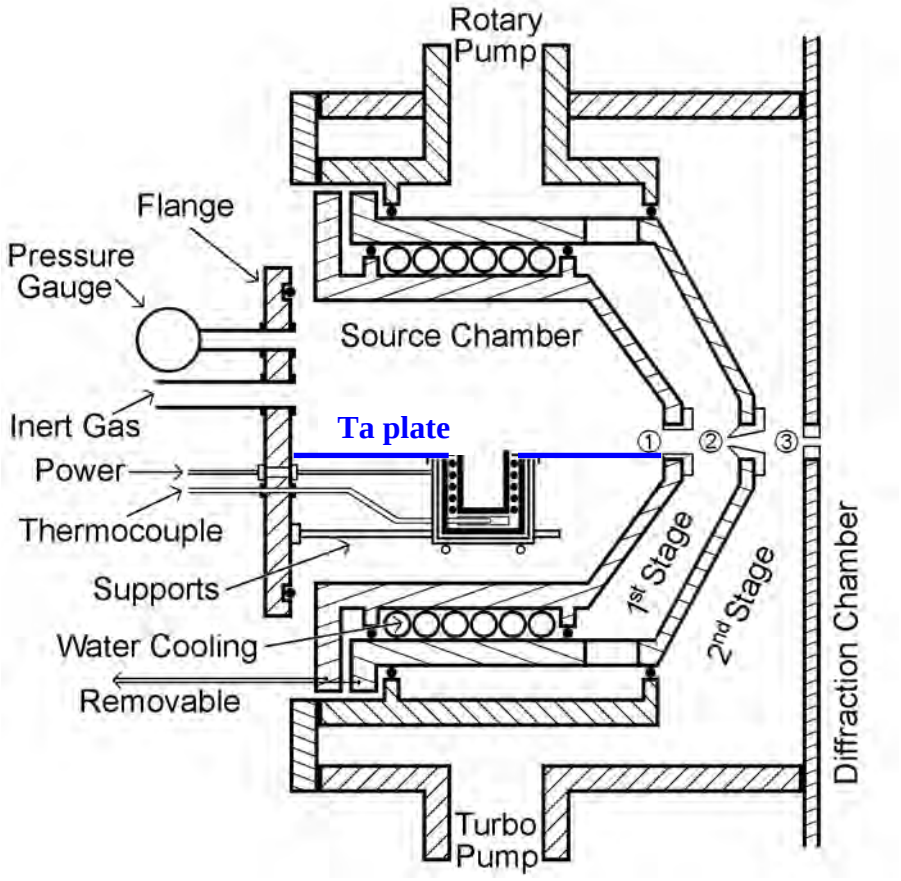

Figure 2-2: **Schematic of an inert-gas aggregation (IGA) source and the pumping stages. The numbers 1–3 denote the first, second and third stage nozzle. The tantalum plate was highlighted in blue. After Wurl [4] and Kaufmann [5].**

After the formation of clusters, the clusters are pushed through a series of nozzles because of the inert gas flow. The first-stage nozzle controls the formation of clusters and affects the cluster velocity. As reported by Kaufmann [5], the length and the diameter of the first-stage nozzle should be around 24 mm and 2.5-3.5 mm respectively for antimony clusters. A shorter nozzle or a nozzle with smaller diameter failed to generate a cluster beam with a high enough intensity for the diffraction experiments. The second-stage nozzle and the third-stage nozzle separate out the inert gas and the clusters.

There are limitations to the pressure at each stage, as described by Kaufmann [5]. He reported that the working pressure in the source was 1-10 Torr for argon gas and up to 20 Torr for helium gas, in order to achieve high enough diffraction intensity. The pressure in the first stage is kept below 0.1 Torr by the rotary pump (16 m^3/hr). Then the pressure in the second stage varies between 1×10^{-5} and 2×10^{-4} Torr and is

pumped by a turbo pump (500 l/s). The pressure in the diffraction chamber (or deposition chamber) is typically kept between 1×10^{-6} and 5×10^{-6} Torr by a turbo pump (1500 l/s) during the experiment. The pressure in the second stage is a limiting factor during experiments as the gas flow rate has to be limited to avoid overloading the turbo pump.

The source of the electron beam for the diffraction study is a modified Phillips EM300 Transmission Electron Microscope (TEM). The column of the TEM has been truncated below the condenser lens and mounted on top of the diffraction chamber. In this work, the acceleration voltage was set to 80 kV and the beam current was between 2 and 7 μA. Throughout the study, the filament of the electron gun has been changed a few times. The alignment of the electron gun is necessary before each operation. The gun is aligned by adjusting the tilt of the gun to maximise the current density. Then, to align the electron beam with the cluster beam, a needle on a retractable arm (not shown) in the diffraction chamber is positioned. The needle is located next to the calibration grids. A movable phosphorescent screen (labelled as 'Mobile Viewing Screen' in Figure 2-1) is positioned ~0.1 m above the detector. The shadow cast on the screen by the needle is used to align the electron beam. After the aligned and focused electron beam leaves the condenser, it passes though a beam blanking device. The device is basically a pair of parallel metal plates. When 400 V is applied across the plates, the electron beam is blanked by diverting into a graphite plate. As the graphite plate is connected to an electrometer, the current could be measured.

Figure 2-3 shows a schematic of the electron diffractograph. As the clusters are randomly oriented in the beam, the scattered electrons give rise to a Debye-Scherrer diffraction pattern. This diffraction pattern is recorded by a detector consisting of two linear diode arrays (LDA). Each LDA chip has 2048 pixels which each cover an area of 13μm by 13 μm. The details of the detectors were described in Ref. [5].This detector provides an *in-situ* method of measuring the phase of the unsupported clusters during the experiments. The details of the electron diffraction studied will be covered in Chapter 3. A UHV-compatible IGA system described in Section 2.1.3 is also capable of producing antimony clusters, but without this electron diffraction facility, *in-situ* electron diffraction can not be performed.

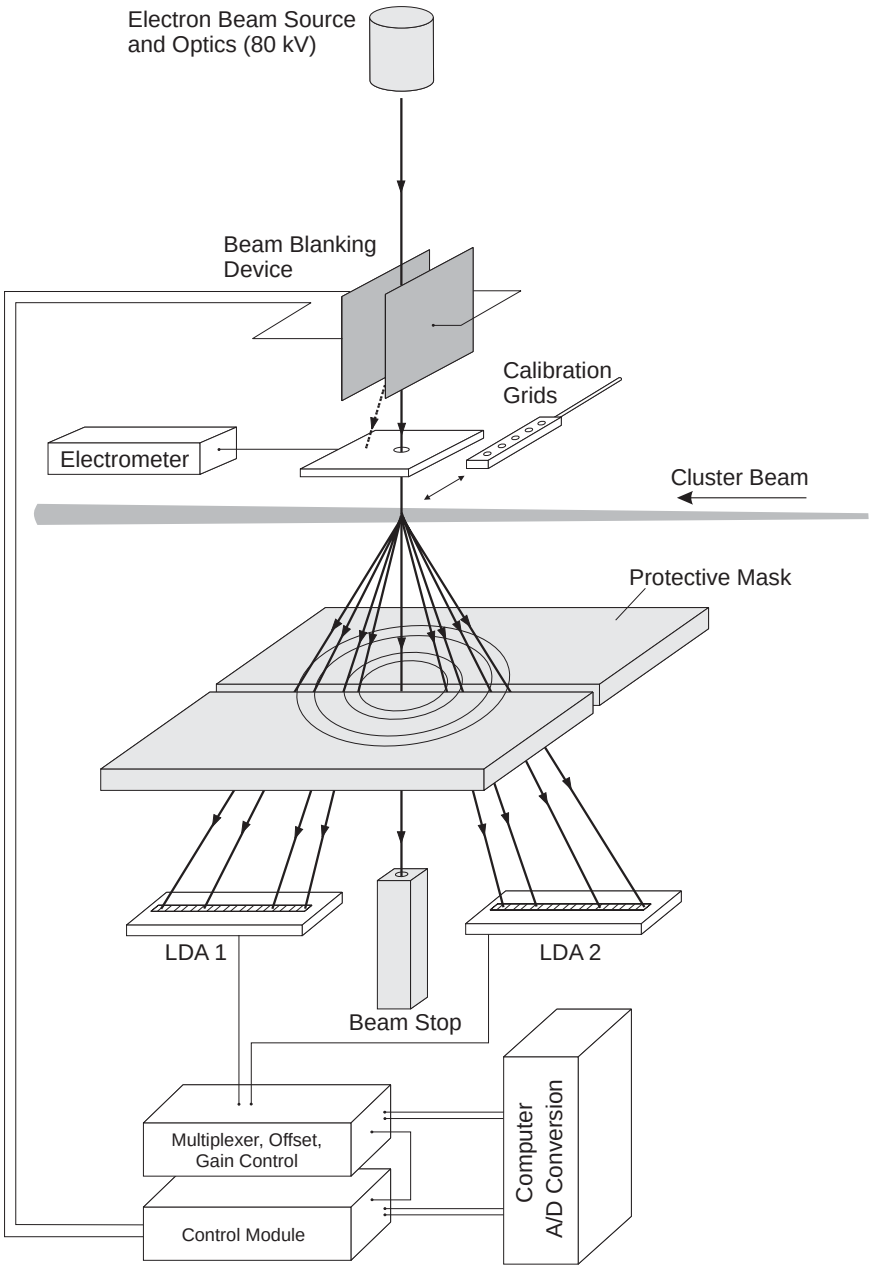

Figure 2-3: **Schematic of the electron diffractograph (not to scale). After Wurl [4] and Kaufmann [5].**

After crossing the electron beam, the clusters could be deposited on a sample or on a film thickness monitor (FTM). Figure 2-4 shows a close-up photograph of a sample arm with a built-in shutter. The shutter protects the samples and the FTM when the deposition is not needed. The grid holder can be replaced by a sample holder. The sample can be moved in and out of the beam for deposition. The Sycon Instruments STM-100/MF FTM is positioned at the back of the sample arm and is about 15 cm downstream from where the cluster beam enters the diffraction chamber.

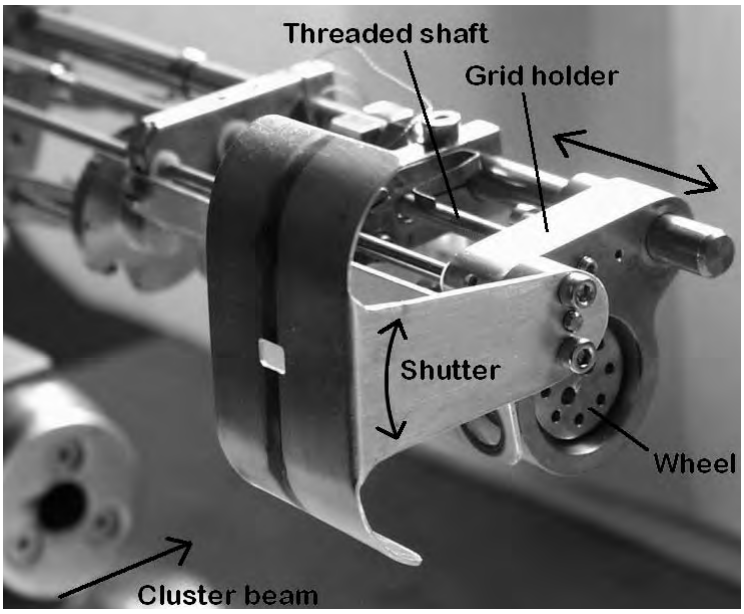

Figure 2-4: The sample arm with the built-in rotating shutter. After Ref. [5, 6]

The deposition steps are summarised below.

- A sample is loaded on a sample arm. Then the sample arm is loaded into the diffraction chamber through a loading port.
- The system is rough pumped to < 10^{-4} Torr, then isolated from the roughing system.
- The system is fine pumped with three turbo pumps at three different locations which are the second stage, the diffraction chamber and the electron gun column.
- A 20 sccm argon flow is slowly introduced into the source. When the source pressure reaches 10^{-1} Torr, the gate valve of the first stage pump is opened, allowing the gas to be pumped away by a rotary pump.
- Metal (i.e. antimony in this work) is thermally evaporated with a resistance-heated crucible. The deposition rate is monitored by the FTM prior to sample deposition.
- The voltage of the electron source is ramped up to 80 kV. The electron beam is aligned before measuring the diffraction patterns from the background gas and the clusters.
- After the desired phase of the clusters is detected, the sample arm is wound into the cluster beam. The clusters are deposited on the sample when the shutter is open.

2.1.3 Ultra-high-vacuum compatible system

Clusters can also be generated in a UHV-compatible system with an evaporation IGA source. Figure 2-5 shows a photo and schematic of the UHV system and the four pumping stages. There are three major differences between the HV and the UHV system. First, the travel distance for the clusters is longer in the UHV system. Second, the pressure in the deposition chamber can go down to an ultra high vacuum (1×10^{-8} Torr). Third, a cryostat or an annealing stage can be inserted into the deposition chamber, allowing $R(T)$ measurements or annealing of samples.

(a)

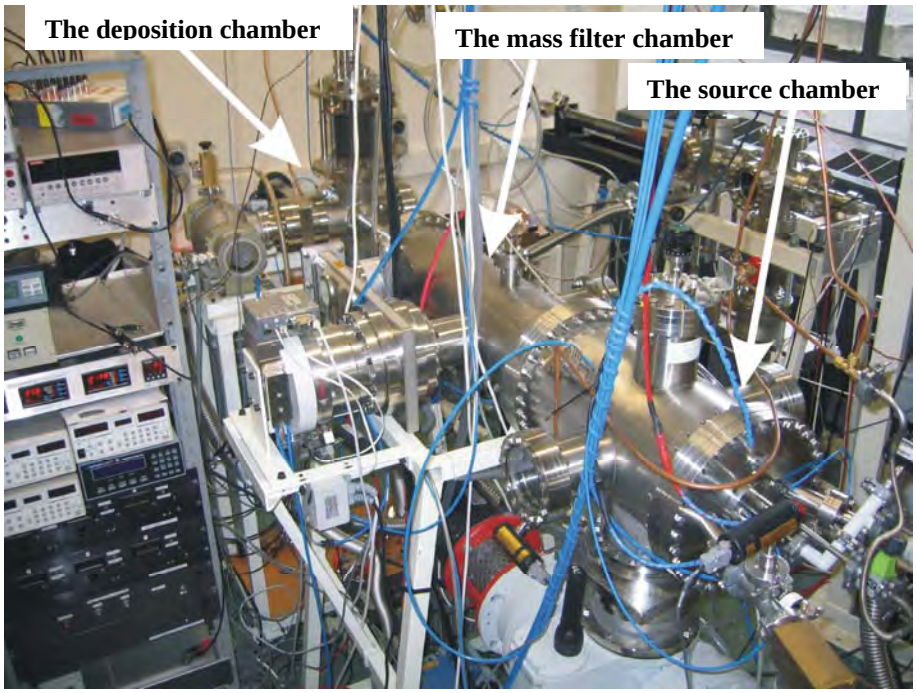

(b)

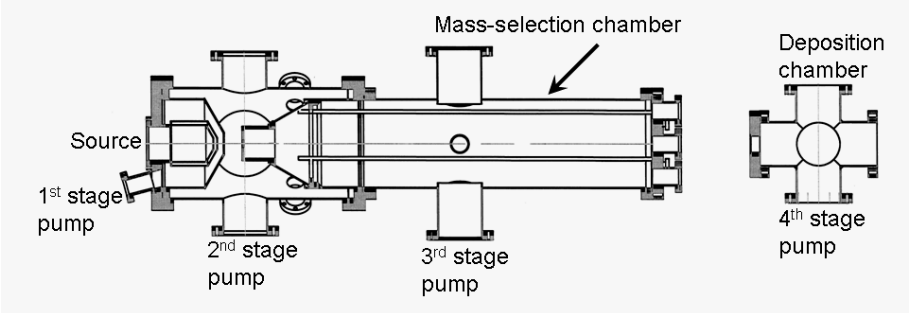

Figure 2-5: **(a) A photo and (b) a side view schematic of the UHV system showing the four pumping stages. After Reichel [7, 9] and Ayesh [8].**

Figure 2-6 shows a photo of the heat shields and the crucible components. As a high temperature is needed in the copper experiments (melting point of Cu is 1080ºC), three layers of tantalum heat shields are required.

Figure 2-7 shows a schematic of the deposition chamber. The FTM is placed in line with the cluster beam. A cryostat or annealing stage can be inserted from the top of the deposition chamber. For cooling down to liquid helium temperature, a heat shield is required for the cryostat. The temperature sensor is mounted at the back of the cold finger, while the samples are placed at the front. The deposition chamber has a 100 mm linear translator, allowing the cryostat or the annealing stage to move up and down along the vertical axis. The temperature range of the cryostat is from 1.2 to 450 K.

Figure 2-6: **Heat shields and crucible for the copper experiments. From left to right: three layer of heat shields, top lid for the heat shield, outer boron nitride crucible, inner boron nitride crucible and a boron nitride lid.**

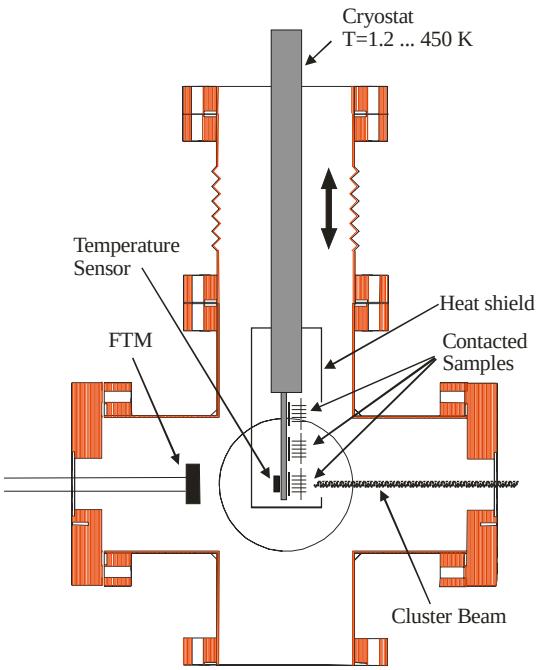

Figure 2-7: **A schematic of the deposition chamber. After Reichel [7]**

2.1.4 Magnetron Sputtering Source

A magnetron sputtering source, developed in a collaboration with the University of Freiburg [10], was used to produced neutral and ionised clusters inside the UHV system [9] in NCD Ltd's laboratory, as shown in Figure 2-8. A schematic of the magnetron sputtering source and the sputtering head is shown Figure 2-9. The shield of the sputtering head is electrically grounded and DC power is applied to the target. The coolant for the aggregation can either be liquid nitrogen or water. Compared to the IGA source, the metal vapour is generated from a sputtering process instead of resistive heating and additional process parameters can be tuned. For example, the power can be adjusted instead of the temperature control in the IGA source. It also has the flexibility of changing the aggregation length, which is the distance between the sputter target and the first-stage nozzle. The inert gases can be introduced from the back of the source chamber or from the sputtering head. There are two main advantages of the magnetron sputtering source over the IGA source. First, the vapour from a high melting point metal can be easily generated by the sputtering source. Second, the ionised clusters from the source allow the deposition to be mass-selected using a mass filter. The detailed description of the system can be found in Ref. [9].

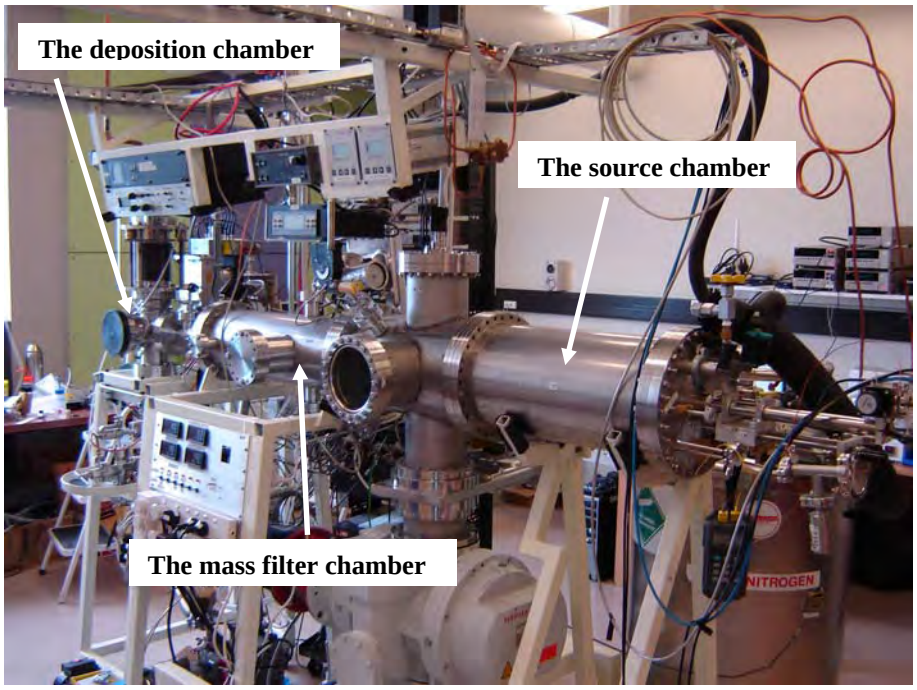

Figure 2-8: A photo of a UHV system equipped with a magnetron sputtering source.

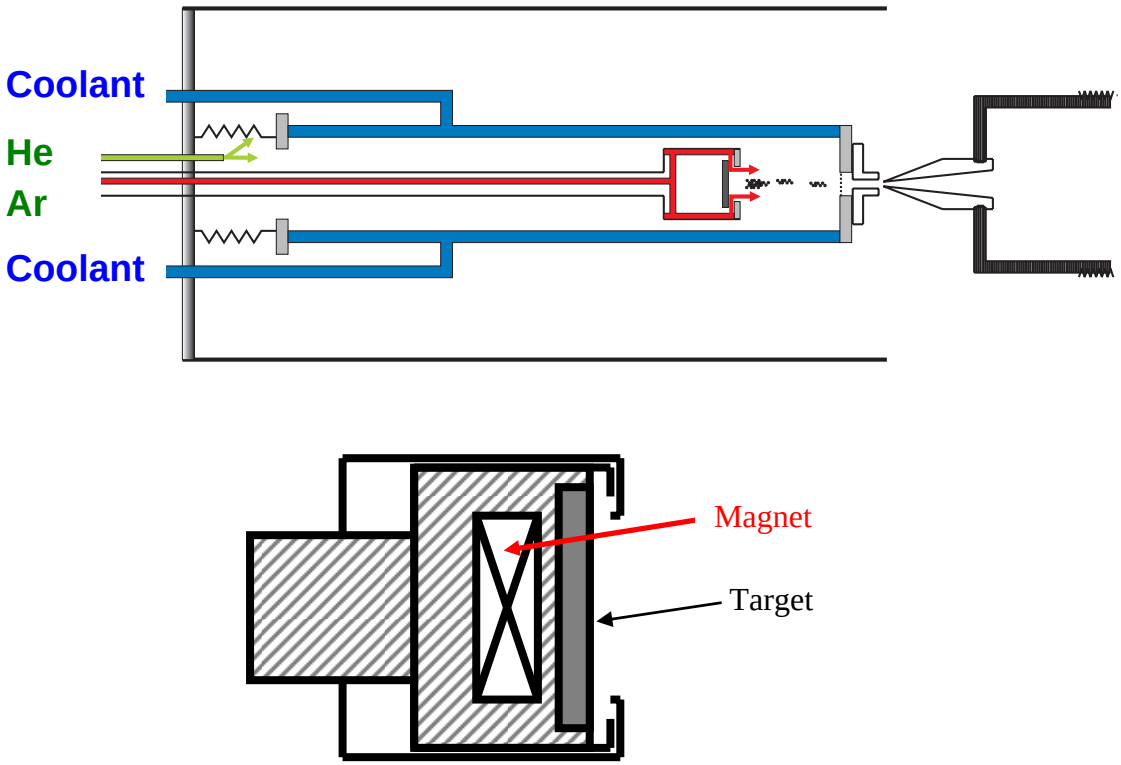

Figure 2-9: **(a) Schematic of a Magnetron Sputtering source. The coolant can either be water or liquid nitrogen. The inert gases can be introduced from the back of the system (green line) or from the sputtering head (red line).(b) Schematic of a Magnetron Sputtering head. The shield of the head is electrically grounded and a DC power is applied to the target. After Reichel [7].**

2.2 Mass filter

This section describes the design and the operation of a mass filter. The mass filter developed by von Issendorff and Palmer [11] has a high resolution with high throughput. Figure 2-10 shows a schematic design of the mass filter. It consists of four plates (plates 1 to 4); plates 2 and 3 have rectangular apertures for the clusters to pass through.

The operation is as follows: First, an ionised cluster beam enters the mass filter between plates 1 and 2. Second, a short high voltage pulse with the pulse time of t_p is applied to plate 2 while the other plates are grounded. The applied pulse accelerates the ionised clusters towards plate 3. The direction of the acceleration is perpendicular to the original direction of the cluster beam. The length of pulse should be short enough so

Figure 2-10: Schematic design for the von Issendorff & Palmer mass selection system. After Reichel [7].

that no clusters can leave the acceleration region during the pulse. Then, the clusters drift through a field free region between plates 2 and 3, and enter the deceleration region between plates 3 and 4. In order to decelerate the clusters to zero velocity in the direction where they gain the additional kinetic energy, a high-voltage pulse with the same magnitude but opposite polarity is applied between plates 3 and 4, as depicted in Figure 2-11. The time taken for the clusters to travel from the acceleration region to the deceleration region depends on the mass of the ionised clusters. Thus, the delay time t_d controls the clusters getting through the exit aperture. In this way, the clusters of the selected mass lose the velocity perpendicular to the original axis and regain the original flight direction, but are now offset in the position.

For measuring the mass spectrum of the cluster beam, a detector is placed at the exit of the mass filter. The detector of the signals is a simple Faraday cup and electrometer combination. The signal strength is proportional to the number of ionized clusters through the mass selection system. The mass distribution is obtained by varying the pulse time t_p and the delay time t_d. The pulse time and delay time for a given mass are determined by the desired lateral distance (a) the ionised clusters cover during the acceleration (and deceleration), and the lateral distance (b) the ionised clusters cover in the field free region respectively [11], i.e.

$$t_p = \frac{2a}{\sqrt{2eV_p / m}} \qquad (Eq.2\text{-}2)$$

$$t_d = \frac{b}{\sqrt{2eV_p / m}} \qquad (Eq.2\text{-}3)$$

where m is the mass of the ionised clusters; $b=y-2a$ where y is the vertical distance

between the centres of the entrance and exit slits; eV_p is the energy the ionised clusters gain from the high voltage pulse:

$$eV_p=(a/d)eV_a \qquad (Eq.2\text{-}4)$$

where V_a is the applied pulse height, and d is the separation between Plates 1 and 2.

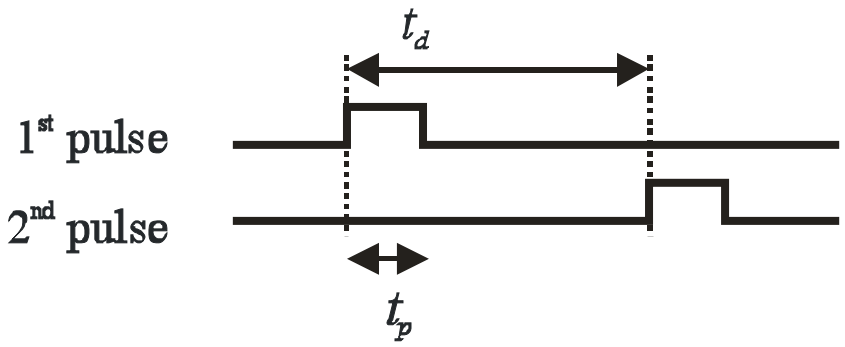

Figure 2-11: **Mode of operations for the von Issendorff & Palmer mass filter and a deflector. For the mass filter, two high-voltage pulses are applied to plate 2 and plate 3 (see Figure 2-10). The timing t_d determines the masses selected. For the deflector, one pulse is applied, while the second pulse is measured on the Faraday cup. The timing t_d determines the time travelled by the clusters.**

The mass resolution ($M/\Delta M$) of the mass filter depends on the exit opening Δx and the spacing x (lateral displacement between the entrance and the exit) of the mass filter. As the $M/\Delta M$ ratio is fixed over the entire mass range, the range of the masses being detected (ΔM) is proportional to the mass selected (M). Therefore, the measured signals have to be corrected by dividing by M in order to achieve the true mass distribution. In this work, the same mass filter reported by Ayesh *et al.* [12] was used. They reported that the $M/\Delta M$ ratio was ~12 for palladium clusters. Further results of experimental and simulation studies are discussed elsewhere [8, 12].

2.3 Deflector

In this work, a deflector built by Andreas Lassesson of Nano Cluster Devices Ltd. was used to measure the velocity of the copper clusters. The deflector is essentially a pair of 6 cm long plates. The same detector as for the mass filter is used. The plates are separated by 1.8 cm and the field free region is 65 cm long.

When a high voltage pulse is applied to the deflector, the ionised cluster beam is bent towards the Faraday cup, as shown in Figure 2-12. Then a pulse is detected from the Faraday cup. The delay time t_d between the two pulses (as depicted in Figure 2-11) is measured by an oscilloscope. The velocity of the clusters is equal to the distance between the deflector and the Faraday cup divided by t_d.

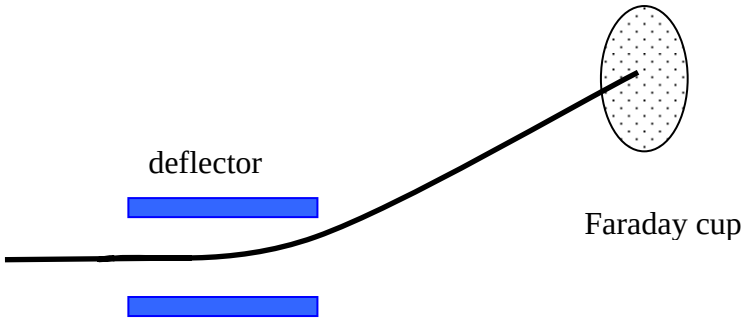

Figure 2-12: Mode of operation for a deflector. Drawing is not to scale.

2.4 Annealing stage

An annealing stage has been designed for this work in order to anneal cluster films at a high temperature (~450ºC). A MDC multiple-port Conflat® flange is used as a support for the two stainless steel water tubes, a water reservoir, a boron nitride spacer and a copper block. Samples are placed on the copper block as shown in Figure 2-13. A K-type thermocouple is attached to the side of the copper block. A heat shield (not shown) is used to prevent the radiation heat loss. At 5 Torr hydrogen pressure, the samples could be heated up to 450ºC in the annealing stage.

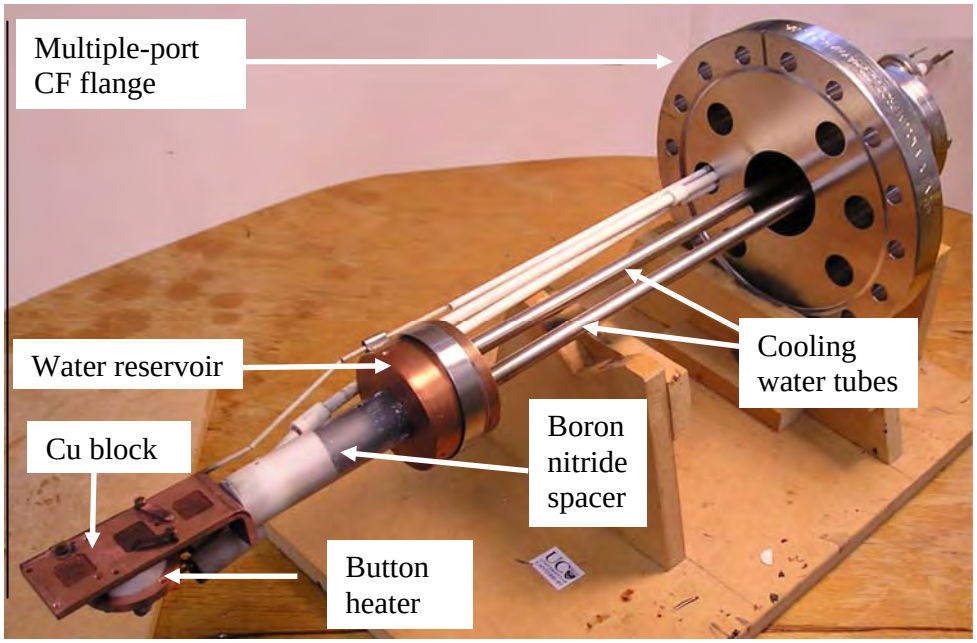

Figure 2-13: A photo of the annealing stage.

2.5 Hydrogen transfer chamber

As hydrogen is a flammable gas, introducing hydrogen into the cluster system requires special handling. A hydrogen transfer chamber was built to control the gas flow into the system. Figure 2-14 shows the hydrogen transfer chamber designed by Ahmad Ayesh of University of Canterbury and Monica Schulze of NCD Ltd. The transfer chamber consists of two Conflat® four-way crosses, two needle valves, a capacitance diaphragm gauge and two leak valves. One leak valve is for the transfer chamber and one is for the deposition chamber. The operation is as follows: Firstly, the deposition chamber is pumped by the turbo pump and the backing pump to below 10^{-5} Torr. Then, the gate valve between the turbo pump and the deposition chamber is closed. The hydrogen chamber and the gas pipe are pumped by a rotary pump and then disconnected by the valve. Around 100 Torr of H_2 gas is introduced to the cross #1 through needle valve #3. The pressure of the H_2 gas is monitored by the capacitance diaphragm gauge. Lastly, the H_2 gas is introduced to the cross #2 which is connected to the deposition chamber through needle valve #4. The pressure of the deposition chamber will be around 5 Torr.

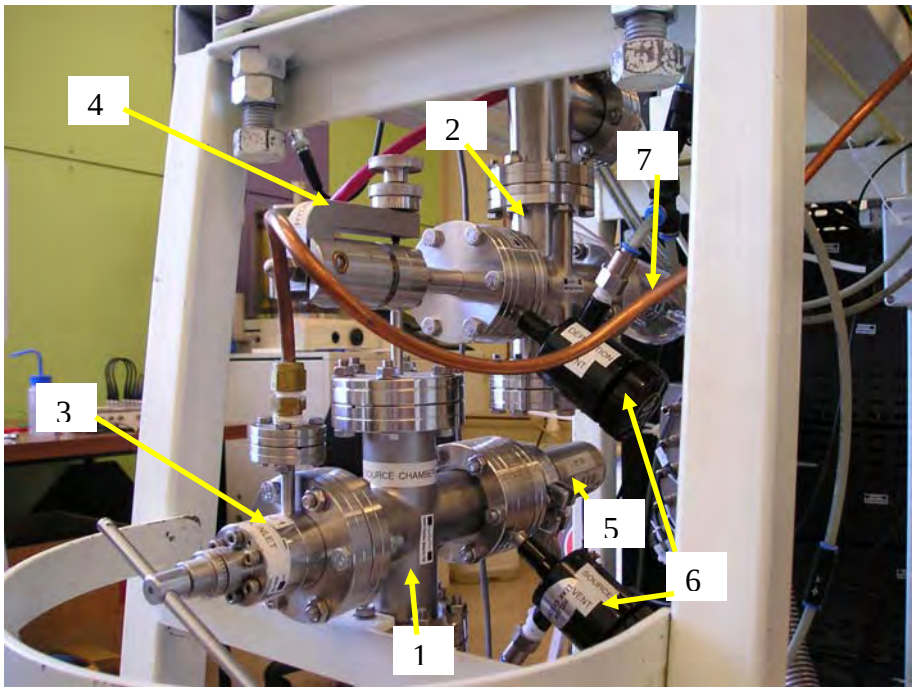

Figure 2-14: **A photo of the hydrogen transfer chamber. The numbers #1-2 denote the two Conflat® four-way crosses; the numbers #3-4 denote the two needle valves. The capacitance diaphragm gauge and the leak valves are labelled as numbers 5 and 6 respectively. The number #7 denotes the ion gauge.**

2.6 Summary

This chapter has described the three different cluster deposition systems. For the amorphous antimony experiments, the HV system was used. The electron diffraction capability of the system allowed the analysis of the phase of the unsupported clusters. The copper clusters were produced in an UHV system with an IGA source or a magnetron sputtering source. The ionised clusters produced by the magnetron sputtering source can be analysed and mass-selected by a mass filter. The velocity of the ionised clusters can be measured by a deflector. The temperature of the deposited samples can be adjusted from 1.2 to 450 K in a cryostat. A high temperature annealing can be achieved with an annealing stage either at vacuum or in a hydrogen environment. To introduce hydrogen gas into the deposition chamber, a hydrogen transfer chamber is required for safety purposes. The description of other analytical tools such as field emission scanning electron microscope (FE-SEM) and atomic force microscope (AFM) were described in Refs. [8, 13].

References

[1] F. F. Abraham, *Homogeneous Nucleation Theory*. New York: Academic Press, 1974.

[2] C. G. Granqvist and R. A. Buhrman, "Ultrafine Metal Particles," *Journal of Applied Physics*, vol. 47, pp. 2200-2219, 1976.

[3] F. Frank, W. Schulze, B. Tesche, J. Urban, and B. Winter, "Formation of Metal-Clusters and Molecules by Means of the Gas Aggregation Technique and Characterization of Size Distribution," *Surface Science*, vol. 156, pp. 90-99, 1985.

[4] A. Wurl, "Electron diffraction studies of unsupported bismuth clusters," *PhD thesis, University of Canterbury*, 2003.

[5] M. Kaufmann, "Electron diffraction studies of unsupported antimony clusters," *PhD thesis, University of Canterbury*, 2006.

[6] M. Hyslop, "Electron Diffraction Studies of Unsupported Clusters," *PhD thesis, University of Canterbury*, 2002.

[7] R. Reichel, "Nano Scale Cluster Devices," *PhD thesis, University of Canterbury*, 2007.

[8] A. Ayesh, "Device fabrication using Bi nanoclusters," *PhD thesis, University of Canterbury*, 2007.

[9] R. Reichel, J. G. Partridge, A. D. F. Dunbar, S. A. Brown, O. Caughley, and A. Ayesh, "Construction and application of a UHV compatible cluster deposition system," *Journal of Nanoparticle Research*, vol. 8, pp. 405-416, 2006.

[10] H. Haberland, "US patent #5110435," 1992.

[11] B. V. Issendorff and R. E. Palmer, "A new high transmission infinite range mass selector for cluster and nanoparticle beams," *Review of Scientific Instruments*, vol. 70, pp. 4497-4501, December 1999 1999.

[12] A. I. Ayesh, A. Lassesson, S. A. Brown, A. D. F. Dunbar, M. Kaufmann, J. G. Partridge, R. Reichel, and J. van Lith, "Experimental and simulational study of the operation conditions for a high transmission mass filter," *Review of Scientific Instruments*, vol. 78, May 2007.

[13] S. A. Scott, "Self-Assembly of Sb and Bi Nanostructures on Graphite," *PhD thesis, University of Canterbury*, 2005.

Chapter 3

Background for cluster-deposited amorphous antimony films

Antimony is a silver-white semi-metal with a density of 6.68×10^3 kg m^{-3} and a melting point of 630.6ºC [1]. Antimony can be used as a doping material in advanced silicon devices [2] and photoconductors [3]. Like other group V(A) materials in the periodic table such as phosphorous and arsenic, antimony has several allotropic modifications. Besides the gray form of antimony, which is the most common form, there is another peculiar form, discovered in 1855 [4]. When the film is heated or scratched, a considerable quantity of heat is released. Thus, this form of antimony is classified as "explosive". After the "explosion", the metal is indistinguishable from ordinary antimony. The explosive antimony is amorphous and the explosion is simply a rapid exothermic crystallization [4, 5].

Researchers discovered that antimony (Sb) in its amorphous phase has an energy bandgap ranging from 0.12 to 0.24 eV [6, 7]. In short, amorphous antimony is a semiconductor similar to tetrahedrally bonded semiconductors such as amorphous Ge [8]. One purpose of the thesis is to investigate the semiconducting behaviour of amorphous antimony cluster films and to see if a gate-controlled (field-effect) conduction modulation can be achieved.

This chapter reviews the literature of antimony films and presents background material on the use of atomic clusters for forming crystalline and amorphous antimony films. Sections 3.1 and 3.2 review the amorphous antimony films produced by molecular beam deposition (MBD) and cluster deposition respectively. Section 3.3 reviews the different transport properties in MBD films, nanowires and cluster films. A previous study at the University of Canterbury of the electron diffraction from unsupported antimony clusters is summarised in Section 3.4. To analyse the deposition of cluster

films, percolation theory, a theory for analysing particles occupying a lattice randomly, is briefly described in Section 3.5.

3.1 Molecular Beam Deposition

There are several ways to prepare amorphous antimony films, such as sputtering by arc melting, evaporation, flash evaporation and cluster deposition [9-16]. It is important to understand the differences among these depositions and the characteristics of the films. Most reports have focused on evaporation techniques, so these reports are reviewed first. There are two ways of producing amorphous antimony by evaporation: (a) to deposit while the substrate is held at room temperature and (b) to deposit at cryogenic substrate temperatures such as liquid oxygen or liquid nitrogen temperatures. Since the substrate temperature plays an important role in the film properties, the conventional evaporation (no substrate cooling) and the evaporation with substrate cooling are discussed in Sections 3.1.1 and 3.1.2 respectively.

3.1.1 Conventional evaporation

In conventional evaporation, antimony is heated in a resistively heated crucible and there is no substrate cooling. The antimony vapour could be generated in different molecular forms depending on its source. Antimony could be evaporated as Sb_4 molecules from elemental antimony and predominantly as mono-atomic Sb molecules from PtSb alloy [9]. When antimony molecules (Sb_4 or Sb) are deposited on the substrate they will diffuse and nucleate on the preferential sites. Depending on the deposition source and the substrate, a number of interesting phenomena have been observed in evaporated thin antimony films.

In 1933, Prins observed that the diffraction patterns of a *thin* amorphous antimony film remained after six months, but the amorphous antimony film with a *medium* thickness (thickness was not mentioned) crystallised within a few hours across the whole film [10]. It was also reported by other groups that the phase of the evaporated films

depended on the deposited thickness [11-14]. Table 3-1 summarises different critical thicknesses above which the amorphous antimony films crystallised. Taft *et al.* identified the semiconducting behaviour of amorphous antimony film by a photoelectric experiment [11] and then examined the transition using $I(V)$ curves. Others reported the transition by the change of resistance of the films or electron diffraction patterns or transmission electron micrographs (TEM). It was found that the critical thickness for crystallisation d_{crit} ranged from 100 to 300 Å for different substrates.

Ghosh *et al.* reported that the amorphous phase could be affected by the vacuum condition of the evaporator [12]. They evaporated amorphous antimony films without applying substrate cooling at two different pressures: 10^{-5} and 5×10^{-8} Torr. It was found that both films were amorphous under TEM when the thickness was below 120 Å. At this thickness, the films were comprised of discrete islands. When the films were thicker and continuous across a pair of electrodes, the film deposited in the high vacuum (10^{-8} Torr) became crystalline and the other remained in its amorphous nature. They proposed that at a low vacuum the antimony islands were covered with a layer consisting of a very large number of adsorbed gas atoms. The Sb_4 tetramer therefore had to penetrate this layer of gases to reach the metal underneath. In this process it would lose a considerable fraction of its energy in collisions with the gas molecules on the surface and liberate some of the adsorbed gas atoms. Finally the cluster reaches the metal layer with insufficient energy to break the 'frozen-in' (amorphous) structure already existing. In a high vacuum however, the loss of energy of the impinging atom clusters was low. Thus they were able to impart a sufficient energy for the crystallization to take place. Even if they were capable of generating crystallization of only a small region of the film, the heat of crystallization liberated could help the crystallization of other neighbouring regions because the crystallization was an exothermic process (explosive) [12].

Table 3-1: Critical thickness for amorphous antimony in conventional evaporations.

No	Year	Substrate	Characterisation method	Critical thickness (Å)	Ref.
1	1954	concentric-sphere phototube	photo-emission and its current voltage characteristic	300	[11]
2	1971	glass substrate	electron diffraction	100	[13]
3	1974	amorphous carbon	TEM and electrical resistance measurement	120	[12]
4	1974	glass substrate	electrical resistance	100-200	[14]

Maki reported the change in resistivity and density during the growth of amorphous antimony films [14, 17]. The resistivity dropped from 2 Ω cm to 10^{-3} Ω cm between 100 and 200 Å. The crystallisation followed shortly after the continuity of the films. Maki observed that the change in density could be divided into two stages: a) the density changed drastically at d_o, at which the coalescence of the islands became dominant; and b) a gradual change in density in the vicinity of d_{crit}, at which the coalescence of islands was almost completed but started to crystallise. For films thicker than d_{crit}, the films were in a crystalline phase. Different densities between amorphous and crystalline antimony films (5.83 and 6.684 g cm^{-1}) were also reported by Aymerich *et al.* using electrolytic deposition [6]. Maki then reported that d_{crit} varied depending on the way the silicon dioxide substrates were prepared [18].

Cohen reported that when the evaporation was conducted without substrate cooling, the distance between the substrate and evaporator source could affect the film property [19]. He showed that the antimony film deposited at 4 cm distance from the source had a positive temperature coefficient of resistance (TCR) and the film deposited at 8 cm distance had a negative temperature coefficient of resistance, when the substrate was not cooled. In this case, the substrate could be heated by the evaporator source as the distance reduced. However, the magnitude of the negative TCR was very small. Therefore, there is insufficient evidence to show that the antimony film prepared by this method is a semiconductor. The next section discusses evaporation with substrate cooling.

3.1.2 Deposition with substrate cooling

As discussed in the previous section, Cohen showed that films deposited at room temperature could have a very small magnitude of TCR, provided the distance from the substrate and the evaporator was far enough. He also demonstrated that antimony evaporated on a liquid oxygen cooled substrate exhibited a semiconducting behaviour: negative TCR regardless of the distance between substrate and evaporator source [19]. The activation energy of the $R(T)$ curves at a low temperature (90 to 130K) and a high temperature (130K to 200K) were 0.07eV and 0.13eV respectively. The thickness and the deposition rate did not have any effect on the activation energy.

Cohen evaporated the amorphous antimony films at three different substrate temperatures (room temperature, 195 K and liquid oxygen temperature) and then measured the resistances at different temperatures. He observed that the $R(T)$ curves were reproducible as long as the substrate temperature did not exceed the temperature at which they were prepared. Figure 3-1 shows a schematic diagram of resistance versus temperature for a 370 Å thick film deposited at liquid oxygen temperature. Each time the sample was heated, the resistance changed when cooled back to liquid oxygen temperature. Irreversible re-crystallisation occurred at room temperature (293 K) and the resistance did not increase at a low temperature. He attributed the semiconducting behaviour of the films to the film defects.

However, Trefny *et al.* reported that films (with thicknesses from 0.38 to 0.96 μm) deposited at 106 K crystallised at a higher temperature [20]. They observed a change of resistance and TCR when the film was heated above 235 K. Thus, the crystallisation temperature did not agree with Cohen's results [19]. However, both Cohen and Trefny did not observe the thickness dependence of the crystallisation described in the previous section.

For the films prepared by evaporation without substrate cooling, re-crystallisation took place when the films reached the critical thickness or became continuous. For the films prepared by evaporation with substrate cooling, they generally re-crystallised at room temperature. Thus, the application of the amorphous antimony as a semiconductor (with

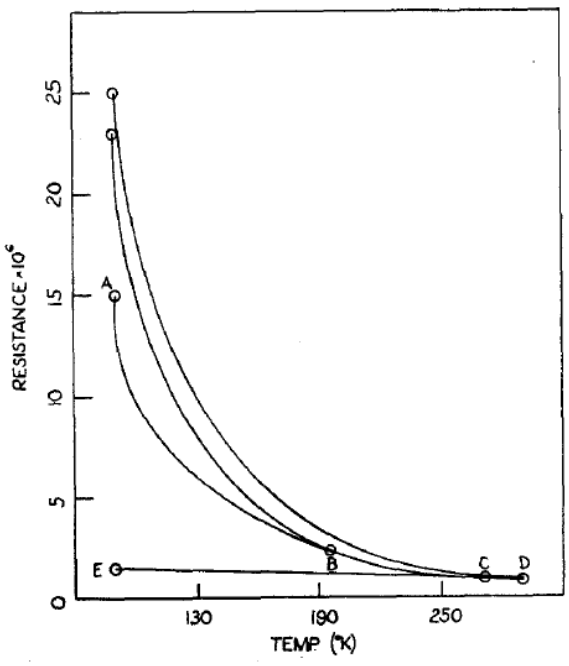

Figure 3-1: **Schematic diagram of resistance versus temperature for a 370Å thick film deposited at liquid oxygen temperature. The sequence of the temperature treatment: a) a steady state after deposition, b) heated to 195 K and cooled down, c) reheated and cooled down and d) reheated to 293 K and cool down to e) After Ref. [19].**

a large TCR) is limited to cryogenic temperatures. The next section presents a cluster deposition technique that has a transition temperature from amorphous to crystalline higher than room temperature.

3.2 Cluster deposition

As described in Chapter 1, clusters are very small particles containing upwards of a few atoms or molecules and have many interesting and unusual properties [21-24]. For example, when metallic clusters are small enough, they transform into semiconductors [22]. The characteristics of clusters (such as diameter, kinetic energy and the amorphous/crystalline phase), the deposition rate, and the substrate temperature control the film growth and properties. Antimony clusters have been produced in various ways, such as flow gas evaporations (FGE) by Tanaka *et al.* [25, 26]; low energy cluster beam depositions (LECBD) by Fuchs *et al.* [27-30] and Mélinon *et al.* [15, 31, 32]; and ionised cluster beam depositions (ICBD) by Takagi *et al.* [33-35]. For all cluster

deposition techniques, the quenching of a molecular vapour inducing the formation of a cluster beam is the basic mechanism, as described in Chapter 2. In particular, LECBD is a technique that deposit clusters at a kinetic energy of ~1 eV, while ICBD is a technique that deposits ionised clusters. In the case of ICBD, since the clusters are ionised, the kinetic energy can be adjusted by applying an external electric field. The kinetic energy of the clusters is one of the important factors influencing the properties of the cluster film.

As depicted in Figure 3-2, depending on the impact energy *E* of the clusters, there are different mechanisms for the cluster-surface interaction, such as soft landing, plastic deformation, fragmentation, implantation, embedding, reflection, sputtering and surface damage [36]. Figure 3-3 shows the reduced impact energy versus the relative binding energies (the cohesive energies) of the surface and the cluster. In this case, The binding energy of antimony cluster is defined as the energy to remove an Sb_4 entity from a cluster.

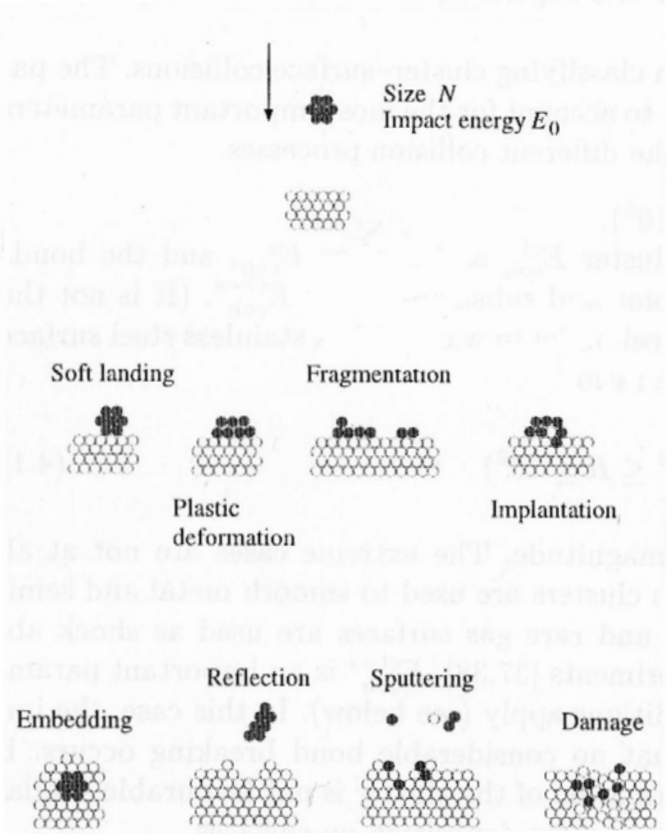

Figure 3-2: Fundamental processes in cluster surface collisions. After Ref. [36].

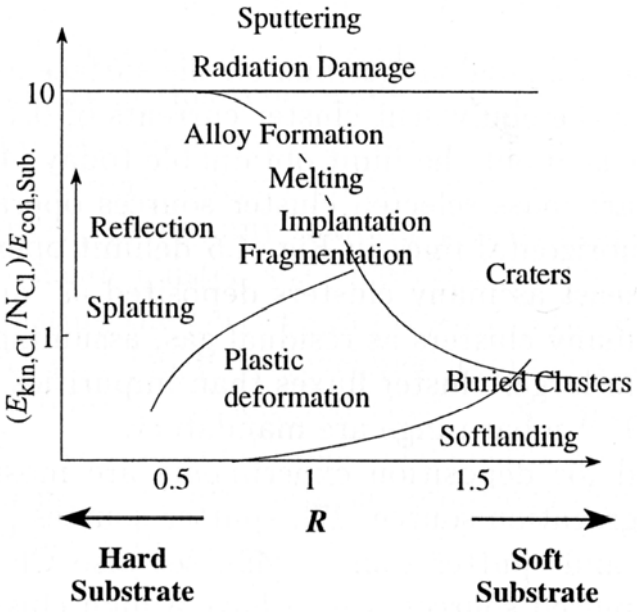

Figure 3-3: Mechanism diagram in cluster surface collisions. Reduced energy vs. relative binding energy $R = E_{cl,\,coh} / E_{s,\,coh}$. After Ref. [36].

Fuchs *et al.* was the first group who grew antimony films by cluster deposition and studied the difference in the properties of the LECBD and MBD films [30]. They observed that the films made of clusters with less than 2 nm diameter only started to crystallise at 623 K [37]. In the same year, Jensen *et al.* also reported that the LECBD allowed the preparation of continuous, stable and amorphous antimony films at room temperature [15]. Their amorphous films, which were made of clusters with 10 nm diameter, crystallized at 323 K and 350 K for 97 nm and 13.5 nm thick films respectively [32]. Each amorphous domain crystallised individually in the normal rhombohedral Sb structure without any shape or grain size modification [15].

Tanaka *et al.* reported the activation energy for crystallisation was 1.4 - 1.85 eV for clusters with 30 nm diameter and 1.72 - 2.01 eV for clusters with 10 nm diameter, using flow gas evaporation [25, 26]. They suggested that the rearrangement of the Sb_4 molecules (a crystallisation process) was suppressed by the high iso-static pressure induced by the surface curvature of the small clusters. However, this assertion contradicts Mélinon *et al.*'s assertion that when the size of the free low energy clusters increases, the surface diffusion becomes low enough to neglect the growth of supported clusters [38]. Therefore, the relation between crystallisation and the cluster diameter is not fully understood.

In summary, the amorphous antimony films prepared by cluster deposition have much higher transition temperature compared to the films prepared by MBD at cryogenic temperatures. The transition temperature of the films depends on the cluster diameter of the films. It would be interesting to examine whether the electronic transport properties of the MBD films and the cluster films are identical, as will be discussed in the next section.

3.3 Electronic transport properties

As described in the previous section, continuous amorphous Sb films can be prepared by MBD at cryogenic temperatures or by cluster deposition. It is important to understand the electronic transport properties of these films in a greater detail, especially for $R(T)$ curves. In addition, it is important to understand the differences in the $R(T)$ between the amorphous antimony and the crystalline antimony. Therefore, there are some reports on the crystalline antimony nanowires, which are worth comparing. This section discusses different electronic transport properties of MBD films, nanowires and cluster films. In particular, the polarity of the TCR for each of these films is described.

3.3.1 MBD films

Hauser prepared amorphous antimony films at 77 K in three different ways: gettering sputtering, evaporation from Sb and evaporation from PtSb [16]. Figure 3-4 shows the $R(T)$ curves of the films. The electrical resistance of all three types of films was well fitted between 30 and 160 K by variable range hopping predicted by Mott [39]:

$$\rho = \rho_o \exp\left[(T_o/T)^{1/4}\right] \qquad (Eq.\ 3\text{-}1)$$

where T_o is approximated to be 10^7 K.

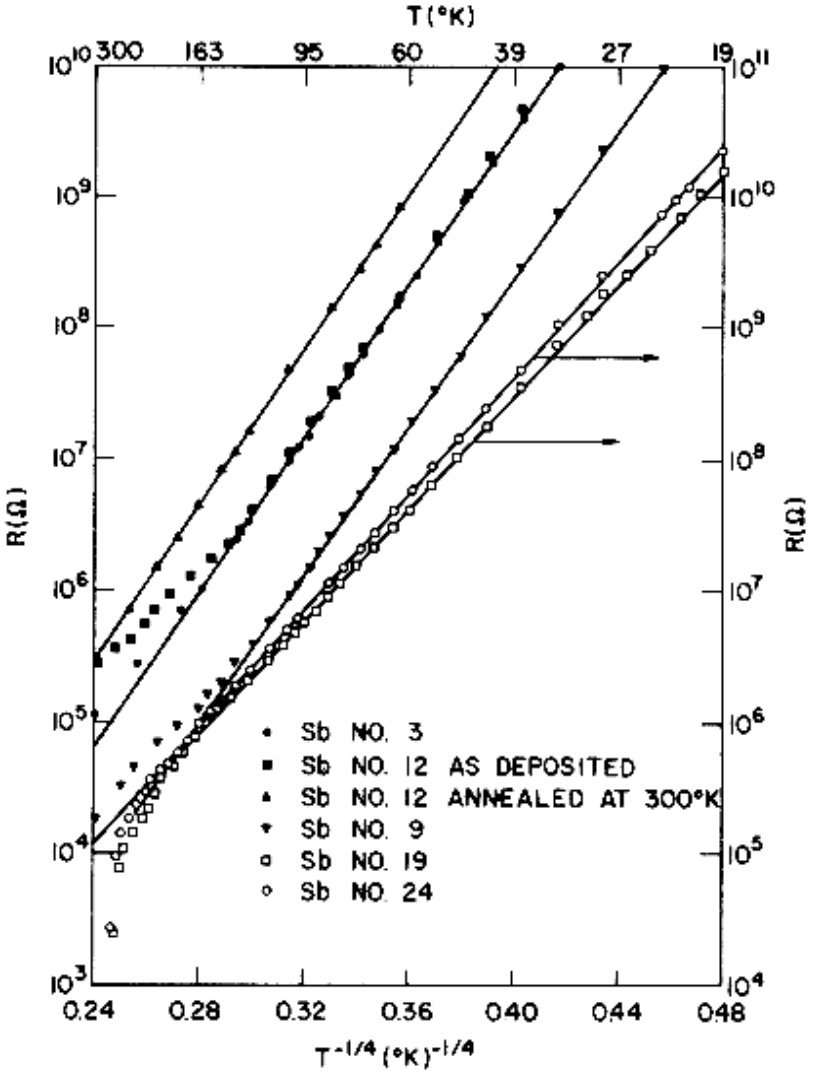

Figure 3-4: **Temperature dependence of the resistance for sputtered Sb films (solid symbols) and evaporated Sb films (open symbols); note that the data for evaporated films are plotted against the right axis. Sb No. 19 was evaporated from pure Sb while Sb No. 24 from PtSb. After Ref. [16].**

The temperature dependence of $T^{-1/4}$ suggested a thermally activated hopping conductivity via localised states similar to amorphous silicon and amorphous germanium [40]. Hauser also reported two different observations for sputtered films and evaporated films. The *sputtered* films underwent an irreversible increase in the resistance above 160 K, and then the films re-crystallised at 40ºC. However, the *evaporated* films underwent a reduction in the resistance above 180 K and recrystallised at 270 K [16]. Thus, he suggested that the evaporated films could have a greater extent of short-range order or micro cracks than sputtered films, because they could be recrystallised easily.

Mackintosh *et al.* prepared amorphous antimony films on sapphire substrates at 77 K. The measured electrical resistances showed a $T^{-1/3}$ behaviour for 2-D (<200 Å) films and a $T^{-1/4}$ behaviour for 3-D films at temperatures between 10 and 77 K [41]. The same $T^{-1/4}$ behaviour was also observed by Möckel *et al.* [42].

3.3.2 Nanowires

This sub-section reviews the experimental results on antimony nanowires prepared in porous anodic alumina templates using the vapour phase deposition technique by three different groups [43-45]. With these templates, nanowires with various diameters were formed by controlling the channel diameter of the templates. By placing the electrodes at both ends of the templates after deposition, the electrical resistance of the array were measured.

Barati *et al.* prepared the antimony nanowires with channel diameters of 20, 100 and 200 nm [43]. Figure 3-5 shows the $R(T)$ curve of a 20 nm antimony nanowire array after post annealing at 175ºC. The post annealing crystallised nanowires and decreased the resistivity after annealing 150-175ºC. The crystalline phase was identified by x-ray diffraction. After annealing, the resistance increased as the temperature decreased. Instead of relating this phenomena to semiconducting behaviour, Barati *et al.* attributed the $R(T)$ curves to the small dimension or the surface scattering but without further explanation.

Zhang *et al.* prepared nanowires with nanowire diameters from 9 to 40 nm [44]. All the nanowires they made had a preferred orientation along the [110] crystal direction. Figure 3-6 shows the $R(T)$ curves of their nanowire arrays. Due to localisation, the TCR could be positive or negative depending on the diameter of the nanowires. For 15 nm and 9 nm nanowires, the TCR was negative and the changes in resistance were only 5 % and 20 % respectively.

Heremans *et al.* also observed the increased in resistance at low temperatures for 10 nm diameter wires [45]. Using a semi-classical transport model, they calculated the critical

diameter for the wires to be semiconducting was around 9 nm. Thus, they commented that the nanowires should be metallic down to 10 nm diameter. Thus, they attributed the $R(T)$ curves of the 10 nm diameter wires to the localisation.

From the previous three examples, it is evident that the TCR may be negative even for crystalline Sb nanowires. At low temperatures such as liquid nitrogen temperature, the resistance of the crystalline Sb nanowires changed by less than an order of magnitude. To qualify as a semiconductor, the changes of resistance over temperatures must be in several orders of magnitude because the carrier density of the semiconductor varies exponentially with the temperature. The next sub-section will discuss the electronic transport of cluster films.

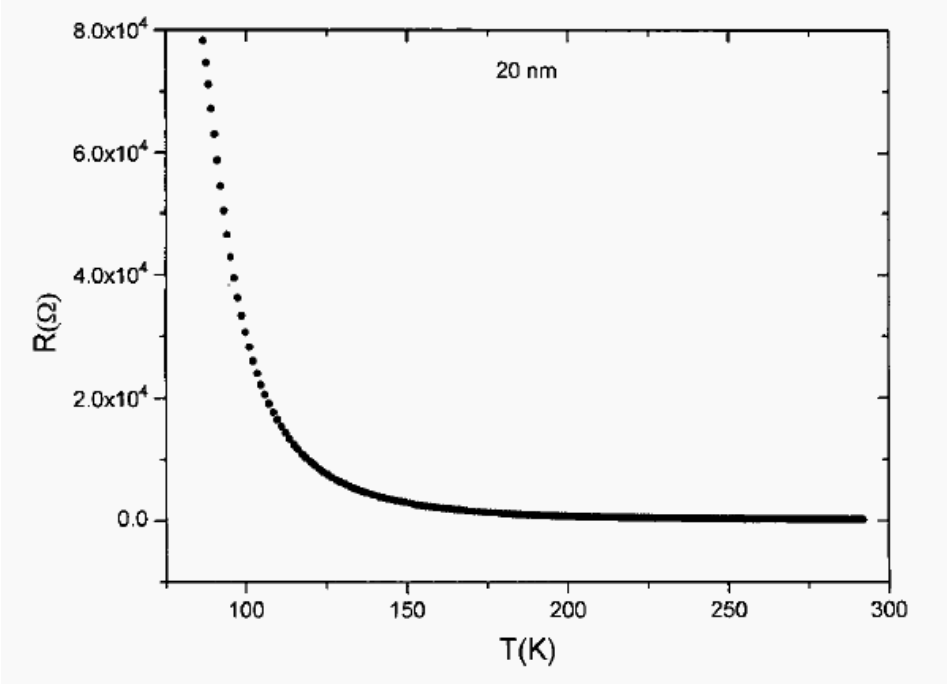

Figure 3-5: Resistance as a function of temperature in a 20 nm Sb nanowire array after post annealed at 175°C. After Ref. [43].

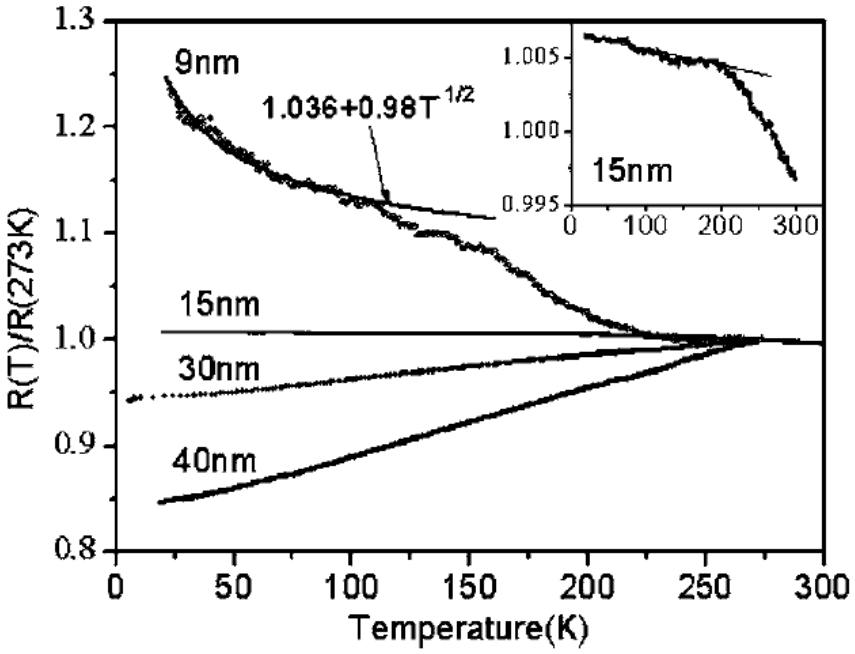

Figure 3-6: **Temperature dependence of the resistance of single crystalline Sb nanowire arrays with different diameters. The inset is a plot for 15 nm Sb nanowires. After [44].**

3.3.3 Cluster films

According to Mélinon *et al.*, the electronic transport in antimony cluster films could be divided into three types: (a) a pure material without localised effect, (b) a weak localisation in crystallised films and (c) a high localisation in amorphous films, as illustrated in Figure 3-7 [38]. The energy diagrams for each mechanism are different. With a perfect stacking of crystalline clusters, the film exhibits metallic behaviour. With a random stacking clusters of different sizes, the film exhibits a metallic behaviour, but the films could give a negative TCR. With a random stacking of disordered (or amorphous) clusters with different sizes, the film exhibits hopping mechanism whereby the resistance is proportional to $T^{-1/4}$.

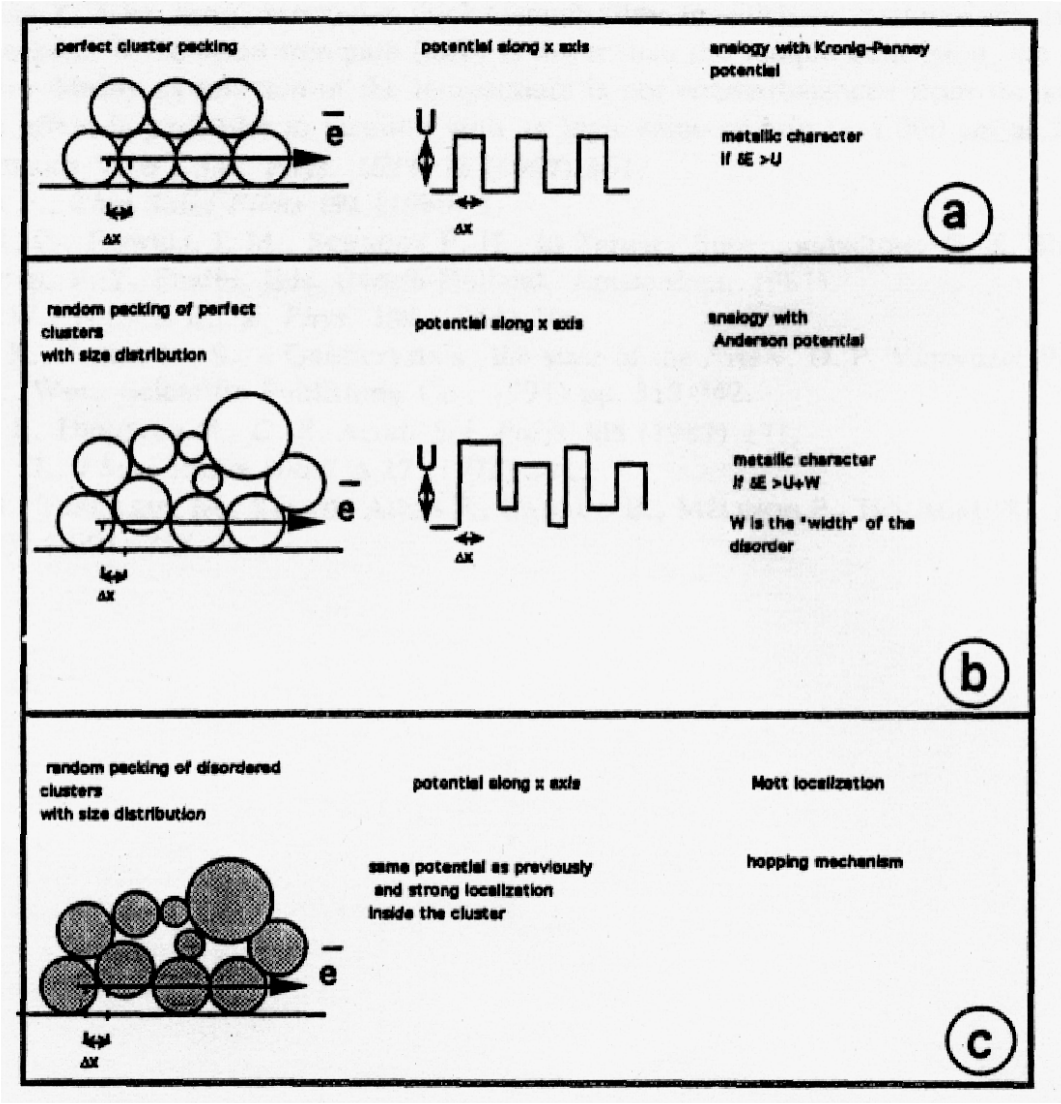

Figure 3-7: **a) Basic mechanisms describing transport properties of ideal LECBD films: a long range ordered packing of single size crystalline clusters; b) experimental crystallized LECBD films; c) experimental amorphous LECBD films. δE represents the free electron energy. After Ref. [38].**

Figure 3-8 shows the conductance values of antimony films prepared by various deposition methods [38]. The order of magnitude for crystalline films ranged from 10^2 to 10^4 $\Omega^{-1}cm^{-1}$. Mott and Mooij predicted the critical conductivity of the insulator-metal transition was around 10^2 $\Omega^{-1}cm^{-1}$ and 7×10^3 $\Omega^{-1}cm^{-1}$ respectively [46, 47]. The conductivity of the LECBD amorphous film was about two orders of magnitude lower than the conductivity of the MBD amorphous film [38].

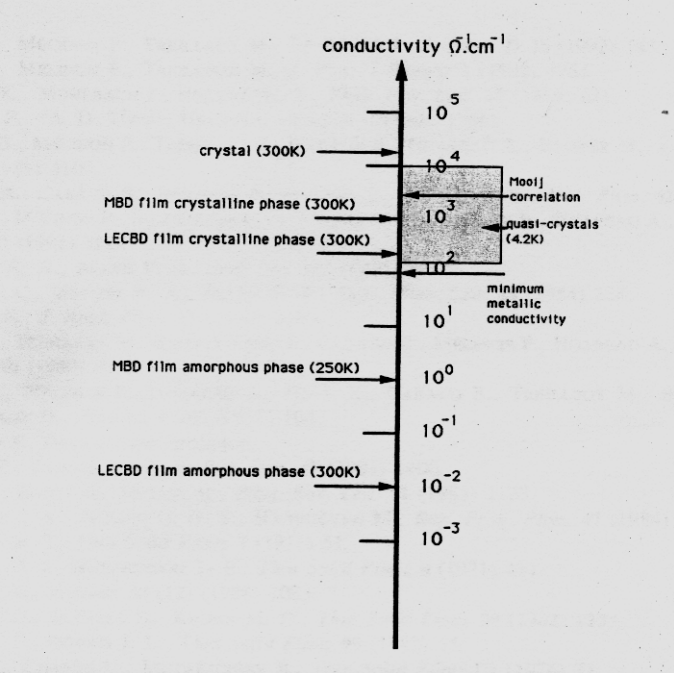

Figure 3-8: **Conductance values of antimony film prepared by various deposition methods. The Mott criterion of the insulator-metal transition predicts the conductivity $\sigma=10^2\ \Omega^{-1}cm^{-1}$ [46]. The order of magnitude of σ is given by the Mooij correlation ($\sigma=7\times10^3\ \Omega^{-1}cm^{-1}$) [47]. The range of σ for quasi crystalline materials was also reported [48]. After Ref. [38].**

Figure 3-9 shows the $R(T)$ curve of a 13.5 nm thick antimony LECBD film after annealing [38]. The film was annealed at 350 K and the resistance changed irreversibly, thus, the film was crystallised prior to the $R(T)$ measurement. The resistance only increased by 6 % when the temperature decreased from 300 K to 160 K, and the TCR was about $4 \times 10^{-4}\ K^{-1}$. Because of the very small grain size and the high disorder between crystallised clusters, the electron localisation could give rise to the anomalies in transport behaviours in the nano-crystallised films, as described by Mélinon *et al.* [38].

For amorphous LECBD films, the electrical conductance was expected to follow a hopping mechanism. This hopping mechanism should be the same as the hopping mechanism observed in amorphous films prepared by evaporation, as predicted by Mott. However, up to date, there has not been any evidence showing the $R \sim T^{-1/4}$ behaviour in amorphous LECBD films.

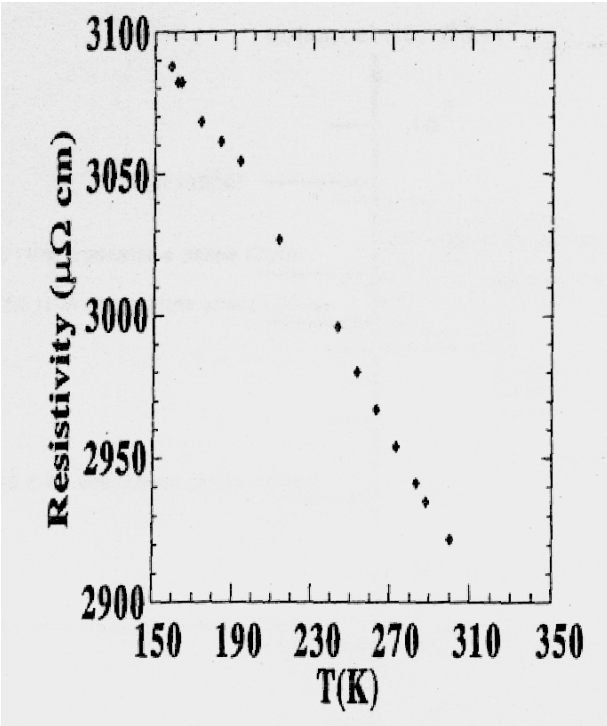

Figure 3-9: **Evolution of the electrical resistivity ρ of a 13.5 nm thick antimony LECBD film. A Sb_{2000} cluster beam was used to synthesize the film. After deposition, the film was crystallised (irreversible process) by thermal annealing at 350 K and the ρ(*T*) curve was recorded. The ρ(*T*) curve showed a negative TCR of Sb crystallized LECBD films. After Ref. [38].**

In some reports, other amorphous semiconductors, such as silicon and germanium, were demonstrated having electrical characteristics of a transistor [40, 49, 50]. For example, the source/drain current could be modulated by applying in a gate bias [49]. Although amorphous antimony films were claimed as a semiconductor, the characteristics of the transistor has not yet been demonstrated. Thus, it is important to prove that amorphous antimony is a semiconductor through a gate effect observation.

The next section will discuss the previous experiments regarding amorphous antimony cluster studies at the University of Canterbury.

3.4 Electron diffraction from unsupported Sb clusters

At the University of Canterbury, the electron diffraction studies on unsupported amorphous antimony were conducted by Kaufmann [51]. The system used in his work was described in Chapter 2. The structure of the clusters prior to deposition is important in determining the properties of the resultant films. Electron diffraction is a powerful technique for analysing the structure of a material. The first sub-section present the background for electron diffraction study and the second sub-section presents the results reported by Kaufmann [51].

3.4.1 Background study for electron diffraction

As the electron waves enter a crystal, some portion will be reflected by the first lattice layer, and some waves will continue to propagate till they are reflected by the second lattice layer. By the definition of constructive interference, the two reflected waves will remain in phase if the difference in optical path is equal to an integer multiple of the wavelength (*Bragg condition*). As illustrated in Figure 3-10, an incident wave with a vector $\boldsymbol{k_0}$ is scattered by the lattice and results in a scattered wave with a vector $\boldsymbol{k}$. As depicted in Figure 3-11, for a wavelength λ, the vector **s** can be defined by [52]

$$\boldsymbol{s}=(\boldsymbol{k}-\boldsymbol{k_0})/\lambda \qquad (Eq.\ 3\text{-}2)$$

The magnitude of **s**, from here on labelled *s*, is given by

$$s=2\sin\theta/\lambda \qquad (Eq.\ 3\text{-}3)$$

The parameter *s* is referred to as the scattering parameter, and the variation in the intensity of scattered electrons over a range of θ or *s* creates the diffraction pattern.

The diffraction patterns from clusters can be determined using the kinematic theory [52]. The kinematic theory is based on the Born approximation which assumes that the scattered waves are considerably weaker than the primary waves. The kinematic theory can be expressed by the Debye equation which allows the scattering intensity *I* to be calculated as a function of the scattering parameter *s* [52]:

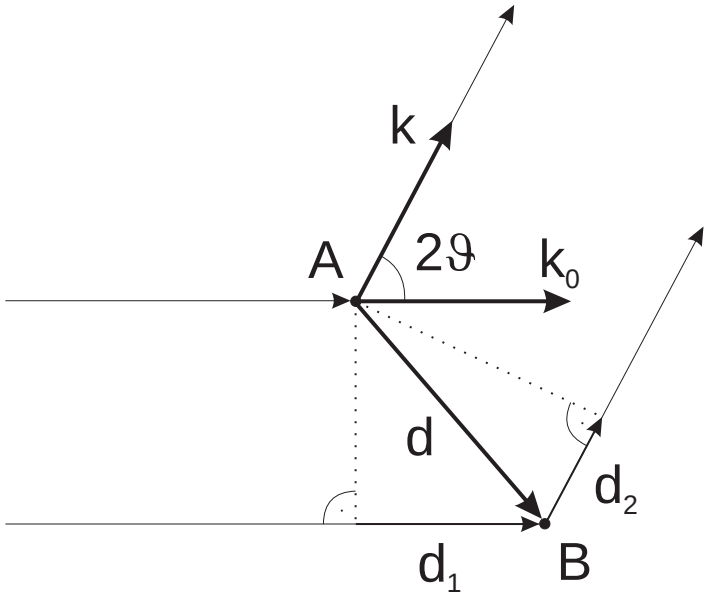

Figure 3-10: **Schematic of the diffraction process: scattering by two layers of lattice. After [52]**

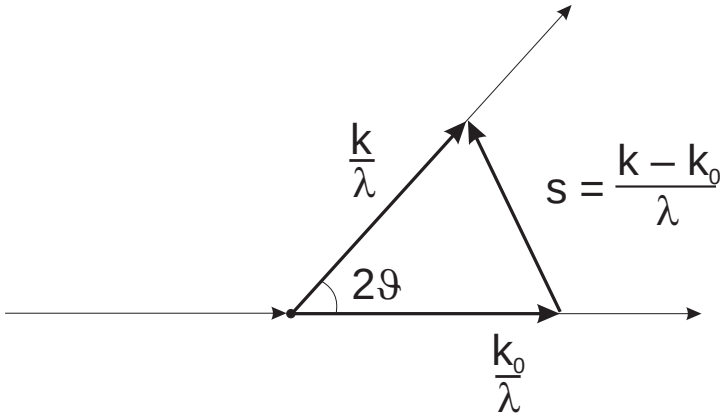

Figure 3-11: **The relationship between the vectors *s*, *k*, and k_0. After [52]**

$$I_N(s) = I_0 N f^2(s)\left(1 + \frac{D(s)}{N}\sum_{n\neq m}\frac{\sin(2\pi s r_{mn})}{2\pi s r_{mn}}\right) \qquad (Eq.\ 3\text{-}4)$$

where I_0 is the intensity of the incident beam, N is the number of atoms in a cluster, $f(s)$ is the atomic scattering factor, r_{mn} is the distance between atoms in layer m and n. D is the Debye-Waller factor which is given by:

$$D(s) = \exp\left(-\frac{4\pi^2 s^2 (\Delta r)^2}{3}\right) \qquad (Eq.\ 3\text{-}5)$$

where Δr is the root-mean-square (rms) displacement of the atoms from their equilibrium position at a given temperature. The effect of the Debye-Waller factor is an increasing attenuation of the diffraction pattern as s is increased.

At the University of Canterbury (see Chapter 2 or Ref. [51]), the 80 kV electrons were scattered by the calibration films or the unsupported (or free) clusters and then the diffraction rings were recorded by the linear diode array underneath. As the location of the linear array detector might not be necessarily at the centre of the diffraction rings, a calibration process was needed. The calibration factor was given by (see Chapter 3 in Ref. [53]):

$$\left(\frac{s}{c}\right)^2 = (wn)^2 + 2bwn + (d^2 + b^2) \qquad (Eq.\ 3\text{-}6)$$

where n is the pixel number, w, b and d are the pixel width, lateral distance and vertical distance between the centre of the diffraction rings and the detectors respectively, as depicted in Figure 3-12.

Based on the positions of the known peaks of the calibration patterns, the parameters A, B and C could be determined by a least-square fitting procedure [51]:

$$s^2 = An^2 + Bn + C \qquad (Eq.\ 3\text{-}7)$$

Figure 3-13 shows the raw diffraction pattern of the clusters and the diffraction pattern from the gas background [51]. Figure 3-14 shows the resulting diffraction pattern after subtracting the gas background [51].

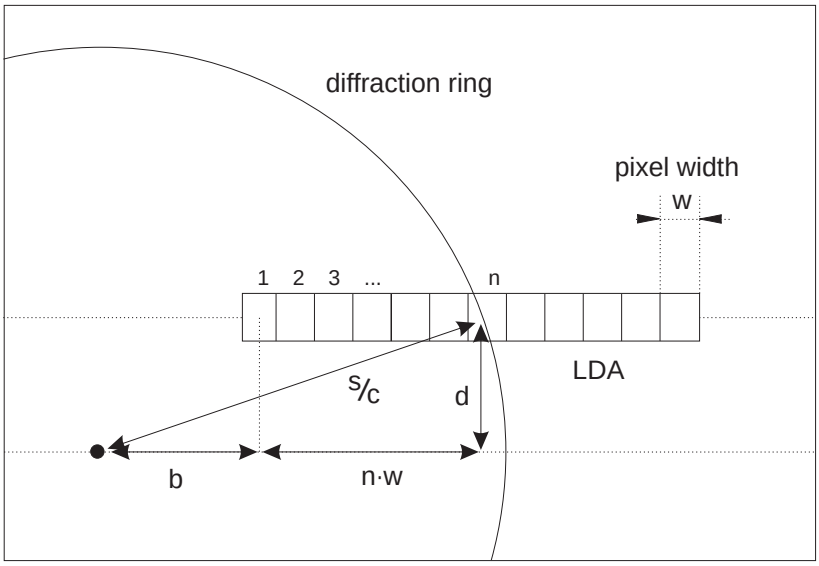

Figure 3-12: **Calibration of the detector chips. The chip can be offset in two directions, *b* and *d* respectively. *w* is the pixel width and *n* the pixel number where one of the diffraction peaks lies. The factor *c* converts the physical distance on the detector to the scattering parameter *s*. After [53].**

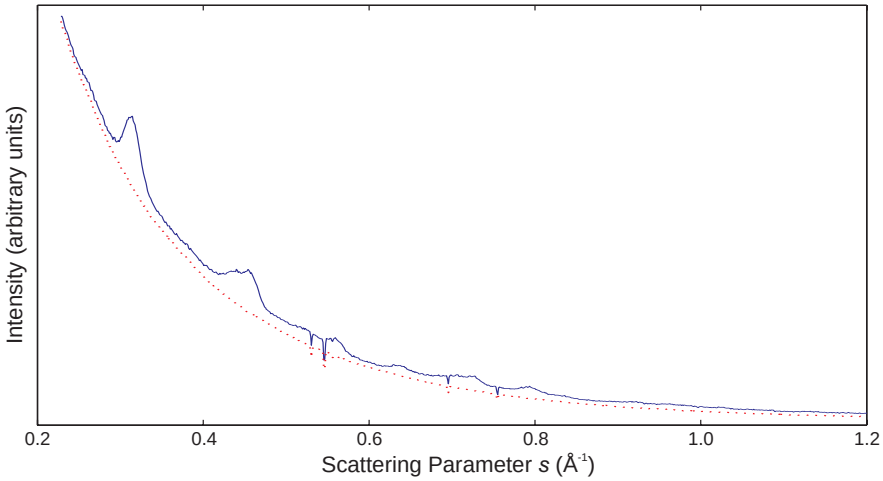

Figure 3-13: **Raw diffraction pattern of the clusters before the gas background was subtracted. The dotted line indicates the gas background. After [51].**

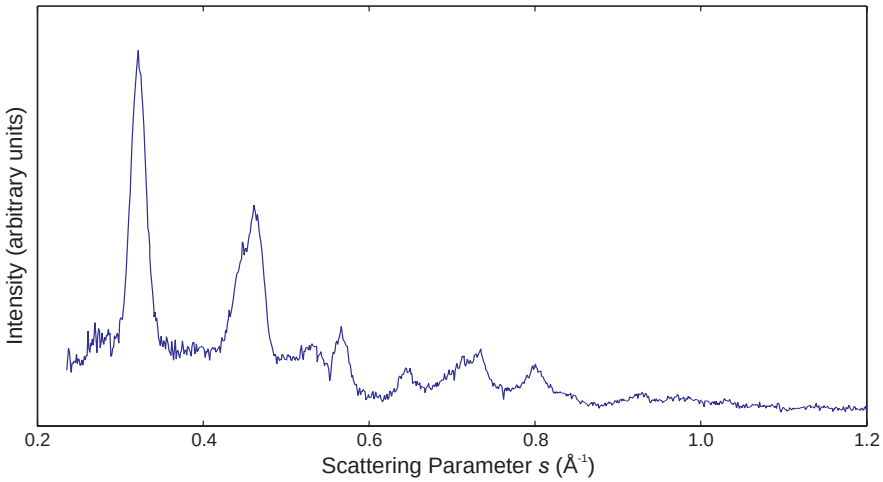

Figure 3-14: Resulting diffraction pattern after the gas background was subtracted from the raw pattern in Figure 3-13. After [51].

3.4.2 Electron diffraction study of unsupported Sb clusters

Figure 3-15 shows the diffraction patterns of antimony clusters formed in an IGA source using argon as the cooling gas and by increasing the gas flow rate from 58 to 170 sccm (standard cubic centimetre per minute) [51]. The temperature was left constant at 625ºC. At 58 sccm, the diffraction pattern of amorphous antimony clusters was obtained with the characteristic broad peaks at $s \sim 0.33$ Å^{-1} and at $s \sim 0.52$ Å^{-1}. As the flow rate increased, the deposition rate dropped, hence the noise level of the patterns increased. Thus, the deposition rate was an important factor for ensuring a good diffraction signal. At 105 sccm and above, the clusters changed to the crystalline phase. Crystalline clusters have several sharp diffraction peaks (for example $s \sim 0.32$, 0.46 and 0.56 Å^{-1} in Figure 3-14) [51].

Figure 3-16 shows the diffraction patterns of Sb clusters using argon as the cooling gas and by increasing the temperature from 675 to 825ºC. The gas flow rate was fixed at 82 sccm. Similar to the effect of the gas flow, a transition from the amorphous phase to the crystalline phase was observed [51].

The amorphous structure shown in Ref. [51] was in agreement with the structure found for Sb thin film deposition. Kauffmann explained that the presence of compression in the clusters due to the effect of surface tension might cause these differences. The size

distribution of all the amorphous samples investigated in his study was fairly narrow and lies between 30 and 40 nm [51]. The clusters all had a very regular spherical shape and did not adhere to the sample surface very well [51]. In this thesis, Kaufmann's work is expanded, and a regime has been found where a good coverage of amorphous antimony clusters can be obtained (Chapter 4) in order to allow electrical measurements. The coverage of the clusters can be analysed in percolation theory, as described in the next section.

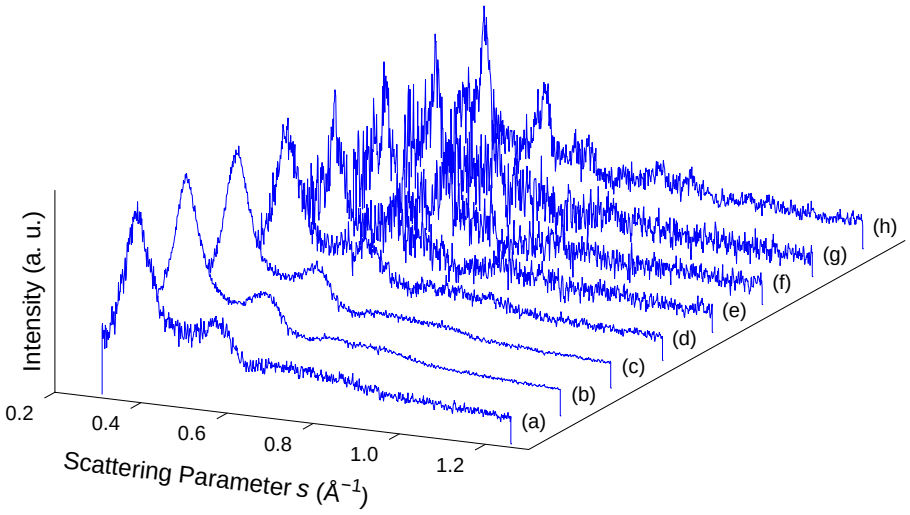

Figure 3-15: **Diffraction patterns of Sb clusters formed in an IGA source using Ar as the cooling gas and by increasing the gas flow rate from (a) 58 sccm to (h) 170 sccm. The temperature was left constant at 625°C. Note: the increase in noise in pattern (e) to (h) was due to the low deposition rate in these experiments. After [51].**

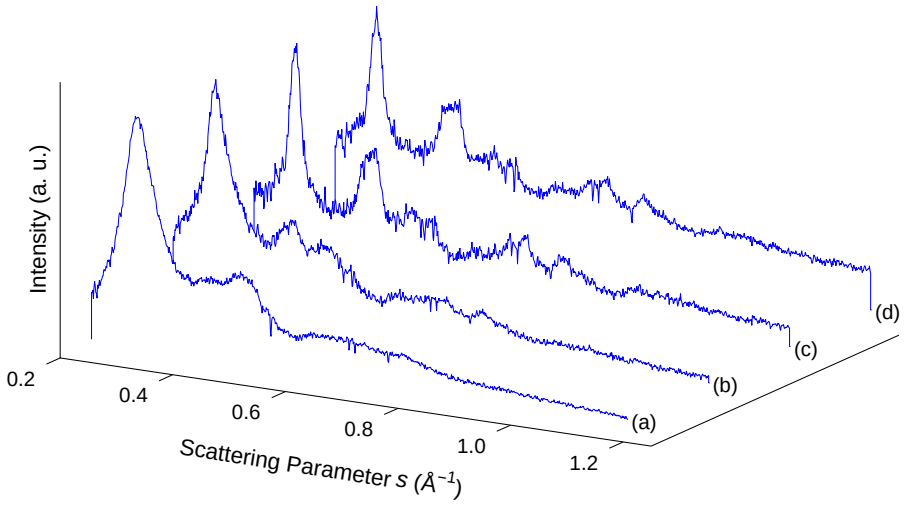

Figure 3-16: **Diffraction patterns of Sb clusters using Ar as the cooling gas and by increasing the temperature in steps of 50 K from (a) 675 °C to (d) 825°C. The gas flow rate was left constant at 82 sccm. The phase of the clusters changed from amorphous to crystalline. After [51].**

3.5 Percolation theory

In order to understand the electrical properties of a cluster film during and after deposition, percolation theory is often applied because of its simplicity and its ability to deal with the effects of the varying richness of interconnections present in a random system.

In any lattice structure, whether it is a honeycomb, a square, or a triangle, each site is randomly occupied with probability *p* and empty with probably (1-*p*) and "*connected structures*" are groups of neighbouring occupied sites [54]. Figure 3-17 shows a square lattice with a fraction *p* of occupied sites. The quantity *p*, which lies between 0 and 1, is called *coverage* or the probability of a site being occupied. When the two nearest neighbour sites are both occupied, they are defined as being connected. In a 2D square lattice, each site can have up to four connections. The structures generated by this method are called lattice animals. It is the lattice animals, their sizes and their distribution as a function of coverage, which the percolation theory is concerned about.

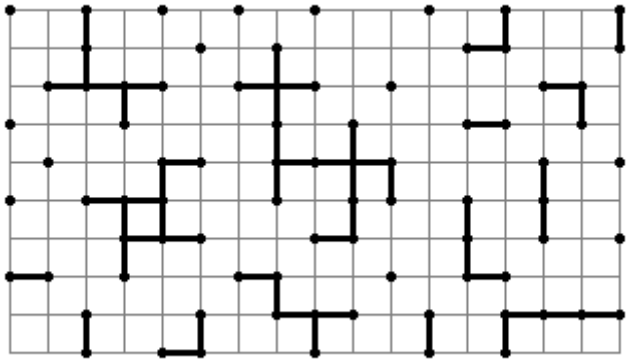

Figure 3-17: A square lattice with a fraction *p* of occupied sites and bonds drawn. After [54].

In an infinite system, the structures generated by connecting neighbouring occupied lattice sites will be small and isolated for $p < p_c$ and form an infinite network for $p > p_c$, where the percolation threshold p_c is equal to 0.5927. More descriptions about percolation theory can be found in Ref. [54]. From percolation theory, various properties of a system related to the probability of occupation of sites within the system can be described by simple power laws. For example, the correlation or the connectivity

length ξ of connected structures, which is defined as the average distance between two sites within the same *cluster*, is given by:

$$\xi \propto (p - p_c)^{-\upsilon} \qquad (Eq.\ 3\text{-}8)$$

where p is the coverage, p_c the percolation threshold, and ν is the power law exponent for ξ.

For the electrical measurements in a percolating process, the electrical conductivity σ could be expressed as:

$$\sigma \propto (p - p_c)^{-t} \qquad (Eq.\ 3\text{-}9)$$

where t is the power law exponent for σ.

Mélinon *et al.* compared the processes of MBD and cluster deposition. They observed a good correlation of the cluster deposition to percolation theory with p_c ~ 50% [31]. In the case of cluster deposition, the film grew by the paving of the substrate by the incident clusters. They attributed the correlation to the low mobility of clusters on the substrate, thus, the growth was entirely governed by the impinging flux. In the case of the Sb_4 deposition, nucleation was the important factor and the growth of the films seemed to involve more complex mechanisms than a random percolation.

In 1979, Smith *et al.* determined t to be around 1.3 experimentally from laser speckle patterns [55]. Then, Feng *et al.* confirmed the same value of t through a mathematical model [56]. Dunbar *et al.* demonstrated that the depositions of bismuth and silver clusters on SiN surfaces followed the prediction of percolation theory [57]. Figure 3-18 shows their experimental conductance σ data for bismuth and antimony plotted as a function of (p-p_c). The power law exponents they found for cluster depositions were 1.27 ± 0.13 and 1.4 ± 0.14, for Bi and Ag respectively. However, the increase in the conductivity during antimony cluster deposition did not follow the same trend. The antimony clusters did not adhere to the substrate in a random distribution because they reflected from the substrate and adhered only to the nucleation sites or another Sb cluster stuck to the substrate.

In this thesis, percolation theory will be applied in characterising the property of antimony cluster deposition. A homogeneous deposition could be identified by a good linear fit of the log(σ)-log(p-p_c) curve.

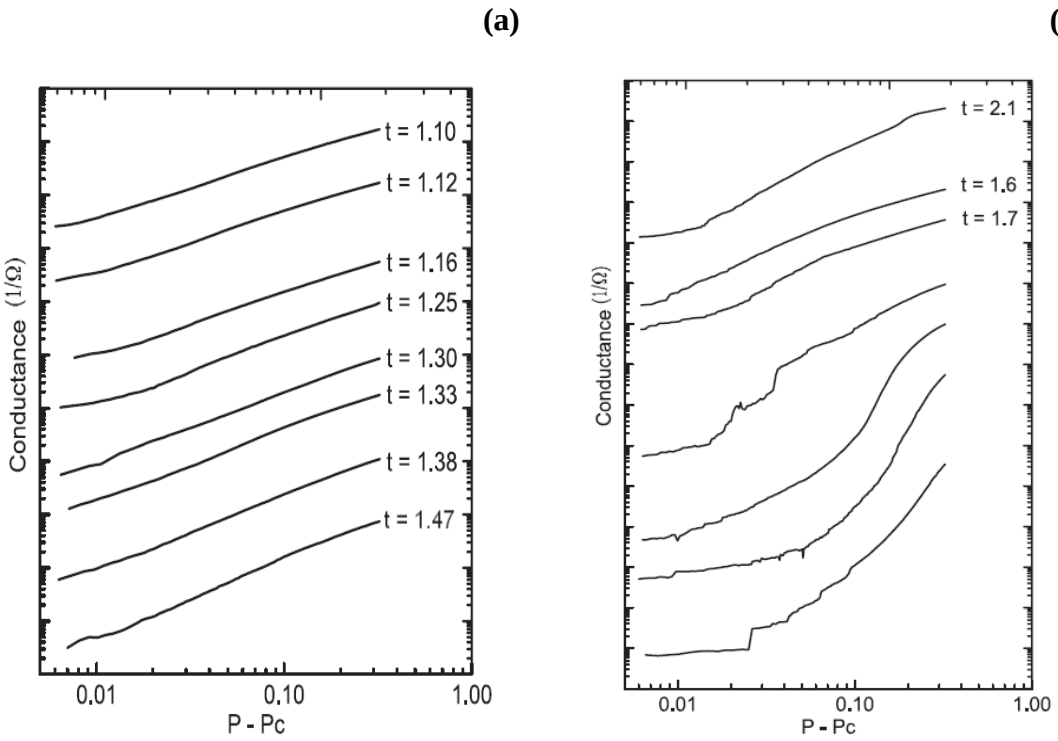

Figure 3-18: The experimental conductance data for (a) bismuth and (b) antimony plotted as a function of (p-p_c). The plots are stacked (each offset by an order of magnitude) in order of decreasing gradient. Only data points in the range p=0.006 to 0.324 are shown and the exponent t from the fits for each data set is displayed at the end of each curve. After Ref. [57].

3.6 Summary

In the past, amorphous antimony films were mostly prepared by molecular beam deposition. The amorphous antimony films prepared at room temperature crystallised when the film grew beyond a critical thickness. In most references, electrical measurements of the amorphous films were not performed because the films were not continuous below the critical thickness. The vacuum condition during MBD was demonstrated to be an important factor governing the film properties. Other factors,

such as the substrate condition or the distance between the evaporator source and the substrate, could affect the phases of the films as well.

When evaporated films were prepared with substrate cooling, the thickness had no impact on the crystallisation. The films were crystallized when the temperature was high enough. Generally, the transition temperature was below room temperature for evaporated films.

Cluster deposition potentially provides a new way of preparing continuous and stable amorphous antimony films. The transition temperature for cluster films ranged from 323 K to 350 K, except for 2 nm clusters. Therefore, the amorphous antimony films could be characterised at room temperature.

Hauser found that the resistivity of the films prepared by three different methods all showed a $R \sim T^{-1/4}$ relation. This relation was predicted by Mott in his variable range hopping model, which was normally observed in amorphous silicon and amorphous germanium films. The transition temperature for sputtered films was 40ºC, but the $R(T)$ started to change irreversibly above 160 K.

The experiments conducted by three different groups using porous anodic alumina templates all showed that the resistance increased at low temperatures for nanowires with diameters from 10 to 20 nm. Heremans *et al.* attributed the $R(T)$ curves to localisation, and commented that the semi-metal to semiconductor transition should be observed at diameter less than 10 nm from their theoretical model.

Mélinon *et al.* proposed three different electronic transport mechanisms in antimony cluster films. It is possible for the crystalline antimony cluster films to exhibit a negative TCR, just like other crystalline nanowires. Thus, the semiconducting behaviour of the amorphous antimony cluster film should be identified by a large TCR (or a $T^{-1/4}$ dependence), and a gate effect.

Previous study at the University of Canterbury focused on the identification of the phase of unsupported clusters. With the phase of the unsupported clusters identified by electron diffraction, it would be interesting to deposit amorphous antimony clusters on

electrically contacted samples and measure the $I(V)$, $R(T)$ curves and the effect of an electric field applied to the gate (similar to field-effect transistors), as will be discussed in Chapter 4. If the transistor behaviour can be observed in amorphous antimony cluster films, it would be a good method for understanding a cluster film.

References

[1] D. R. Lide, *CRC handbook of Chemistry and physics*, 84th ed. New York: CRC Press, 2004.

[2] R. K. Watts, H. S. Luftman, and F. A. Baiocchi, "Shallow junctions for 0.1um normal-type metal-oxide semiconductor-devices," *Journal of Vacuum Science & Technology B*, vol. 10, pp. 515-523, Jan-Feb 1992.

[3] J. W. Beeman, W. L. Hansen, O. D. Dubon, and E. E. Haller, "High performance antimony-doped germanium photoconductors," *Infrared Physics & Technology*, vol. 37, pp. 715-721, Dec 1996.

[4] C. C. Coffin and S. Johnston, "Studies on explosive antimony. I. The microscopy of polished surfaces," *Proceedings of the Royal Society of London Series a-Mathematical and Physical Sciences*, vol. 146, pp. 0564-0570, Oct 1934.

[5] E. Cohen and J. Olie, "Physical and chemical studies on the so-called amorphous antimony," *Zeitschrift Fur Physikalische Chemie--Stochiometrie Und Verwandtschaftslehre*, vol. 61, pp. 588-595, Jan 1908.

[6] F. M. Aymerich and A. Delunas, "On the explosive semiconductor-semimetal transition of antimony," *Physica Status Solidi (A) Applied Research*, vol. 31, pp. 165-170, 1975.

[7] A. J. Mackintosh, R. T. Phillips, and A. D. Yoffe, "Electrical conductivity of amorphous antimony and its dependence on film thickness," *Physica B: Physics of Condensed Matter & C: Atomic, Molecular and Plasma Physics, Optics*, vol. 117-118, pp. 1001-1003, 1982.

[8] J. J. Hauser, "Electron transport and superconductivity in amorphous Sb and its alloys," *Physical Review B*, vol. 11, p. 738, 1975.

[9] A. H. Sommer, "Characteristics of evaporated antimony films as a function of antimony source," *Journal of Applied Physics*, vol. 37, pp. 2789-&, 1966.

[10] J. A. Prins, "Diffraction of electrons in amorphous and in crystalline antimony," *Nature*, vol. 131, pp. 760-761, Jan-Jun 1933.

[11] E. Taft and L. Apker, "Fermi level in amorphous antimony films," *Physical Review*, vol. 96, pp. 1496-1497, 1954.

[12] C. Ghosh and B. P. Varma, "Study of the growth and structure of antimony films on carbon substrates in low adn high vacuum," *Journal of Physics D: Applied Physics*, vol. 7, pp. 1773-1777, 1974.

[13] I. N. Shklyarevskii and A. I. Usoskin, "Optical and structural properties of amorphous antimony thin-films," *Optics and Spectroscopy-Ussr*, vol. 31, pp. 328-&, 1971.

[14] K. Maki, "Changes in electrical-resistivity during amorphous-crystalline phase-transition of antimony films," *Japanese Journal of Applied Physics*, pp. 649-652, 1974.

[15] P. Jensen, P. Mélinon, M. Treilleux, A. Hoareau, J. X. Hu, and B. Cabaud, "Continuous amorphous antimony thin-films obtained by low-energy cluster beam deposition," *Applied Physics Letters*, vol. 59, pp. 1421-1423, Sep 1991.

[16] J. J. Hauser, "Hopping conductivity in amorphous antimony," *Physical Review B*, vol. 9, pp. 2623-2626, 1974.

[17] K. Maki, "Estimation of density changes associated with growth in vacuum-deposited amorphous films of antimony," *Thin Solid Films,* vol. 88, pp. 239-246, 1982.

[18] K. Maki, Y. Shigeta, and N. Ichino, "Change in crystallization thickness dc of amorphous Sb film due to preparation condition of SiOx film substrate," *Proceedings of the Seventh International Vacuum Congress and the Third International Conference on Solid Surfaces,* vol. 3, pp. 2197-2200, 1977.

[19] J. Cohen, "Semiconducting Films of Antimony," *Journal of Applied Physics,* vol. 25, pp. 798-801, 1954.

[20] J. U. Trefny, D. S. Peters, and J. N. Fox, "Thermoelectric properties of amorphous antimony," *Journal of Non-Crystalline Solids,* vol. 65, pp. 215-222, 1984.

[21] W. A. de Heer, "The physics of simple metal clusters: experimental aspects and simple models," *Reviews of Modern Physics,* vol. 65, p. 611, 1993.

[22] B. V. Issendorff and O. Cheshnovsky, "Metal to insulator transitions in clusters," *Annual Review of Physical Chemistry,* vol. 56, pp. 549-580, 2005.

[23] A. Perez, P. Melinon, V. Dupuis, P. Jensen, B. Prevel, J. Tuaillon, L. Bardotti, C. Martet, M. Treilleux, M. Broyer, M. Pellarin, J. L. Vaille, B. Palpant, and J. Lerme, "Cluster assembled materials: A novel class of nanostructured solids with original structures and properties," *Journal of Physics D-Applied Physics,* vol. 30, pp. 709-721, Mar 1997.

[24] G. A. Breaux, D. A. Hillman, C. M. Neal, R. C. Benirschke, and M. F. Jarrold, "Gallium cluster "magic melters"," *Journal of the American Chemical Society,* vol. 126, pp. 8628-8629, 2004.

[25] K. Tanaka and S. Iwama, "Size dependent crystallization of nanometer-sized amorphous Sb particles," *Nanostructured Materials,* vol. 9, pp. 121-124, 1997.

[26] K. Tanaka, S. Iwama, and K. Mihama, "Crystallization of nanometer-sized amorphous Sb particles formed by flowing gas evaporation technique," *Japanese Journal of Applied Physics Part 2-Letters,* vol. 37, pp. L669-L671, Jun 1998.

[27] G. Fuchs, P. Melinon, F. S. Aires, M. Treilleux, B. Cabaud, and A. Hoareau, "Cluster-beam deposition of thin metallic antimony films - Cluster-size and Deposition-rate effects," *Physical Review B,* vol. 44, pp. 3926-3933, Aug 1991.

[28] G. Fuchs, P. Melinon, Y. Yan, B. Cabaud, A. Hoareau, M. Treilleux, and V. Paillard, "Films of controlled nanosize grains deposited by low-energy cluster beam," *Zeitschrift Fur Physik D-Atoms Molecules and Clusters,* vol. 26, pp. S249-S251, May 1993.

[29] G. Fuchs, M. Treilleux, F. S. Aires, P. Melinon, B. Cabaud, and A. Hoareau, "Crystallization of thin antimony deposits on amorphous-carbon," *Thin Solid Films,* vol. 204, pp. 107-114, Sep 1991.

[30] G. Fuchs, M. Treilleux, F. Santos Aires, B. Cabaud, P. Melinon, and A. Hoareau, "Cluster-beam deposition for high-quality thin films," *Physical Review A (General Physics),* vol. 40, pp. 6128-9, 1989.

[31] P. Mélinon, P. Jensen, J. X. Hu, A. Hoareau, B. Cabaud, M. Treilleux, and D. Guillot, "Comparison of molecular and cluster deposition - Evidence of different percolation processes," *Physical Review B,* vol. 44, pp. 12562-12564, Dec 1991.

[32] P. Jensen, P. Melinon, M. Treilleux, A. Hoareau, J. X. Hu, G. Fuchs, and B. Cabaud, "Low-Energy Cluster Beam Deposition - a way to new materials,"

Nuclear Instruments & Methods in Physics Research Section B-Beam Interactions with Materials and Atoms, vol. 79, pp. 219-222, Jun 1993.

[33] T. Takagi, "Ionized cluster beam technique for thin film deposition," *Zeitschrift fur Physik D (Atoms, Molecules and Clusters),* vol. 3, pp. 271-8, 1986.

[34] T. Takagi, "History and current status of the ionized cluster beam technique," *ICBT '86: Proceedings of the International Workshop on Ionized Cluster Beam Technique. ,* pp. 1-16, 1986.

[35] I. Yamada, H. Usui, and T. Takagi, "Formation mechanism of large clusters from vaporized solid material," *Journal of Physical Chemistry,* vol. 91, pp. 2463-8, 1987.

[36] W. Harbich, *Metal clusters at surfaces: structure, quantum properties, physical*: Springer, 2000.

[37] G. Fuchs, M. Treilleux, F. S. Aires, B. Cabaud, P. Melinon, and A. Hoareau, "Electron-irradiation effects in amorphous antimony thin-films obtained by cluster-beam deposition," *Philosophical Magazine B-Physics of Condensed Matter Statistical Mechanics Electronic Optical and Magnetic Properties,* vol. 63, pp. 715-725, Mar 1991.

[38] P. Mélinon, G. Fuchs, B. Cabaud, A. Hoareau, P. Jensen, V. Paillard, and M. Treilleux, "Low-Energy Cluster Beam Deposition - Do You Need It ?," *Journal De Physique I,* vol. 3, pp. 1585-1603, Jul 1993.

[39] N. F. Mott, "Conduction and switching in non-crystalline materials," *Contemporary Physics,* vol. 10, pp. 125-&, 1969.

[40] J. J. Hauser, "Electrical properties of amorphous-Ge alloys and electron tunneling in amorphous-semiconductors," *Physical Review B,* vol. 9, pp. 2544-2557, 1974.

[41] A. J. Mackintosh, R. T. Phillips, and A. D. Yoffe, "The electrical-conductivity of amorphous antimony and its dependence on film thickness," *Physica B & C,* vol. 117, pp. 1001-1004, 1983.

[42] D. Möckel, W. Rössler, and F. Baumann, "Electrical-resistivity of amorphous Sb films and Sb-Au films," *Physica Status Solidi a-Applied Research,* vol. 49, pp. 103-110, 1978.

[43] M. Barati, J. C. L. Chow, P. K. Ummat, and W. R. Datars, "Temperature dependence of the resistance of antimony nanowire arrays," *Journal of Physics-Condensed Matter,* vol. 13, pp. 2955-2962, Apr 2001.

[44] Y. Zhang, L. Li, G. H. Li, and L. D. Zhang, "Electrical transport properties of single-crystal antimony nanowire arrays," *Physical Review B (Condensed Matter and Materials Physics),* vol. 73, pp. 113403-3, 2006.

[45] J. Heremans, C. M. Thrush, Y. M. Lin, S. B. Cronin, and M. S. Dresselhaus, "Transport properties of antimony nanowires," *Physical Review B,* vol. 63, Feb 2001.

[46] N. F. Mott, "Metal-insulator transition," *Reviews of Modern Physics,* vol. 40, pp. 677-683, 1968.

[47] J. H. Mooij, "Electrical conduction in concentrated disordered transition metal alloys," *Physica Status Solidi (A) Applied Research,* vol. 17, pp. 521-530, 1973.

[48] K. Kimura, K. Kishi, T. Hashimoto, S. Takeuchi, and T. Shibuya, "Electrical resistivities of stable quasicrystals," *Materials Science & Engineering A: Structural Materials: Properties, Microstructure and Processing,* vol. A133, pp. 94-97, 1991.

[49] M. J. Powell, "The physics of amorphous-silicon thin-film transistors," *IEEE Transactions on Electron Devices,* vol. 36, pp. 2753-2763, 1989.

[50] T. A. Abtew, M. L. Zhang, and D. A. Drabold, "Ab initio estimate of temperature dependence of electrical conductivity in a model amorphous material: Hydrogenated amorphous silicon," *Physical Review B,* vol. 76, Jul 2007.

[51] M. Kaufmann, "Electron diffraction studies of unsupported antimony clusters," *PhD thesis, University of Canterbury,* 2006.

[52] A. Guinier, *X-ray diffraction in crystals, imperfect crystals, and amorphous bodies*. San Francisco: W. H. Freeman, 1963.

[53] A. Wurl, "Electron diffraction studies of unsupported bismuth clusters," *PhD thesis, University of Canterbury,* 2003.

[54] D. Stauffer, *Introduction to Percolation Theory*. London: Taylor and Francis, 1985.

[55] L. N. Smith and C. J. Lobb, "Percolation in two-dimensional conductor-insulator networks with controllable anisotropy," *Physical Review B (Condensed Matter),* vol. 20, pp. 3653-8, 1979.

[56] S. Feng, B. I. Halperin, and P. N. Sen, "Transport properties of continuum systems near the percolation threshold," *Physical Review B,* vol. 35, p. 197, 1987.

[57] A. D. F. Dunbar, J. G. Partridge, M. Schulze, and S. A. Brown, "Morphological differences between Bi, Ag and Sb nano-particles and how they affect the percolation of current through nano-particle networks," *European Physical Journal D,* vol. 39, pp. 415-422, 2006.

Chapter 4

Deposition and characterisation of amorphous antimony clusters

As described in Chapter 3, the $R(T)$ data from the literature showed that amorphous antimony films were semiconducting. The amorphous phase of these antimony films were mostly detected on supported thin film samples. Kaufmann [1] developed a cluster deposition process which enabled the phase of unsupported antimony clusters to be identified. The aim of this chapter is to use a combination of cluster deposition and electron diffraction from unsupported clusters to attempt to make cluster deposited semiconducting amorphous antimony films. The literature has shown that the resistance of semiconducting amorphous films generally follows a $R \sim T^{-1/4}$ relation (refer to chapter 3 for details). In addition, the electrical conductance of a semiconducting film should be modulated significantly under the influence of gate bias. Thus, the exponential fits of the $R(T)$ curves and the change of drain current due to a gate bias are the two criteria that prove amorphous antimony cluster films are semiconducting.

Section 4.1 describes the experimental procedure and the sample preparation. Two types of samples were used, namely multiple contact samples and inter-digitated samples. Section 4.2 describes some general observations regarding source pressure, cluster spot size and deposition rate. There were four different source configurations (by varying nozzles and the internal plate), termed configurations A, B, C and D. Initially, a series of experiments were conducted using configurations A and B which were the same as Kaufmann's source configurations [1]. From the multiple contact samples, some preliminary electrical data such as $I(V)$ and $R(T)$ are presented. The film morphology and other problems associated with the electrical measurements with configurations A and B are discussed in Section 4.3. A considerable effort has been made to obtain uniform films which are appropriate for electrical measurements using configurations C and D, as described in Section 4.4. Then, the electrical parameters of the uniform cluster films are characterised and discussed in Section 4.5. The electrical

measurements during the deposition are related to percolation theory. The post-deposition measurements provide information regarding the coalescence, the degree of oxidation, resistance-temperature curves and gate field effect of the films. The chapter concludes with a summary of amorphous antimony cluster films, highlighting the results of the present study which are different from the literature.

4.1 Experimental description

This section describes the cluster deposition, the electron diffraction of the antimony clusters and the sample preparation.

4.1.1 Cluster deposition

Chapter 2 described the generation of clusters in an inert-gas aggregation (IGA) source. In an IGA source, the crucible temperature, inert gas flow, a tantalum plate and the nozzle dimensions of the first stage nozzle are important to the cluster generation. The first stage nozzle is located between the source chamber and the first pumping stage. The tantalum plate is located above the heat shield of the crucible. This sub-section describes the source configuration and the main process parameters for the evaluation of antimony clusters.

Table 4-1 shows four different combinations of the source configuration. An experiment could be run with or without the use of a Tantalum plate which separated the source into two halves. There were two types of first stage nozzle, 3.5 mm and the 2.5 mm in diameter respectively. The second stage and third stage nozzles remained unchanged throughout the experiments. The four configurations are referred as configuration A, configuration B, configuration C and configuration D in the text.

Table 4-1: Four combinations of the source configuration.

Config.	Using a Ta plate	First Stage Nozzle		Second Stage Nozzle		Third Stage Nozzle	
		Length (mm)	Diameter (mm)	Length (mm)	Diameter (mm)	Length (mm)	Diameter (mm)
A	No	24.5	3.5	4	1.5	2	1.5
B	No	24.5	2.5	4	1.5	2	1.5
C	Yes	24.5	3.5	4	1.5	2	1.5
D	Yes	24.5	2.5	4	1.5	2	1.5

4.1.2 Electron Diffraction

This sub-section describes the procedure for measuring and analysing the electron diffraction patterns of the unsupported antimony clusters. The electron diffraction apparatus described in Chapter 2 (Section 2.1.1) highlighted the locations of the electron gun and the detector. The detector consisted of two linear diode arrays, namely LDA1 and LDA2 which were situated directly below the electron gun. During an experiment, the diffraction rings were generated when electrons interacted with the clusters or the calibration samples. The diffraction rings were recorded by the LDA chips.

In order to calibrate the electron diffraction signals, two types of calibration samples were used, polycrystalline thallium chloride (TlCl) and aluminium (Al)[a]. The calibration was performed before and after the cluster depositions. Figure 4-1 shows the typical electron diffraction patterns of these two calibration samples on LDA1 and LDA2. The intensity of the electron diffraction signal corresponded to the electron counts during the detection. It was obvious that the electron diffraction peaks were not at the same location in LDA1 and LDA2. In the design of the apparatus, the location of LDA1 and LDA2 was deliberately not made symmetrical to the centre of the diffraction rings. The detectors were shifted out along the radial direction to increase the detection range on LDA2. The pixel numbers in the x-axis had not been converted to correspondent scattering parameters as in Ref.[1] because the information in the pixel

[a] The Al and TlCl samples were commercially available from Electron Microscopy Sciences.

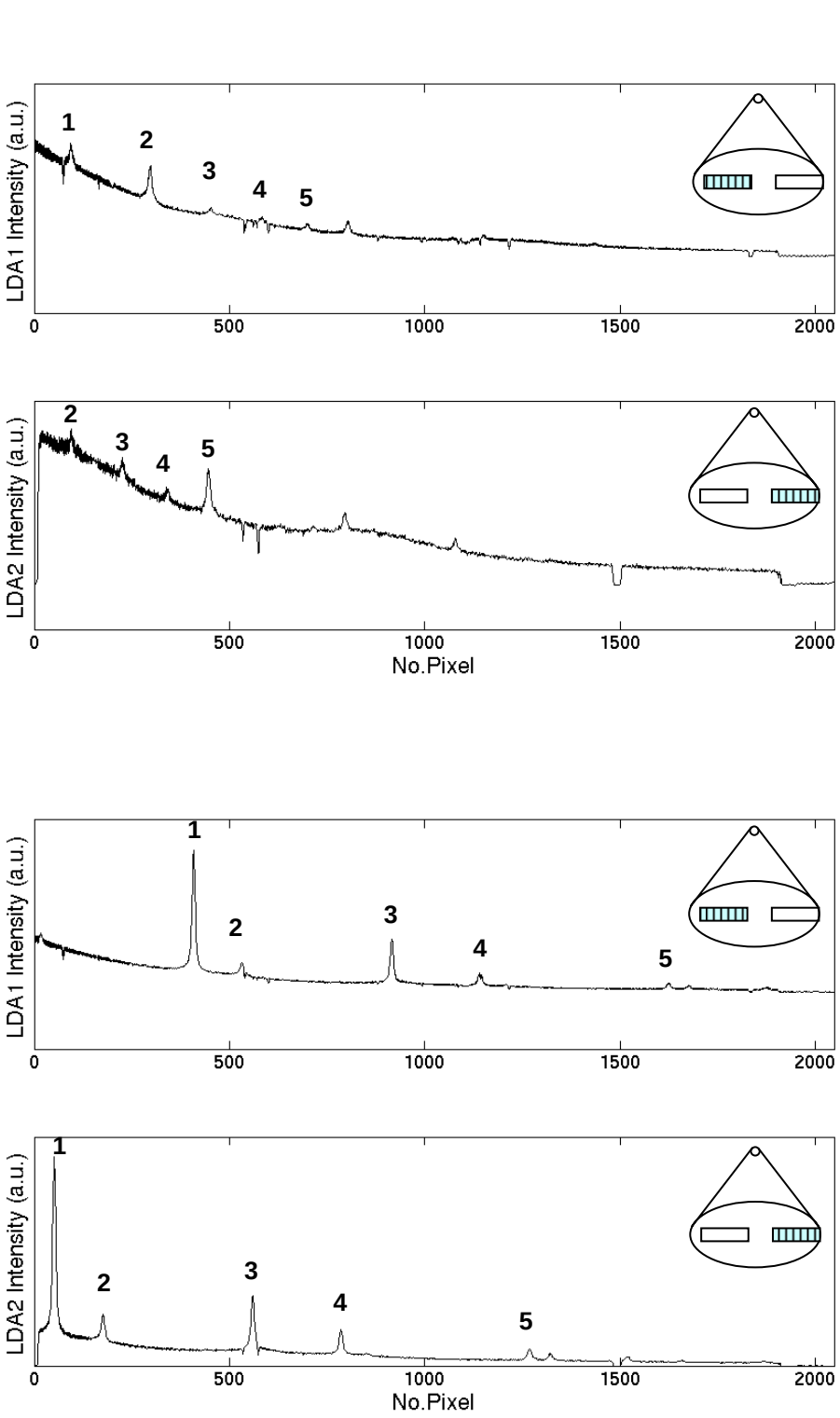

Figure 4-1: **Electron diffraction patterns for (a) TlCl and (b) Al thin films. The numbers 1-5 denote the diffraction peaks of the films. LDA1 and LDA2 are the two different detectors. The y-axis indicates the electron intensity in arbitrary units while the x-axis denotes the pixel number for the detectors. Insets indicate the location of the LDA chips relative to the diffraction rings.**

domain gave enough information about the phase of the antimony clusters and it was not the intention in this work to study the diffraction patterns themselves.

Figure 4-2 shows the electron diffraction signal for antimony clusters produced in configuration A at 625-630ºC and 725-775ºC crucible temperatures. In configuration A, clusters produced at 625-630ºC crucible temperatures were amorphous phase and clusters produced at 725-775ºC crucible temperatures were crystalline phase. At high deposition rate (in this case: 8 $Ås^{-1}$ for amorphous phase and 21 $Ås^{-1}$ for crystalline phase), the intensity of the diffraction signals was high and therefore, the patterns were scaled to compare with the signal from deposition with low rate (in this case: 5.8 $Ås^{-1}$ for amorphous phase and 1.7 $Ås^{-1}$ for crystalline phase). In this work, the clusters deposited on the samples were produced in the low deposition rate regime, in order to make uniform film, as will be explained later. Although the signals at low deposition rate regime were noisy, the peaks were still noticeable. Amorphous antimony clusters had one broad peak between LDA1 pixels 200 and 250 and another broad peak at LDA1 pixel ~ 500; on the other hand, crystalline antimony clusters had five narrow peaks at LDA1 pixels 170, 430, 630, 930 and 1050. These signatures enabled the phase of the clusters to be identified in this work.

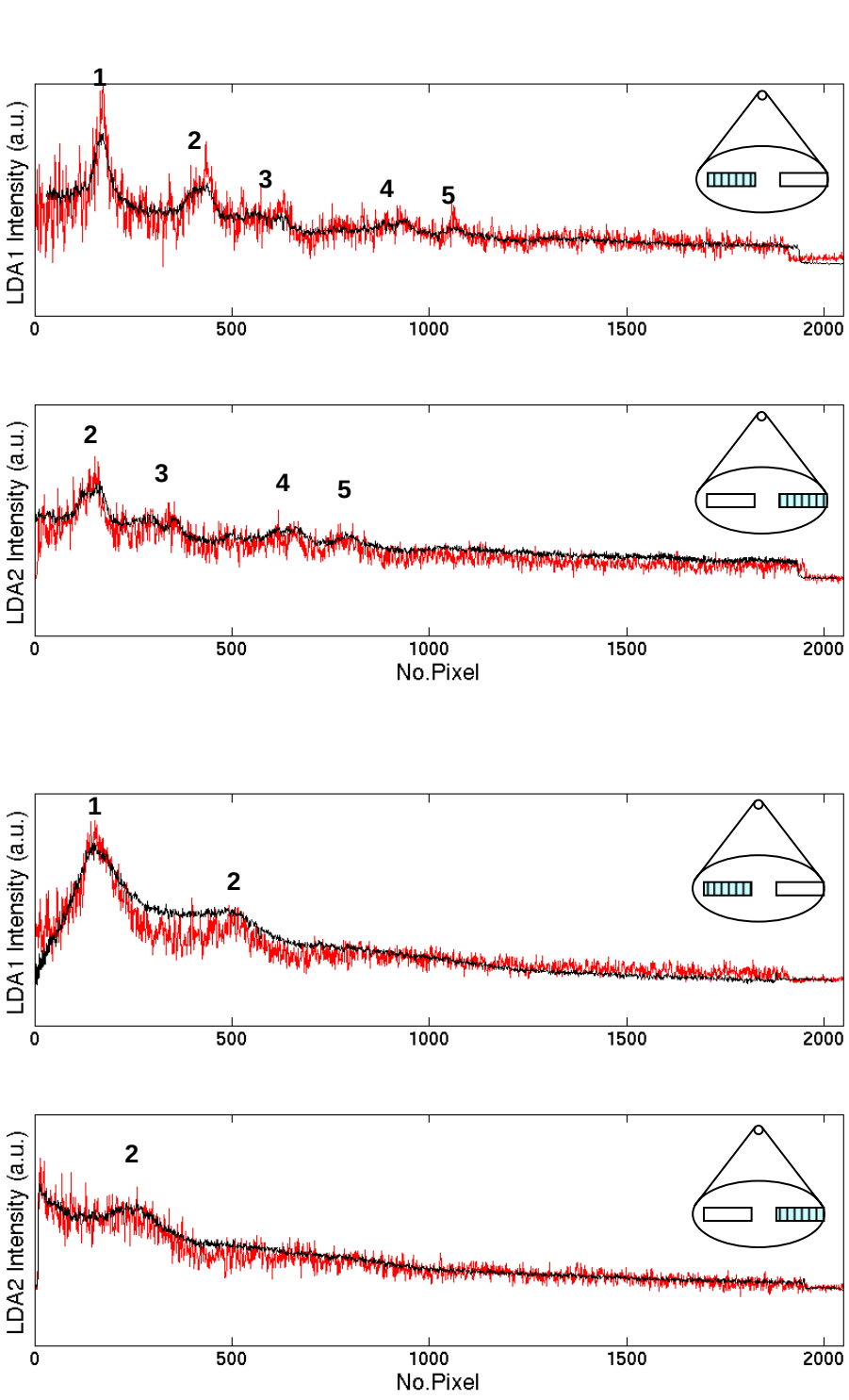

Figure 4-2: **Electron diffraction patterns for (a) crystalline Sb clusters and (b) amorphous Sb clusters. The numbers 1-5 denote the diffraction peaks. LDA1 and LDA2 are two different detectors. The y-axis indicates the electron intensity in arbitrary units while the x-axis denoted the pixel number for the detectors. The deposition rates were 21 Ås^{-1} (black) and 1.7 Ås^{-1} (red) for crystalline clusters and 8 Ås^{-1} (black) and 5.8 Ås^{-1} (red) for amorphous clusters. Insets indicate the location of the LDA chips relative to the diffraction rings.**

4.1.3 Sample preparation

This sub-section describes the preparation of the samples used for electrical characterisation. There were two types of samples used, namely, multiple contact samples and inter-digitated samples. Both samples were made from silicon wafers coated with 100 nm silicon dioxide and 100 nm silicon nitride.

In order to measure four-point resistances, samples with multiple contacts were required. Figure 4-3 shows the images of a multiple contact sample from an optical microscope and a scanning electron microscope (SEM). A multiple contact sample was passivated by photo-resist. A small rectangular opening was made to allow deposited clusters to be in contact with eight gold contacts underneath.

The multiple contact samples were made through four lithography processes. If back-gated contacts were required, an additional lithography process was necessary. Each lithography process consisted of three steps, namely photo-resist coating, exposure and development. First, an ultra-violet (UV) sensitive photo-resist (AZ1518) was spun onto a wafer (or a fraction of a wafer) at 4000 rpm for one minute. Second, the photo-resist was soft-baked on a hot plate at 95ºC for two minutes. Next, the photo-resist was exposed to UV light through a reticle in a mask aligner. There are five different layouts of the reticle shown in Figure 4-4, namely, (a) back-gate contacts, (b) large-scale contacts, (c) small-scale contacts, (d) bond-pad opening and (e) window opening. After the exposure, the photo-resist was developed using AZ300 developer.

Figure 4-4 (a) shows the layout of the back-gate contacts. To make the back-gate contacts, samples with developed photo-resist were etched in a reactive-ion etcher (RIE). After etching using a plasma mixture of CHF_3/Ar at -20ºC and 0.01 Torr, the silicon nitride and silicon dioxide were removed, leaving openings to the silicon substrate. When the large-scale contacts were made, two of the pads were able to connect directly to the underlying substrate through these openings.

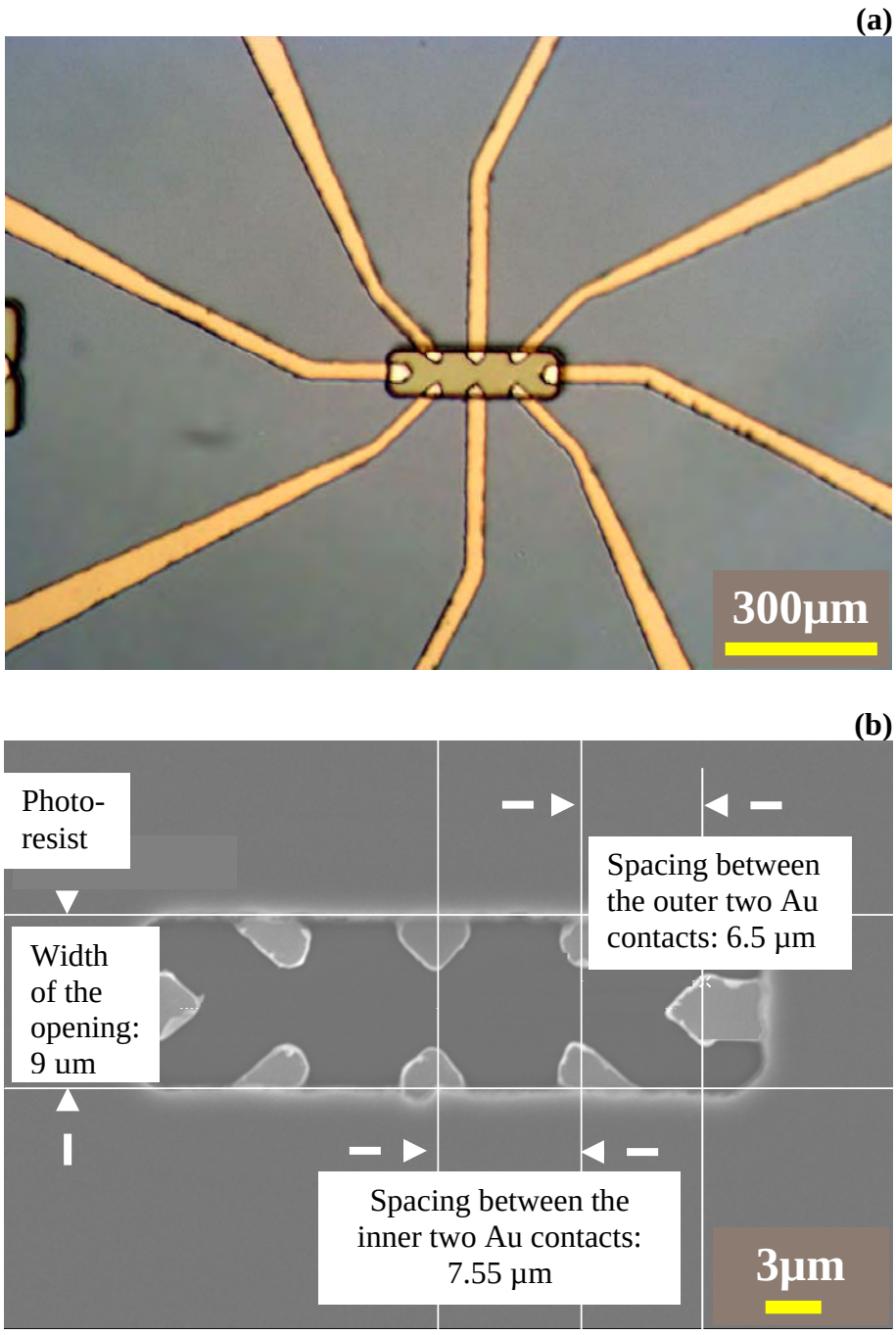

Figure 4-3: **A multiple contact sample was passivated by photo-resist. A small rectangular opening was made to allow deposited clusters to be in contact with eight gold contact tips. (a) Optical image and (b) SEM image**

Figure 4-4(b) shows the layout of large-scale contacts relative to the back gate contacts. Figure 4-4(c) shows the layout of small-scale contacts relative to the large-scale contacts. The metallisation of large-scale contacts and small-scale contacts was achieved through a lift-off process. The lift-off process included the patterning of photo-resist, evaporation of metals, and the removal of photo-resist. After the photo-resist was developed, samples were mounted into a thermal evaporator. At a base pressure of 10^{-6} Torr, 5 nm NiCr, which consisted of 80% nickel and 20% chrome, and 40 nm gold (Au) were thermally evaporated. Then, the photo-resist and the unwanted metals were removed using acetone and iso-propyl alcohol (IPA). The remaining metals formed the metallisation of the multiple contact samples.

Once the metallisation was completed, samples were passivated using photo-resist. The photo-resist was exposed using two masks, namely bond pad opening shown in Figure 4-4 (d) and window opening shown in Figure 4-4 (e). The bond pad opening allowed the probe pins to connect to the samples. The window opening allowed the clusters to land on a confined area at the centre of the samples.

The preparation of the multiple contact samples was extremely time-consuming because each sample required at least four masking steps and the yield was quite low (typically less than 10 %). Moreover, because of the small window opening (330 μm × 9 μm), any mis-alignment of the cluster beam relative to this opening would result in a failure for the sample deposition. Since it was not necessary to have a four-terminal resistance measurement to measure the non-linear $I(V)$ characteristic [2], simple inter-digitated samples were used later.

Figure 4-5 shows the layout of an inter-digitated sample. There were four contact pads on the sample. Each pad connected to a comb-like electrode with a spacing of 100 μm. Thus, three pairs of inter-digitated electrodes were formed. If the cluster beam was aimed at the centre of the sample, it was possible to have three pairs of electrodes connected to the clusters. With three pairs of electrodes, the alignment of the cluster beam to the sample was not as critical as for the multiple contact sample, since it was acceptable to get only one pair of electrode working. There was 4 mm allowance for the cluster alignment in the inter-digitated samples, as compared to 330 μm allowance in the multiple contact samples.

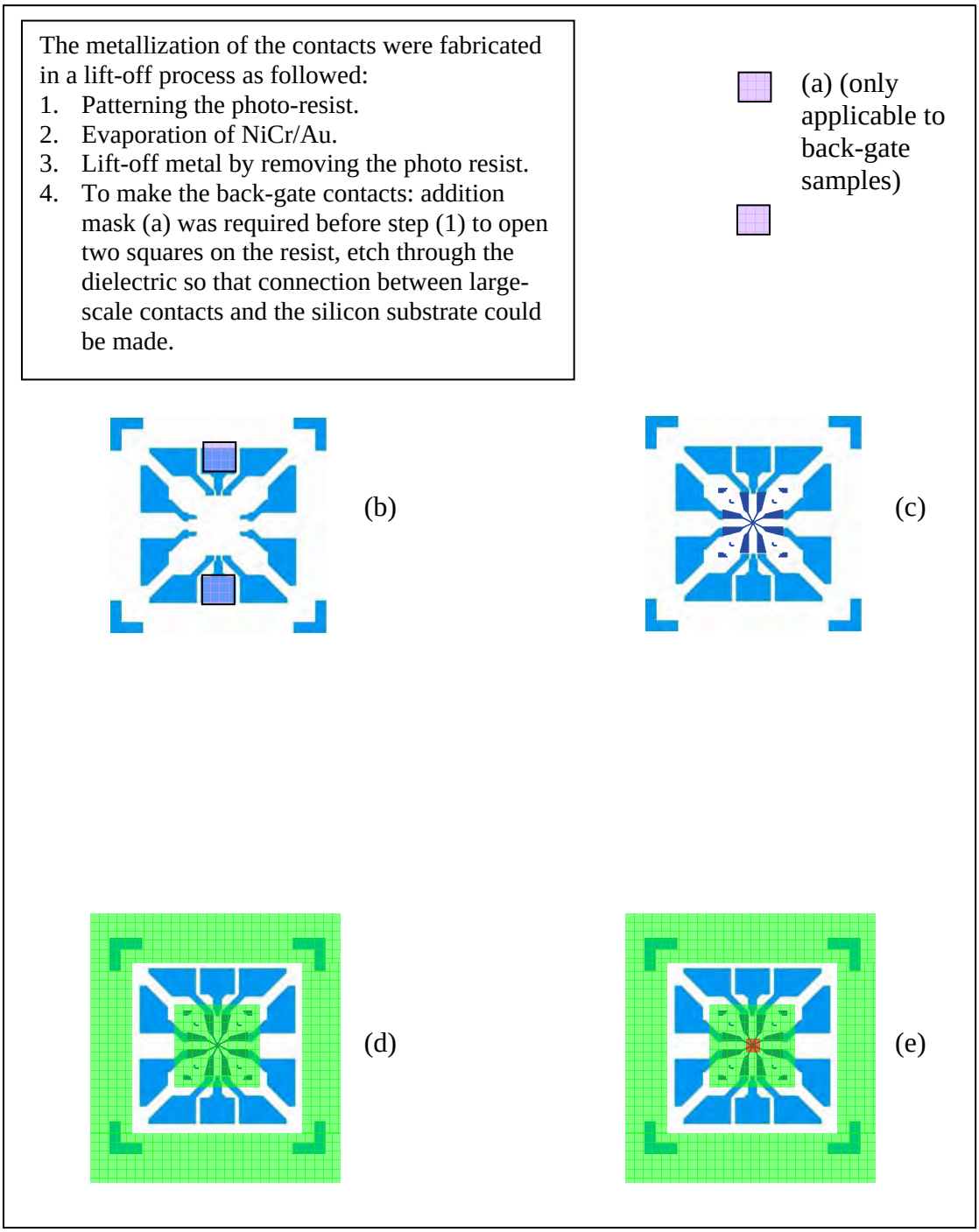

Figure 4-4: **Five masks in making multiple contact samples: (a) back-gated contacts, (b) large-scale contacts, (c) small-scale contacts, (d) bond pads opening and (e) window opening. Inset briefly describes the making of large-scale contacts and small-scale contacts.**

The fabrication process of the inter-digitated samples was similar to the process steps involved in the making the metallisation of the multiple contact samples. The samples were fabricated by patterning photo-resist on SiN coated substrates, thermal evaporating 5 nm NiCr (80% Ni and 20% Cr) and 50 nm of Au, and removing photo-resist and the unwanted metals.

Figure 4-5: Photo of an inter-digitated sample used in the experiments with the scale of millimetres.

4.2 General observations

This section provides general observations regarding the source pressure, the spot size of the antimony cluster beam and deposition rate with different source configurations.

4.2.1 Source pressure

The source pressure is an important factor affecting the nucleation and transportation of the clusters. Therefore, the effects of gas flow rate, the crucible temperature and the source configurations on source pressure were studied.

Figure 4-6 shows the source pressure as a function of crucible temperature in configuration D. The source pressure was quite stable for crucible temperatures in the range 615 – 645ºC at all flow rates. The source pressure was mainly a function of gas flow and was not affected by the temperature of the crucible.

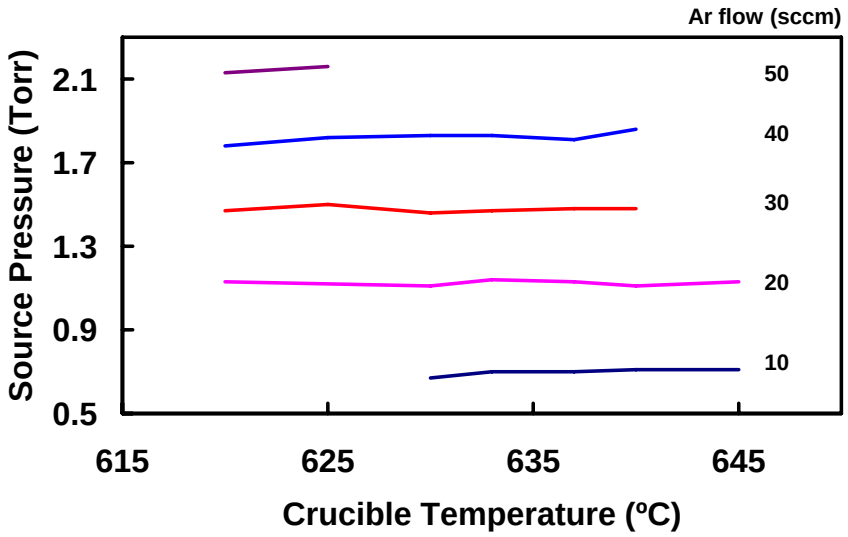

Figure 4-6: **Source pressure as a function of crucible temperature at different argon flows in configuration D.**

According to the ideal gas law,

$$PV=nRT \qquad (Eq.\ 4\text{-}1)$$

where P is the source pressure, V is the volume of the chamber, n is the number of moles, R is the universal gas constant (8.3145 J/mol K) and T is the gas temperature, if the source pressure was stable at different operating temperature, it also implied that the gas temperature T was not affected by the crucible temperature.

Figure 4-7 shows the source pressure as a function of argon flow rate in configurations A and C. The source pressure was not affected when the tantalum plate was inserted. The source pressure varied linearly with the argon flow with or without the plate. The only difference between the two data sets was that when the plate was not used, antimony clusters could only be produced at a high argon flow rate. The source pressures were 1.1 mbar at 20 sccm argon flow and 1.4 mbar at 30 sccm argon flow for both configurations A and C. By changing the nozzle diameter from 3.5 mm to 2.5 mm, the source pressure did not vary greatly.

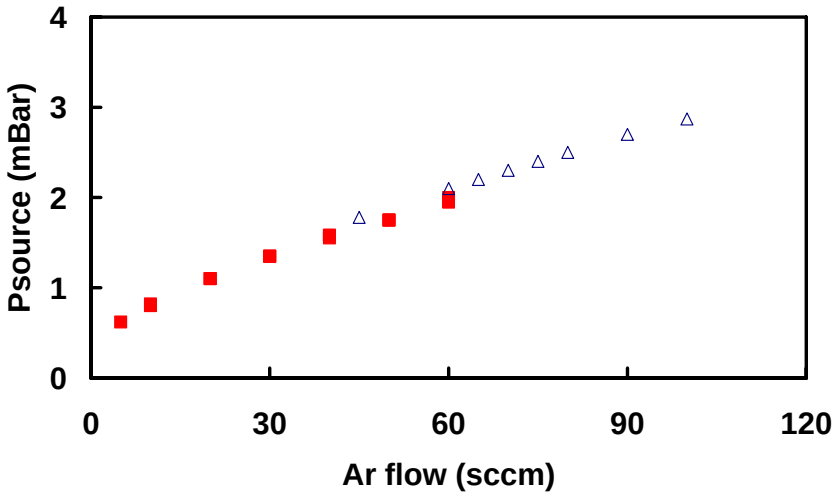

Figure 4-7: **Source pressure as a function of argon flow rate in configurations A (triangles) and C (squares) at crucible temperatures between 620 and 650ºC. No cluster was produced below 45 sccm in configuration A, thus, the source pressure was not recorded. Different argon flow range was selected between the two configurations because the operating conditions for the amorphous antimony clusters to be detected were different in each source configurations.**

4.2.2 Spot size of the cluster beam

In order to characterise the deposition rate, the spot size of the cluster beam on the crystal film of the film thickness monitor (FTM) is very important. If the beam covers the whole oscillating crystal film, the actual deposition rate will be the same as the deposition rate registered in the FTM. Therefore, this sub-section aims to describe the spot size of the cluster beam with different source configurations. An experiment was set up to measure the spot size of the cluster beam. Because of the bouncing of clusters off a hard substrate and the poor optical contrast between the cluster spots and the silicon background, a piece of white paper was used to capture the cluster spot.

Figure 4-8 shows the measured spot size as a function of argon flow rate for configurations A and D. The depositions were carried out at ~ 1 $Å s^{-1}$ deposition rate for 3 minutes for each spot. This deposition rate was similar to the deposition rate for the inter-digitated samples. The spots were circular and the spot sizes were around 3.6 mm for configuration D. For configuration A, the spots were circular and the spot sizes were around 3.4 mm, except for deposition at 65 sccm argon flow. In configuration A, when the flow rate was at 65 sccm, the cluster spot was small and irregular. It was speculated

that the clusters bounced off the paper at this condition. In all other depositions shown in Figure 4-8, the spots grew from near the centre and eventually formed a circular shape, as shown in the inset of Figure 4-8.

The clusters on the paper could not be imaged in the SEM due to the electron charging on the paper. Thus, clusters were deposited on a SiN sample coated with 20 nm gold in a separate experiment. The SEM result revealed that no cluster was observed outside of a 4 mm spot size which agreed with the spot size measured.

After a long deposition time on the FTM crystal in each run, the spot sizes on the crystal were around 8mm for all depositions. The FTM crystal was located about 10cm behind the paper and the cluster beam was diverging, therefore the spot sizes were larger than the spot sizes on the paper. Since the spot size was smaller than the diameter of the FTM crystal (10mm), the actual deposition rate should be corrected by $(10/8)^2$.

In short, the spot sizes of the cluster beam on the samples were around 3-4 mm, as long as the deposition time was long and the clusters were not bouncing. The spot sizes on the FTM were around 8mm. The next section will discuss the relation of deposition rate and various process parameters.

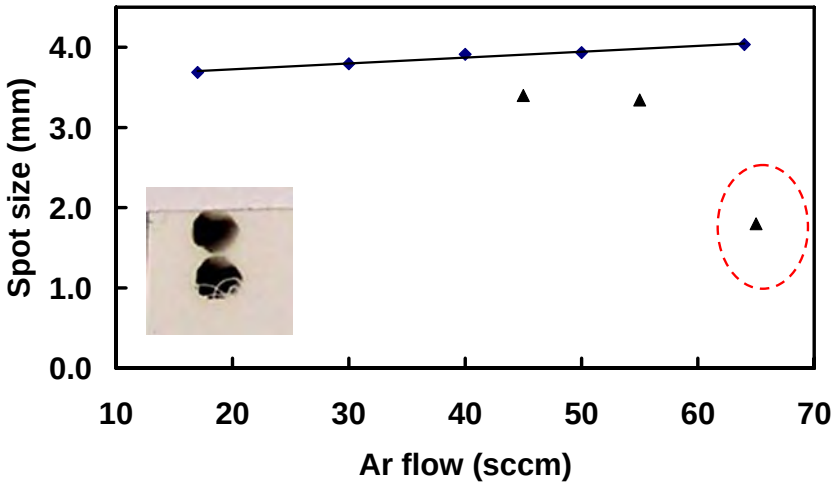

Figure 4-8: **The measured spot size as a function of argon flow rate for configuration A (triangles) and configuration D (diamonds). Inset shows two spots from configuration A at 45 and 55 sccm flows. Similar circular spot shapes were observed for all spots except for the spot at 65 sccm in configuration A (as circled in the main figure).**

4.2.3 Deposition rate

The deposition rate was measured by the film thickness monitor (FTM) which was positioned at the back of the sample arm and is about 15 cm downstream from where the cluster beam enters the diffraction chamber (see Chapter 2). The deposition rate was determined by measuring the oscillation frequency of a quartz crystal over time. The more material is deposited onto the crystal, the lower the frequency. The monitor was mainly used to tune the cluster source and compare different source parameter settings. It was also used to calculate the deposition time.

Figure 4-9 shows the deposition rate as a function of argon flow rate at different crucible temperatures in configurations A, C and D. When the crucible temperature was stable for at least five minutes, the deposition rate was registered. The deposition was plotted as a function of argon flow rate. An interesting phenomenon was observed: there was an optimum flow rate to produce highest deposition rate at all crucible temperatures.

The maximum peaks were at 65 sccm in configuration A and at 30 sccm in configurations C and D, as shown in Figure 4-9 (a-c). The shift in the peaks was mainly due to the use of tantalum plate. As depicted in Figure 4-10, when the plate was used, the gas flowed only through the top part of the source, but not the bottom part, thus making the cooling more effective.

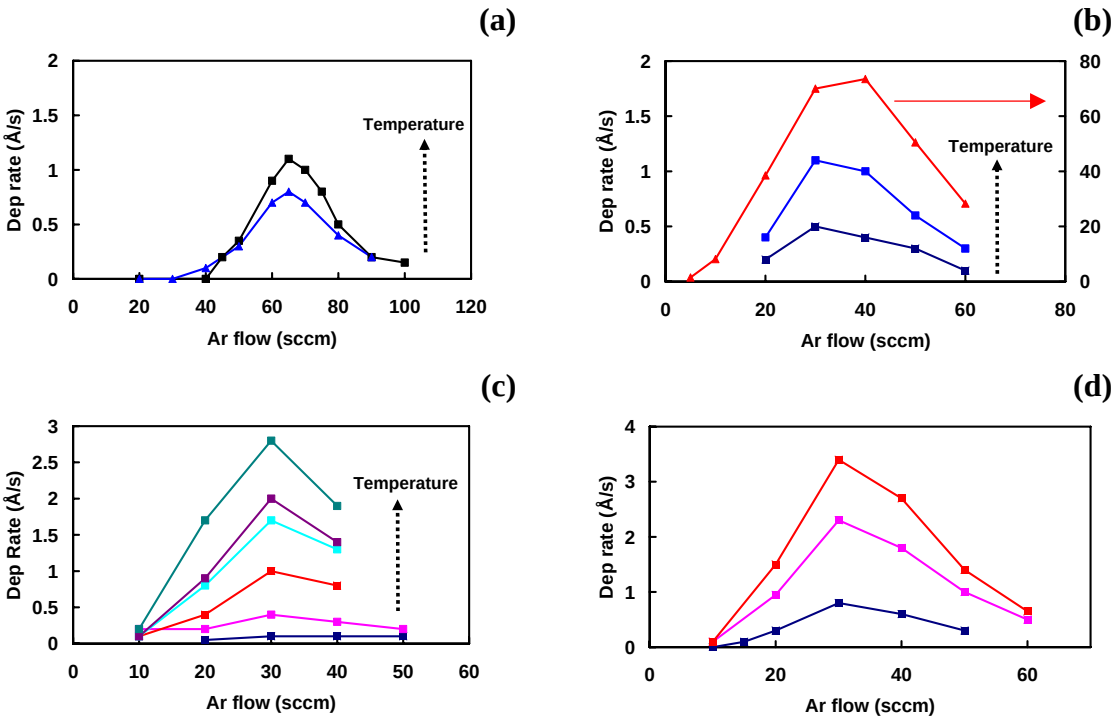

Figure 4-9: **Deposition rate as a function of argon flow rate at different crucible temperatures in different source configurations. (a) Configuration A: 630ºC (triangles) and 640ºC (squares). (b) Configuration C: 620ºC, 625ºC and 650ºC. Note scale changes for data highlighted in red (c) Configuration D: 620ºC, 625ºC, 630ºC, 633ºC, 637ºC and 640ºC. (d) High deposition rate was achieved for Configuration D: 610ºC, 615ºC and 617ºC.**

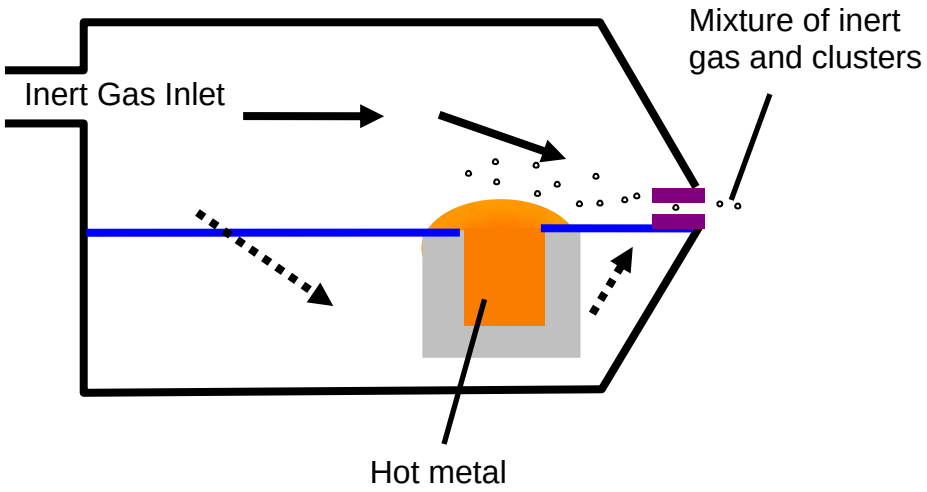

Figure 4-10: **The schematic of the gas flow in an IGA source. When the plate was used, the gas flowed through only the top part of the source (solid arrows), but not the bottom part (dashed arrows). Drawing is not to scale.**

When the plate was in use and the diameter of the first stage nozzle changed from 3.5 mm to 2.5 mm, the optimum gas flow remained the same (~ 30sccm), as illustrated in Figure 4-9 (b) and (c). Therefore, the diameter of the first stage nozzle did not have any effect on the deposition rate.

As indicated in Figure 4-9 (b), the deposition rate increased by more than ten times when the crucible changed from 625 to 650ºC, because the density of metal vapour was expected to increase very fast with temperature.

However, in the same configuration, Figure 4-9 (d) shows a high deposition rate at crucible temperatures between 610 and 617ºC, compared to the deposition rates at crucible temperature between 620 and 640ºC in Figure 4-9 (c). This showed that the deposition rate could not be compared between experiments. The reason was that the deposition rate was very sensitive to the actual crucible temperature. The accuracy of the crucible temperature measurement depended on the physical contact between the crucible and the thermocouple. Thus, the measured temperature might not necessarily reflect the actual crucible temperature. Although no conclusion could be drawn for the deposition rate for different first stage nozzle, the consistent trend of the deposition rate was a good indication of the stability of the process.

4.3 Configurations A and B

Initially the process conditions were the same as reported by Kaufmann[1]. The source was set up according to either configurations A or B (refer to Table 4-1). In these configurations, the tantalum plate was not used, and the bore diameter of the first stage nozzle was either 3.5 mm (configuration A) or 2.5 mm (configuration B). The antimony clusters were deposited on multiple contact samples. The preparation of the multiple contact samples was described in Section 4.1.3.

Table 4-2 shows the process conditions of the multiple contact samples. The source temperature was between 630ºC and 725ºC; the argon flow rate was between 35 and 60 sccm. The phases of the clusters were identified by comparing the peaks to Figure 4-2.

Diffraction patterns (not shown) indicated that the deposited clusters were crystalline when the crucible temperature was ~ 725ºC and amorphous when the crucible temperatures were between 630ºC and 650ºC.

Figure 4-11 highlights the faceted shape of the crystalline clusters and the spherical shape of the amorphous clusters under SEM. The two SEM images were taken from samples MC#1 and MC#3. The phase of the clusters was identified by the electron diffraction patterns described in Section 4.1.2. This observation was consistent with Ref.[3].

Table 4-2: **List of multiple contact samples. All samples had amorphous clusters except multiple contact samples #1 and #7 which had crystalline clusters.**

multiple contact sample	Configuration	Crucible Temperature (ºC)	Ar flow rate (sccm)	Deposition Rate (Ås^{-1})	Deposition Time (s)
MC#1	A	725	60	4.5	200
MC#2	B	650	37	4.0	270
MC#3	B	630	48	5.8	165
MC#4	B	650	50	5.4	147
MC#5	B	650	45	3.6	1800
MC#6	B	650	45	3.5	660
MC#7	B	726	45	1.5	220

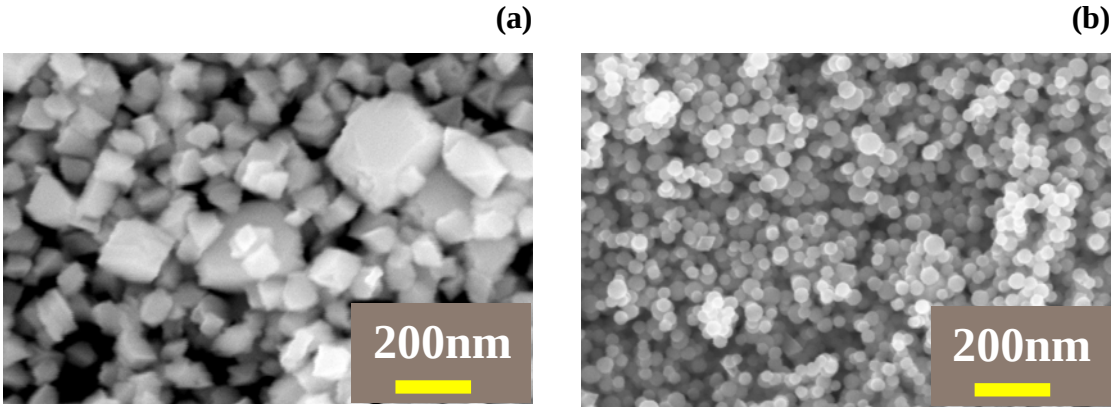

Figure 4-11: **SEM images of (a) crystalline antimony clusters (sample MC#1) and (b) amorphous antimony clusters (sample MC#3). The crystalline clusters were faceted and the amorphous clusters were spherical.**

4.3.1 *I*(*V*) and *R*(*T*) for multiple contact samples

This sub-section describes the electrical characterisation, such as *I*(*V*) and *R*(*T*) measurements on the multiple contact samples. All samples (MC#1 - MC#7) showed a linear *I*(*V*) curve over a small voltage range (~30 mV). Schulze *et al.* [4] showed that application of much larger voltages can modify the structure and electrical characteristics of nano-particle films. Figure 4-12 shows a linear *I*(*V*) curve of sample MC#3 at room temperature. However, the *I*(*V*) curve of sample MC#1 was slightly different. Figure 4-13 shows the reduction of the two-terminal resistance from 125 kΩ to 25 kΩ for sample MC#1 when the voltage was swept between -30 mV and +30 mV continuously. The step change in resistance has been discussed by Ayesh [5].

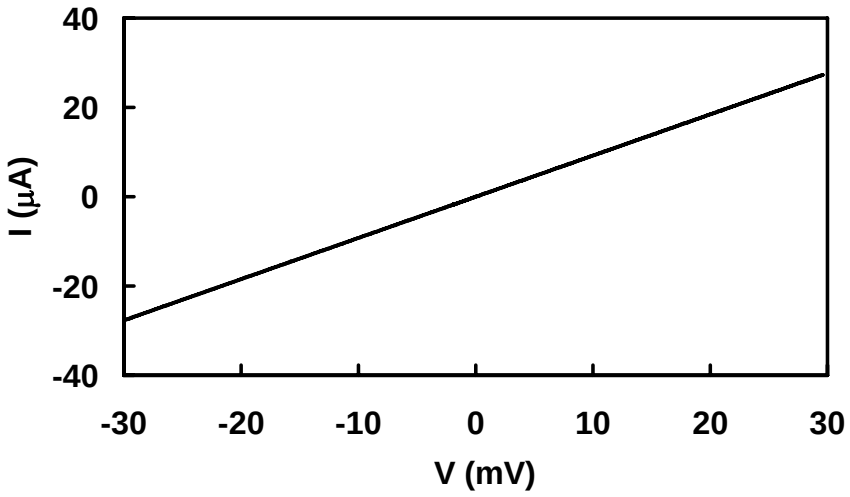

Figure 4-12: ***I*(*V*) curve with four terminal resistance measurement of sample MC#3 at room temperature**

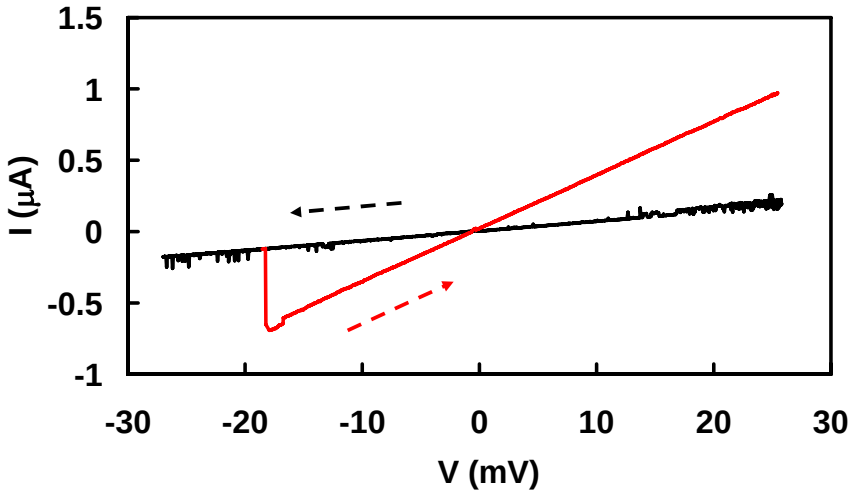

Figure 4-13: Resistance changed from 125kΩ to 25kΩ during a continuous voltage sweep. (sample MC#1)

Figure 4-14 shows the damage caused electrostatic-discharge (ESD) in sample MC#2. The clusters near the two pins on the left were blasted away because of the ESD damage and the connection between these two pins was open. Outside these two pins, some clusters were fused due to high temperature during the ESD event. The electrical measurements still could be performed on other unaffected pins.

As described in the literature [6, 7], there are many factors which can cause ESD failures. A good layout design could increase the ESD susceptibility of a product [6]. There were two possible factors that caused the low ESD susceptibility of multiple contact samples. The first was related to the sharp tips of the contacts underneath the window. It is well known that if a material is formed into a sharp point, the electric field becomes concentrated at the tip. Therefore, the intense electric field at the sharp tips of the small-scale contacts increased the probably of the discharges. Secondly, it was related to the spacing between the pins. As the electric field was inversely proportional to the spacing, smaller spacing created a higher electric field within the samples. In the design of the multiple contact samples, the spacing between the tips was ~7 μm, as shown in Figure 4-3 (b). Hence, the intense electric field due to the small spacing between the pins and the sharp tips made the multiple contact samples more susceptible to ESD damages. The ESD damage was not observed in the inter-digitated samples because the gap spacing was wide (~100 μm) and there was no sharp tip for the electrodes.

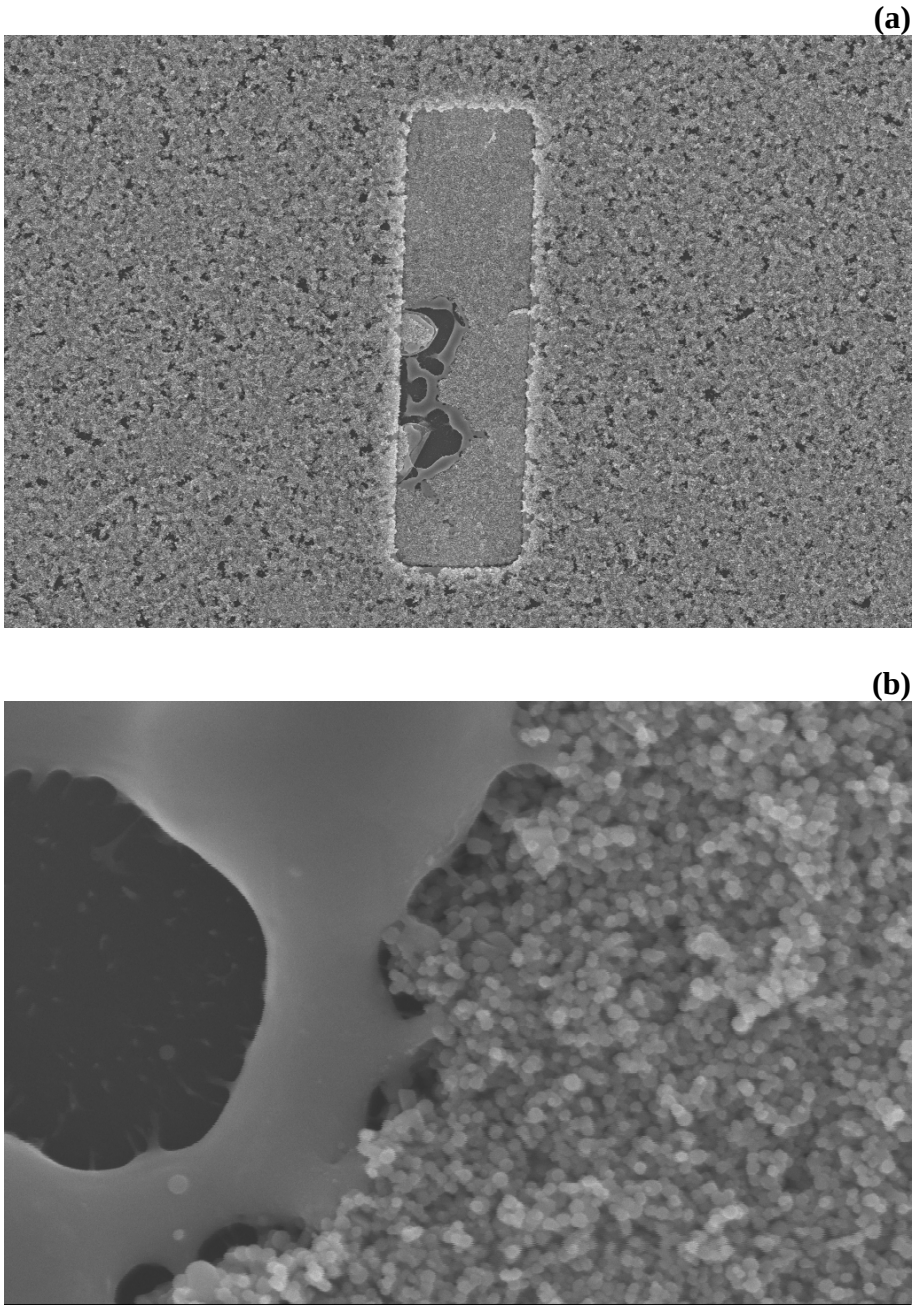

Figure 4-14: **(a) Full coverage of antimony cluster in sample MC#2. (b) High magnification SEM image showed that clusters were fused between two contacts.**

Figure 4-15 shows the $R(T)$ measurement of sample MC#3. This sample was cooled with liquid nitrogen in the cryostat and the resistance was measured during warming up. The change in resistance (R/R_o) was computed and plotted against the temperature T. The (R/R_o) in sample #3 increased as the temperature decreased. In the $R(T)$ measurements, the temperature coefficient of resistance was characterised. In the literature, temperature coefficient of resistance is compared at room temperature. In this text, the temperature coefficient of resistance α is defined as:

$$\frac{(R - R_o)}{R_o} = \alpha \times (T - T_o) \qquad (Eq.\ 4\text{-}2)$$

where R_o is the resistance at T_o and T_o is 290 K. At this temperature, the temperature coefficient of resistance (α) was -7.35×10^{-3} K^{-1}.

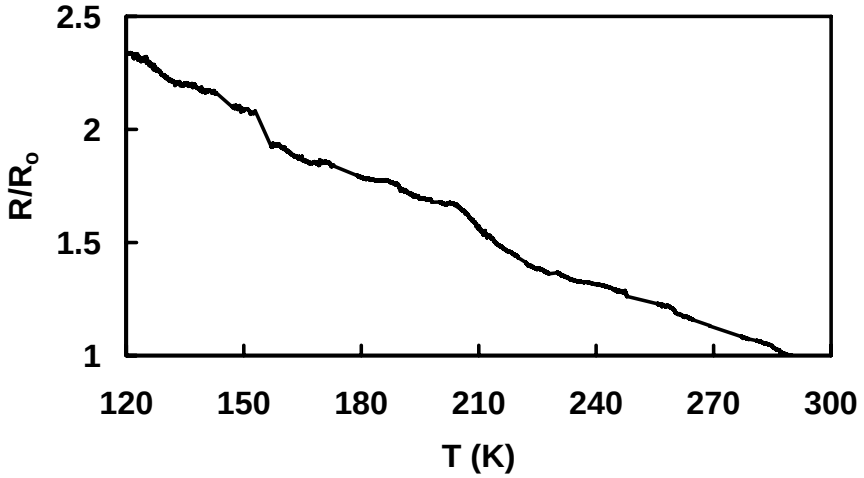

Figure 4-15: Change resistance as a function of temperature T for sample MC#3. R_o, the resistances at 290K (T_o) was 1433 Ω.

The next two sections describe two major problems encountered: film morphology and the consistency of the cluster spot location.

4.3.2 Film morphology

In order to identify the amorphous phase with a distinctive diffraction pattern, high deposition rates (> 3Ås^{-1}) registered at the film thickness monitor (FTM) were necessary [1]. To achieve this deposition rate, a high argon gas flow (≥ 45 sccm) was necessary in either configuration A or configuration B. With the high gas flow, the clusters gained high kinetic energy, and bounced off the hard substrate. Figure 4-16 shows that the film morphology of Sb clusters deposited on sample MC#6. In this case, clusters bounced at 3.5 Ås^{-1} deposition rate and only adhered well onto gold contacts, defects or other clusters on the photo-resist or SiN, and subsequent formed clumped clusters. Thus, the amorphous antimony cluster films produced from configurations A and B were not uniform.

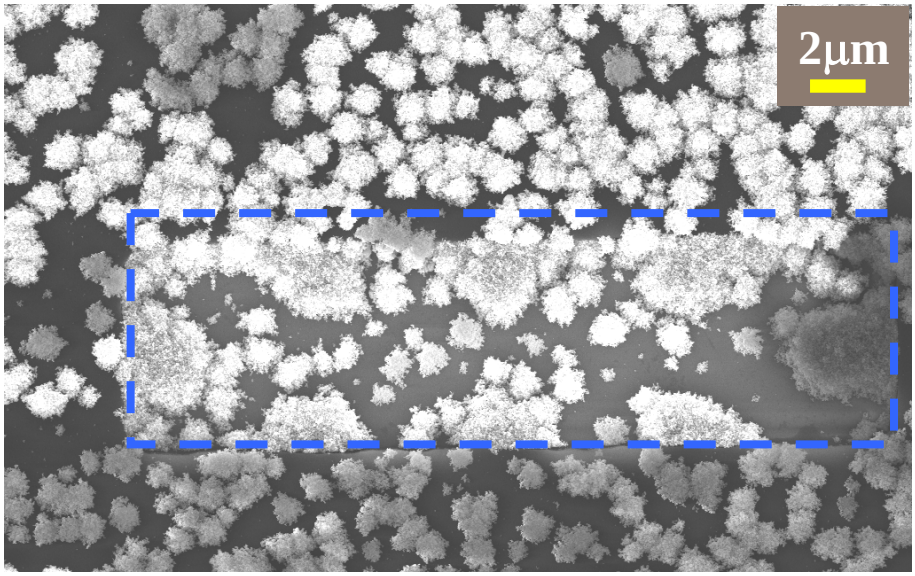

Figure 4-16: **Film morphology of Sb clusters in sample MC#6. At 3.5 Ås^{-1} deposition rate, clusters bounce away from substrate but stick well to the gold contacts, defects or other clusters on the photo-resist and SiN substrate. As a result, a clumped cluster film was formed. Photo-resist covered the samples except the small window (highlighted in a dashed rectangular).**

Because of the clumping, the electrical paths could be easily disconnected at low temperature due to the contraction of the cluster films. A uniform film was needed for electrical characterisations. In order to produce uniform film, the amorphous clusters needed to be generated with different process conditions, such as using a gas mixture of argon and helium gases [2], or using different source configurations. As reported by Reichel [2], when He/Ar ratio increased, smaller clusters were produced. With smaller clusters, the adhesion could probably be improved as long as the velocity did not increase drastically. After several attempts, the amorphous phase of the antimony clusters could not be identified in the argon and helium mixture. Kaufmann also reported that the amorphous antimony clusters were only made using pure argon gas [1]. Therefore, source configurations C and D, which had a tantalum plate, were tried. The detailed results will be presented in Section 4.4.

4.3.3 Inconsistency of the cluster spot location

During the experiments, the location of the cluster spot was not repeatable. Thus, it was difficult to deposit clusters onto the small window at the centre of the multiple contact sample. In the deposition of some multiple contact samples (not listed in Table 4-2), the cluster spot was located out of the window and thus, no onset was observed during the deposition. As described in Section 4.1.3, the capture area of the inter-digitated samples (3 mm × 100 μm) is much larger than the small window (330 μm × 9 μm) in the multiple contact samples. Therefore, inter-digitated samples were used for following experiments to alleviate this problem.

4.4 Configurations C and D

This section describes a series of results and analysis for clusters made in configurations C and D. In these two configurations, a tantalum plate was used (see Chapter 2). The bore diameters of the first stage nozzle were 3.5 mm and 2.5 mm in configurations C and D respectively.

A tantalum plate was used previously in the study of unsupported bismuth clusters [8]. On the other hand, the source used in the study of unsupported amorphous antimony [1] did not have the plate. Thus, it was the intention of this section to study the effects of the tantalum plate systematically and thoroughly on amorphous antimony clusters.

When the tantalum plate was inserted, the effects of the operating process conditions, such as gas flow rate and the crucible temperature, were studied. In order to register noticeable deposition rate, the minimum argon flow rate was 35 sccm for configurations A and B, and 15 sccm for configurations C and D. The crucible temperature range for amorphous phase clusters was 630 to 645ºC for configurations A and B, and 610 to 725ºC for configurations C and D. Therefore, the process margin to produce amorphous antimony clusters was wider in configurations C and D, compared to the process margin in configurations A and B.

In this study, clusters were deposited on inter-digitated samples. Table 4-3 lists the details of the inter-digitated samples. Samples #19-41 were deposited with the tantalum plate (Configurations C or D). Samples #43 and 44 were deposited without the tantalum plate (Configuration A), for the purpose of comparison.

Table 4-3: List of inter-digitated samples. All samples had amorphous Sb clusters

Sample no.	Configuration	Crucible Temperature (ºC)	Ar gas flow (sccm)	Deposition Rate ($Ås^{-1}$)	Deposition Time (s)
#19	C	615	26	2.8	60
#20	D	617	30	3.4	20
#25	D	610	30	0.9	156
#26	D	617	20	1.0	80
#27	D	612	30	0.9	76
#30	D	620	30	0.9	88
#31	D	633	15	0.7	112
#34	D	622	16	0.9	600
#35	D	620	17	0.9	242
#36	D	625	17	0.9	113
#38	D	628	30	0.9	80
#41	C	630	16	1.0	280
#43	A	630	65	1.1	NA*
#44	A	641	45	0.9	638

*: Due to mis-alignment, the clusters were landed on bond pad but not in between the electrodes. Thus, no onset was observed.

4.4.1 Film morphology

As explained in Section 4.3.2, a uniform film was essential for electrical characterisation, but the clusters clumped together because of bouncing and formed non-uniform films. In configurations A and B, it was not possible to reduce the argon flow rate further and still generate amorphous clusters. Thus, a tantalum plate was introduced to shift the operating gas flow to a lower range. However, the film was still non-uniform even when the argon flow rate was reduced to 26 sccm in configuration C, as illustrated in Figure 4-17 (a).

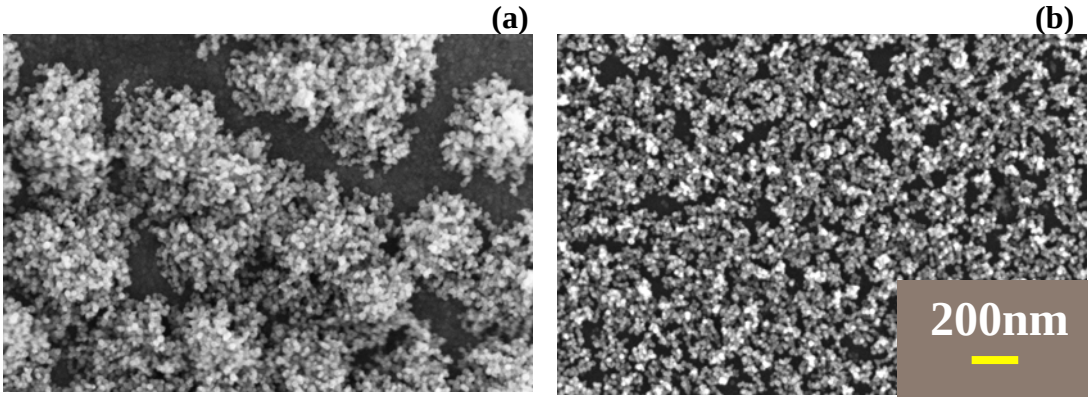

Figure 4-17: **Two different film morphologies. (a) A film with lumps of clusters was produced using configuration C (sample #19). (b) A more uniform cluster film was produced using configuration D (sample #20). Both figures have the same scale.**

Figure 4-17 shows different film morphologies for the films produced in configurations C and D for samples #19 and #20. In both depositions, the crucible temperature registered was ~ 615ºC and the argon flows were 26 sccm and 30 sccm. In sample #19, which was produced from configuration C, clusters bounced off the substrate and only adhered to the defects and other clusters on the substrates, producing a non-uniform film that was similar to Figure 4-16.

By changing the first nozzle to the 2.5 mm nozzle in the case of configuration D, a more uniform film was observed in sample #20, as shown in Figure 4-17 (b). Uniform films were obtained for other samples in configurations D (samples #35-38). Since the clusters showed similar deposition on the substrate and on the film, the clusters seem to adhere to both surfaces at a similar rate. To understand the adhesion-bouncing behaviour of clusters, the cluster properties in different source configurations are discussed in the next three sections.

4.4.2 Cluster velocity

As described in Section 4.4.1, the clusters produced in configuration C bounced off the substrate, but the clusters produced in configuration D adhered more uniformly to the substrate. To understand the bouncing behaviour, the cluster velocity was studied. In the IGA source, the argon gas imparts momentum to the clusters and moves them toward the sample. There are three main parameters that influence the cluster velocity, namely slipping, gas flow rate and the bore diameter of the first nozzle. Slipping causes the cluster velocity to be different from the velocity of the gas molecules. In this study, it was assumed that there was negligible slip between the cluster velocity and the gas velocity. Hence, the velocity of the clusters was calculated based on the velocity of the argon gas.

A crude estimation of the cluster velocity, which was same as Ref. [5, 9] was used, with an assumption of non-turbulent and sub-sonic gas flow. The number of gas molecules entering the source must be the same as the number of gas molecules leaving from the first stage nozzle (conservation of mass) at a fixed period. As the temperature of the gas molecules was independent of the temperature of the crucible (see Section 4.2.1), *nRT* was constant at a given gas flow. Therefore, *PV* was the same at the gas inlet and inside the source chamber.

$$P_1V_1 = P_2V_2 \qquad (Eq.\ 4\text{-}3)$$

By taking the time derivative of *Eq 4-3*,

$$P_1 \frac{dV_1}{dt} = P_2 \frac{dV_2}{dt} \qquad (Eq.\ 4\text{-}4)$$

By substituting the flow $F = dV/dt$,

$$P_1F_1 = P_2F_2 \qquad (Eq.\ 4\text{-}5)$$

where F_1 is the flow rate monitored by mass flow controller and F_2 is the flow at the first stage nozzle.

Assuming z sccm (standard cubic centimetre per minute) argon molecules are injected into the gas inlet, there will be z cm^3 of gas entering the source at one atmospheric pressure (1013.25 mbar). Thus, the F_2 at the first stage nozzle is given by:

$$P_1F_1 = P_2F_2$$

$$\rightarrow 1013.25(mbar) \times z/60\ (cm^3s^{-1}) = P_{source}\ (mbar) \times F_2\ (cm^3s^{-1}).$$

$$\rightarrow F_2 = 1013.25 \times z/(60 \times P_{source}) \qquad (Eq.\ 4\text{-}6)$$

The gas velocity v is calculated based on F_2 divided by the bore area of the nozzle (πr^2).

$$v = F_2/(\pi r^2) \qquad (Eq.\ 4\text{-}7)$$

By substituting *Eq. 4-6* into *Eq. 4-7*,

$$v = 1013.25 \times z/(60 \times P_{source} \times \pi r^2) \qquad (Eq.\ 4\text{-}8)$$

Using *Eq. 4-8*, the effect of the argon flow rate on cluster velocity could be evaluated. By changing the argon flow rate from 45 sccm to 26 sccm (a reduction of 42 %), the velocity only reduced by 6 % at the 3.5 mm nozzle. As depicted in Figure 4-7, the source pressure reduced as the argon flow rate decreased. Therefore, the effect of low flow rate, which was supposed to slow down the clusters, was cancelled out by the effect from the reduction of the source pressure. It was found that the flow rate was not the main factor affecting the cluster velocity.

The effect of the nozzle diameter on cluster velocity was studied. At 30 sccm argon flow, the source pressures were 1.4 mbar and the cluster velocities were 28 ms^{-1} and 56 ms^{-1} at the 3.5 mm nozzle and the 2.5 mm nozzle, respectively. By changing the nozzle diameter from 3.5 mm to 2.5 mm, the effective area decreased by ~ 50% and therefore the velocity was doubled The cluster velocity significantly increased by reducing the bore diameter of the first stage nozzle.

4.4.3 Cluster diameter

This sub-section describes the effect of flow rate, the tantalum plate and the nozzle diameter on cluster diameter.

Firstly, the effect of flow rate was examined when the 3.5 mm nozzle was used. Figure 4-18 shows the effect of flow rate on cluster diameter for inter-digitated samples #43, #44 and #19. The cluster diameters were 40±3nm, 35±6nm and 25±4nm at 65, 45, 25 sccm argon flows respectively. The average cluster diameter was calculated from ten randomly picked clusters in the SEM images. It was obvious that higher flow rate, which resulted in higher source pressure, produced larger clusters. This observation is consistent with the homogeneous nucleation theory described in Chapter 2 – Increasing gas pressure limits the vapour diffusion and provides better cooling. This results in a cooler, denser vapour and a higher nucleation rate. The increased number of clusters results in more aggregation and larger clusters.

Secondly, the effect of flow rate was studied when the 2.5 mm nozzle was used. Figure 4-19 shows the effect of the first stage nozzle on cluster diameter in samples #19, #26 and #30. The 3.5 mm nozzle was used in sample #19 and the 2.5 mm nozzle was used in samples #26 and #30. Figure 4-19 (a) has a different magnification from Figure 4-18 (c) so that it can be compared with Figure 4-19 (b-c). At 26 sccm argon flow, clusters with 25 nm diameter were deposited on sample #19; as for samples #26 and #30, a consistent cluster diameter (15nm) was observed when the clusters were produced at 20 and 30 sccm argon flows.

In Figure 4-19, the crucible temperatures were slightly different for samples #19, #26 and #30. To rule out the influence of the crucible temperature, an experiment was conducted at a fixed crucible temperature (at 617°C). Figure 4-20 shows small clusters for the depositions at 15-30 sccm argon flow with the 2.5 mm nozzle. The clusters, produced at 15-30 sccm argon flow, were spherical and the diameter was 15±2.6 nm.

As discussed in Section 4.2.1, the source pressure remained the same when the diameter of the first nozzle changed from 3.5 mm to 2.5 mm. Since the source pressure was the same, the clusters produced should have similar diameter. However, it was obvious that the clusters produced in configuration D were smaller than those produced in configuration C even though the argon flow and the source pressure was comparable in the depositions. In short, in configurations A, B and C, the source pressure influenced the cluster diameter directly; in configuration D, the cluster diameter was consistently ~ 15 nm and was independent of the source pressure at the flow between 15 to 30 sccm.

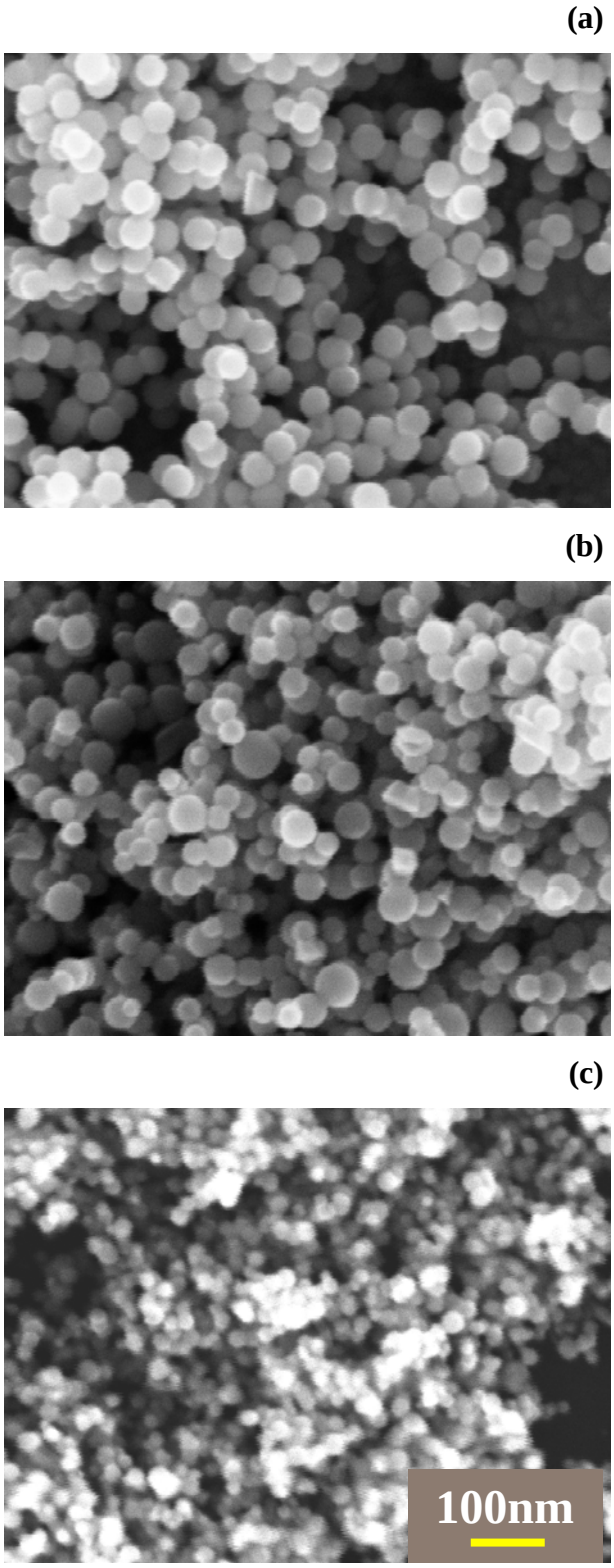

Figure 4-18: **Effects of the argon flow rate on cluster diameter for samples (a) #43, (b) #44 and (c)#19 using 3.5 mm nozzle. At 65, 45 and 26 sccm argon flow, the source pressures were 2.2, 2 and 1.2 mbar and the average cluster diameters were 40, 35 and 25 nm, respectively. The tantalum plate was used only in sample #19. All figures have same scale. The magnification is 150 kX.**

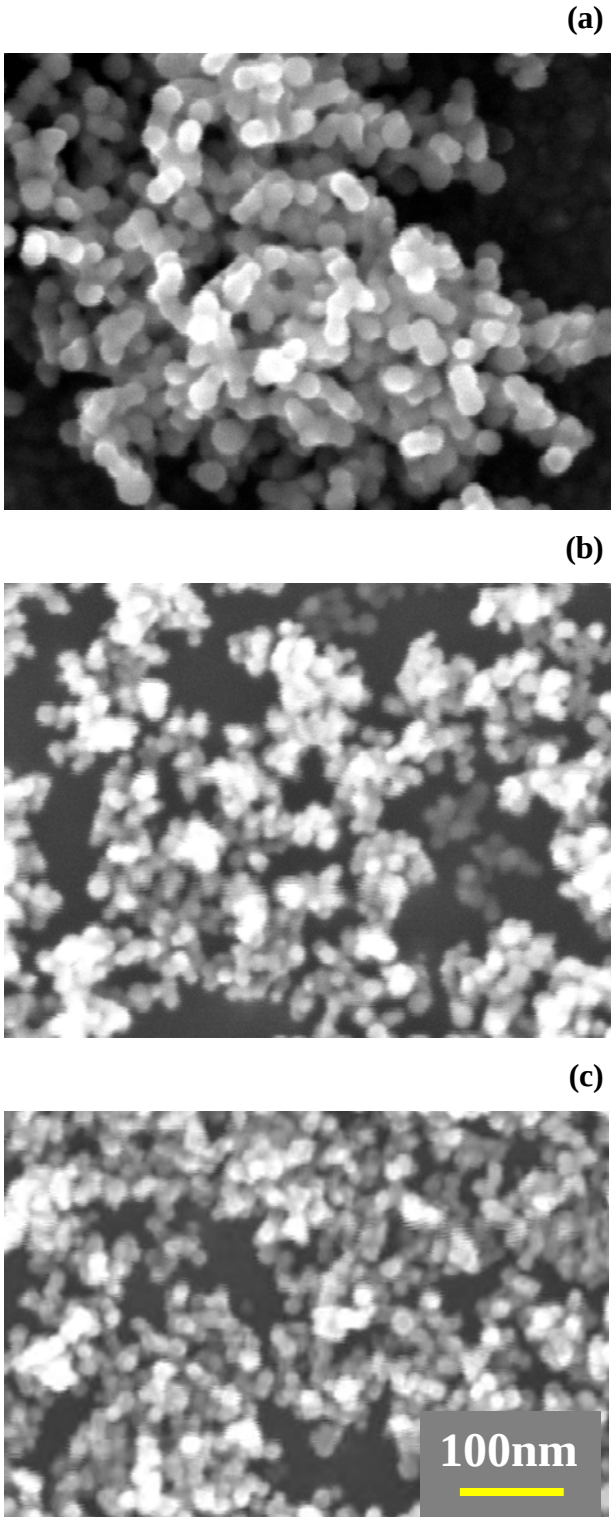

Figure 4-19: **Effects of the first stage nozzle on cluster diameter for samples (a) #19, (b) #26 and (c) #30 when the tantalum plate was used. (a) Using the 3.5 mm nozzle, the cluster diameter was 25 nm at 26 sccm argon flow rate. Using the 2.5 mm nozzle, the cluster diameter was consistently 15 nm at (b) 20 sccm and (c) 30 sccm. Thus, the cluster diameter was not affected by argon flow rate in configuration D. All figures have the same scale. The magnification is 200 kX.**

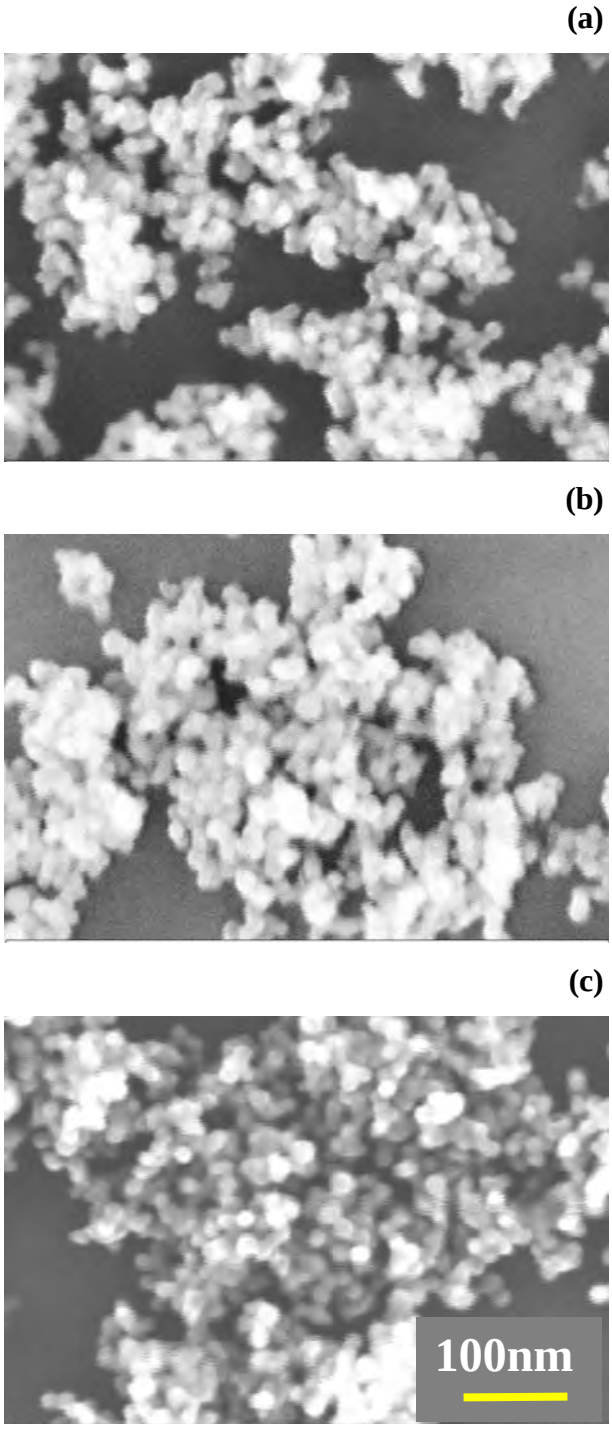

Figure 4-20: **Similar cluster diameters for depositions with configuration D at 617°C crucible temperature and at (a) 15 sccm, (b) 20 sccm and (c) 30 sccm argon flow. The average cluster diameters were all ~ 15 nm. All figures have the same scale. The magnification is 200 kX.**

4.4.4 Kinetic energy

This sub-section describes the kinetic energy of the clusters calculated from the information obtained in Sections 4.4.2 (cluster velocity) and 4.4.3 (cluster diameter). This is used to identify the mechanisms for bouncing/adhesion, and ultimately assist in determining system parameters for uniform cluster film deposition.

The kinetic energy of the clusters, *E*, was calculated as followed:

$$E=\tfrac{1}{2}mv^2 \qquad (Eq.\ 4\text{-}9)$$

The mass, *m* was calculated from the density of antimony ρ and the volume of a cluster V_{cl}:

$$m = \rho \times V_{cl}$$

$$m = \rho \times (4/3 \times \pi r^3)$$

$$m = 1/6\ \pi \times \rho \times D^3 \qquad (Eq.\ 4\text{-}10)$$

where *D* is the cluster diameter.

Figure 4-21 shows the calculated kinetic energy of a cluster as a function of the argon flow rate for the 3.5 mm nozzle and the 2.5 mm nozzle. In the calculation, the cluster diameter was 15 nm in the case of the 2.5 mm nozzle; as for the 3.5 mm nozzle, the cluster diameters were 25, 35 and 40 nm at 26, 45 and 65 sccm argon flow respectively.

Since the cluster diameter varied in the case of the 3.5 mm nozzle, the change of the kinetic energy from 25 sccm to 65 sccm flow was significantly higher than the change of kinetic energy from 25 sccm to 40 sccm for the 2.5 mm nozzle. There were two factors affecting the kinetic energy in the calculation, namely the mass of the clusters and the clusters velocity. As discussed previously, the mass of the clusters changed with the gas flow, and the velocity was lower in the case of the 3.5 mm nozzle; however, the mass of the cluster remained the same and the velocity was high in the case of the 2.5 mm nozzle. From Figure 4-21, the kinetic energy of the clusters in both cases was about the same at low flow rate (~25 sccm).

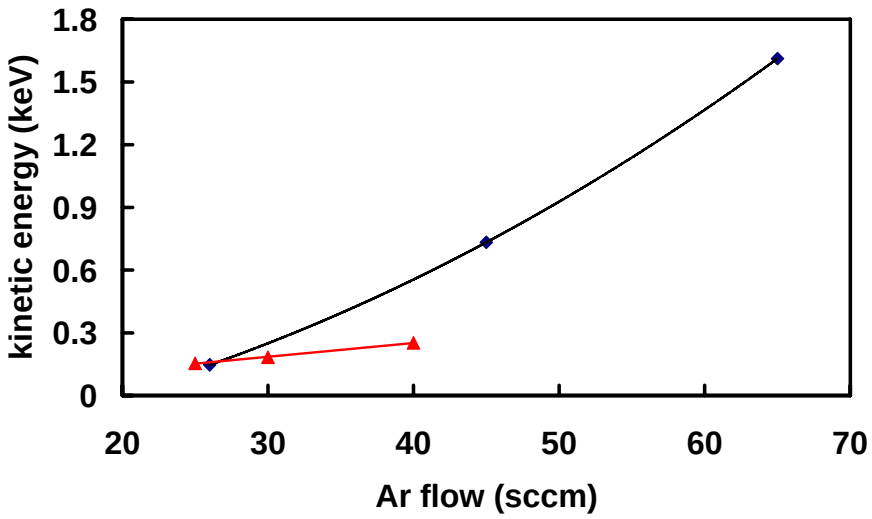

Figure 4-21: **Kinetic energy as a function of argon flow rate for the 3.5 mm nozzle (blue diamonds) and the 2.5 mm nozzle (red triangles).**

In Section 4.4.1, two different film morphologies were shown in Figure 4-17 at the flow rates between 25 and 30 sccm. The different film morphologies could be due to different bouncing of the clusters for the two configurations. In the calculation of kinetic energy, the clusters produced at ~25 sccm flow rate have similar kinetic energy for both configurations. Therefore, the adhesion could be due to some other factors rather than kinetic energy, such as the cluster velocity, as described below.

During normal impact, clusters were expected to bounce off the substrate if the kinetic energy available after the impact was greater than the adhesion energy to the surface [10]. As explained in Ref. [9], when the impact velocity of clusters was high enough, the clusters could deform. In the macroscopic simulations of bouncing spheres [11, 12], plastic deformation also plays an important role when the velocity was higher than the threshold velocity. The threshold velocity for antimony clusters was estimated to be around 9 - 30 ms^{-1} [13]. When the cluster velocity was higher than the velocity above the plastic deformation threshold, the clusters deformed and lost some of the kinetic energy. Once the kinetic energy after impact was lower than the adhesion energy of the substrate, the clusters adhered. Thus, it was speculated that the bouncing of the clusters was affected by the plastic deformation model: clusters from the 2.5 mm nozzle at low flow (~ 25 sccm) region deformed, lost their kinetic energy and adhered to the substrate and produced the film morphology as in Figure 4-17 (b).

4.5 Electrical characterisation

This section describes the electrical characterisation of amorphous antimony films produced in configuration D. Section 4.4 showed that uniform cluster films could be produced in source configuration D at low argon flows. Thus, this configuration was used to deposit clusters on the inter-digitated samples listed in Table 4-3. Electrical measurements were performed *in-situ* with 30 mV bias across the electrodes and the conductance (G) was monitored. The bias voltage was chosen to match Dunbar's experiments [14]. Figure 4-22 shows the conductance onset curve of sample #31.

Although the clusters generated by Dunbar *et al.* [14] were most likely to be crystalline phase (due to the high crucible temperature, 760ºC), the onset curves were quite similar to the onset of sample #31. In both cases, there were three regions in the curves. Firstly, when the shutter was open at time zero, the conductance showed a small increase in the first 15 seconds, followed by a gradual decrease from 15 seconds to 66 seconds for sample #31. This was attributed to the electron emission due to the impact of the clusters on the gold contacts. Next, there was a region of random noise before the onset of the conductance. This random noise was likely caused by the tunnelling of electrons between the contacts as described by Balberg *et al.* [15]. The time when the deposition passed the tunnelling region to a continuous increasing conductance (an indication of onset) was quite important. Therefore, τ_{onset} was defined as the time when the conductance first became consistently greater than 10^{-9} Ω^{-1}. After the onset, the conductance increased rapidly. Once the shutter was closed, the conductance continued to increase due to coalescence. The coalescence started in a very short time (typically from a few seconds up to two minutes) after the deposition.

Current-voltage $I(V)$ curves were measured *in-situ*. Figure 4-23 shows linear $I(V)$ curves for sample #38. All the $I(V)$ curves had the same slope. The linearity of the $I(V)$ curves over a wide voltage range proved that the contacts were ohmic and there was no non-linear $I(V)$ behaviour in the cluster films.

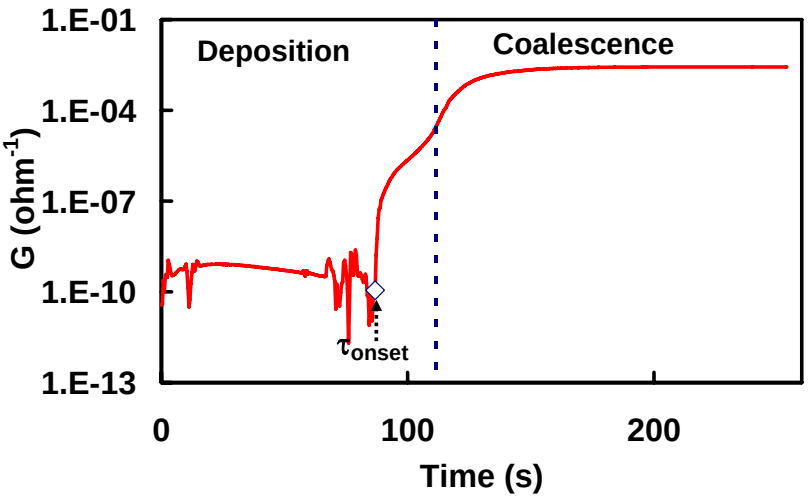

Figure 4-22 : **Conductance onset as a function of time for sample #31. The shutter was closed after the dashed lines. τ_{onset} (diamond) was defined as the time when the conductance first became consistently greater than 10^{-9} Ω^{-1}.**

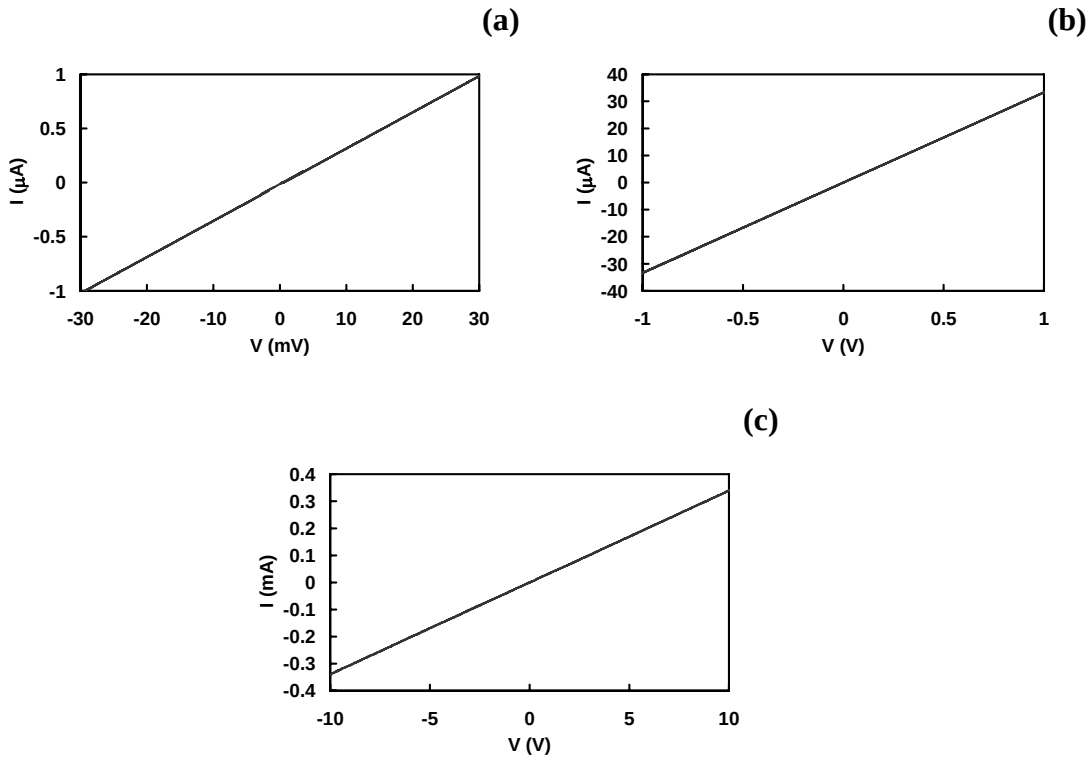

Figure 4-23: **Linear *I*(*V*) curves were observed with three different voltage ranges: (a) 30 mV, (b) 1 V and (c) 10 V for sample #38. All curves had the same slope.**

4.5.1 Percolation and onset of conductance

As described in Chapter 3, percolation theory can be used in a system when a very large lattice is occupied randomly with probability *p*, independent of its neighbours. The beauty of percolation theory is that the mechanism of the occupation can be related by simple power laws. In the case of cluster deposition, the conductance exponent *t* of the power law predicted by percolation theory [14, 16, 17] is given by:

$$G \propto (p - p_c)^t \qquad (Eq.\ 4\text{-}11)$$

where *G* is the conductance; *p* is the coverage; and p_c is the critical coverage for percolation.

The exponent *t* was shown to be close to the theoretical value of 1.3 for bismuth and silver clusters but not for antimony in Ref. [14], due to cluster bouncing and clumping. Figure 4-24 shows the conductance as a function of (p-p_c) from Ref. [14]. The experimental conductivity data for antimony clusters were plotted as a function of (p-p_c) in a log-log scale. The top three curves were quite linear but the bottom four were non-linear due to the bouncing or the formation of clumps. The data were selected from p = 0.006 to 0.324. A wide range of *t* value was observed for antimony clusters as compared to the bismuth clusters [14].

Since configuration A was used in Dunbar's experiments, it was necessary to analyse the deposition using percolation theory for clusters produced in configuration D. Figure 4-25 shows the conductance as a function of surface coverage for sample #31. The surface coverage $p_{surface}$ was computed using the approach used in Ref. [14]. The total coverage was assumed to be directly proportional to the deposition time and the critical coverage $p_c \sim 0.676$ occurs at the critical time τ_c i.e. ,

$$p_c = k\tau_c. \qquad (Eq.\ 4\text{-}12)$$

Then, in order to account for the stacking of clusters, the surface coverage was calculated by solving the differential equations relating to the probability of stacking at coverage *p* [14].

$$p_{surface} = 1\text{-}e^{-p} \qquad (Eq.\ 4\text{-}13)$$

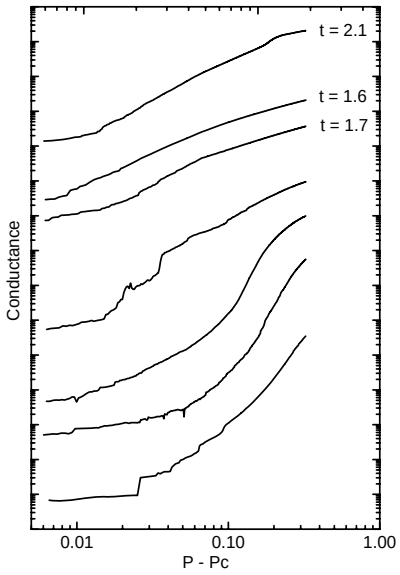

Figure 4-24: **The experimental conductivity data for antimony clusters plotted as a function of (p-p_c) in a log-log scale by Dunbar *et al.* [14]. The top three curves were quite linear but the bottom four were non-linear due to bouncing or formation of clumps. Only data points in the range of p=0.006 to 0.324 were shown.**

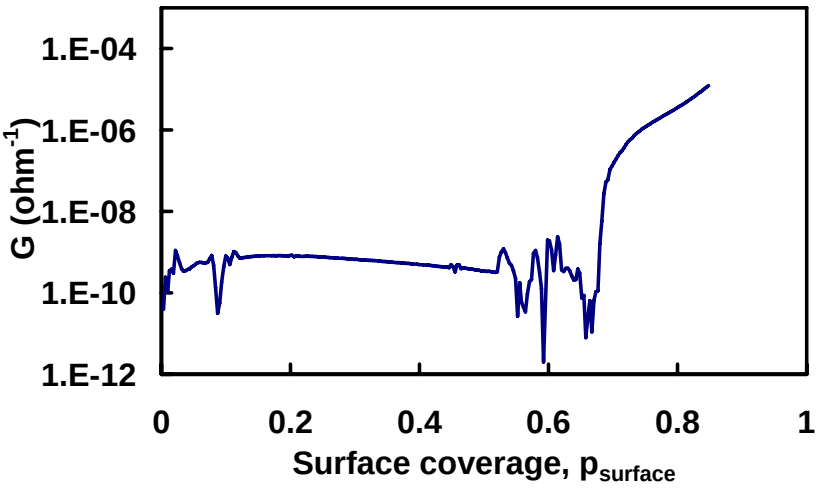

Figure 4-25: **Conductance as a function of surface coverage for sample #31.**

The values of *k* were different even for samples with the same deposition rate because the onset times among these samples were quite different. The observation suggested that the local deposition rate between the gaps of the contacts was different from the average deposition rate registered in the film thickness monitor (FTM).

Since the coverage was proportional to the deposition time, the percolation conductance could be related to the percolation time. The critical time τ_c for percolation was calculated with the sliding least squares fit method used by Dunbar *et al.* [14]. In this case, the data were plotted as log(*G*) vs. log(τ-τ_c), and the following fitting was used.

$$G=a(\tau-\tau_c)^t \qquad (Eq.\ 4\text{-}14)$$

The exponent, *t*, could be obtained from the slope of the fit on the log-log curves. Figure 4-26 demonstrates two examples with τ_c = 87 s and 89 s from sample # 31, using the algorithm of the sliding-least squares method as follows.

1. Set the first τ_c to be the time when deposition started.
2. The data range from τ_c to (τ_c + τ_{range}) was selected for each value of τ_c. The τ_{range} was either 10 seconds or till the end of deposition (whichever is smaller). The minimum coverage and maximum coverage of these data range were referred as p_{min} and p_{max}.
3. Plot log(*G*) vs. log (τ-τ_c) using the selected data.
4. Within this range, the R^2 value was obtained by fitting a straight line $G=a(\tau-\tau_c)^t$ into the log(G) vs. log(τ-τ_c). The R^2 is the square of the Pearson product moment correlation coefficient.

$$R = \frac{\sum (x-\bar{x})(y-\bar{y})}{\sqrt{\sum (x-\bar{x})^2 \sum (y-\bar{y})^2}},$$

where $\bar{x}$ and $\bar{y}$ are the known data points.

5. Increase the τ_c by 1 second (or 0.5 when near to maximum)
6. Repeat steps from #2 to #5. until a good fitting was obtained as shown in Figure 4-26 (a).
7. The calculation of R^2 using different τ_c was shown in Figure 4-27. When maximum R^2 was reached, τ_c and *t* were found.

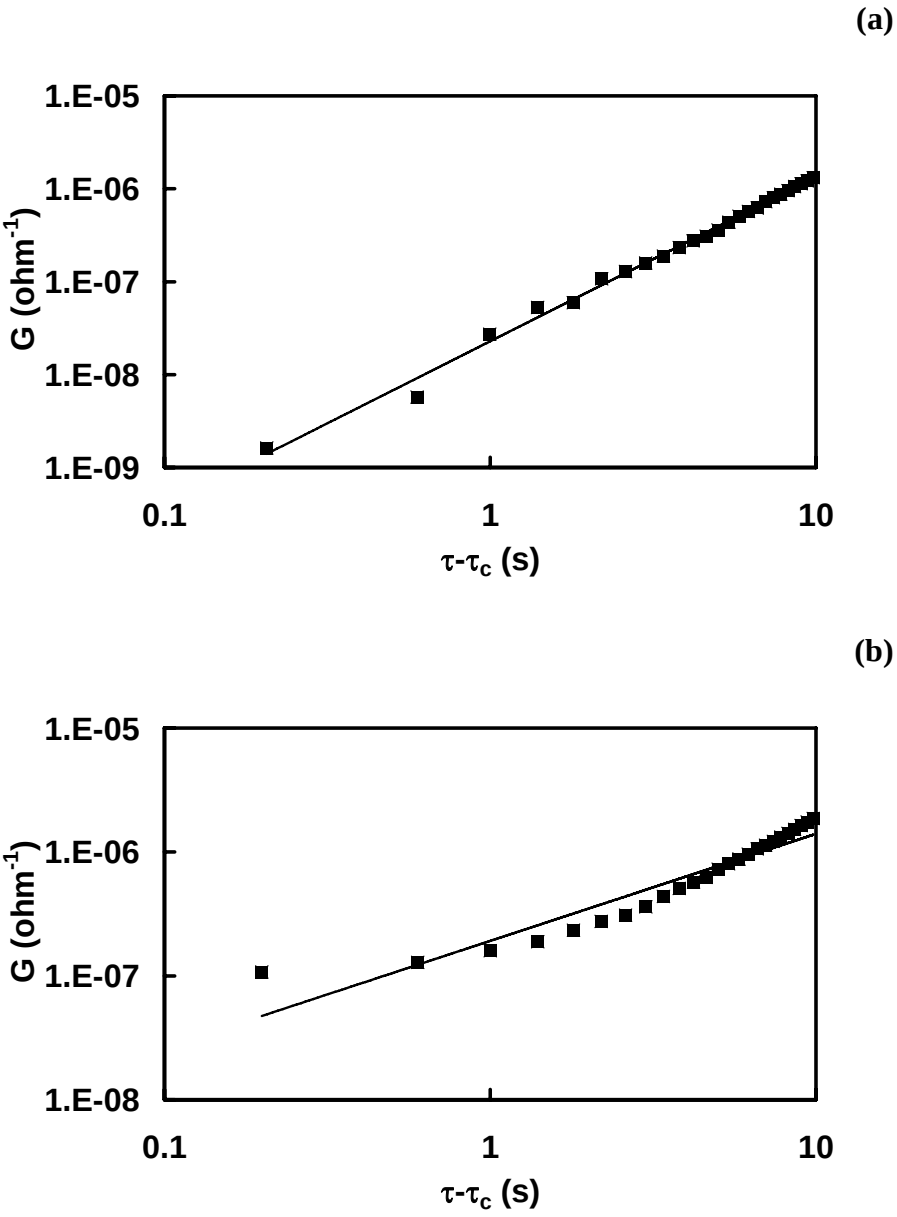

Figure 4-26: **Log of conductance *G* as a function of log(τ-τ$_c$) for τ$_c$ = (a) 87 s and (b) 89 s in sample #31. With a line of $G=a(\tau-\tau_c)^t$ fitted, the R^2 value was obtained. The R^2 values were (a) 0.9942 and (b) 0.9059 respectively.**

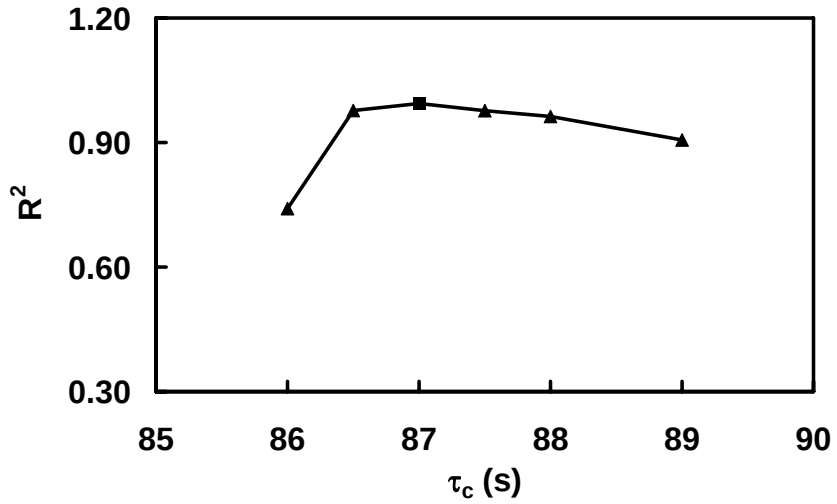

Figure 4-27: **A plot of R^2 fitting parameter as a function of τ_c for sample #31a (same as Figure 4-26). The best-fit value of τ_c was taken at the maximum of the curve (square). The approach was similar the approach adopted in Ref. [14].**

Table 4-4 summarises the onset time, the critical time and the fitting parameters for samples #31, #35, #36 and #44. The amorphous clusters were deposited on two pairs of electrodes in sample #31. Thus, the results from the two films were denoted as samples #31a and #31b. From the depositions in configuration D, it was found that the difference between the critical time for percolation and the onset time τ_{onset} (time when $G > 1\times10^{-9}$) was within ±1 second error. The exponent t was 1.85±0.07 for samples with configuration D, but not for sample with configuration A; the fitting parameter R^2 was above 0.97 for all samples, except sample #44 (configuration A). The minimum coverage p_{min} and the maximum coverage p_{max} in the fitting were within the linear region of Figure 4-25 after the onset.

Table 4-4: **The onset time and fitting parameters for log(G) vs. log(τ-τ_c) plots for samples #31a, #31b, #35, #36 and #44. τ_{range} was 10 seconds. Sample #36 has low p_{max} because of the short deposition.**

Sample	Config.	τ_{onset} (s)	τ_c (s)	t	R^2	p_{min}	p_{max}
#31a	D	86.8	87	1.77	0.994	0.679	0.754
#31b	D	93.6	93	1.94	0.992	0.677	0.747
#35	D	134.8	134.8	1.84	0.985	0.697	0.725
#36	D	108	108	1.84	0.973	0.678	0.703
#44	A	588	591.5	0.19	0.868	0.680	0.691

The p_{max} of samples #35 and #44 were low, because of the low local deposition rate. Thus, the effect of a wider data range was studied. Table 4-5 shows the fitting parameters using a new data range. Instead of (τ_c+10), the data range was selected from τ_c to (τ_c+ τ_{range}), where τ_{range} is 20 and 46.5 seconds for samples #35 and #44 respectively. It was found that the τ_c did not change when the p_{max} was 0.775 for sample #35. However, the τ_c was two seconds smaller than the τ_{onset} and the exponent *t* was still low (0.90). Thus, this proved that the ten seconds selection was adequate for deposition using configuration D. A wider data range for sample #44 could not be made because the deposition stopped at *p*=0.733.

Table 4-5: The onset time and fitting parameters for log(G) vs. log(τ-τ_c) plots for samples #35and #44. τ_{range} was 20 and 46.5 seconds respectively.

Sample	Config.	τ_{onset}	τ_c	*t*	R^2	p_{min}	p_{max}
		(s)	(s)				
#35	D	134.8	134.8	1.99	0.997	0.697	0.775
#44	A	588	586	0.90	0.958	0.680	0.733

As for configuration D, the consistency in the exponent *t* (1.85±0.07) and the consistency between the τ_{onset} and τ_c proved that the depositions of clusters were uniform and the onset of conductance happened at the percolation threshold, as compared to the deposition in configuration A. Clearly, the percolation exponent of 1.85±0.07 for antimony clusters was different from bismuth and silver clusters which were 1.27±0.13 and 1.40±0.14 respectively [14]. Halperin, Feng and Sen [18, 19] reported that the universal value of *t* should be ~ 1.3 in the case of two dimensional inverted Swiss-cheese model. However, for a non-random distribution of the size of the discs and spheres in two-dimension and three-dimension, the exponent *t* could be greater than 1.3, which was the case for the antimony clusters. In the case of three-dimensional percolation, the universal value for *t* was 2 [16]. It was possible that the percolation nature in the depositions, using configuration D, was close to a three-dimensional percolations.

4.5.2 Coalescence

After the deposition, the cluster films continued to evolve. Figure 4-28 shows the evolution of conduction *G* after the depositions in configurations D. The conductance of the films continued to increase after the shutter was closed. The increase in conductance was due to the coalescence of the clusters.

The relation between the final stabilised conductance and its initial conductance was investigated. Figure 4-29 shows the final conductance G_{final} as a function of the initial conductance G_o for samples deposited in configuration D. The final conductance G_{final} was measured when the conductance of the film reached a stable value, while the initial conductance, G_o was taken at the time when deposition stopped. The following relation was found.

$$G_{final}=0.0217G_o^{0.3} \qquad (Eq.\ 4\text{-}15)$$

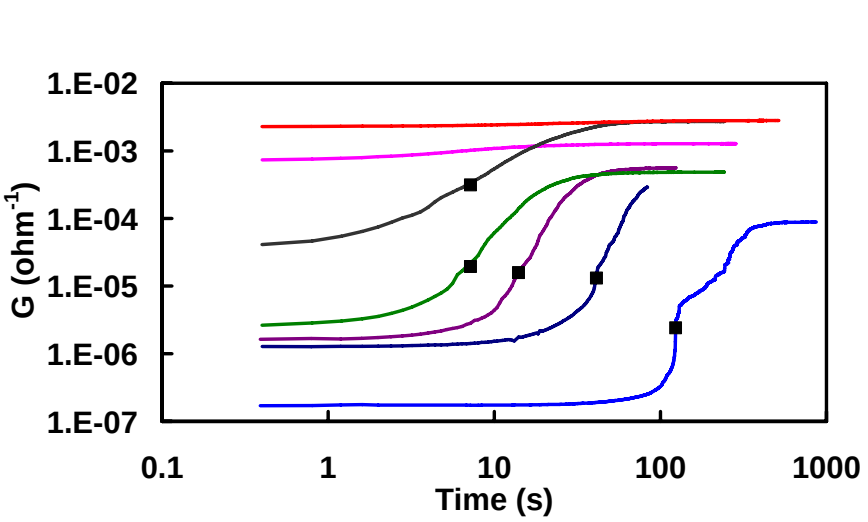

Figure 4-28: **Evolution of the conductance after the shutter was closed for samples #25, #27, #30, #31a, #31b, #35 and #36. All samples were made in configuration D. The conduction continued to increase up to the stable value G_{final}. t_{trans} (squares) was defined as the time when the conductance increased by ten times from the initial conductance.**

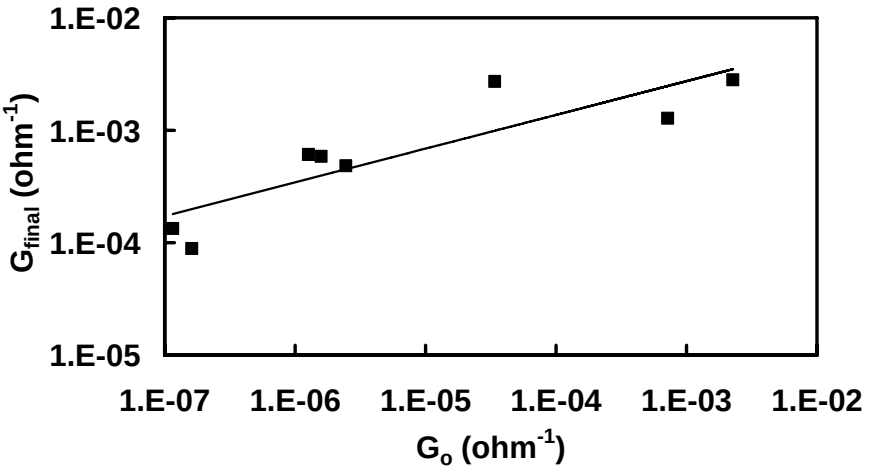

Figure 4-29: **Final conductance G_{final} as a function of initial conductance G_o during the coalescence. All samples (#25, #26, #27, #30, #31a, #31b, #35 and #36) were deposited using in configuration D.**

As shown in Figure 4-28, the slopes of the conductance curves were different in each sample. Therefore, it was hard to define the exact timing when the coalescence started. For simplicity, transition time t_{trans} was defined as the time when the conductance increased by a decade (10 times), after the deposition. Figure 4-30 shows t_{trans} as a function of the initial conductance, G_o. By fitting a line in the log-log plot, the following relation was obtained.

$$t_{trans}=0.0757\ G_o^{-0.42} \qquad (Eq.\ 4\text{-}16)$$

Before coalescence, the conductance G_o could be characterised using the following equation.

$$G_o=\sigma Wd/L \qquad (Eq.\ 4\text{-}17)$$

where the σ is the conductivity, W, L and d are the width, length and the thickness of the cluster film. The width W was assumed to be the same as the cluster spot size (see Section 4.2.2) and the length L was defined as the gap between the electrodes. Since W and L were constant, the initial conductance G_o should be proportional to the thickness of the cluster films.

By substituting $d \sim G_o$ into *Eq. 4-15* and *Eq. 4-16*,

$$G_{final} \sim d^{0.3} \qquad (Eq.\ 4\text{-}18)$$

$$t_{trans} \sim d^{-0.42} \qquad (Eq.\ 4\text{-}19)$$

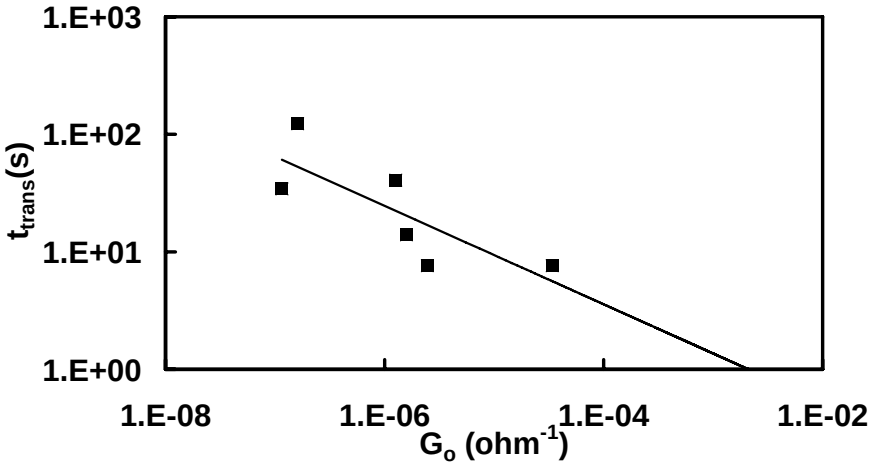

Figure 4-30: **Transition time t_{trans} as a function of the initial conductance, G_o. The transition time was defined as the period when the deposition stopped until the conductance increased by a decade (10 times). All samples (#25, #26, #27, #30, #31a, #31b, #35 and #36) were deposited using in configuration D.**

It was interesting that the coalescence followed a power law relation. During coalescence, the necks between the clusters grow to reduce the surface energy, resulting in the increase in conductance. Cluster coalescence can occur by a variety of mechanisms, such as diffusion mechanisms [20] or viscous flow [21]. In these mechanisms, Sb atoms or Sb_4 molecules move to reduce to total surface energy of the clusters.

4.5.3 Oxidation after exposure to air.

In order to measure the film resistance at various substrate temperatures, the samples were transferred to a cryostat in the UHV system (described in Chapter 2). The process of unloading the samples from the sample arm and re-loading to a cryostat was generally completed within 30 minutes. This sub-section describes the changes in the conductance due to the oxidation during the sample transfer. The conductance was measured before the samples were vented to air and after the samples were transferred to a cryostat and pumped down to a vacuum. The conductance was measured from the slope in the $I(V)$ curves. Table 4-6 lists G_1 and G_2 which are the conductance before and after the sample transfer. It was found that the change in conductance was all below 20%, except for sample #31b. Since the conductance was maintained within the same

Table 4-6: Conductances G_1 and G_2 which are the conductance before and after the sample transfer. For samples #30 and #31, two pairs of electrodes (referred as a and b) were measured separately.

Sample	G_1 (Ω^{-1})	G_2 (Ω^{-1})	$(G_2-G_1)/G_1$
#26	4.90×10^{-5}	5.20×10^{-5}	6%
#30a	2.55×10^{-3}	2.09×10^{-3}	-18%
#30b	9.09×10^{-4}	7.56×10^{-4}	-17%
#31a	2.54×10^{-3}	2.13×10^{-3}	-16%
#31b	4.62×10^{-4}	2.87×10^{-4}	-38%

order of magnitude, the electrical characterisations were continued. *R*(*T*) curves for these samples were studied in next section.

4.5.4 *R*(*T*) curves

This sub-section discusses the *R*(*T*) results for samples deposited with source configuration D. The samples used were the inter-digitated samples described in Section 4.1.3. Five samples were cooled to liquid nitrogen temperature, and sample #31a was heated to 450 K.

After the samples were loaded into a cryostat, the chamber was pumped down to a vacuum ($< 5 \times 10^{-6}$ Torr). Then the samples were cooled down to liquid nitrogen temperature and the resistance was measured while the samples were warming up without applying any external heating. In this way, the thermal-lag between the sample and the temperature sensor was kept to the minimum.

Figure 4-31 shows the change of resistance (R/R_o) as a function of temperature *T* in sample #30a. Using *Eq. 4-1*, the temperature coefficient of resistance (α) at room temperature could be obtained. Table 4-7 lists the temperature coefficient calculated from five samples at room temperature. The resistance of the five samples at 290 K ranged from 480 Ω to 22.7 k Ω. Although the resistance of sample #31b increased about 38 % due to oxidation as described in previous section, the temperature coefficient was not significantly different from other samples. As a whole, the temperature coefficient of resistance was $(-2.2 \pm 0.2) \times 10^{-4}$ K^{-1}.

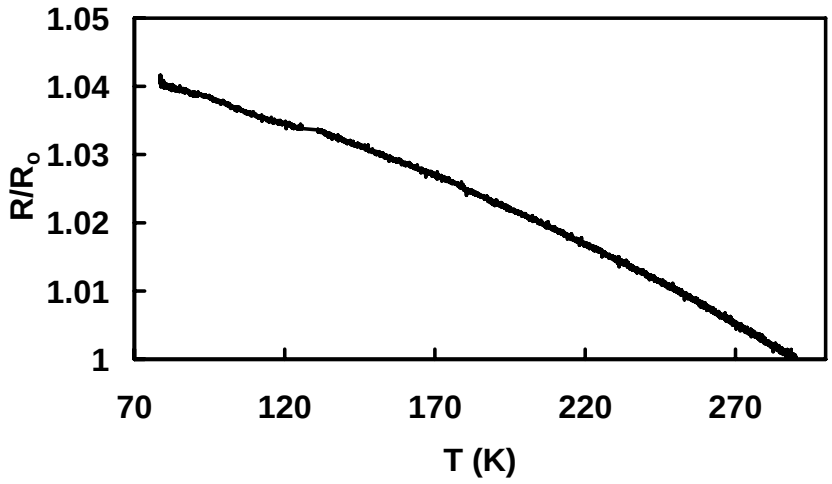

Figure 4-31: **Change of resistance as a function of temperature T for sample #30a. R_o, the resistance at 290 K (T_o) was 486 Ω.**

Table 4-7: **The temperature coefficient of resistance at room temperature was calculated for samples #26, #30a, #30b, #31a, #31b. R_o was the resistance of the samples at 290 K.**

Sample	R_o (Ω)	α (x 10^{-4}) (K^{-1})
26	22 740	-2.34
30a	486	-1.99
30b	1347	-2.39
31a	479	-2.27
31b	2636	-2.06

Figure 4-32 shows that the resistance does not vary linearly with $T^{1/4}$. The $T^{1/4}$ dependence of resistance, reported in the literature [22], was not observed in all five samples.

Figure 4-33 shows the change of resistance as a function of *T* in sample #31a after the annealing. The sample was heated to 450 K and then cooled down without applying any external cooling. To avoid the thermal lag between the sample and the temperature sensor, the resistance was measured during cooling. The resistance varied roughly linearly with *T* and temperature coefficient of resistance at room temperature was found to be -3.67×10^{-4} K^{-1}.

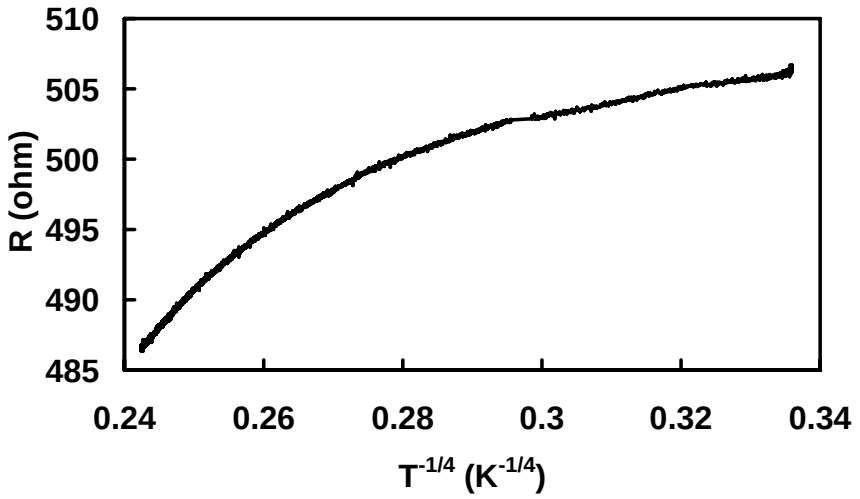

Figure 4-32: **A plot of the resistance as a function of $T^{-1/4}$ for sample #30a. The resistance does not vary linearly with the $T^{-1/4}$.**

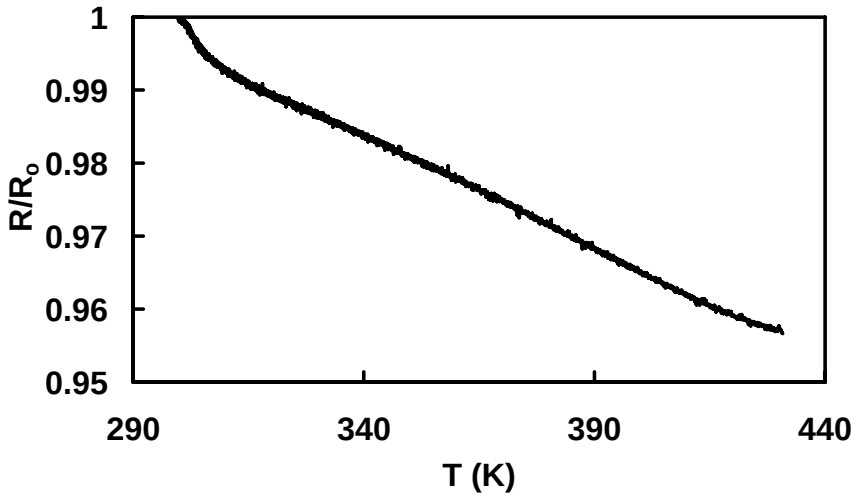

Figure 4-33: **Change of resistance as a function of T in sample 31a after annealing. The sample was heated to 450 K and the resistance was measured during cooling. R_o the resistance at 299 K (T_o) was 477 Ω after annealing.**

As described in Chapter 3, Jensen *et al.* reported that the crystallisation temperatures for amorphous antimony clusters were 323 K and 350 K for 97 nm and 13.5 nm films, respectively [23]. They also showed that the resistance decreased by five order of magnitude when the sample was annealed at 373 K. However, the resistance of sample 31a only reduced by 1 % after it was annealed at 450 K. The temperature coefficient of resistance at room temperature (-3.67×10^{-4} K^{-1}) was in the same order of magnitude as the coefficient before annealing. Therefore, the electrical property of the cluster film did not change significantly.

Compared to the temperature coefficient of resistance at room temperature for other semiconductors such as Si ($\alpha = -7.5 \times 10^{-2}$ K^{-1}), Ge ($\alpha = -4.8 \times 10^{-2}$ K^{-1}), poly Si-Ge alloy ($\alpha = -2 \times 10^{-2}$ K^{-1}), or amorphous Si ($\alpha = -2 \times 10^{-2}$ K^{-1}) [24-26], the temperature coefficients of resistance ($- 2.2 \times 10^{-4}$ K^{-1}) in samples # 26, #30a, #30b, #31a and #31b were two order of magnitude lower.

The small temperature coefficient of resistance and the small change in the resistance after annealing suggest that the cluster films were very different from the cluster films reported by Jensen *et al.* [23]. It was possible that the amorphous clusters were modified either during the deposition or after the deposition. During the deposition, the deformation of clusters (as described in Section 4.4.4) might alter the amorphous structure of the clusters. Alternatively, during coalescence which was a process of the neck growth process in between the clusters, the atoms or Sb_4 molecules [27] move around and possibly change the crystalline structure of the clusters. In that case, the semiconducting property of the clusters could be destroyed.

4.5.5 Effect of gate bias and tunnelling

This sub-section describes attempts to study the gate effect and the electron tunnelling in the cluster films.

In order to study the gate effect, sample #34 was deposited using configuration D. Figure 4-34 shows the drain current as a function of an applied gate voltage. The source/drain current was measured by applying 30 mV across the electrodes. A ±10V sweep of gate voltage was applied to the silicon substrate at room temperature and at liquid nitrogen temperature. If the film was semi-conducting, the intrinsic carrier concentration would be lower at low temperature, thus, the carriers induced by the gate bias should result in a significant change in the source/drain current. However, no change in the drain current with the changes in gate voltage was observed at room temperature or at liquid nitrogen temperature.

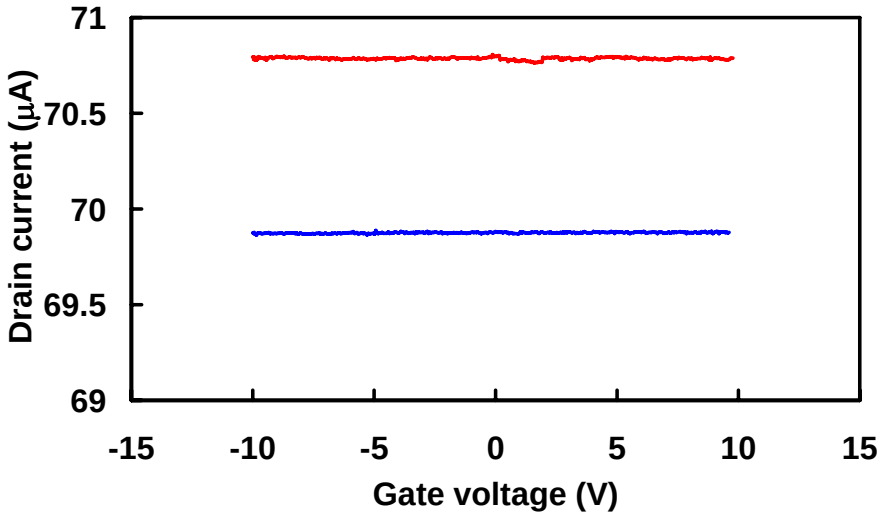

Figure 4-34: **No gate effect was observed at room temperature (upper line: highlighted in red) and at liquid nitrogen temperature (lower line: highlighted in blue) for sample #34.**

An attempt was made to deposit a cluster film with coverage just below the percolation threshold. The purpose of this experiment was to obtain a sub-threshold coverage $p < p_c$, and to produce a discontinuous film. If the electrons should tunnel from cluster to cluster in a discontinuous film, some interesting behaviour might be observed.

Since the cluster beam was off-centre and not homogeneous, onsets of the two pairs of electrodes on the same sample normally occurred at different times. Thus, a controlled experiment was performed by monitoring the onset of the first pair. The deposition was stopped when the onset of the first pair of the electrodes was observed and then the $I(V)$ curve was measured on the second pair of the electrodes. However, only random noise was observed in the $I(V)$ measurement and in the continuous resistance measurement at 30 mV. Thus, due to the inhomogeneous nature of the cluster beam, the deposition just below the percolation coverage was difficult to achieve.

4.6 Summary and recommendation

This chapter describes a systematic approach to producing homogeneous amorphous antimony cluster films. The amorphous phase of the unsupported antimony clusters was identified by electron diffraction patterns. Initially, the amorphous antimony clusters were produced using Kaufmann's source configurations [1]. However, because of the high gas flow needed in these configurations, inhomogeneous films were obtained. A tantalum plate was then inserted in the source, and resulted in a robust process which enabled the use of low gas flows to produce amorphous antimony clusters. Changing the bore diameter of the first stage nozzle from 3.5 mm to 2.5 mm altered the cluster diameter, cluster velocity and film morphology significantly.

It was found that the large clusters ($\geq$ 25 nm) bounced away from the substrate but adhered to gold contacts, defects and other clusters on the surface. As a result, the clusters clumped together and formed non-uniform films. As for the small clusters (~15 nm) produced in a source system using a tantalum plate and the 2.5 mm nozzle, uniform films were produced.

Several interesting phenomenon were observed. First, the source pressure was stable at different operating temperature. Second, at a fixed flow rate, the source pressure remained the same even when the diameter of the first stage nozzle changed from 3.5 mm to 2.5 mm or when the tantalum plate was inserted. Third, the spot sizes were quite consistent as long as the clusters were not bouncing. Since the spot size on the FTM crystal was smaller than the diameter of the crystal itself, the actual deposition rate had to be corrected. Next, there was an optimum flow rate to produce a maximum deposition rate at a fixed crucible temperature. The optimum flow rates were 65 sccm when a tantalum plate was not used and 30 sccm when the tantalum plate was inserted. Last, higher flow rates produced higher source pressures and therefore making larger the cluster diameter in configurations A, B and C; however, the cluster diameter was consistently ~ 15 nm for a flow between 15 to 30 sccm in configuration D.

Based on the calculation of velocity and kinetic energy, the 15 nm clusters from configuration D and the 25 nm clusters from configuration C had the same kinetic energy at 25 sccm argon flow, but the film morphology of these two depositions were very different. It was speculated that the high velocity of the 15 nm clusters could have caused the clusters to deform; therefore, there was some energy lost during the plastic deformation. When the kinetic energy after impact was lower than the adhesion energy of the substrate, the clusters adhered to the substrate. As a result of more uniform deposition, a consistent percolation exponent (1.85) was obtained.

After deposition, the electrical conductance of the films increased over time. However, the change in conductance did not necessary happen immediately after the deposition. It was found that the thinner the cluster films, the longer time it took before the coalescence started.

All $I(V)$ curves obtained were linear. For one sample, the consistent slope in the $I(V)$ curve over a wide voltage range showed that the contacts were ohmic and there was no non-linear $I(V)$ behaviour in the cluster films.

In order to measure the $R(T)$ curves for the films, the samples were transferred to a separate system equipped with a cryostat. As the transfer required vacuum breaks for the samples, some oxidation had taken place. Since the increases in resistance were less than 20 % for four samples and about 40 % for one sample, the electrical measurements were continued in the cryostat chamber.

In the $R(T)$ measurements, the temperature coefficient of resistance at room temperature was $(-2.2 \pm 0.2) \times 10^{-4}$ K^{-1}. The value of this coefficient was two orders of magnitude lower than the temperature coefficient of resistance of other semiconductors at room temperature. After annealing sample #31a at 450 K, the temperature coefficient of resistance did not change much and the resistance only decreased by 1 %. According to the literature, the amorphous antimony films should have crystallised at temperature above 350 K. From the small temperature coefficient of resistance and a small change in resistance after annealing, it was concluded that the cluster films were not amorphous nor semi-conducting. This was supported by the fact that no gate effect was observed

when the gate was biased up to ±10V at both room temperature and liquid nitrogen temperature.

Although a considerable effort has been made to produce uniform films which were suitable for electrical measurements, the antimony cluster films do not show semiconducting behaviour. Perhaps, the deposition conditions have modified the supported antimony clusters. For example, while small clusters (~15 nm) allowed uniform deposition, the coalescence could destroy the semiconducting behaviour. To prevent coalescence, a different substrate or different contacts could be tried. Alternatively, if the velocity of the large clusters could be further reduced, it might be possible to make a uniform film with large clusters. The reduction of the cluster velocity could be achieved by ionizing clusters and then applying an electric field to slow the clusters down. Since the coalescence could be more pronounced in small clusters, the semiconducting behaviour might be preserved in a uniform film comprised of larger clusters.

References

[1] M. Kaufmann, "Electron diffraction studies of unsupported antimony clusters," *PhD thesis, University of Canterbury,* 2006.

[2] R. Reichel, "Nano Scale Cluster Devices," *PhD thesis, University of Canterbury,* 2007.

[3] M. Kaufmann, A. Wurl, J. G. Partridge, and S. A. Brown, "Structure of unsupported antimony nanoclusters," *European Physical Journal D,* vol. 34, pp. 29-34, Jul 2005.

[4] M. Schulze, S. Gourley, S. A. Brown, A. Dunbar, J. Partridge, and R. J. Blaikie, "Electrical measurements of nanoscale bismuth cluster films," *European Physical Journal D,* vol. 24, pp. 291-294, 2003.

[5] A. Ayesh, "Device fabrication using Bi nanoclusters," *PhD thesis, University of Canterbury,* 2007.

[6] T. Diep and C. Durvury, "Electrostatic Discharge (ESD)," *Texas Instruments Application Report - SSYA010 (January),* 2001.

[7] R. J. Peirce, "The most common causes of ESD damage," *EE-Evaluation Engineering,* vol. 41, pp. 56-59, Nov 2002.

[8] A. Wurl, "Electron diffraction studies of unsupported bismuth clusters," *PhD thesis, University of Canterbury,* 2003.

[9] R. Reichel, J. G. Partridge, F. Natali, T. Matthewson, S. A. Brown, and A. Lassesson, "From the adhesion of atomic clusters to the fabrication of nanodevices," *Applied Physics Letters,* vol. 89, Nov 2006.

[10] J. G. Partridge, S. A. Brown, A. D. F. Dunbar, R. Reichel, M. Kaufmann, C. Siegert, S. Scott, and R. J. Blaikie, "Templated-assembly of conducting antimony cluster wires," *Nanotechnology,* vol. 15, pp. 1382-1387, 2004.

[11] C. Thornton and Z. Ning, "Theoretical model for the stick/bounce behaviour of adhesive, elastic-plastic spheres," *Powder Technology,* vol. 99, pp. 154-162, 1998.

[12] K. L. Johnson, *Contact Mechanics*. Cambridge: Cambridge University Press, 1985.

[13] A. Awasthi, S. C. Hendy, P. Zoontjens, S. A. Brown, and F. Natali, "Molecular dynamics simulations of reflection and adhesion behavior in Lennard-Jones cluster deposition," *Physical Review B (Condensed Matter and Materials Physics),* vol. 76, pp. 115437-11, 2007.

[14] A. D. F. Dunbar, J. G. Partridge, M. Schulze, and S. A. Brown, "Morphological differences between Bi, Ag and Sb nano-particles and how they affect the percolation of current through nano-particle networks," *European Physical Journal D,* vol. 39, pp. 415-422, 2006.

[15] I. Balberg, D. Azulay, D. Toker, and O. Millo, "Percolation and tunneling in composite materials," *International Journal of Modern Physics B,* vol. 18, pp. 2091-2121, Jun 2004.

[16] D. Stauffer, *Introduction to Percolation Theory*. London: Taylor and Francis, 1985.

[17] H. E. Stanley, "Scaling, universality, and renormalization: Three pillars of modern critical phenomena," *Reviews of Modern Physics,* vol. 71, pp. S358-S366, Mar 1999.

[18] B. I. Halperin, S. Feng, and P. N. Sen, "Differences between Lattice and Continuum Percolation Transport Exponents," *Physical Review Letters,* vol. 54, pp. 2391-2394, 1985.

[19] S. Feng, B. I. Halperin, and P. N. Sen, "Transport properties of continuum systems near the percolation threshold," *Physical Review B,* vol. 35, p. 197, 1987.

[20] P. Jensen, "Growth of nanostructures by cluster deposition: Experiments and simple models," *Reviews of Modern Physics,* vol. 71, p. 1695, 1999.

[21] R. S. Garabedian and J. J. Helble, "A Model for the Viscous Coalescence of Amorphous Particles," *Journal of Colloid and Interface Science,* vol. 234, pp. 248-260, 2001.

[22] J. J. Hauser, "Hopping Conductivity in Amorphous Antimony," *Physical Review B,* vol. 9, pp. 2623-2626, 1974.

[23] P. Jensen, P. Melinon, M. Treilleux, A. Hoareau, J. X. Hu, G. Fuchs, and B. Cabaud, "Low-Energy Cluster Beam Deposition - a Way to New Materials," *Nuclear Instruments & Methods in Physics Research Section B-Beam Interactions with Materials and Atoms,* vol. 79, pp. 219-222, Jun 1993.

[24] R. A. Serway, *Principles of Physics,* Second ed. Texas: Saunders College, 1998.

[25] S. Sedky, P. Fiorini, M. Caymax, C. Baert, L. Hermans, and R. Mertens, "Characterization of bolometers based on polycrystalline silicon germanium alloys," *IEEE Electron Device Letters,* vol. 19, pp. 376-378, Oct 1998.

[26] T. A. Abtew, M. L. Zhang, and D. A. Drabold, "Ab initio estimate of temperature dependence of electrical conductivity in a model amorphous material: Hydrogenated amorphous silicon," *Physical Review B,* vol. 76, Jul 2007.

[27] K. Tanaka and S. Iwama, "Size dependent crystallization of nanometer-sized amorphous Sb particles," *Nanostructured Materials,* vol. 9, pp. 121-124, 1997.

Chapter 5

Literature review for ultra-large scale integrated (ULSI) interconnects

As integrated circuit (IC) technology advances, the packing density of devices on ICs is required to increase continuously. In order to achieve this, the metal connections (known as interconnects) have to be made smaller and smaller at each technology node. In the most recent technology, billions of transistors and interconnects must now be fabricated with dimensions in the nanoscale regime [1]. For instance, there are 1.72 billion transistors fabricated in Intel's Itanium-2, 64-bit microprocessor (codenamed Montecito) and more than a billion transistors on a typical 8 Gb FLASH Memory chip. Placing more than one million components per chip is referred to as ultra-large scale integration (ULSI). This chapter provides a comprehensive background study of ULSI interconnects and the potential candidates for future development, which include metallic cluster-related applications. Section 5.1 briefly describes the history of the interconnect development. Section 5.2 provides an overview of the copper damascene process. Section 5.3 highlights the potential problems of the present technology. Section 5.4 summarises the potential candidates in the literature. Section 5.5 discusses the unique properties of metallic clusters and their potential for interconnect applications.

5.1 The history of interconnects

In 1965, Gordon Moore, a co-founder of Intel, predicted that the performance of integrated circuits (mainly the number of transistors) would be doubled every 18 months [2]. Since then, Moore’s law has become the driving force for the technology development process in the late twentieth and early twenty-first centuries.

In the 1960s, single level metal interconnects were used. Figure 5-1 shows a schematic of the process steps used to produce a single level metal interconnect. First, a SiO_2 film

is deposited on a wafer. This oxide layer is also known as an inter-layer dielectric (ILD) layer. Then via holes are etched in the ILD layer, and these vias allow thin and narrow aluminium lines to make contact with the circuit devices fabricated within the silicon substrate. To prevent the diffusion of aluminium into the silicon substrate, a diffusion barrier such as titanium or titanium nitride is often deposited prior to the aluminium deposition. After the metals are patterned through lithographic and etching processes, a passivation layer is deposited over the entire wafer.

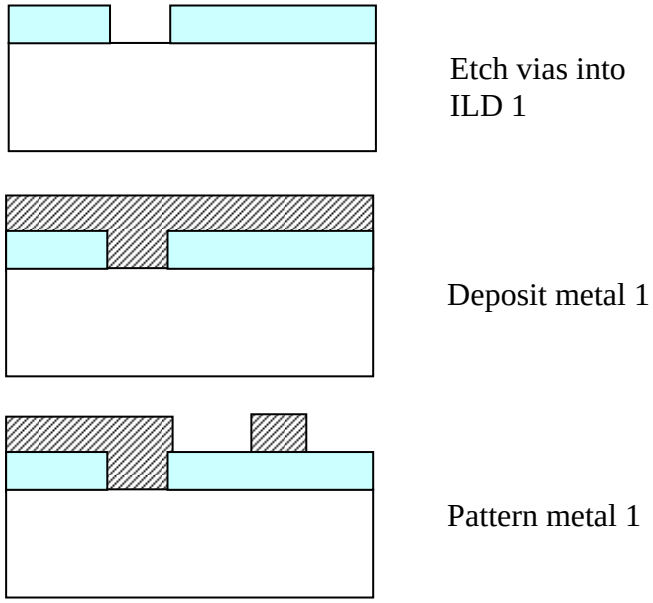

Figure 5-1: Schematic of process steps used to produce a single-level metal interconnect.

As the density and the complexity of ICs increased with decreasing feature size (Moore's law), it became necessary to have more than one level of interconnect. Figure 5-2 shows a schematic of a double level metal structure used in early ICs. After the formation of the first metal level, an ILD layer is deposited and patterned, followed by the metallisation of a second metal layer in the same manner.

As shown in Figure 5-2, the topography of the wafer is uneven after the first metal deposition, and even more so after the second metal. To enable three level metal interconnects (or more), a technique for planarising the ILD after it was deposited was needed. The technique developed was chemical mechanical polishing (CMP) of the SiO_2 ILD layer. Figure 5-3 compares two scenarios: (a) when no planarisation is used and (b) when planarisation is achieved. Clearly, the vias vary widely in depth when

planarisation is used. Therefore, the filling of trenches with different aspect ratios (ratio of trench depth to trench opening width) is needed.

As the aluminium deposition process was not able to fill the deep and narrow vias, a tungsten plug process was used. A tungsten plug is made by a tungsten deposition, followed by an etch-back or CMP. A review of the tungsten plug can be found in Ref. [3].

As the interconnects are reduced in size (and packed more closely), the RC delay increases, as both the resistance and the inter-trace capacitance per unit length increases. Figure 5-4 shows the simulations of the intrinsic gate delay and the interconnect delay in different technology nodes [4]. By reducing the gate length of the transistors, the gate delay decreases. However, as the spacing of the metal lines is reduced, the interconnect delay increases. It has been generally agreed that beyond the 0.25 µm technology node, the overall circuit performance would be dominated by the efficiency with which devices were connected, rather than by the speed of individual transistors [5]. There are two ways of reducing the RC delay of the interconnects: reducing the resistance of the metal lines (by using a lower resistivity metal such as Cu) and reducing the dielectric constant of the ILD layer (by using a so-called low-k dielectric), which determines the capacitance between the metal lines.

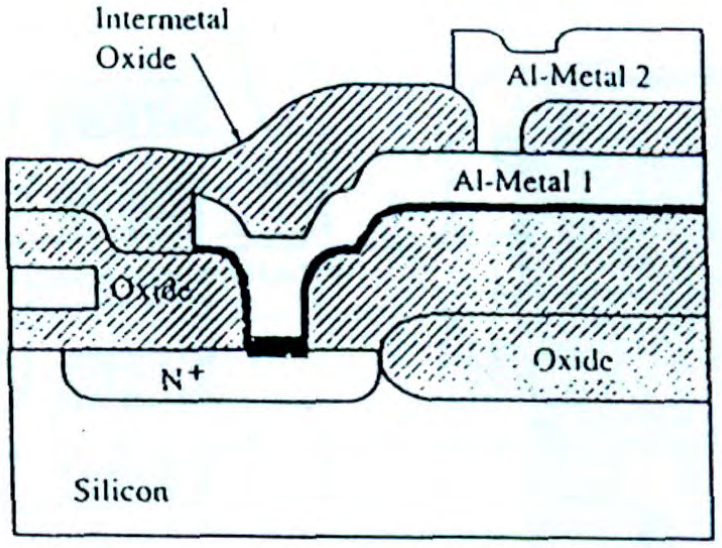

Figure 5-2: Schematic of a double level metal structure used in early ICs. After Ref. [5].

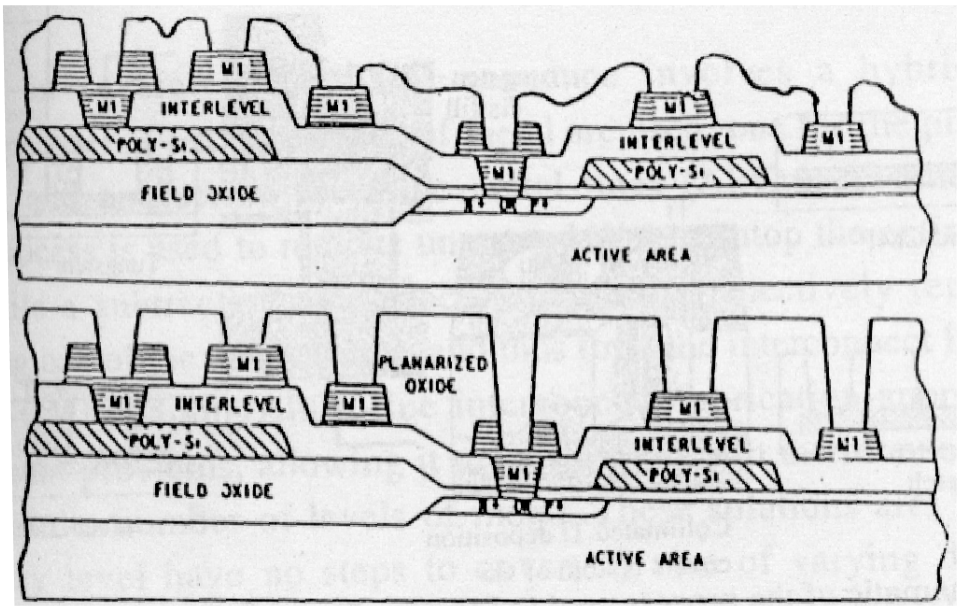

Figure 5-3: **a) If no planarisation is used, the via holes between adjacent metal levels all have approximately the same depth; b) If planarisation of the ILD layer is achieved, the vias will vary widely in depth. After Ref. [5].**

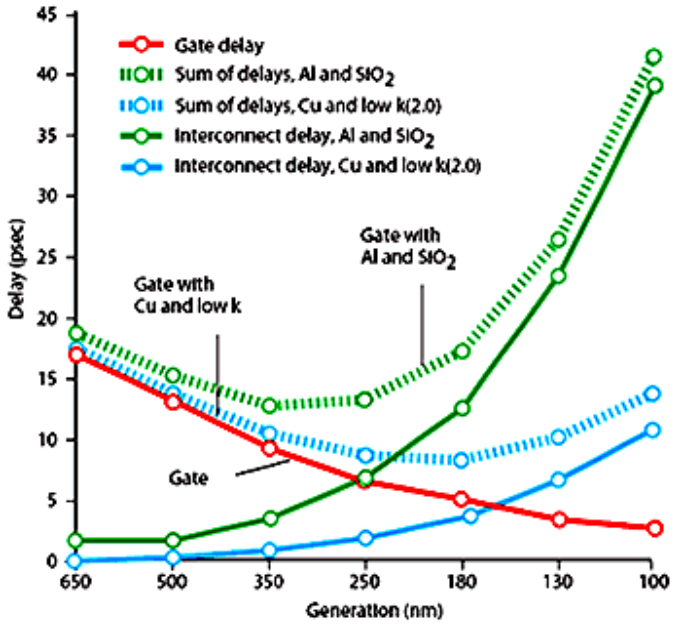

Figure 5-4: **Simulations of delay times as a function of technology nodes. There are two types of the interconnects simulated: aluminium metallisation with SiO_2 as the ILD layer, and copper metallisation with a low-k dielectric as the ILD layer. The dielectric constant of the low-k dielectric is 2. After Ref. [4]**

In 1998, IBM announced the shipment of the world's first copper-based microprocessors [6]. Then, other semiconductor manufacturers started to migrate from aluminium metallization to copper metallization. The migration was primarily driven by the need to reduce the RC delay of the interconnects in advanced integrated circuits. Copper has been chosen because it is a better electrical conductor and has a ten times longer lifetime in electro-migration reliability tests than aluminium.

However, four major issues needed to be solved when migrating from aluminium metallisation to copper metallisation [7]. First, copper diffuses very fast in silicon. As copper ions are detrimental to active devices, a good diffusion barrier is needed. Second, copper diffuses fast in the surrounding dielectric. The out-diffusion of the copper from the ILD layer could cause a short circuit to the neighbouring metal lines. Thus, the copper wires need to be encapsulated by a good diffusion barrier. Third, it is difficult to plasma etch copper using a dry etching process because the by-product from the etching (copper halide) is not volatile at room temperature. Therefore, the deposition and etching methods used for aluminium metallisation do not work for copper metallisation. Last, the copper is vulnerable to oxidation. Unlike aluminium which can be self-passivated by its oxide (a self-limiting process), a copper oxide film is porous and thus the oxidation process continues throughout the film. Thus, a passivation layer is important for the copper metallisation. To resolve these four problems, a series of complex process steps commonly known as a damascene process [8] are required, as explained in the next section.

5.2 Copper damascene process

In the twelfth century, the artisans of Damascus developed a special technique whereby decorative noble metals were hammered into grooves made in armaments or other metal objects after which the excess material was removed by polishing. As a result, this technique is called “damascening”. At present, the damascene process is used in the semiconductor industry to resolve the issues in copper metallization.

Figure 5-5 shows the process flow for a single damascene process. Firstly, the dielectrics are deposited, and patterned with photo-resist and plasma-etched to form via holes/trenches. Via holes, which are cylindrical in shape, allow the connection between different metal levels, whilst the trenches are rectangular metal lines. Secondly, a thin diffusion barrier and a copper seed layer are deposited. Next, copper is electro-plated. In the plating process, an electrical current is applied to a copper seed layer in an electrolyte solution, and the copper ions are reduced and deposited on the seed layer. The plating process is quite often followed by a post-metallisation anneal to stabilise the films. Because of the overburden of excess copper above the via holes or trenches, CMP is used to remove the excess copper and planarise the surface.

In the "dual damascene" approach both via holes and lines are etched into the dielectric prior to metal deposition and CMP, as shown in Figure 5-6. Since both lines and vias are filled in one single step and only one CMP step per metal layer is required, the number of steps in a dual damascene process is less than the steps used in the single damascene process. Therefore, the dual damascene process is favourable over the single damascene because of fewer process steps and lower cost. The following sub-section will briefly describe the materials used for damascene processes.

5.2.1 Dielectric materials

The ILD layer in the damascene process plays an important role in the speed of the circuits. As the dielectrics fill the gap between the metal lines, the capacitance of the dielectric contributes to the RC delay. The capacitance between the metal lines is given by :

$$C = \frac{k\varepsilon_0 A}{d} \qquad (Eq.\ 5\text{-}1)$$

where k is the dielectric constant, ε_0 is the permittivity of space (8.854×10^{-12} Fm^{-1}), A is the projected area between a pair of metal lines and d is the separation.

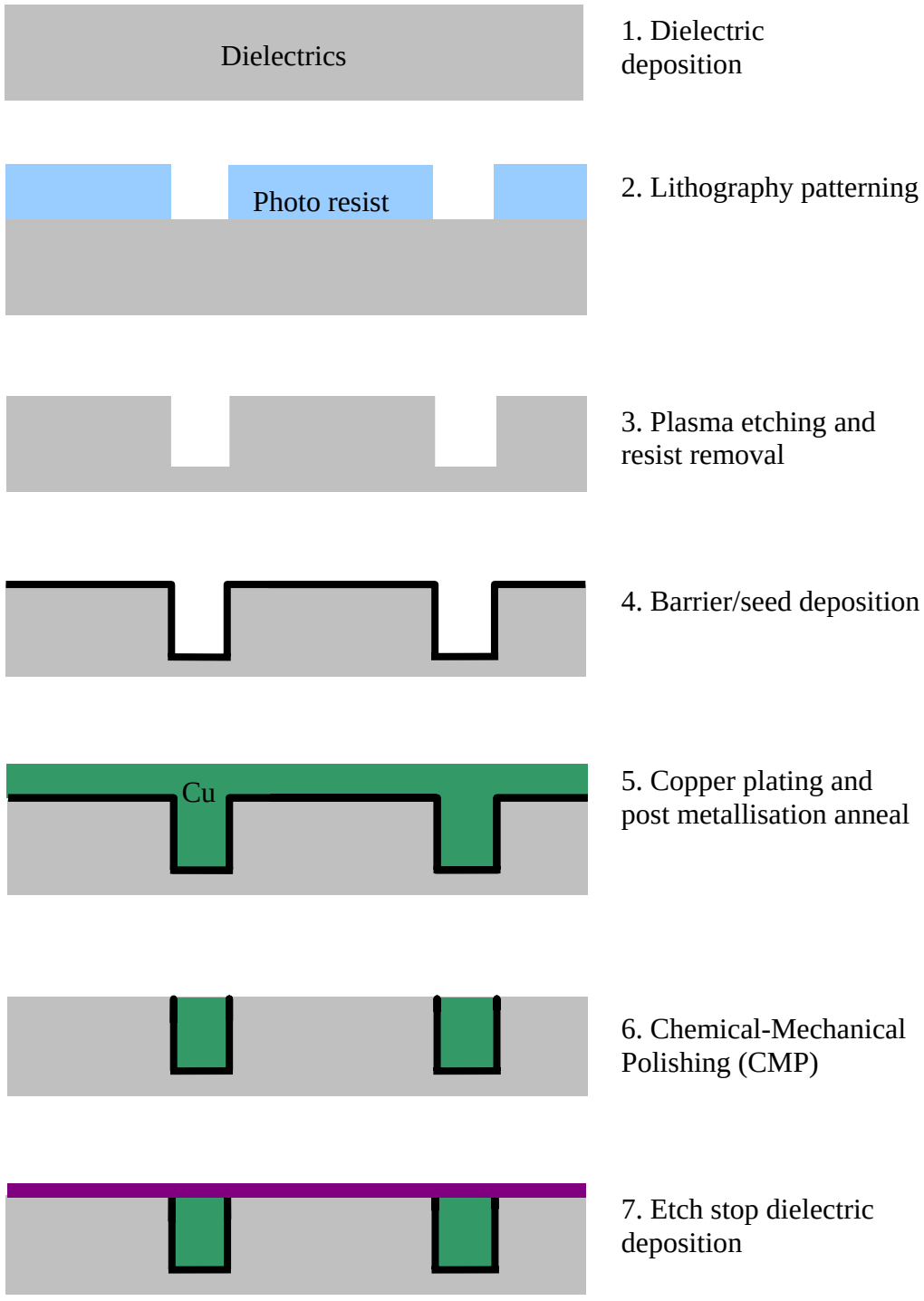

Figure 5-5: Schematics of the process flow for single damascene structures.

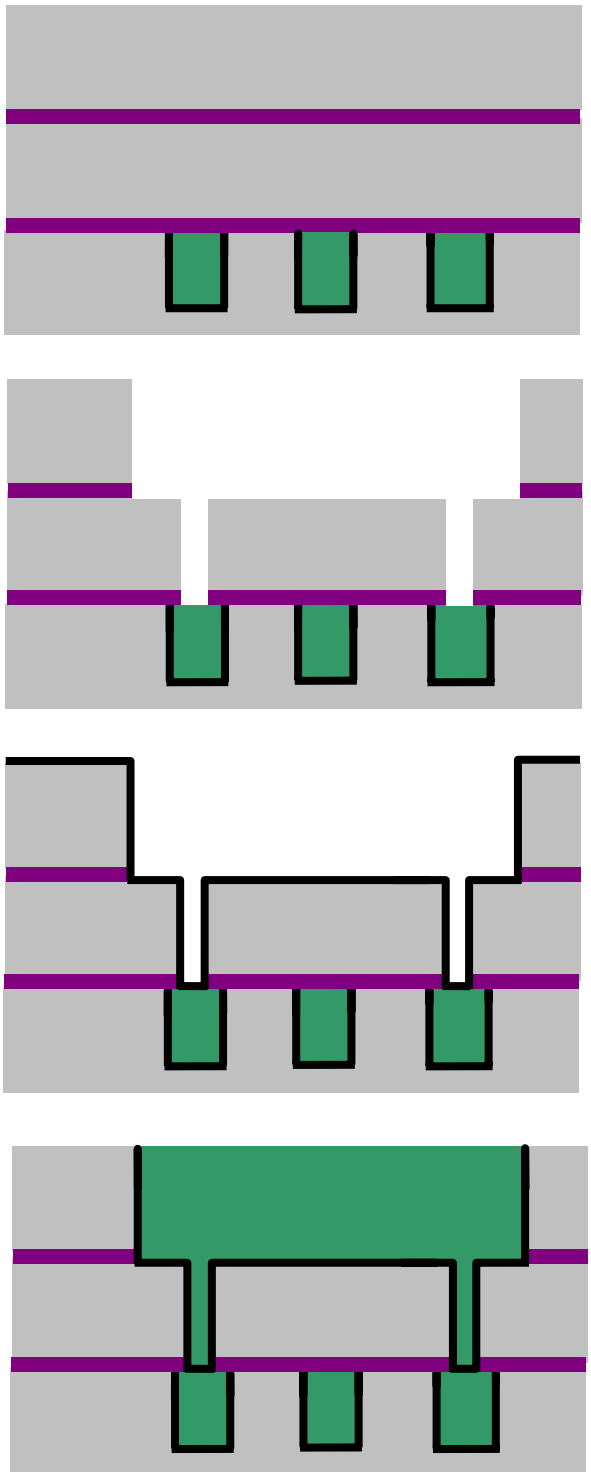

Figure 5-6: Schematics of the process flow for dual damascene structures.

As part of the continuous improvement in the circuit speed over the last 50 years, the dielectrics have been changed from SiO_2 ($k \sim 4$) to other low-k materials. The available low-k materials in production are: Fluorosilicate glass (FSG: $k \sim 3.7$), Coral™ by Novellus Systems Inc. ($k = 2.85$), and Black Diamond™ by Applied Materials Inc. ($k < 3.0$) [9]. The value of k can be further reduced by introducing pores into the dielectric materials. The porous materials are often referred to as the ultra-low-k materials. Introducing pores (air: $k = 1$) makes integration very difficult, due to the mechanical weakness and other process interaction issues [10].

5.2.2 Diffusion barrier and seed layer

In a damascene structure, the copper interconnects are surrounded by a diffusion barrier or etch-stop dielectric. These layers prevent the out-diffusion of copper from the interconnects. Since copper diffuses very fast in most materials, refractory metals or their compounds such as tantalum or tantalum nitride are used. A copper seed layer on top of the barrier serves as a nucleation layer on which the subsequent copper plating process takes place. Recently, ruthenium has been reported as a potential diffusion barrier and a replacement for the copper seed layer [11].

5.2.3 Deposition techniques for barrier/Cu seed layers

The diffusion barrier layer and the copper seed can be deposited by physical vapour deposition (PVD) [12] or chemical vapour deposition (CVD) methods [13]. The Cu seed layer deposited by electro-less plating [14] is still in the research phase.

A PVD technique, also known as sputtering, uses inert gas ions to sputter off the atoms from a target and allows the target atoms to deposit on the wafers. In general, the deposition of the barrier/seed layers is characterised in terms of step coverage and sidewall coverage. The step coverage is defined as the ratio of the film thickness at the bottom of the trenches and the film thickness on the top plateau. The sidewall coverage is defined as the ratio of film thickness on the sidewall of the trenches and the film

thickness on the top plateau. It would be ideal for the step coverage to be greater than one, so that the filling in the trenches is faster than the deposition on the top plateau. As for the sidewall coverage, it has to be optimised for the following reasons. If the sidewall coverage is too high, it will cause the narrowing of the top opening of the trenches and prevent the subsequent filling of trenches. If the sidewall coverage is too low, the diffusion barrier or the copper seed layer could be too thin or even be discontinuous and cause some integration issues. For example, copper could out-diffuse through the thin diffusion barrier on the sidewalls.

Figure 5-7 illustrates how overhangs are formed at the top trench corners in a non-directional PVD deposition. A receiving angle is defined as the maximum angle for a particular location to receive the incoming flux. The receiving angles are 270º at the top corner, 180º at the top surface and 90º at the bottom corner. Since the top corners of the trenches have a larger receiving angle, they tend to form overhangs and close the openings of the trenches. Therefore, the PVD deposition is not suitable for very narrow trenches as in sub-0.25 µm technologies. An ionised PVD (iPVD) process was proposed by various groups to improve the deposition [15-24].

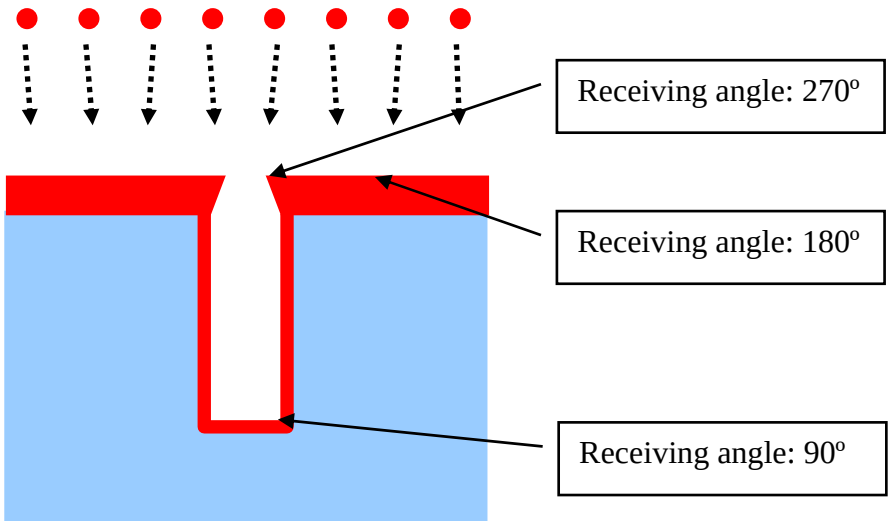

Figure 5-7: **Overhangs are formed because of the large receiving angle at the top trench corners in a non-directional PVD deposition.**

For the iPVD process, the target atoms are ionised and moved towards the wafers with a high directionality under a vertical electric field. Thus, the target ions can reach the bottom of high aspect ratio trenches or vias without closing the top opening. Figure 5-8 shows the effect of argon flow on the barrier deposition in an iPVD system. The pressure of argon plays an important role in a good deposition. The iPVD tools can be equipped with various sources, for example, ionised metal plasma (IMP) by Applied Materials Inc. [15] and hollow cathode magnetron (HCM) by Novellus Systems Inc. [16]. The iPVD techniques provide target ions which have a high directionality and a good step coverage. However, the sidewall coverage could be compromised by the directionality of the deposition.

To further improve the uniformity and the sidewall coverage, an ion induced atomic layer deposition (iALD^{TM}) variation of a PVD system was introduced by Novellus [25]. This technique is quite different from the conventional thermal atomic layer deposition (ALD) or plasma-enhanced ALD. Both conventional thermal ALD and plasma-enhanced ALD are the improved versions of the CVD process, but the precursors react with a surface one-at-a-time in a sequential manner [26-28]. As for the iALD process, the synergistic ion/reactant surface kinetic reactions enhance the deposition rate compared to conventional ALD process and produce films with low resistivity.

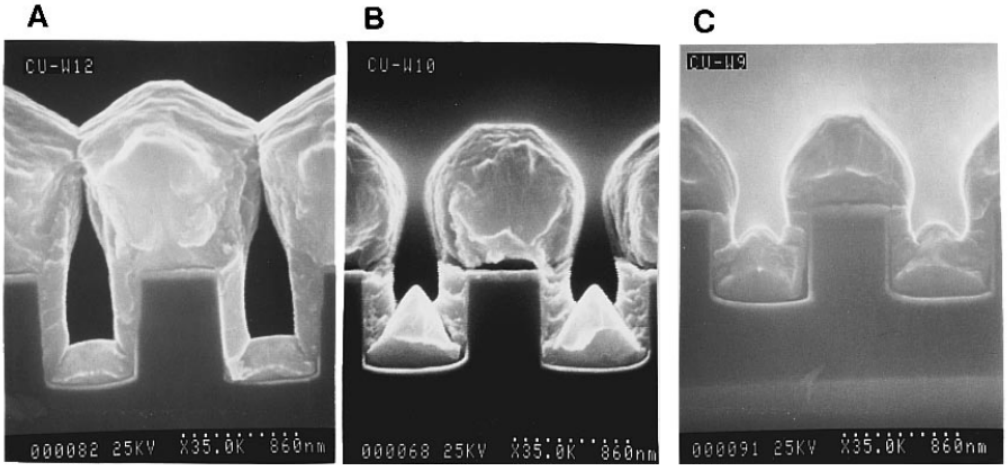

Figure 5-8: Effect of increasing argon pressure on deposit morphology using ionised magnetron sputtering: (a) 5, (b) 20 and (c) 40 mTorr. After Ref. [20]

Since the iPVD and iALD processes are capable of depositing ultra-thin and super-conformal[a] films, they are ideal for diffusion barrier deposition. However, the throughputs of both iPVD and iALD techniques are not adequate for copper fill. A conformal and ultra-thin diffusion barrier could help to reduce the resistance of the interconnects while maintaining the copper integrity in 45 nm technology and beyond.

A CVD technique is different from the "line of sight" iPVD method. In a CVD process, it is the chemical reaction between two gases or the decomposition of a precursor, which produces the deposition. In order to have a super-conformal deposition, the reaction/decomposition process is made in a cold wall system and the deposition is limited to the surfaces of the wafers by increasing the substrate temperature.

Although CVD for TaN [29, 30] and copper seed layers [31] are available, they are not widely used because of process issues and the manufacturing costs. For example, the CVD-Cu process is a slow deposition process and often tends to leave seams, defects, or micro-voids at the centre of the holes and trenches. In some CVD processes such as metal organic CVD (MOCVD) copper, additional plasma annealing is required to remove the carbon impurities incorporated in the film. Furthermore, iPVD copper is preferred because of its strong (111) texture and better adhesion to the plated copper [32].

5.2.4 Electro-chemical deposition (ECD) for Cu fill

After the deposition of the diffusion barrier and the copper seed layer, trenches and vias are generally filled with Cu in an electro-chemical deposition (ECD) also known as electro-plating. Copper ECD has been the norm in advanced metallisation because of its low cost, high deposition rate, low temperature process, good electro-migration resistance and feature-filling capabilities. In 1998, IBM demonstrated an electro-plating process with bottom up filling (also known as super-filling) [33]. Figure 5-9 shows the difference of bottom-up filling and conventional plating due to the use of different

[a] A super-conformal film is defined as the thickness of the film is the same everywhere along a morphologically uneven surface.

additives. The conventional plating produces conformal deposition, while the bottom-up filling enhances the deposition within the trenches. The bottom-up filling performance achieved through the aid of various additives such as accelerator, inhibitor (or suppressor) and leveller, was described in various articles [33, 34]. In a plating process, accelerators locally accelerate the plating current at a given voltage when they adsorb on the Cu surface during electroplating. On the other hand, suppressors tend to form a current-suppressing film on the entire wafer surface. High accelerator concentration within the cavities of small features enhances the deposition, but comparable concentrations of accelerator and inhibitor on the surface hinders the deposition. The flux at the shoulders is much higher than at the sidewalls and the bottom due to shape-induced field-concentration effects. Because of the diffusion controlled mechanism, the deposition at the shoulders is suppressed. As a result, highly polarized electrolytes, which maintain strong current suppression on the wafer surface and aid in uniform nucleation within features, are beneficial to high aspect ratio feature filling. A leveller is a second class of current suppressing molecules and is commonly used for reducing the roughness of a surface, smoothing defects such as scratches and controlling the profile of the films. Now, this super-filling process has formed the basis for all advanced plating processes.

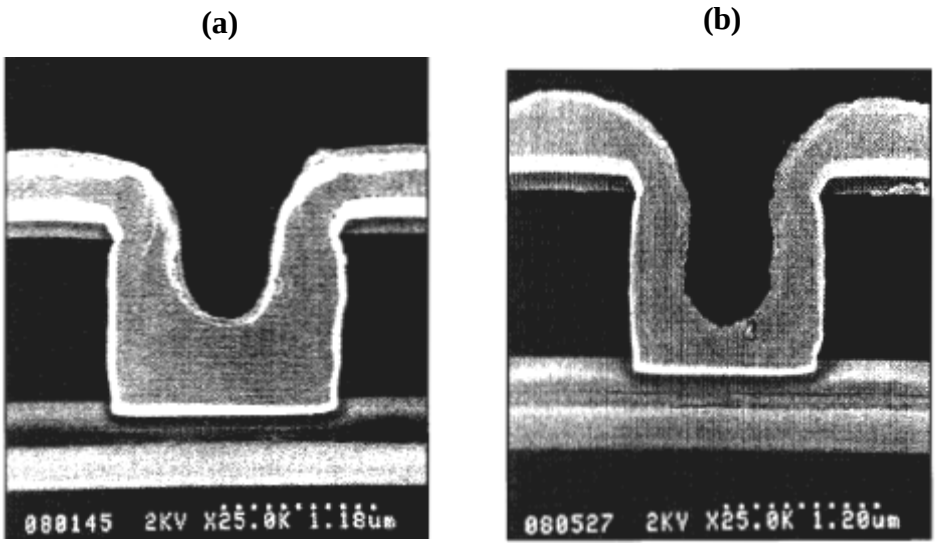

Figure 5-9: **Cross sections of partially filled lines showing the profiles of electroplated copper (plating was done from a plating solution containing different additives: (a) superfilling; (b) edge-rounding only. After [33].**

5.2.5 Post-metallisation annealing

Post-metallisation annealing is commonly used between the ECD copper fill and the CMP process. The purpose of the annealing is to eliminate the self-annealing effect in electroplated copper films [35]. Self-annealing is a phenomenon of copper films undergoing micro-structural transitions at room temperature. The transitions involve changes in grain size and texture over time, which results in changes in sheet resistance and hardness [35-40], because of the influences of defect density and impurity in the copper films.

To eliminate self-annealing, a high temperature annealing in a forming gas (N_2/H_2) is often required to promote the grain growth of electro-plated copper films [41]. The annealing conditions can be optimized to stabilise grain growth, to reduce the post-CMP defects and to obtain a reasonable electro-migration lifetime [42].

5.2.6 Chemical Mechanical Polishing (CMP)

A key process to realize the damascene process is chemical mechanical polishing (CMP). CMP is used to remove the excess copper and barrier on the top plateau and to planarise the dielectric surface. Figure 5-10 shows that problems such as dielectric erosion and copper dishing arise due to the combination of the chemical and the mechanical effects. Copper dishing refers to the excess copper removal in wide trenches, while dielectric erosion refers to the removal of dielectric due to over-polishing. In order to minimise the dishing and erosion, additional design rules, such as “fill” design rules, are necessary for ensuring a good yield [43]. Because of these additional rules, the cycle time for the chip production and the complexity of the layout are increased. Therefore, the elimination or reduction of copper CMP would therefore be a great value to the IC industry.

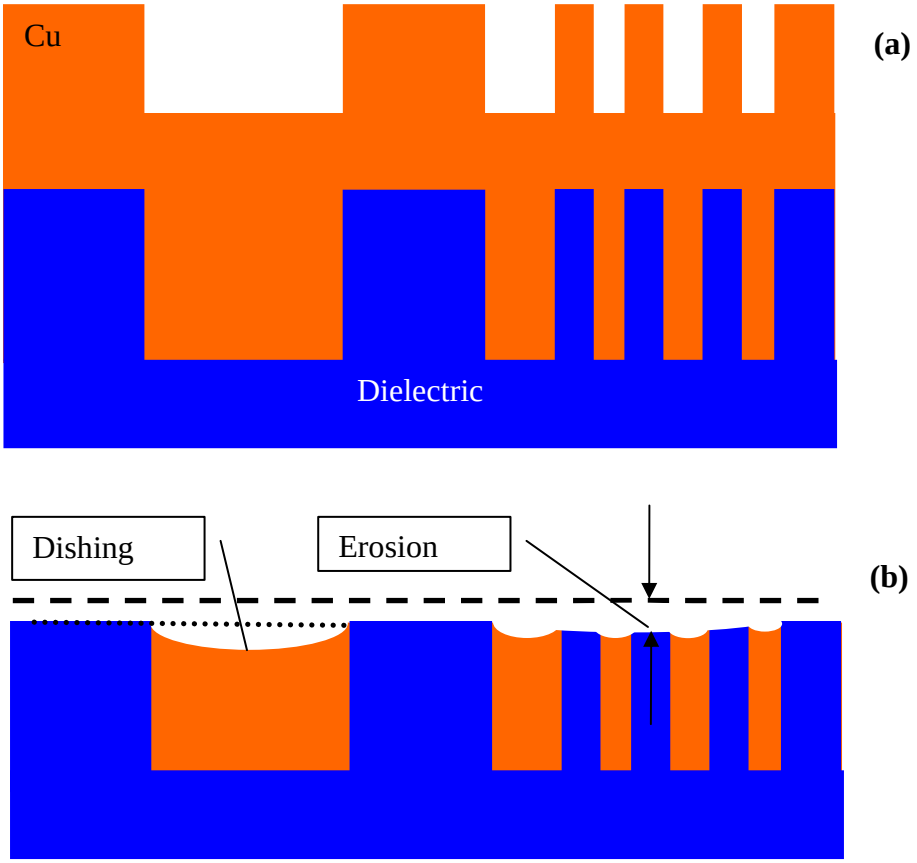

Figure 5-10: **Schematics of CMP dishing and erosion. (a) before polishing. (b) after CMP. The dash line in (b) indicates the original height of the dielectric.**

5.2.7 Etch-stop Dielectric

To prevent the out-diffusion of the copper from the top surface, an etch-stop dielectric is deposited after the copper CMP. The dielectric could be silicon nitride or SiC [44], which are typically deposited using CVD processes.

In this section, an overview of the copper damascene process was described. The next section will discuss the potential problems of the existing copper processes.

5.3 Problems in the existing processes in the future

In order to continue the progression to smaller dimensions and higher performance, many different challenges relating to interconnect processing must be solved [10]. This section describes some of the potential problems for the existing damascene process.

5.3.1 Filling of copper in high aspect ratio trenches

As the pitch decreases and the aspect ratio (depth to width) increases, it is difficult to fill damascene trenches without voids or key holes. Key-hole formation within the damascene structures compromises the reliability of the interconnects [7]. Figure 5-11 shows barrier and seed conformality in covering ~64 nm wide trench. The copper seed (deposited by PVD) is continuous with an overhang that occupies ~28 nm of the trench width. The opening is acceptable for good trench fill by ECD, but there is a risk that the copper seed will close up at the top corners and seed layer will become discontinuous for smaller features [45].

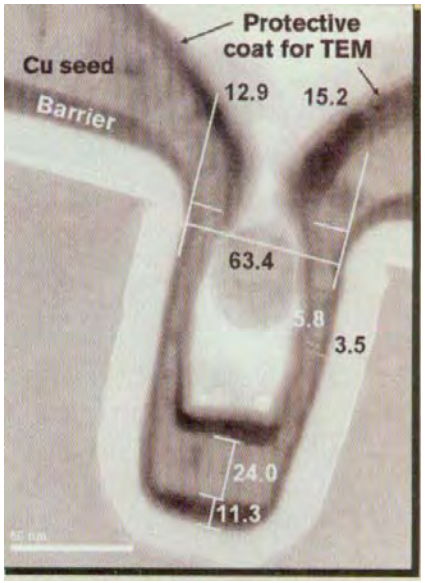

Figure 5-11: Barrier and seed conformality in covering ~64 nm wide trench. After Ref. [45].

5.3.2 Problems in CMP

Both CMP dishing and dielectric erosion are related to the over-polishing which is unavoidable because of the non-uniform copper overburden across an 8-inch or 12-inch wafers. The non-uniformity in the copper overburden forces technologists to use more polishing time than required. It would be ideal if the overburden of the copper could be reduced, thus, a shorter polishing duration could be possible. Dishing and erosion could be effectively alleviated when the copper is deposited selectively between the damascene features and the dielectric surfaces.

Furthermore, CMP processes have encountered greater challenges with the integration of ultra-low-k dielectrics [10]. Minimizing or even eliminating copper CMP would be highly desirable from a process integration point of view. A more selective copper deposition into deep and narrow trenches and vias would therefore be an advantage for technological advancement.

5.3.3 Resistivity of the interconnects

As the dimensions reduce, the interconnect exhibits a higher electrical resistance when at least one of the dimensions (width, height) approaches the mean free path of electrons (~39 nm in bulk copper at room temperature). For wires with the width and height of 100 nm and above, the resistivity exhibits a film-like behaviour with a separate contribution to the resistivity of each small dimension (width and height) [46]. On the other hand, for structures of less than 100 nm dimensions, two main scattering mechanisms are responsible for the increase in resistivity, surface scattering and grain-boundary scattering [47]. In short, the resistivity of copper inside the trenches is influenced by their surface, line width, grain size and crystal orientation. Smooth surfaces on all sides are important to maximize elastic scattering of electrons [48, 49]. Wu *et al.* emphasized that the grain-boundary scattering was more dominant than the surface scattering as the dimensions approached the mean free path of electrons [50]. Except for the phonon scattering that only depends on temperature, the surface scattering and the grain boundary scattering depend on the trench size, the grain size

and the surface conditions. A pronounced increase in resistivity was observed by Jiang *et al.* [51] when the feature sizes were several times larger than the electron mean free path in copper. Inevitably, keeping the resistivity low in nanoscale features is the key for future technology nodes. Copper films with giant grains and <200> orientation were demonstrated with low resistivity and a long electro-migration[b] lifetime [52]. In short, the surface roughness and the grain size distribution of a copper film are the main factors determining the resistivity in the interconnect structures. The next section will discuss the potential candidates reported for the copper fill process.

5.4 Potential Cu fill candidates in the literature

According to the International Technology Roadmap for Semiconductors (ITRS) in 2006, the solution for 25 nm technology and beyond is not known yet [1]. The section describes two types of copper fill candidates: advanced copper filling deposition and copper reflow.

5.4.1 Advanced copper filling

In the development of advanced copper filling, several selective copper filling processes have been reported, as summarised in Table 5-1. In these papers, the filling of copper was demonstrated in vias or trenches. The width of the features ranged from 0.1 to 1 μm and the aspect ratios ranged from 1.2 to 9. The deposition rate, which was important for manufacturability, ranged from 40 to 825 nm/min.

Similar to the ECD process, electro-less plating [53, 54] and electro-chemical mechanical deposition (ECMD) [55] could also have a preferential deposition between trenches and top plateaus. Electro-less plating does not require an electron current in the plating process, thus, the seed layer is not needed. The ECMD process combines the use

[b] Electromigration is the transport of material caused by the gradual movement of the ions in a conductor due to the momentum transfer between conducting electrons and diffusing metal atoms.

Table 5-1: Summary of latest publications on various selective Cu fill processes.

Year	Technique	Trenches /vias	width (μm)	Aspect Ratio	Dep. Rate (nm/min)
2001	CVD with a catalytic surfactant [56]	Both	0.3	3.3	40
2001	Electroless plating [53, 54]	Vias	0.2	5	75-120
2005	Electro-Chemical Mechanical Deposition (ECMD) [55, 57]	Trenches	0.6	1.2	300-825
2006	Electro-chemical Deposition (ECD) [58]	Trenches	0.1	6	50-100

of ECD and CMP and therefore, the trenches are always open for plating. In both processes, the bottom-up filling is achieved by controlling the additives and external forces (such as solution circulation, mechanical force and electrical field).

As described previously, CVD is a surface reaction process, thus, a conformal deposition is expected, rather than a bottom up filling process. However, CVD-Cu process using iodine as a catalytic surfactant was demonstrated with the bottom up filling capability [56], but the deposition rate of 40 nm/min was low compared to 200 nm/min in the CVD-Cu process in Ref. [59] and 50-100 nm/min in the copper plating process in Ref. [58].

Up to date, the best deposition is still the ECD process because it can fill the 0.1 μm trenches with a high aspect ratio [58]. However, since ECD, electroless plating, ECMD and CVD processes all require organic additives or precursors, they do not produce copper films with ultra-high purity. The amount of impurities depends on the electric current applied during plating [40]. One solution is to deposit Cu from an ultra-high purity target using an evaporation source or a sputtering source. However, such techniques have limitations in filling high aspect ratio features, as described in Section 5.2.3.

In the literature, some research groups have improved the performance of the iPVD techniques for copper filling, as summarised in Table 5-2. The two iPVD techniques seem promising in filling narrow and high aspect ratio features. However, due to lack of selectivity, the thickness of copper overburden could be the same as the trench height.

As a result, a long duration CMP is required to remove the thick overburden. The long polishing time will then cause serious dishing and erosion problems.

Cui *et al.* demonstrated the filling of 0.1µm via holes using laser assisted direct imprint (Table 5-2). In their technique, a copper film was melted using a laser beam and then pushed into the via holes by a quartz plate [60]. The draw back was that the stress built up during the rapid cooling could potentially affect the interconnect reliability. Furthermore, fabricating a quartz plate that matched the curvature of all large silicon wafers was almost impossible. Instead of filling the features with a superior directionality or a rapid surface melting followed by pressing, copper reflow techniques could be used, as discussed in the next section.

Table 5-2: Summary of latest publications on PVD related Cu filling processes.

Year	Technique	trenches /vias	width (µm)	Aspect Ratio
1995	iPVD (magnetron sputtering) [20]	Trenches	0.6	1.1
1999	iPVD (ionised metal plasma) [17]	Trenches	0.1	8
2006	E-beam evaporation + laser-assisted direct imprint [60]	Vias	0.1	5

5.4.2 Copper reflow

As the features become smaller, they become increasingly difficult to fill by deposition alone. Thus, the subsequent annealing procedure used to eliminate self-annealing effects could aid the filling process. This technique is referred to as a copper reflow. At annealing temperatures $\leq$ 450 °C, surface diffusion due to capillary forces is considered the dominant material transport mechanism in a copper thin film [61]. This section discusses the copper reflow processes reported in the literature.

Table 5-3 describes the reflow techniques suggested for copper metallisation. The reflow could be performed in a vacuum, an atmospheric pressure or a high pressure (120-200 MPa).

Table 5-3: The reflow processes reported in the literature.

Year	Technique	trenches /vias	width (μm)	Aspect Ratio
1996	PVD + reflow in vacuum at 450ºC [62]	Trenches	0.6	0.8
1996	PVD + atmospheric reflow at 400ºC [63]	Trenches	0.2-0.5	2.5
2003	PVD/ECD+ high pressure reflow (at 400-550ºC in 120-200 MPa argon) [64]	Vias	0.28	4.3

Abe *et al.* reported that the surface roughness of the underlying barrier layer (such as W, Mo, Ti) was the main factor influencing the copper reflow when annealed at 450ºC in vacuum [62]. They concluded that a smooth surface could lead to a poor wettability, therefore promoting the reflow. Mikagi *et al.* also demonstrated copper reflow in barrier-metal-free trenches in a forming gas at 400ºC [63]. Thus, the reflow of copper could work on different underlying surfaces.

Onishi *et al.* proposed that the hydrogen embedded in the ECD film could soften the copper and facilitate the reflow of copper at an elevated temperature [64, 65]. The hydrogen was generated during the ECD process. They showed that at a high pressure and a high temperature (400-550ºC), the ECD copper could be pushed into the 0.28 μm via holes [64].

Friedrich *et al.* used a 3D Monte Carlo method to simulate sputtered copper film reflow from 250ºC-450ºC [66]. As shown in Figure 5-12, they simulated that the reflow time increased as the temperature decreased. Figure 5-13 shows that the trenches could be filled by the reflow for aspect ratios between 1.5 and 2 for both 0.5 μm and 1 μm copper deposition. Figure 5-14 shows that above an aspect ratio of 2, bridging or capping could occur and a key-hole could evolve to a circle which intrinsically had a low total surface free energy. As a result, the reflow technique could only fill up to medium aspect ratio trenches.

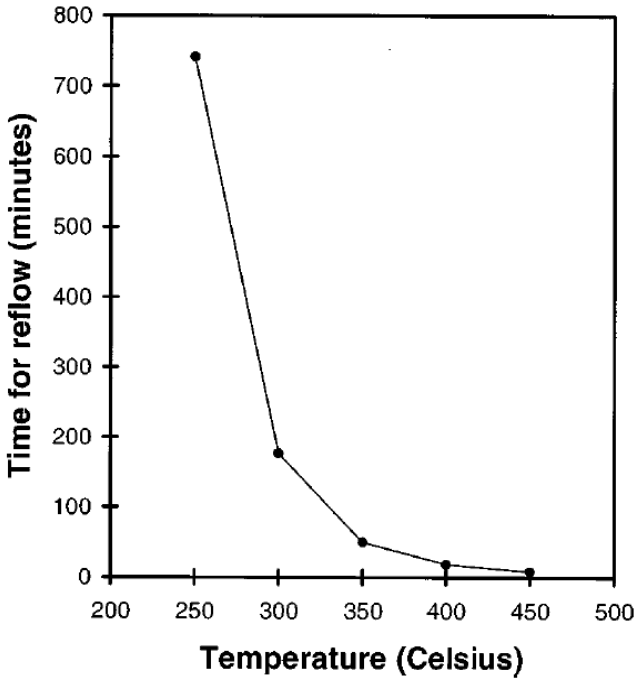

Figure 5-12: **Reflow time vs. the annealing temperature for 1.25µm Cu film over a 0.35µm 2:1 aspect ratio trench. Ref. [66]**

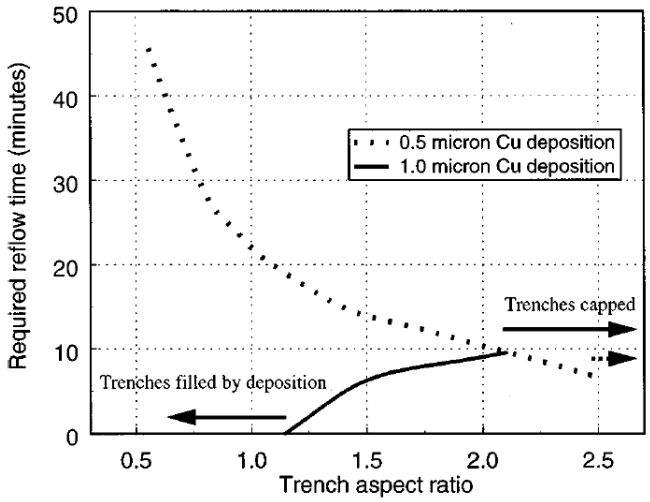

Figure 5-13: **Required annealing time for filling as a function of the trench aspect ratio for as-deposited Cu thicknesses of 0.5µm (dashed line) and 1.0µm (solid line) using a sputtered copper film at . The depth of the trenches is 0.5 µm. After Ref. [66]**

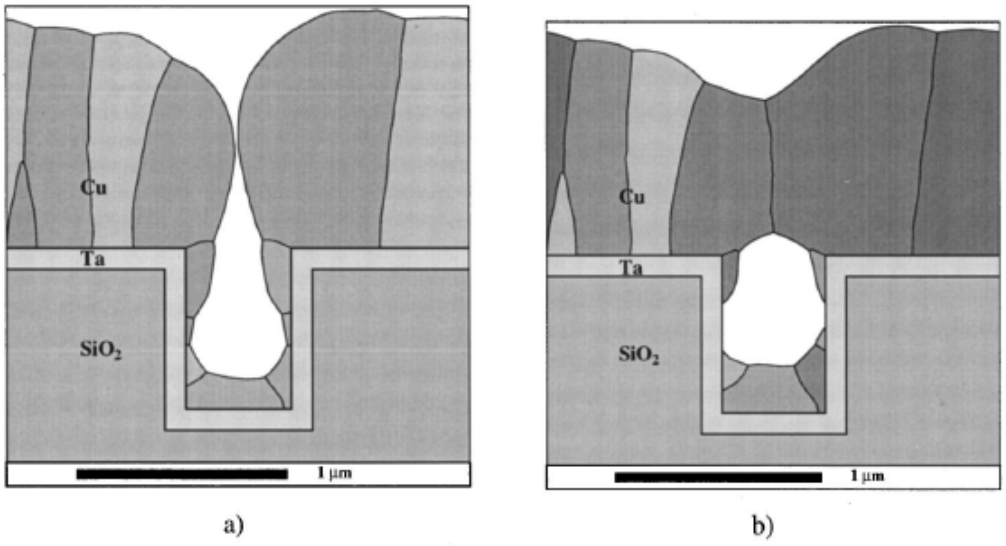

Figure 5-14: **Bridging or capping of the trench may occur during deposition or during the reflow process. The as-deposited Cu film on Ta (a) is reflowed. During reflow, the film above the trench closes off resulting in the formation of a void within the trench (b) This particular simulation also dewetted along the sidewalls. After Ref. [66]**

Annealing in a hydrogen environment could be a useful technique to enhance the diffusion of copper and it is comparable with the post-metallisation annealing step in the damascene process. There are numerous reports on hydrogen annealing for copper interconnects, for example, molecular hydrogen annealing, atomic hydrogen annealing [67], deuterium annealing [68], hydrogen remote plasma annealing [69] and forming gas anneal [63].

Recently, copper reflow has been demonstrated in oxygen ambient [70-72]. Prater *et al.* reported a reduction in resistivity when copper was deposited in a partially oxidised environment [73]. They concluded that the cuprous oxide produced a smooth surface and hence a lower resistivity. Kim *et al.* reported that copper films (produced by MOCVD method) had low resistivity when reflowed in an oxygen ambient at 450ºC [70, 72]. From these two reports, they seem to suggest that oxides within the metal lines improve the resistivity. However, the reliability of the copper films that contain oxides has not been reported.

The factors determining the reflow of copper thin films could affect the sintering of copper clusters in a similar way. The next section will review the reports on the nanoscale cluster depositions.

5.5 Cluster deposition on pre-textured surfaces

As described in the previous section, advanced copper filling and copper reflow are two potential candidates for advanced metallisation. As for the copper filling, the selective deposition reported in the literature could not be realised without the aids of additives. However, the inclusion of additives into the films could compromise the resistivity and reliability. Thus, a new technique is needed for an excellent copper filling. On the other hand, some of the unique properties of metallic clusters could possibly offer a new field of research for interconnect application. This section discusses two special properties of metallic clusters that could potentially be applied to the interconnect application: the bouncing behaviour and the sintering behaviour.

5.5.1 Bouncing clusters

In 1994, Haberland *et al.* [74] demonstrated the use of cluster beams for filling micron-scale holes with copper. In their paper, energetic clusters (10eV/atom) and elevated substrate temperatures were recommended to fill 0.8 µm via holes, as illustrated in Figure 5-15. One year later, Gatz *et al.* [75] demonstrated the metallization of non-planar surfaces. In the latter case, the formation of the features was performed by depositing through a mask, as depicted in Figure 5-16. However, filling with clusters into the high aspect ratio nanoscale trenches required by interconnect industry has not been demonstrated. Furthermore, the bouncing characteristic (as will be described later), which could potentially lead to a selective deposition, has not been applied in the sub-µm interconnect structures. Therefore, there is a potential to produce bouncing clusters for advanced interconnects.

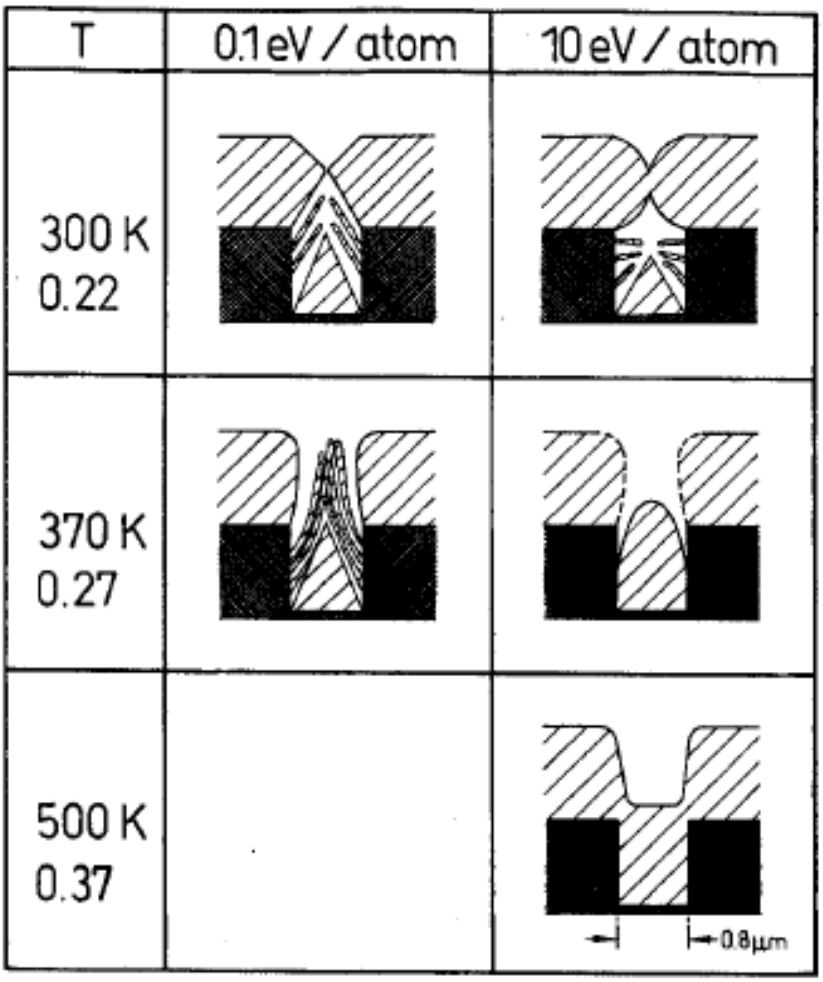

Figure 5-15: **Morphology of SEM for different substrate temperatures and kinetic energies for copper clusters. To fill the 0.8µm holes, energetic clusters (10eV/atom) and the substrate temperature of 500 K were required. The substrate temperature is also given divided by the Cu melting point (1375 K). After Ref. [74].**

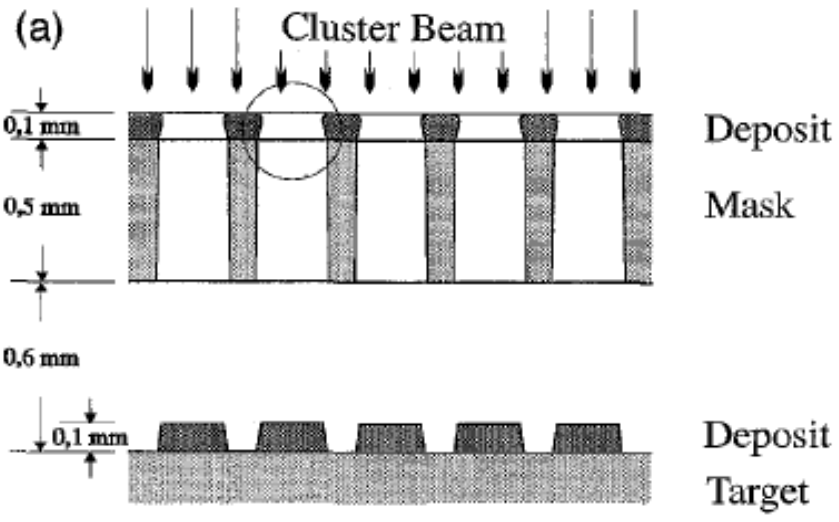

Figure 5-16: **Clusters were deposited through a mask in Ref. [75].**

Recently, Partridge *et al.* reported that metallic clusters could bounce or slide in a template yielding nanowires depending on the kinetic energy and the momentum of the clusters [76]. Figure 5-17 shows a SEM image of clusters accumulated at the bottom of a V-groove. The V-grooves were made by preferential KOH etching of a silicon substrate followed by oxidation. Clusters bounced off the top plateau, slid or bounced along the sidewalls and accumulated at the bottom of the V-grooves.

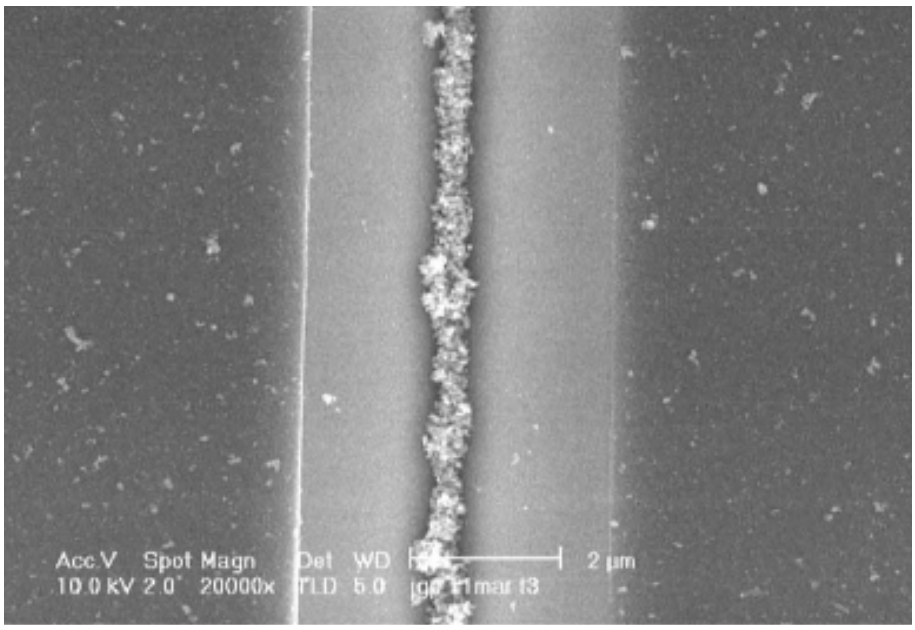

Figure 5-17: SEM image of clusters accumulated at the bottom of a Si V-groove. Ref. [76]

The transition from adhesion to reflection (or bouncing) was verified by molecular dynamics simulations [77]. Figure 5-18 shows that the probability of sticking depends on the incident cluster velocity. Therefore, at an optimum velocity, clusters could bounce off an unpatterned substrate. It would be interesting to try to make the clusters accumulate at step edges or the bottom of a trench of near trapezoid shape in the case of the damascene process, and this is one of the major topics of this thesis.

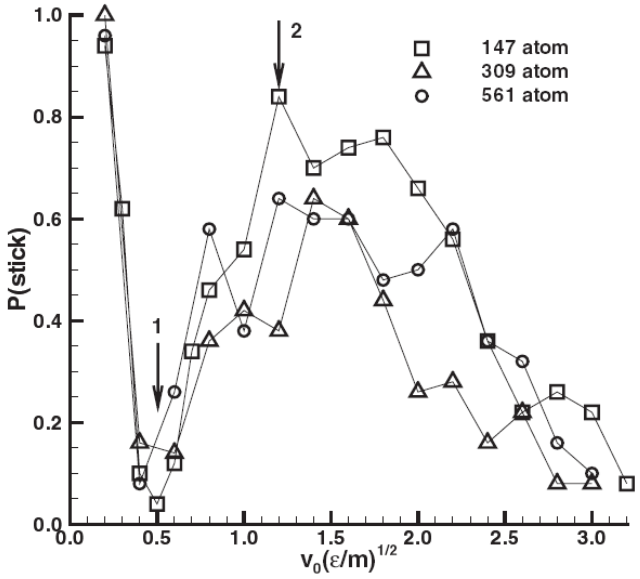

Figure 5-18: **The probability of sticking as a function of incident velocity for different cluster size. Note the minimum and maximum in adhesion probability at labels 1 and 2, respectively [77]**

5.5.2 Sintering of clusters

As described in Section 5.2, the post metallisation anneal is an important step in the damascene process. The reason for this step is to eliminate the "self annealing" effect. On the other hand, at high temperatures, copper reflow was used by some research groups to fill in the trenches as described in Section 5.4.2. If cluster-based selective deposition is to be used for trench/via filling, then sintering and/or reflow steps will also be necessary.

Numerous experiments demonstrated that the melting point of clusters decreases when the cluster size reduces [78-82] (a so-called thermodynamic size effect), as discussed in chapter 1. The high surface/volume ratio of the clusters is expected to enhance surface melting and coalescence [83, 84] during the annealing process. In this section, the review of the sintering of clusters is divided into two parts: initial stage and grain reorientation.

Initial sintering

In order to understand the sintering mechanism of copper nanoscale clusters, the initial stage of the sintering is critical. In 1955, Kingery *et al.* studied the initial stages of cluster sintering [85]. Figure 5-19 shows two models of the initial sintering stage for small spherical particles: (A) material was filled between the spheres but the centres of the spheres were not moving and (B) the centres of the spheres were approaching. In the two models, three mechanisms were discussed: viscous flow [86], evaporation-condensation and volume diffusion. In the first mechanism, the material transport was governed by a viscous flow of the material. In the second mechanism, the sintering was caused by the reduction in the vapour pressure over a small negative radius of curvature (P_1) due to the surface energy. In the third mechanism, the sintering was governed by the volume diffusion of the material. Depending on whether the spheres were approaching each other (model A vs. B), the volume diffusion rates could be slightly different.

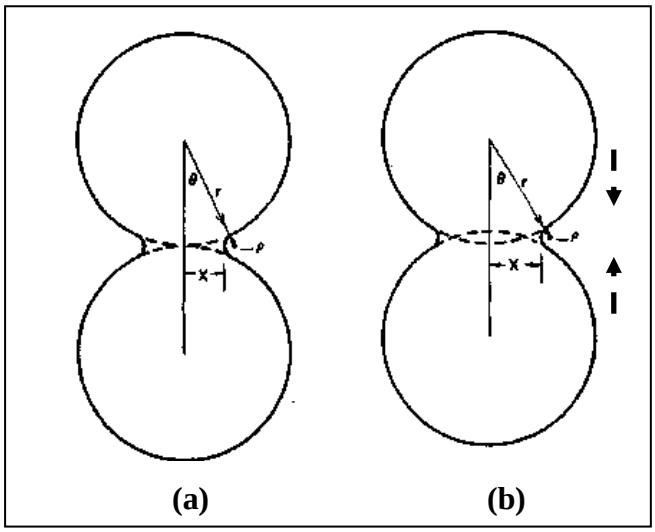

Figure 5-19: **Two models for initial stages of sintering of small spheres: (a) material is filling in between the spheres but the centres are not moving (b) the spheres are approaching each other [85]. *x* is the radius of the neck and *r* is the radius of the clusters.**

The calculation of sintering rates due to volume diffusion depends on the diffusion path. In general, the free energy at the small radius of curvature is less than at a plane surface. Therefore, there is a greater concentration of vacancies at the neck, and the materials will diffuse toward the neck. Alternatively, the vacancy concentration can be assumed constant at the neck and the vacancies diffuse towards the surface of the large spheres. Based on these two different diffusion paths, two estimates for the diffusion rate for model A could be found. For model B, the vacancies diffuse to the grain boundary, thus, there is no difference between models A and B.

On the other hand, Nichols *et al.* reported two types of sintering due to surface diffusion [87]. The neck growth could be proportional to either $t^{1/7}$ or $t^{1/6}$. The equations from Ref. [85] and [87] are summarised in Table 5-4. The parameter values used for the diffusion calculations are summarised in Table 5-5. Comparing the two estimates in model A and the estimate model B in volume diffusion, the diffusion is fastest in model B. Thus, the estimate from model B will be compared with other sintering mechanisms.

Table 5-4: Equations for different material transport mechanisms in different model, summarised from Ref. [85] and Ref. [87]

	Model A	Model B
Viscous flow	$\frac{x^2}{r} = \frac{3\gamma t}{2\eta}$	
Evaporation-condensation	$\frac{x^3}{r} = \frac{3\pi M\gamma (M/2\pi RT)^{1/2} P_0 t}{d^2 RT}$	
Volume Diffusion	(i) $\frac{x^5}{r^2} \cong \frac{10\pi\gamma a^3 D_V t}{kT}$ or (ii) $\frac{x^5}{r^2} \cong \frac{40\gamma a^3 D_V t}{kT}$	$\frac{x^5}{r^2} \cong \frac{80\gamma a^3 D_V t}{kT}$
Surface diffusion ($x \sim t^{1/7}$)	$\frac{x^7}{r^3} = \frac{28(Ds\gamma\Omega^2\upsilon)t}{kT}$	
Surface diffusion ($x \sim t^{1/6}$)	$\frac{x^6}{r^2} = \frac{25(Ds\gamma\Omega^2\upsilon)t}{kT}$	
Symbols notation: x: radius of the neck; r: radius of the spheres; γ: the surface energy; η: viscousity; t: sintering time; M: Molecular weight; d: density; P_0: Equilibrium vapour pressure over a flat surface; R: universal gas constant (8.3145 J/mol K); k: Boltzmann constant (1.38066×10^{-23} J/K); T: Temperature; a: atomic radius; Ω: atomic volume; υ: the number of diffusing atoms per unit surface area ($\sim\Omega^{-2/3}$)		

Table 5-5: Values used for the transport mechanism estimations.

Parameters	Symbol	Values	Unit	Remark
Vapour pressure	P_0	1×10^{-9}	Pa	Vapour pressure for bulk Cu at 450ºC. Extrapolated from Ref.[88].
Viscosity	η	1×10^{16}	Pa s	Assumed to be the same as SiO_2 at 450ºC
Surface energy	γ	2.61	Jm^{-2}	(100) Cu at 200ºC [89]
Atomic radius	a	0.361×10^{-9}	m	[90]
Volume self-diffusion	D_v	$1.33 \times 10^{-5} \times \exp(-23821/T)$	m^2s^{-1}	Interpolated from ref. [91]. At 450ºC, $D_v=9.6\times10^{-20}$
Surface self-diffusion	D_s	$0.63 \times 10^{-4} \times \exp(-13681/T)$	m^2s^{-1}	Interpolated from ref. [92]. At 450ºC, $D_s=3.81\times10^{-13}$
Molecular weight	M	1.055×10^{-25}	kg/atom	[90]
Density	ρ	8920	$kg\ m^{-3}$	[90]

In the interconnect application, the processing temperature is kept below 450ºC. Higher processing temperatures are expected to cause decomposition of the low-*k* dielectrics. Therefore, the transport models are compared at 450ºC. Using Matlab, the ratio of the neck size to the particle radius (*x/r*) could be plotted with respect to the time and the annealing temperature. Figure 5-20 shows the curves of neck growth at 450ºC using five different models. Sintering by viscous flow or evaporation-condensation is unlikely to happen because the annealing temperature is far below the melting point of copper. The surface diffusion by $t^{1/7}$ has the shortest sintering time. When the neck of the two clusters is the same as the cluster diameter (*x/r*=100%), the subsequent sintering is governed by surface diffusion, surface tension or surface energy.

Figure 5-21 shows the cluster-size effect at 450ºC using the surface diffusion equation. Three different cluster diameters were compared: 30, 15 and 10 nm. It was found that the smaller the clusters, the faster the sintering. This trend agreed with the "size effect" reported in the literature.

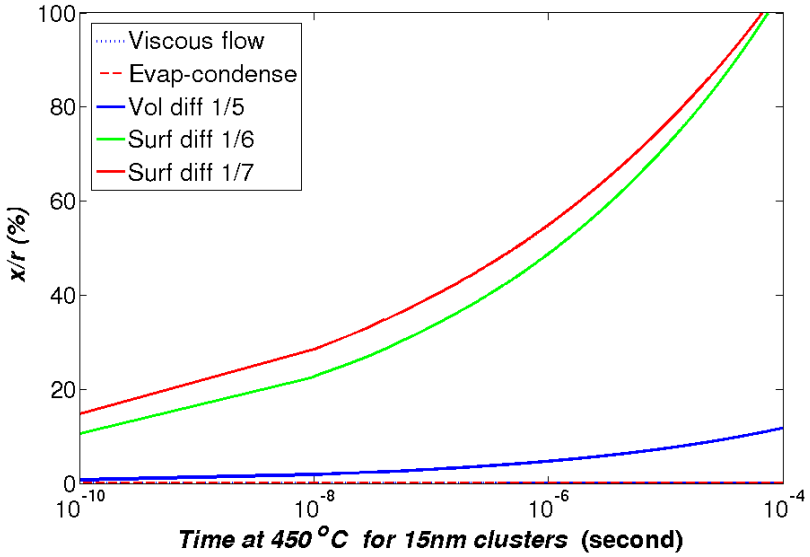

Figure 5-20: **Growth of the neck at 450°C using different models for clusters with 15 nm diameter.**

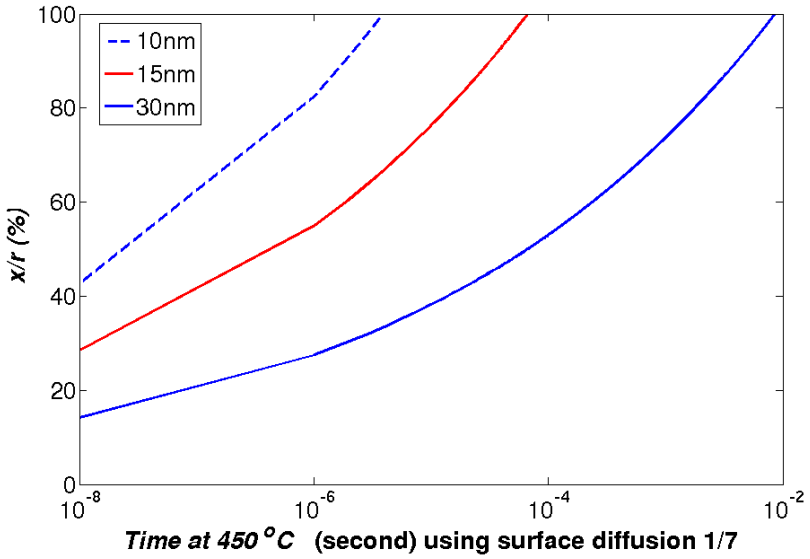

Figure 5-21: **Growth of the neck at 450°C for 30 nm diameter clusters (solid blue curve), 15 nm diameter clusters (solid red curve) and 10 nm diameter clusters (dashed blue curve) using $t \sim x^{1/7}$ surface diffusion estimation.**

Figure 5-22 shows the growth of the neck between two 15 nm clusters at 450ºC using the viscous flow, evaporation-condensation and volume diffusion (model B) at a longer time scale. Even if the surface diffusion was hindered by the thin oxide shell, it appeared that volume diffusion could take place within a few seconds.

Grain reorientation

Yeadon *et al.* proposed that the copper clusters which were initially randomly orientated underwent re-orientation upon annealing by a mechanism involving sintering and grain growth [93]. The phenomenon is referred to as a contact epitaxial growth. From their experiments, 4-20 nm clusters became epitaxial on a clean <001> copper thin film at 200-600ºC. Figure 5-23 is a schematic of how the as-deposited clusters sinter into the copper thin film by surface diffusion (same argument as Kingery's model [85]), and then resume the orientation of the thin film by grain-boundary motion in their model. If the copper clusters could be sintered into copper thin films with the same crystal orientation, it could be possible to produce single crystal or giant grained interconnects by sintering nanoscale clusters. As discussed in Section 5.3.3, copper films with giant grains and <200> orientation have a low resistivity and a long electro-migration lifetime [52].

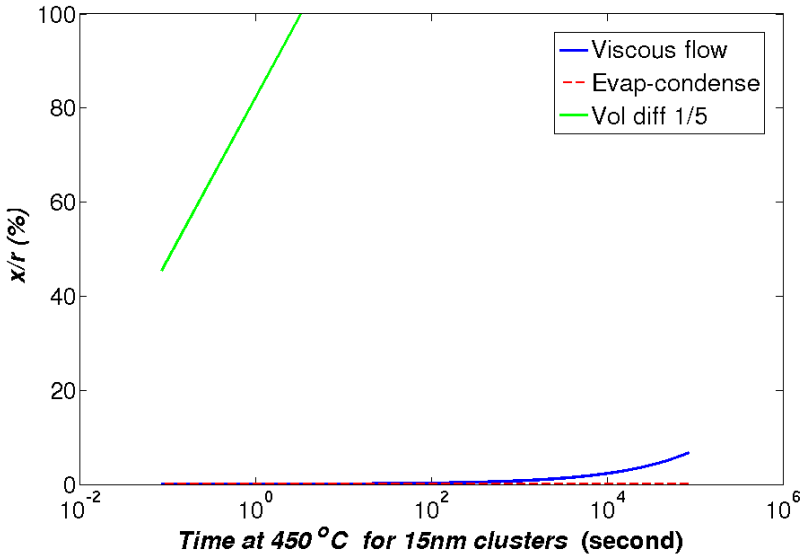

Figure 5-22: **Growth of the neck between two 15 nm diameter clusters at 450ºC using the viscous flow (solid blue curve), evaporation-condensation (red dashed curve) and volume diffusion (model B) (green curve).**

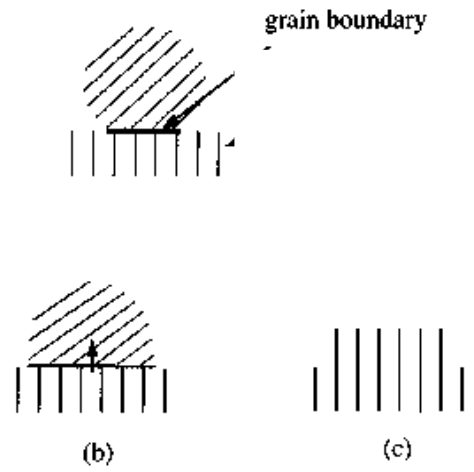

Figure 5-23: **Cross-sectional schematic diagram of the reorientation process occurring upon annealing an as-deposited copper nanoparticle. (a) Particle prior to annealing, showing the initial contact area between the particle and substrate. After significant neck growth by surface diffusion, (b), it becomes energetically favourable for the grain boundary to move through the particle and the particle assumes the same orientation as the substrate (c)**

5.6 Summary

Due to the driving force of technological and social needs (Moore's law), the dimensions of the interconnects are shrinking continuously. As the dimensions reduce, the circuit speed is dominated by the RC delay of the interconnects. To improve the resistivity of the interconnects and the electron-migration lifetime, copper metallisation has replaced aluminium metallisation for sub-0.25 µm technologies. To overcome various problems for copper metallisation, damascene processes are used universally.

In this chapter, an overview of copper interconnect processing was presented and various copper deposition techniques and copper reflow techniques were reviewed. In the PVD processes, high purity copper films can be deposited, but the poor selectivity could be a problem for the subsequent CMP process. In the CVD processes, a high selectivity and an excellent filling can be achieved, but impurities could be embedded into the copper film. The application of the copper reflow technique could be feasible but it was limited to medium aspect ratio trenches.

On the other hand, some unique properties of metallic clusters were reviewed. Bouncing clusters could accumulate at the bottom of V-grooves through a self-assembly process. Nanoscale clusters, which have a high surface to volume ratio, were expected to have a lower melting point than the bulk. The calculation from various reports showed that the surface diffusion was the fastest transport mechanism, followed by volume diffusion, in the initial sintering stage. From the contact epitaxy model, clusters could re-align their crystal orientation upon annealing through sintering and grain growth. As a result, fabricating single-crystal or giant-grained interconnects with a low resistance and a long electro-migration lifetime could be achievable. With the bouncing and sintering properties of metallic clusters, a metallic cluster deposition technique could be the potential candidate for the interconnect application.

References

[1] "International Technology Roadmap for Semiconductors, 2006 (Update), *http://public.itrs.net.*"

[2] G. E. Moore, "Cramming more components onto integrated circuits," *Electronics,* vol. 38, 1965.

[3] P. J. Ireland, "High aspect ratio contacts: A review of the current tungsten plug process," *Thin Solid Films,* vol. 304, pp. 1-12, 1997.

[4] M. T. Bohr, "Interconnect scaling - The real limiter to high performance ULSI," *IEDM Tech Digest.*, p. 241, 1995.

[5] W. Stanley, *Silicon processing for the VLSI era* vol. 4: Lattice Press, 2002.

[6] "*http://www-03.ibm.com/press/us/en/pressrelease/2486.wss.*"

[7] S. Wolf, *Silicon Processing for the VLSI Era: Deep-Submicron Process Technology* vol. 4: LATTICE PRESS, 2002.

[8] R. V. Joshi, "New damascene structure for sub-micrometer interconnect wiring," *IEEE Electron Device Letters,* vol. 14, pp. 129-132, 1993.

[9] C. Case, "Fundamentals of Low-k Chemistry," in *Future Fab Intl.* . vol. 17, 2004.

[10] M. Fayolle, G. Passemard, O. Louveau, F. Fusalba, and J. Cluzel, "Challenges of back end of the line for sub 65 nm generation," *Microelectronic Engineering,* vol. 70, pp. 255-266, Nov 2003.

[11] T. N. Arunagiri, Y. Zhang, O. Chyan, M. El-Bouanani, M. J. Kim, K. H. Chen, C. T. Wu, and L. C. Chen, "5 nm ruthenium thin film as a directly plateable copper diffusion barrier," *Applied Physics Letters,* vol. 86, p. 083104, 2005.

[12] K. W. Lee, H. J. Shin, J. W. Hwang, S. W. Nam, Y. J. Moon, Y. J. Wee, I. G. Kim, W. J. Park, J. H. Kim, S. J. Lee, K. K. Park, H. K. Kang, and K. P. Suh, "Highly manufacturable Cu/low-k dual damascene process integration for 65nm technology node," in *Interconnect Technology Conference, 2004. Proceedings of the IEEE 2004 International*, Burlingame, CA, United States, 2004, pp. 57-59.

[13] P. Motte, M. Proust, J. Torres, Y. Gobil, Y. Morand, J. Palleau, R. Pantel, and M. Juhel, "TiN-CVD process optimization for integration with Cu-CVD," *Microelectronic Engineering,* vol. 50, pp. 369-374, Jan 2000.

[14] W. L. Goh and K. T. Tan, "The use of electroless copper seed in electrochemical deposited copper interconnect," *Thin Solid Films,* vol. 462-463, pp. 275-278, 2004.

[15] Y. Tanaka, Z. Xu, P. Gopalraja, J. Forster, G. Yao, H. Zhang, J. Nulman, and F. Chen, "Sub-quarter micron metallization using ionized metal plasma (IMP) technology," *Vacuum,* vol. 51, pp. 729-733, 1998.

[16] E. Klawuhn, G. C. D'Couto, K. A. Ashtiani, P. Rymer, M. A. Biberger, and K. B. Levy, "Ionized physical-vapor deposition using a hollow-cathode magnetron source for advanced metallization," *Journal of Vacuum Science and Technology, Part A: Vacuum, Surfaces and Films,* vol. 18, pp. 1546-1549, 2000.

[17] O. R. Monteiro, "Novel metallization technique for filling 100-nm-wide trenches and vias with very high aspect ratio," *Journal of Vacuum Science & Technology B*, vol. 17, pp. 1094-1097, May-Jun 1999.

[18] P. Siemroth and T. Schulke, "Copper metallization in microelectronics using filtered vacuum arc deposition -- principles and technological development," *Surface and Coatings Technology*, vol. 133-134, pp. 106-113, 2000.

[19] S. M. Rossnagel, "Filling dual damascene interconnect structures with AlCu and Cu using ionized magnetron deposition," *Journal of Vacuum Science & Technology B: Microelectronics Processing and Phenomena*, vol. 13, pp. 125-129, 1995.

[20] P. F. Cheng, S. M. Rossnagel, and D. N. Ruzic, "Directional deposition of Cu into semiconductor trench structures using ionized magnetron sputtering," *Journal of Vacuum Science & Technology B: Microelectronics Processing and Phenomena*, vol. 13, pp. 203-208, 1995.

[21] C. A. Nichols, S. M. Rossnagel, and S. Hamaguchi, "Ionized physical vapor deposition of Cu for high aspect ratio damascene trench fill applications," *Journal of Vacuum Science and Technology B*, vol. 14, p. 3270, 1996.

[22] W. Wang, J. Foster, A. E. Wendt, J. H. Booske, T. Onuoha, P. W. Sandstrom, H. Liu, S. S. Gearhart, and N. Hershkowitz, "Magnetic-field-enhanced rf argon plasma for ionized sputtering of copper," *Applied Physics Letters*, vol. 71, pp. 1622-1624, 1997.

[23] P. J. Stout, D. Zhang, S. Rauf, and P. L. G. Ventzek, "Comparing ionized physical vapor deposition and high power magnetron copper seed deposition," *Journal of Vacuum Science & Technology B*, vol. 20, pp. 2421-2432, Nov-Dec 2002.

[24] S. Wickramanayaka, H. Nagahama, E. Watanabe, M. Sato, and S. Mizuno, "Using I-PVD for copper-based interconnects," *Solid State Technology*, vol. 45, pp. 67-68, 2002.

[25] "*http://www.novellus.com/products/product_lines/inova/inova.htm.*"

[26] B. S. Lim, A. Rahtu, and R. G. Gordon, "Atomic layer deposition of transition metals," *Nature Materials*, vol. 2, pp. 749-754, Nov 2003.

[27] A. U. Mane and S. A. Shivashankar, "Growth of (1 1 1)-textured copper thin films by atomic layer deposition," *Journal of Crystal Growth*, vol. 275, pp. e1253-e1257, 2005.

[28] H. Kim, A. J. Kellock, and S. M. Rossnagel, "Growth of cubic-TaN thin films by plasma-enhanced atomic layer deposition," *Journal of Applied Physics*, vol. 92, pp. 7080-7085, 2002.

[29] X. M. Chen, G. G. Peterson, C. Goldberg, G. Nuesca, H. L. Frisch, A. E. Kaloyeros, B. Arkles, and J. Sullivan, "Low-temperature chemical vapor deposition of tantalum nitride from tantalum pentabromide for integrated circuitry copper metallization applications," *Journal of Materials Research*, vol. 14, pp. 2043-2052, 1999.

[30] M. H. Tsai, S. C. Sun, C. P. Lee, H. T. Chiu, C. E. Tsai, S. H. Chuang, and S. C. Wu, "Metal-organic chemical vapor deposition of tantalum nitride barrier layers for ULSI applications," *Thin Solid Films*, vol. 270, pp. 531-536, 1995.

[31] S. Riedel, J. Rober, and T. Gessner, "Electrical properties of copper films produced by MOCVD," *Microelectronic Engineering*, vol. 33, pp. 165-172, 1997.

[32] K. Weiss, S. Riedel, S. E. Schulz, M. Schwerd, H. Helneder, H. Wendt, and T. Gessner, "Development of different copper seed layers with respect to the

copper electroplating process," *Microelectronic Engineering*, vol. 50, pp. 433-440, 2000.

[33] P. C. Andricacos, C. Uzoh, J. O. Dukovic, J. Horkans, and H. Deligianni, "Damascene copper electroplating for chip interconnections," *IBM Journal of Research and Development*, vol. 42, pp. 567-574, 1998.

[34] J. Reid, "Copper electrodeposition: Principles and recent progress," *Japanese Journal of Applied Physics, Part 1: Regular Papers and Short Notes and Review Papers*, vol. 40, pp. 2650-2657, 2001.

[35] T. Ritzdorf, L. Graham, S. Jin, C. Mu, and D. Fraser, "Self-annealing of electrochemically deposited copper films in advanced interconnect applications," in *Interconnect Technology Conference, 1998. Proceedings of the IEEE 1998 International*, 1998, pp. 166-168.

[36] S. Lagrange, S. H. Brongersma, M. Judelewicz, A. Saerens, I. Vervoort, E. Richard, R. Palmans, and K. Maex, "Self-annealing characterization of electroplated copper films," *Microelectronic Engineering*, vol. 50, pp. 449-457, 2000.

[37] M. Stangl, V. Dittel, J. Acker, V. Hoffmann, W. Gruner, S. Strehle, and K. Wetzig, "Investigation of organic impurities adsorbed on and incorporated into electroplated copper layers," *Applied Surface Science*, vol. 252, pp. 158-161, 2005.

[38] W. H. Teh, L. T. Koh, S. M. Chen, J. Xie, C. Y. Li, and P. D. Foo, "Study of microstructure and resistivity evolution for electroplated copper films at near-room temperature," *Microelectronics Journal*, vol. 32, pp. 579-585, 2001.

[39] J. M. Paik, Y. J. Park, M. S. Yoon, J. H. Lee, and Y. C. Joo, "Anisotropy of grain boundary energies as cause of abnormal grain growth in electroplated copper films," *Scripta Materialia*, vol. 48, pp. 683-688, 2003.

[40] M. S. Yoon, Y. J. Park, and Y. C. Joo, "Impurity redistributions in electroplated Cu films during self-annealing," *Thin Solid Films*, vol. 408, pp. 230-235, 2002.

[41] A. K. Sikder, A. Kumar, P. Shukla, P. B. Zantye, and M. Sanganaria, "Effect of multistep annealing on mechanical and surface properties of electroplated Cu thin films," *Journal of Electronic Materials*, vol. 32, pp. 1028-1033, 2003.

[42] G. B. Alers, D. Dornisch, J. Siri, K. Kattige, L. Tam, E. Broadbent, and G. W. Ray, "Trade-off between reliability and post-CMP defects during recrystallization anneal for copper damascene interconnects," in *Reliability Physics Symposium, 2001. Proceedings. 39th Annual. 2001 IEEE International*, Orlando, FL, 2001, pp. 350-354.

[43] S. Lakshminarayanan, P. Wright, and J. Pallinti, "Design rule methodology to improve the manufacturability of the copper CMP process," Burlingame, CA, USA, 2002, pp. 99-101.

[44] S. A. Lytle, S. Karthikeyan, I. O. Oladeji, T. J. Lee, H. M. Li, A. Zhang, K. G. Steiner, S. M. Merchant, M. Oh, S. W. Jessen, G. W. Gibson Jr, D. Ramappa, J. A. Taylor, T. Y. Tse, M. Hariharaputhiran, G. Hua, H. T. Kim, L. N. Mattern, N. Kamat, P. K. H. Chew, D. P. Chesire, S. H. Kang, S. C. Vitkavage, R. O. Adebanjo, T. M. Wolf, T. Kook, R. Y. S. Huang, A. Cuthbertson, S. J. Hillenius, and D. E. Ibbotson, "Overcoming Cu/CVD low-k integration challenges in a high performance interconnect technology," Washington, DC, 2001, pp. 611-614.

[45] L. Peters, "Copper barriers hold up under stress," in *Semiconductor International*. vol. 30, 2007, p. 51.

[46] H. Marom, J. Mullin, and M. Eizenberg, "Size-dependent resistivity of nanometric copper wires," *Physical Review B*, vol. 74, 2006.

[47] W. Steinhogl, G. Schindler, G. Steinlesberger, M. Traving, and M. Engelhardt, "Comprehensive study of the resistivity of copper wires with lateral dimensions of 100 nm and smaller," *Journal of Applied Physics*, vol. 97, 2005.

[48] F. Chen and D. Gardner, "Influence of line dimensions on the resistance of Cu interconnections," *IEEE Electron Device Letters*, vol. 19, pp. 508-510, 1998.

[49] S. M. Rossnagel and T. S. Kuan, "Alteration of Cu conductivity in the size effect regime," *Journal of Vacuum Science & Technology B: Microelectronics Processing and Phenomena*, vol. 22, pp. 240-247, 2004.

[50] W. Wu, S. H. Brongersma, M. Van Hove, and K. Maex, "Influence of surface and grain-boundary scattering on the resistivity of copper in reduced dimensions," *Applied Physics Letters*, vol. 84, pp. 2838-2840, 2004.

[51] Q.-T. Jiang, M.-H. Tsai, and R. H. Havemann, "Line width dependence of copper resistivity," in *International Interconnect Technology Conference, Proceedings of the IEEE 2001*, Burlingame, CA, USA, 2001, pp. 227-229.

[52] T. Takewaki, H. Yamada, T. Shibata, T. Ohmi, and T. Nitta, "Formation of giant-grain copper Interconnects by a low-energy ion-bombardment process for high-speed ULSIs," *Materials Chemistry and Physics*, vol. 41, pp. 182-191, Aug 1995.

[53] H. H. Hsu, K. H. Lin, S. J. Lin, and J. W. Yeh, "Electroless copper deposition for ultralarge-scale integration," *Journal of the Electrochemical Society*, vol. 148, pp. C47-C53, Jan 2001.

[54] V. M. Dubin, Y. ShachamDiamand, B. Zhao, P. K. Vasudev, and C. H. Ting, "Selective and blanket electroless copper deposition for ultralarge scale integration," *Journal of the Electrochemical Society*, vol. 144, pp. 898-908, Mar 1997.

[55] B. M. Basol, C. E. Uzoh, H. Talieh, D. Young, P. Lindquist, T. Wang, and M. Cornejo, "Electrochemical mechanical deposition (ECMD) technique for semiconductor interconnect applications," *Microelectronic Engineering*, vol. 64, pp. 43-51, 2002.

[56] P. Hyungsang, K. Wonyong, C. Seung-Man, P. Ki-Chul, K. Ho-Kyu, M. Joo-Tae, S. Kyuchan, L. Hyunbae, K. Ohgyum, and K. Sangwon, "Superfilling CVD of copper using a catalytic surfactant," in *International Interconnect Technology Conference*, Burlingame, CA, USA, 2001, pp. 12-14.

[57] T. Wang, P. Lindquist, S. Erdemli, E. C. Basol, R. Zhang, C. E. Uzoh, and B. M. Basol, "Characterization of copper layers grown by electrochemical mechanical deposition technique," *Thin Solid Films*, vol. 478, pp. 345-351, 2005.

[58] Y. Chonan, T. Komiyama, J. Onuki, T. Nagano, H. Akahoshi, T. Itabashi, T. Saito, and K. Khoo, "Filling a narrow and high aspect-ratio trench with electro-Cu plating," *Materials Transactions*, vol. 47, pp. 1417-1419, May 2006.

[59] T. Nguyen, L. J. Charneski, and S. T. Hsu, "Manufacturability of chemical vapor deposition of copper," *Journal of the Electrochemical Society*, vol. 144, pp. 2829-2833, Aug 1997.

[60] B. Cui, W. Wu, C. Keimel, and S. Y. Chou, "Filling of nano-via holes by laser-assisted direct imprint," *Microelectronic Engineering*, vol. 83, pp. 1547-1550, Apr-Sep 2006.

[61] L. J. Friedrich, D. S. Gardner, S. K. Dew, M. J. Brett, and T. Smy, "Study of the copper reflow process using the GROFILMS simulator," *Journal of Vacuum Science & Technology B: Microelectronics Processing and Phenomena*, vol. 15, p. 1780, 1997.

[62] K. Abe, Y. Harada, K. Hashimoto, and H. Onoda, "Formation of copper interconnects by the reflow of sputtered copper films," *Electronics and Communications in Japan Part Ii-Electronics*, vol. 79, pp. 105-114, Aug 1996.

[63] K. Mikagi, H. Ishikawa, T. Usami, M. Suzuki, K. Inoue, N. Oda, S. Chikaki, I. Sakai, and T. Kikkawa, "Barrier metal free copper damascene interconnection technology using atmospheric copper reflow and nitrogen doping in SiOF film," *International Electron Devices Meeting*, pp. 365-368, Dec 8-11 1996.

[64] T. Onishi, H. Fujii, T. Yoshikawa, J. Munemasa, T. Inoue, and A. Miyagaki, "Effects of the high-pressure annealing process on the reflow phenomenon of copper interconnections for large scale integrated circuits," *Thin Solid Films*, vol. 425, pp. 265-274, 2003.

[65] T. Onishi and T. Yoshikawa, "Application of high-pressure annealing process to dual damascene copper interconnections," *Materials Transactions*, vol. 43, pp. 1605-1614, 2002.

[66] L. J. Friedrich, S. K. Dew, M. J. Brett, and T. Smy, "Integrating system and feature scale models to study copper reflow," *Journal of Vacuum Science & Technology B: Microelectronics and Nanometer Structures*, vol. 17, pp. 186-193, 1999.

[67] T. Miyake, H. Petek, K. Takeda, and K. Hinode, "Atomic hydrogen enhanced reflow of copper," *Applied Physics Letters*, vol. 70, pp. 1239-1241, 1997.

[68] Y. L. Wu and Y. C. Hwang, "Deuterium post-metallization anneal of electrochemical-plated Cu film deposited on different barrier materials," *Thin Solid Films*, vol. 461, pp. 294-300, Aug 2004.

[69] K. K. Choi, J. H. Yun, and S. W. Rhee, "Effect of hydrogen remote plasma annealing on the characteristics of copper film," *Thin Solid Films*, vol. 429, pp. 255-260, Apr 2003.

[70] S. H. Kim and D. W. Kim, "Reflow characteristics of copper in an oxygen ambient," in *Advances in Nondestructive Evaluation, Pt 1-3*. vol. 270-273 Zurich-Uetikon: Trans Tech Publications Ltd, 2004, pp. 820-825.

[71] S. Y. Lee, S. H. Choi, J. Y. Kang, and C. O. Park, "Reflow of copper in oxygen anneal ambients," *Journal of Applied Physics*, vol. 88, pp. 5946-5950, 2000.

[72] S.-Y. Lee, D.-W. Kim, S.-K. Rha, C.-O. Park, and H.-H. Park, "Reflow of copper in an oxygen ambient," *Journal of Vacuum Science & Technology B: Microelectronics and Nanometer Structures*, vol. 16, pp. 2902-2905, 1998.

[73] W. L. Prater, E. L. Allen, W. Y. Lee, M. F. Toney, J. Daniels, and J. A. Hedstrom, "Reduction of resistivity in Cu thin films by partial oxidation: Microstructural mechanisms," *Applied Physics Letters*, vol. 84, pp. 2518-2520, 2004.

[74] H. Haberland, M. Mall, M. Moseler, Y. Qiang, T. Reiners, and Y. Thurner, "Filling of micron-sized contact holes with copper by energetic cluster impact," *Journal of Vacuum Science & Technology A: Vacuum, Surfaces, and Films*, vol. 12, pp. 2925-2930, 1994.

[75] P. Gatz and O. F. Hagena, "Cluster beams for metallization of microstructured surfaces," *Applied Surface Science*, vol. 91, pp. 169-174, Oct 1995.

[76] J. G. Partridge, S. A. Brown, A. D. F. Dunbar, R. Reichel, M. Kaufmann, C. Siegert, S. Scott, and R. J. Blaikie, "Templated-assembly of conducting antimony cluster wires," *Nanotechnology,* vol. 15, pp. 1382-1387, 2004.

[77] A. Awasthi, S. C. Hendy, P. Zoontjens, and S. A. Brown, "Reentrant Adhesion Behavior in Nanocluster Deposition," *Physical Review Letters,* vol. 97, p. 186103, 2006.

[78] H. Haberland, "Metal clusters and nuclei: some similarities and differences," *Nuclear Physics A,* vol. 649, pp. 415C-422C, Mar 1999.

[79] P. Jensen, "Growth of nanostructures by cluster deposition: Experiments and simple models," *Reviews of Modern Physics,* vol. 71, p. 1695, 1999.

[80] L. C. A. van den Oetelaar, A. Partridge, S. L. G. Toussaint, C. F. J. Flipse, and H. H. Brongersma, "A surface science study of model catalysts. 2. Metal-support interactions in Cu/SiO2 model catalysts," *Journal of Physical Chemistry B,* vol. 102, pp. 9541-9549, Nov 1998.

[81] G. A. Breaux, D. A. Hillman, C. M. Neal, R. C. Benirschke, and M. F. Jarrold, "Gallium cluster "magic melters"," *Journal of the American Chemical Society,* vol. 126, pp. 8628-8629, 2004.

[82] I. Shyjumon, M. Gopinadhan, O. Ivanova, M. Quaasz, H. Wulff, C. A. Helm, and R. Hippler, "Structural deformation, melting point and lattice parameter studies of size selected silver clusters," *European Physical Journal D,* vol. 37, pp. 409-415, Mar 2006.

[83] O. H. Nielsen, J. P. Sethna, P. Stoltze, K. W. Jacobsen, and J. K. Norskov, "Melting a Copper Cluster - Critical-Droplet Theory," *Europhysics Letters,* vol. 26, pp. 51-56, 1994.

[84] L. Wang, Y. Zhang, X. Bian, and Y. Chen, "Melting of Cu nanoclusters by molecular dynamics simulation," *Physics Letters A,* vol. 310, pp. 197-202, 2003.

[85] W. D. Kingery and M. Berg, "Study of the Initial Stages of Sintering Solids by Viscous Flow, Evaporation-Condensation, and Self-Diffusion," *Journal of Applied Physics,* vol. 26, pp. 1205-1212, 1955.

[86] J. Frenkel, *J. Phys.(U.S.S.R),* vol. 9, p. 385, 1945.

[87] F. A. Nichols and W. W. Mullins, "Morphological Changes of a Surface of Revolution Due to Capillarity-Induced Surface Diffusion," *Journal of Applied Physics,* vol. 36, pp. 1826-&, 1965.

[88] D. R. Lide, *CRC handbook of Chemistry and physics,* 84th ed. New York: CRC Press, 2004.

[89] S. P. Riege and C. V. Thompson, "Modeling of texture evolution in copper interconnects annealed in trenches," *Scripta Materialia,* vol. 41, pp. 403-408, Jul 1999.

[90] J. G. Speight, *Lange's Handbook of Chemistry,* 16th ed.: McGraw Hill, 2005.

[91] K. Maier, C. Bassani, and W. Schule, "Self-Diffusion in Copper between 359 and 632 Degrees C," *Physics Letters A,* vol. A 44, pp. 539-540, 1973.

[92] K. Hoehne and R. Sizmann, "Volume and surface self-diffusion measurements on copper by thermal surface smoothing," *Physica Status Solidi (a),* vol. 5, pp. 577-589, 1971.

[93] M. Yeadon, J. C. Yang, M. Ghaly, R. S. Averback, and J. Murray Gibson, "Novel interactions of supported clusters: contact epitaxy," *Materials Science and Engineering B,* vol. 67, pp. 76-79, 1999.

Chapter 6

Trench filling by nanoscale copper clusters

As described in Chapter 5, the manufacturers of semiconductor integrated circuits are actively looking for solutions for filling damascene trenches. Previously, the use of cluster beams for filling micron-scale holes with copper [1] and for the metallization of non-planar surfaces [2] have been demonstrated. However, up to date, there is no previous demonstration of the cluster filling process in high aspect ratio nanoscale trenches which are currently deployed for interconnects by industry.

This chapter presents a technology based on nanoscale cluster deposition for interconnect applications. The structures of the samples used are described in Section 6.1. The cluster depositions are demonstrated with an IGA source and a magnetron sputtering source, as illustrated in Section 6.2. Cluster properties such as cluster velocity and the reflection on different substrates are discussed in Section 6.3. Then, Section 6.4 presents the trench filling and Section 6.5 discusses the sintering of clusters within the trenches. The chapter concludes with a summary highlighting the potential of cluster deposition.

6.1 Sample structures

According to the latest International Technology Roadmap for Semiconductors (ITRS) 2007 [3], there will be a challenge in filling up the nanoscale trenches beyond the 25 nm technology node. However, for a process developer, it is very difficult to produce damascene structures with such small dimensions. For example, the wiring width (defined from the half pitch) of metal 1 in the 25 nm technology node is 68 nm [3]. Therefore, damascene structures for evaluating the metal 1 wires of such a dimension and with a suitable coating of diffusion barrier and seed layer are required. Although the electron beam lithography facility at the University of Canterbury is capable of patterning such dimensions, the etching and barrier/seed deposition requires

advanced processing tools which are only available in a few research centres. As a result, most of the development processes such as electro-deposition were evaluated in high aspect ratio trenches rather than narrow trenches that follow the ITRS roadmap [4-7]. Apart from the V-groove samples, the other samples with aspect ratios ranging from 1.4:1 to 5:1 were prepared by semiconductor manufacturers. The studies of trench filling on commercially prepared wafers could provide direct evidence of the feasibility of the technology. The wafers were supplied by Novellus Systems Inc., Applied Materials Inc. and Texas Instruments Inc., and were fabricated based on state-of-the-art wafer processing. This section briefly describes the fabrication of the V-groove samples and the trench structures of the commercially prepared samples.

Previously, the formation of mesoscale wires through self-assembly of antimony clusters was demonstrated in V-groove samples [8], therefore, the bouncing of copper clusters was studied in the V-groove samples in the initial stage. Figure 6-1 shows a schematic diagram of the V-groove sample fabrication: (a) photo-resist AZ1518 is spun on a three-inch wafer coated with silicon dioxide; (b) the photo-resist is exposed through a mask, developed and baked; (c) with the alternating 3.5 μm wide photo-resist lines, the wafer is subsequently etched using a buffered hydrofluoric (HF) acid solution (the oxide under the photo-resist strips is protected from etching in HF); (d) after etching the exposed oxide, the wafer is anisotropically etched by a KOH solution, leaving V-grooves on the wafer and (e) the photo-resist and the oxide are removed by piranha (H_2SO_4+H_2O_2) cleaning and a dilute HF cleaning before a new layer of SiO_2 is re-grown. The details of the process was described by Ayesh [9].

The commercially prepared wafers used in this study have different types of coatings: a tantalum nitride (TaN) barrier on SiO_2 trenches, ion-induced Atomic Layer Deposition (iALD) TaN barrier/ruthenium (Ru) barrier on low-k dielectric (CORAL^{TM}) trenches [15], and tantalum (Ta) barrier / copper seed on SiO_2 trenches, representing a selection of existing and future barrier/seed technologies as summarized in Table 6-1. There were trenches with different widths on the wafers; thus, the highest aspect ratio referred to the depth of the trenches divided by the narrowest width of the measured trenches. The thickness of the diffusion barrier layer and the copper seed layer were quoted by the suppliers but they were not the measured thickness on the patterned wafers.

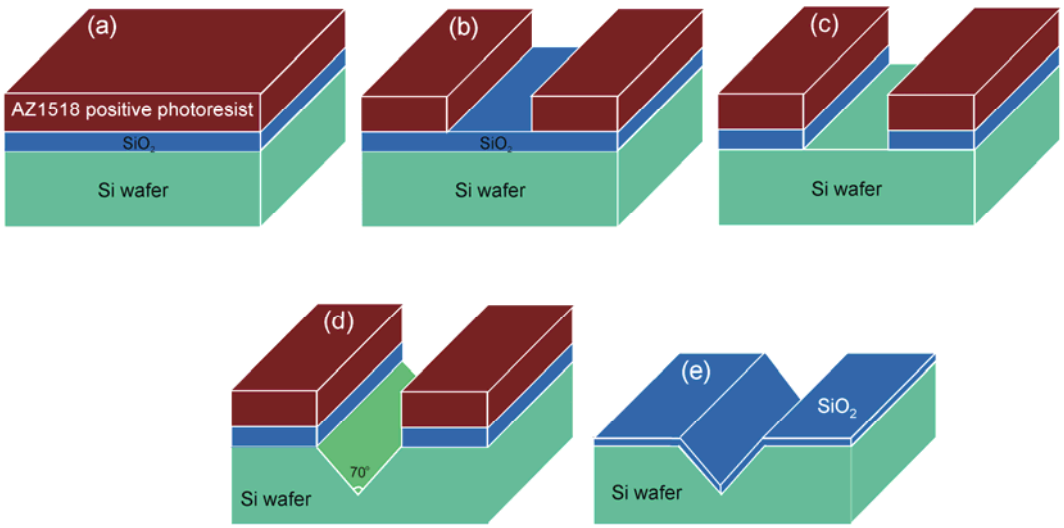

Figure 6-1: **Schematic diagram shows the V-groove fabrications. The dimensions in the figure are not scaled. The photo-resist was spun on the wafer (a), exposed and developed (b), SiO_2 etching (c), KOH etching (d), and growing a new SiO_2 layer (e). After Ayesh [9]**

In this study, the trench filling is analysed by cleaving the samples and cross-sectional SEM (XSEM) imaging. It is important for the structures to be long enough (for example, about a few millimetres) so that the location of the structure can be viewed by the naked eye and cut through by cleaving. There are some very narrow trenches on the wafers supplied, but not all of them could be used for XSEM. The structures used for XSEM are normally referred to as SEM bars. The SEM bars are grouped by structures with different lines and spaces. The width of the lines is the width of the damascene trenches and the space refers to the spacing between the trenches. The pitch is defined as the line width plus the spacing. Figure 6-2 shows a top view SEM of the SEM bar structures on a CU sample. Each group has about 8-15 trenches. Table 6-2 summarises the line, the space and the pitch of these structures.

Table 6-1: **Details of the three different dielectric, diffusion barrier and copper seed layer combination used prior to deposition.**

Sample code	Dielectric	Trench depth (nm)	Highest aspect ratio	Ta based-Barrier /thickness	Cu Seed /thickness	Supplier
TaN	SiO_2	1000	5:1	1000 Å TaN	-	Novellus
RU	CORAL™	340	3.5:1	25 Å TaN and 25 Å Ru	-	Novellus
CU	SiO_2	120	1.4	250 Å Ta	1000 Å	Texas Instruments

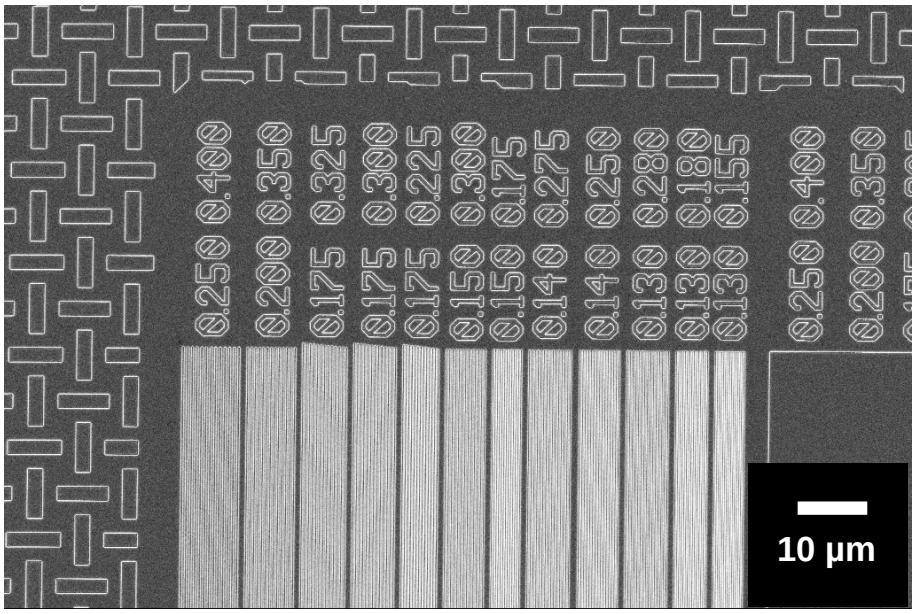

Figure 6-2: **SEM (Top view) of SEM bar structures on the CU samples. The line and space are labelled at each end of the SEM bars.**

Table 6-2: **The line, the space and the pitch of the SEM bars on the CU samples. The line and space are obtained from Figure 6-2.**

No	line (µm)	space (µm)	pitch
1	0.25	0.4	0.65
2	0.2	0.35	0.55
3	0.175	0.325	0.5
4	0.175	0.3	0.475
5	0.175	0.225	0.4
6	0.15	0.3	0.45
7	0.15	0.175	0.325
8	0.14	0.275	0.415
9	0.14	0.25	0.39
10	0.13	0.28	0.41
11	0.13	0.18	0.31
12	0.13	0.155	0.285

Figure 6-3 shows an XSEM image of a TaN sample. All the trenches in the sample are 1 µm deep. The narrowest width of the trenches is 200 nm, therefore, the highest aspect ratio in this work is 5:1. Since TaN reflects more electrons than the dielectric, it appears brighter in the XSEM. The sidewall coverage and the step coverage (see their definition in Section 5.2.3) were both about 30 %. From the XSEM images, the slope the trenches θ could be measured, as shown in Figure 6-4. It appears that the narrower the trenches, the steeper the sidewalls. Since the narrowest trenches are the most critical structures

for filling, the collection of clusters from the slope of V-grooves is different from these trenches. Thus, it is certainly valuable in assessing these structures.

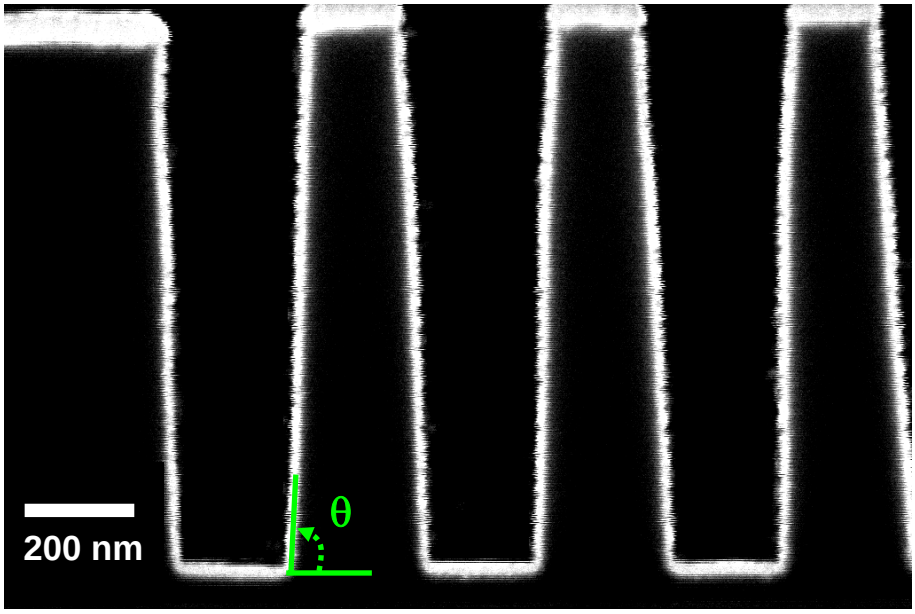

Figure 6-3: **XSEM of a TaN sample. The patterned SiO_2 trenches are coated with TaN diffusion barrier (bright region). The sidewall coverage and the step coverage of the diffusion barrier are both about 30 %. The trench slope is defined by θ.**

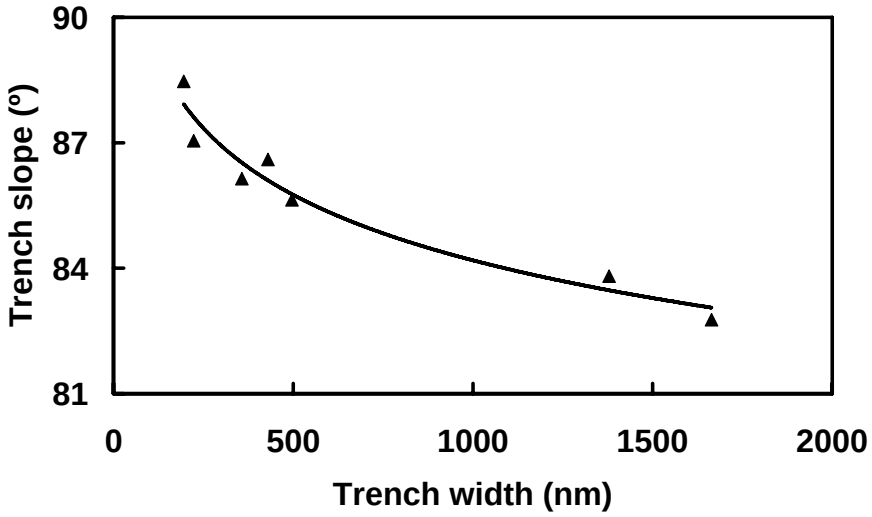

Figure 6-4: **Trench slope θ measured using XSEM as a function of the trench width for a TaN sample. It appears that the narrower the trenches, the steeper the sidewalls.**

Figure 6-5 shows an XSEM of a RU sample (see Table 6-1). The patterned CORAL™ trenches are coated with TaN/Ru diffusion barriers. The diffusion barriers are not visible because they are thinner than 5 nm. Due to the low mechanical strength and the low electrical conductivity of the dielectric, the charging from the electrons of the SEM

creates enough local heating and deforms the films. A similar phenomenon was observed in polymers [10].

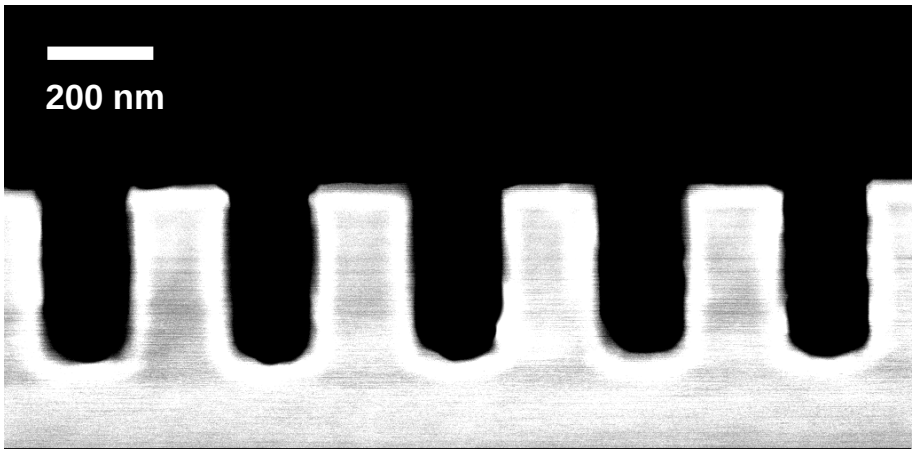

Figure 6-5: **XSEM of a RU sample. The patterned CORAL™ trenches are coated with TaN/Ru diffusion barriers. The diffusion barriers are not visible because they are thinner than 5 nm.**

Figure 6-6 shows an XSEM image of a CU sample (see Table 6-1). The tantalum diffusion barrier, which has a different texture than copper, is visible under the SEM. Although, the copper seed layer has filled half of the SiO_2 trenches, making the trenches less than ideal for the evaluation of filling, the samples are adequate for demonstration of the sintering process.

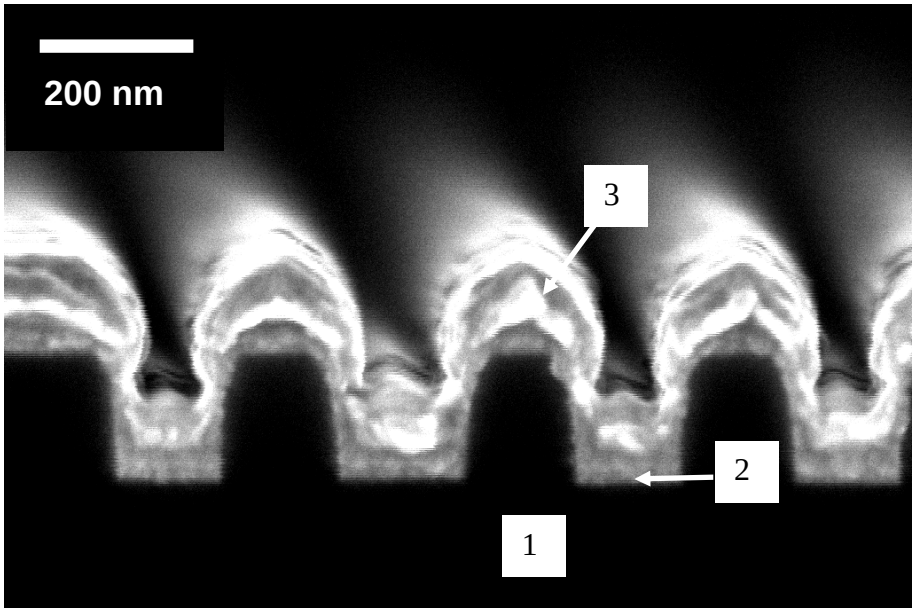

Figure 6-6: **XSEM of the CU sample. Labels 1, 2 and 3 denote the SiO_2 dielectric, the Ta diffusion barrier and the copper seed layer respectively.**

6.2 Experimental procedure

In this work, nanoscale copper clusters were generated in an ultra-high-vacuum compatible system (operating pressure ~10^{-6} Torr) with either an IGA source or a magnetron sputtering source. The source chamber of both systems is cooled by water. In the IGA source, the copper pellet was of 99.9999 % purity and the copper target in the magnetron sputtering source was of 99.99 % purity.

6.2.1 UHV IGA system

During the experiment, the C-type thermocouple in the source broke several times; thus, the deposition was controlled by increasing the power injected to the filament until the deposition rate reached 1 $Ås^{-1}$. The argon flow rate was set between 185 and 250 sccm. At 250 sccm argon flow, the pressure at the mass filter chamber (see Chapter 2) was approaching the limit of the turbo-pump (~ 1×10^{-3} Torr). Hence, the range of the argon flow rate was limited by the pumping capability of the system. The first stage nozzle was 4 cm long and had a 1.14 mm straight-through hole. The aggregation length, the distance between the centre of the crucible and the entrance of the first stage nozzle, was 6 cm.

The filling of the trenches in one TaN sample using the IGA source was only meant to prove that the filling of the copper cluster deposition was achievable in the IGA source. The IGA source was also used for the characterisation of the resistivity in Chapter 7. In this chapter, most of the samples were deposited by using the magnetron sputtering source.

6.2.2 UHV Magnetron sputtering source system

In experiments, 100 W DC power was applied to the sputter head and the aggregation length was 11 cm, unless otherwise stated. An argon/helium mixture (< 1ppm impurities) was introduced into the source chamber to generate a plasma, to assist in the cluster aggregation, and to transport the clusters towards the exit of the source. The clusters were accelerated by the gas as it expanded through a throated nozzle (de Laval nozzle) into the ultra-high-vacuum chamber [11]. Figure 6-7 shows a schematic of the de Laval nozzle, the working principle of which was described by Falkovich *et al.* [12].

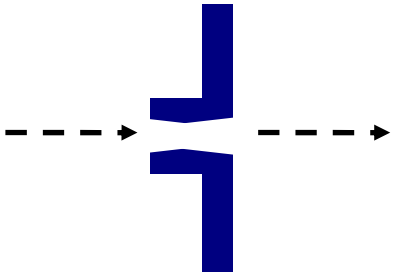

Figure 6-7: Schematic of the de Laval nozzle. The diameters of the entry and exit holes are 0.49 cm and 0.55 cm respectively. The diameter of the throat is 0.33 cm.

In the magnetron sputtering source, the argon flow rate could be increased to as high as 800 sccm without causing a problem for the turbo pump, because of the use of the de Laval nozzle. With a 0.33 cm diameter hole and a diverging exit, the gas was expected to expand and therefore the gas was separated from the cluster beam by the skimmer (the third nozzle) between the second stage and the mass filter chamber. In this case, most of the gas could be pumped away by the Roots pump at the second stage before entering the mass filter chamber.

When 1000 V was applied to the deflector (described in Section 2.3), the deposition rate reduced to one third. Therefore, approximately one third of the clusters deposited onto the samples were neutral and roughly the same proportions were positively or negatively charged. Similar ratios were also measured in Ref. [13].

6.3 Cluster characterisation

Before investigating the filling of clusters in different trenches, the clusters generated by the IGA source and the magnetron sputtering source were characterised. This section describes the cluster properties, such as cluster diameter, cluster velocity, the reflection of clusters on different surfaces and the bouncing of clusters in V-grooves. The cluster diameters were analysed by using XSEM and mass filter and the cluster velocity was measured by the deflector (see Section 2.3).

6.3.1 Cluster diameter

First the relation between the cluster diameter and the argon flow rates (185 and 250 sccm) using the IGA source were studied. Figure 6-8 shows an SEM image of the copper clusters deposited using the IGA source at 250 sccm argon flow. The cluster diameter ranged from 20 to 60 nm. Coalescence of clusters was also observed in the film. Figure 6-9 shows an SEM of the clusters produced at 185 sccm argon flow. The mean and the standard deviation of the cluster diameters, calculated from twenty randomly picked clusters in the SEM image, were 44 nm and 12 nm respectively. A high resolution TEM with clusters deposited at 185 sccm argon flow on an amorphous carbon TEM grid in Figure 6-10, shows that the clusters have a 2 nm oxide shell (after four weeks in the atmosphere). The oxide shell can be easily identified because of larger lattice spacing (~4.3 Å) compared to the copper (~3.6 Å) [14].

Using the magnetron sputtering source, clusters produced at different gas flows were compared. Figure 6-11 shows the diameter of the clusters deposited at an 800/0 Ar/He flow is around 15 ± 5 nm measured from the SEM image. As it was difficult to measure the exact cluster diameter by the SEM at these dimensions, a different approach was taken. Figure 6-12 shows the size distributions of the copper ions at three different gas flows measured by using the mass filter. The signal intensity was corrected by dividing the measured signal by the mass of the clusters (see Section 2.2 in Chapter 2 for details). The maximum peak of the distribution shifted from 13.5 nm to 12.8 nm when

the argon flow was reduced from 800 sccm to 600 sccm. The reduction of the cluster diameter was not significant. However, by introducing 100 sccm helium to 600 sccm argon flow, the peak of the size distribution was reduced to 8 nm. Therefore, the effect of the helium on cluster diameter was quite significant. The next section will discuss the cluster velocity in the argon and helium mixtures.

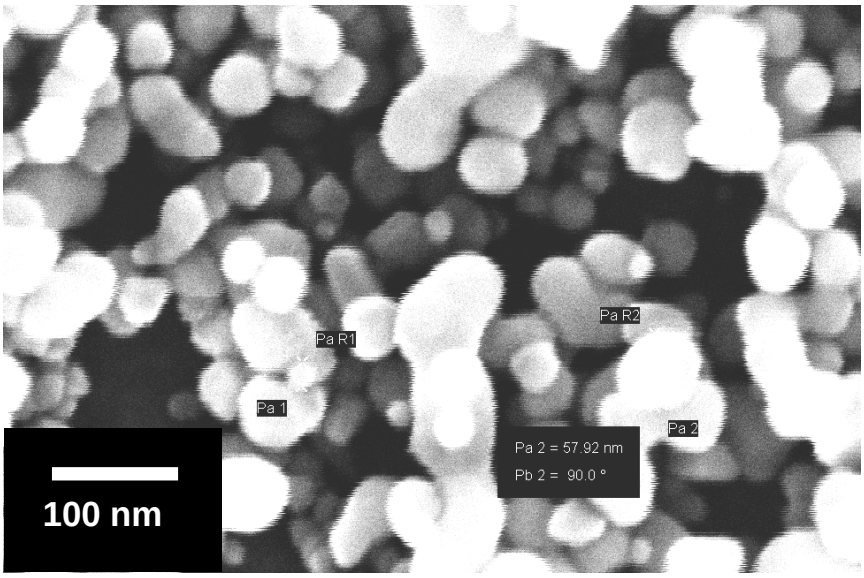

Figure 6-8: **Clusters ranging from 20 to 60 nm in diameter were produced by the IGA source at 250 sccm argon flow.**

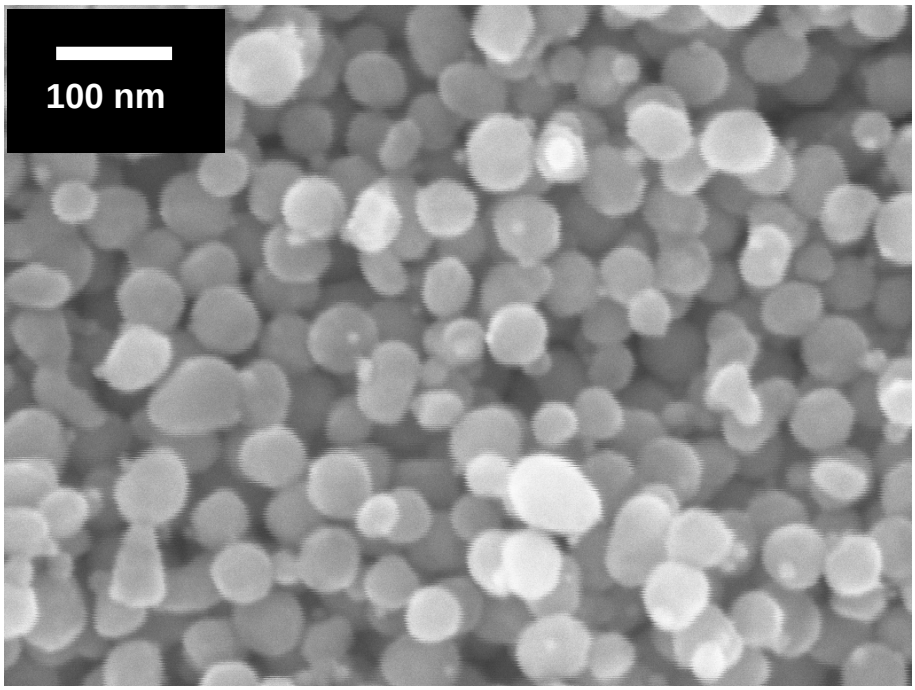

Figure 6-9: **Cu clusters generated in the IGA source at 185 sccm argon flow. The diameter of the clusters is 43 ± 12 nm.**

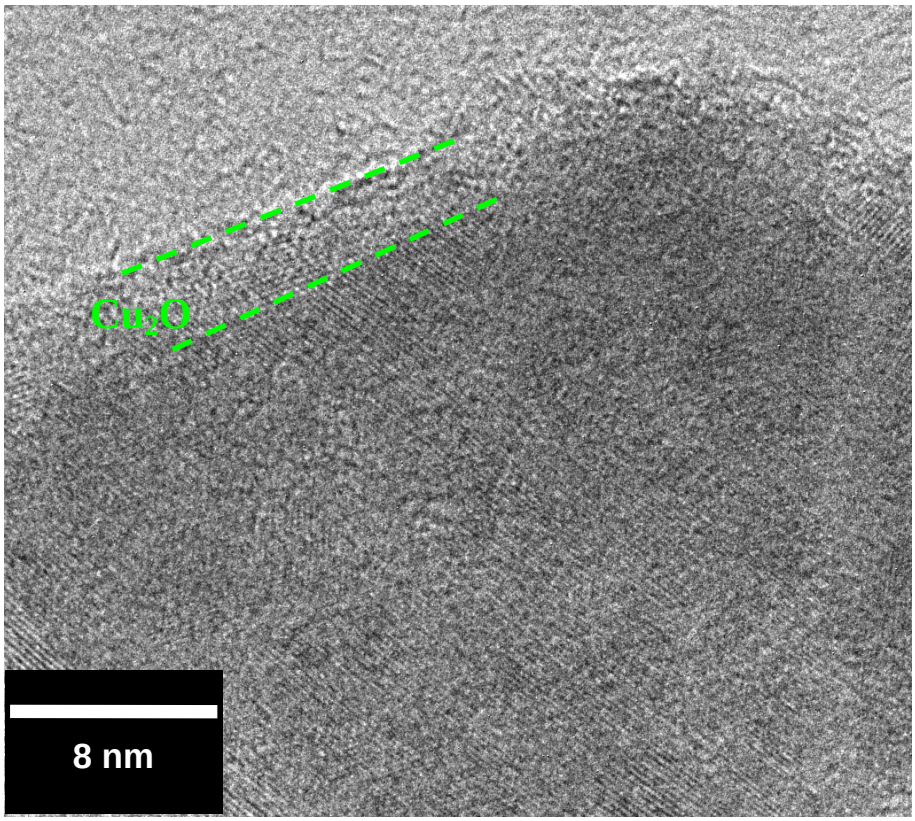

Figure 6-10: **High resolution TEM image of a copper cluster, showing the oxide shell of 2 nm thickness.**

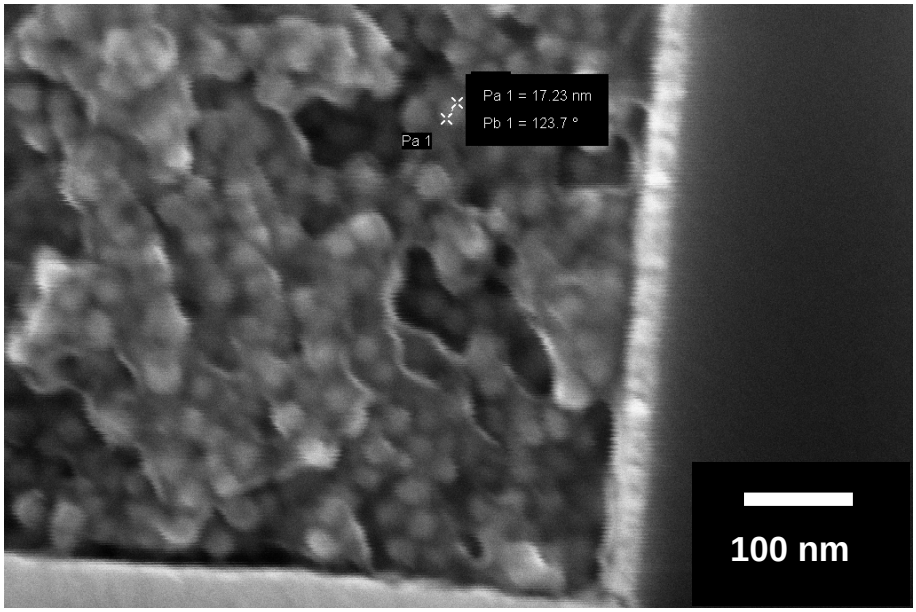

Figure 6-11: **XSEM showing clusters generated in the magnetron sputtering source at 800/0 Ar/He flows. The surface of the sample was covered with photo-resist to ensure that the clusters were not disturbed during cleaving and inspection. Most likely the clusters were not oxidized after the air exposure.**

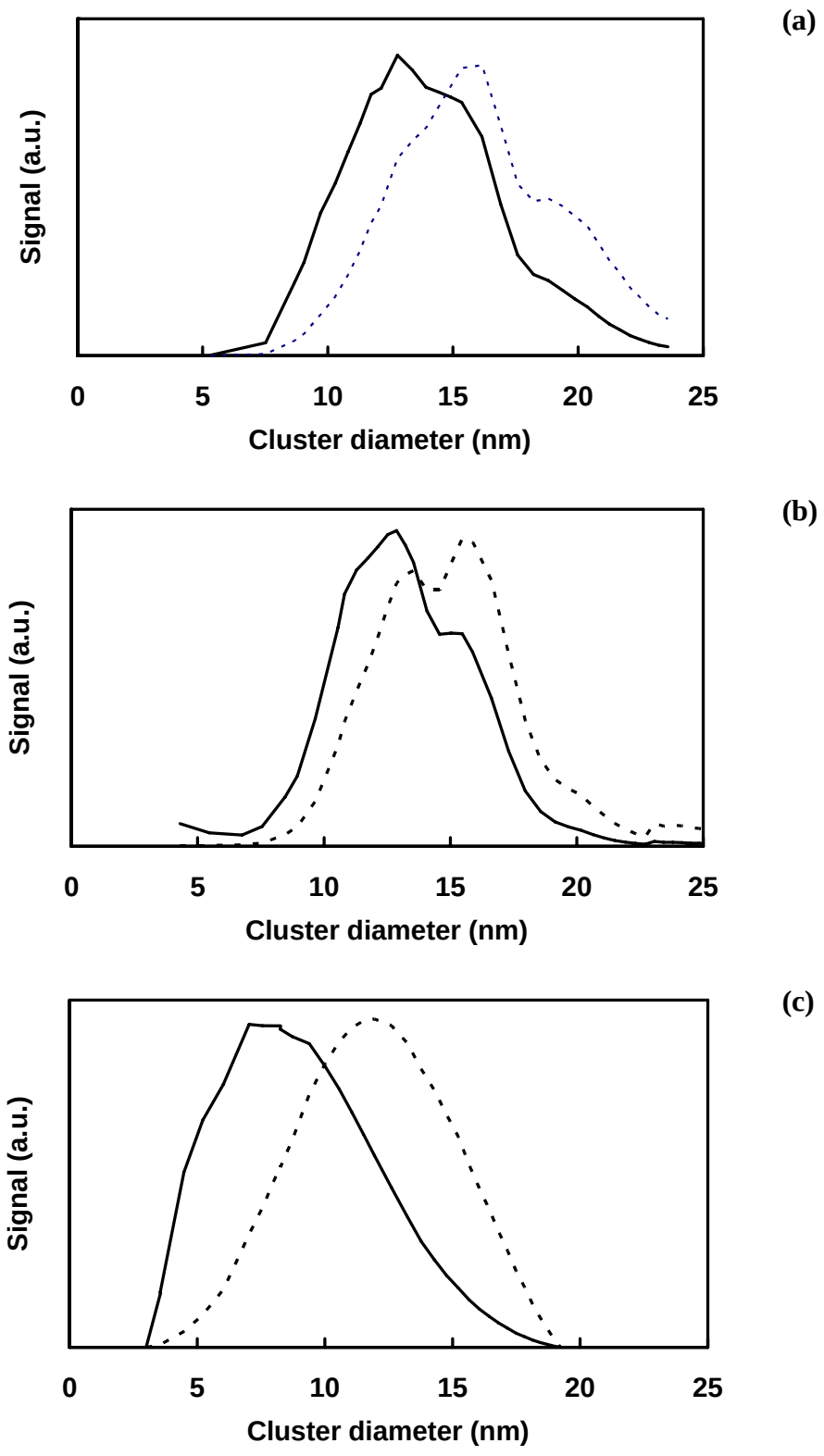

Figure 6-12: **The size distribution of the copper ions at different Ar/He flow ratios: (a) 800/0, (b) 600/0, (c) 600/100. The signal measured by using a mass filter (dashed line) is compared with the corrected signal (solid line) in arbitrary units.**

6.3.2 Cluster velocity

As described in Section 6.2.2, two thirds of the clusters were ionised in the magnetron sputtering source, therefore enabling the velocity measurements of the clusters. This section discusses the cluster velocity from the measurement, and the calculation of the velocity of the gas molecules.

The operation of the deflector was described in Chapter 2. Notably, the velocity of the clusters could be calculated by dividing the distance between the deflector and the Faraday cup over the time delay between the input and output pulses measured by an oscilloscope. The period between pulses was set at 9 ms and the width of the pulse was set at 600 μs.

Table 6-3 shows the process conditions used for the cluster velocity measurements. The main process parameters were argon flow rate and helium flow rate. The power and the aggregation length L_{agg} varied from run to run, but they should not affect the cluster velocity. Except for deposition 700/50, all the measurements consisted of more than 25 data points.

Figure 6-13 shows the cluster velocity measured by the deflector as a function of the pulse voltage applied to the deflector at 600 sccm argon flow. The DC power to the magnetron sputtering source was 100 W and the L_{agg} was 10 cm. The clusters of a given mass could be selected by controlling the magnitude of the voltage pulses. By applying 180V, the velocity of ~15 nm clusters could be measured.

Figure 6-14 shows the velocity of ~15 nm clusters measured by the deflector as a function of Ar/He gas flows. For the same helium flows (0 or 100 sccm), the cluster velocity did not increase significantly as the argon flow increased. However, by increasing the helium flow from 0 to 100 sccm, the cluster velocity increased from 250 ms^{-1} to 300 ms^{-1}. Therefore, the helium flow rate was the main factor influencing the cluster velocity.

Table 6-3: Process conditions used for cluster velocity measurements.

Deposition	Ar flow rate (sccm)	He flow rate (sccm)	Power (W)	L_{agg} (cm)	# of data point
600/0	600	0	80-100	10-12	36
800/0	800	0	80-100	10-12	35
700/50	700	50	90	11	9
600/100	600	100	80-100	10-12	40
800/100	800	100	80-100	10-12	30

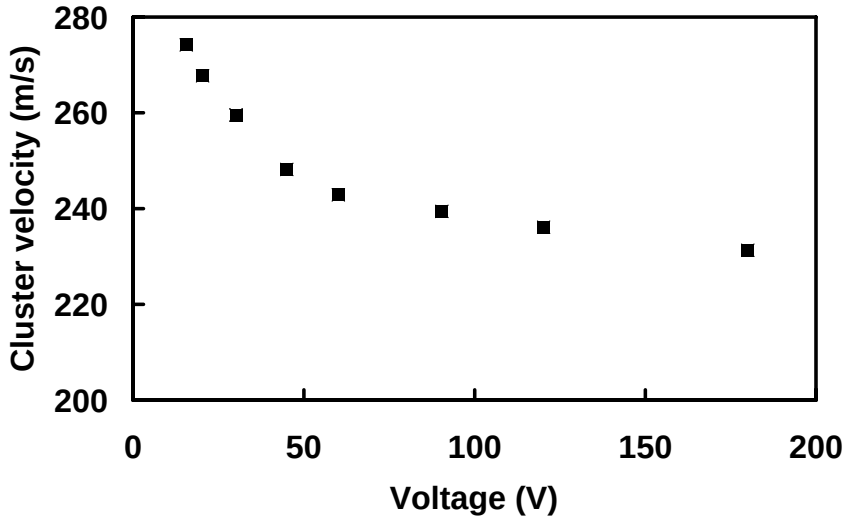

Figure 6-13: Cluster velocity measured by the deflector as a function of the pulse voltage applied to the deflector at 600 sccm Ar flow only. The DC power of the deposition was 100 W and the aggregation length was 10 cm.

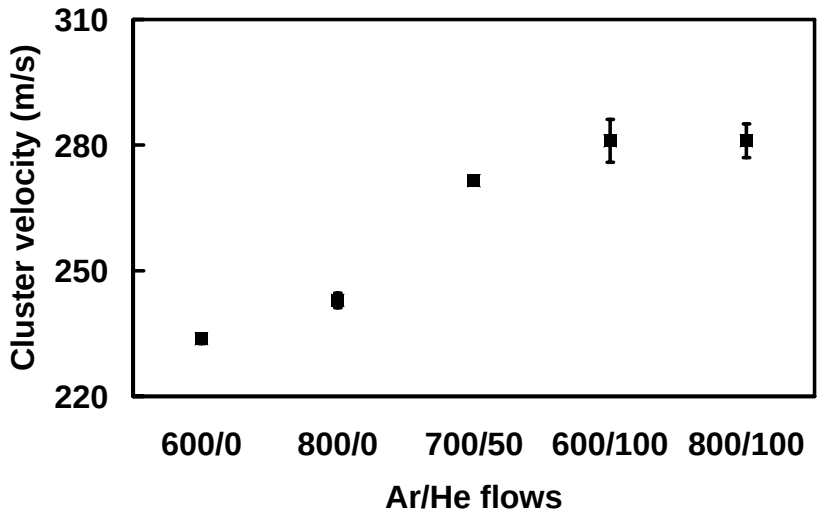

Figure 6-14: Cluster velocity measured by the deflector as a function of Ar/He gas flows. Clusters with ~15 nm diameter were selected.

Using *Eq. 4-8* from Chapter 4, the velocity of the gas can be estimated. Table 6-4 summarises the flow rate, the source pressure and the calculated gas velocity. Clearly, there was a discrepancy between the cluster velocity and the gas velocity calculated by using *Eq. 4-8,* especially when helium was introduced. Thus, a different method of velocity calculation was used.

Table 6-4: Calculation of gas velocity using *Eq. 4-8*.

Ar flow rate (sccm)	He flow rate (sccm)	Total flow rate (sccm)	Source pressure (Torr)	Nozzle diameter (mm)	Cal. gas velocity (ms^{-1})	Measured cluster velocity (ms^{-1})
600	0	600	2.25	3.32	390	234
600	100	700	3.19	3.32	321	281
700	50	750	3.19	3.32	345	272
800	0	800	2.84	3.32	412	243
800	100	900	3.72	3.32	354	281

Since the de Laval nozzle was used in the experiment, the gas is expected to accelerate when it is compressed through the throat of the nozzle. As the gas enters a nozzle, it travels at subsonic velocities. As the throat contracts down the gas is forced to accelerate until at the nozzle throat, where the cross-sectional area is the smallest, the gas will travel at a transonic speed (about mach 0.8-1.2). From the throat the cross-sectional area then increases, the gas expands and the linear velocity becomes progressively more supersonic. Therefore the equation of the gas velocity at the nozzle exit is given by [15-17] :

$$v_e = \sqrt{\frac{TR}{M} \times \frac{2k}{k-1} \times \left[1 - \left(\frac{P_e}{P}\right)^{(k-1)/k}\right]} \qquad (Eq.\ 6\text{-}1)$$

where

- v_e is exhaust velocity at nozzle exit, m/s
- T is absolute temperature of inlet gas, K
- R is universal gas law constant, 8314.5 J/(kmol.K)
- M is the gas molecular mass, kg/kmol (also known as the molecular weight)
- k is the specific heat ratio, c_p/c_v, and also an isentropic expansion factor. k is ~ 1.666 at 300K for Ar and He. Ref. [14, 18]
- c_p is specific heat of the gas at constant pressure
- c_v is specific heat of the gas at constant volume
- P_e is absolute pressure of exhaust gas at nozzle exit, which is also the pressure at

the second pumping stage, Pa

P is absolute pressure of inlet gas, Pa

In the case of the mixture of argon and helium gases as the cooling gas for the aggregation, the mean molecular weight M^* is often used. M^* is given by:

$$M^* = \frac{M_1F_1 + M_2F_2}{F_1 + F_2} \qquad (Eq.\ 6\text{-}2)$$

where F_1 and F_2 are the flows of argon and helium respectively, and M_1 and M_2 are 40 and 4 (the molecular weights of argon and helium) respectively.

Figure 6-15 shows the calculated gas velocity using *Eq. 6-1*. Although the absolute value of the velocity is higher than the cluster velocity shown in Figure 6-14, the trend is very similar. Due to the acceleration of gas molecules in the de Laval nozzle, the calculation of the gas velocity using *Eq. 6-1* describes the properties of the clusters better than *Eq. 4-8*. In the de Laval nozzle, the gas molecules were travelling at a supersonic speed, therefore it is understandable that the clusters could not match the speed of the gas molecules. The slip (defined by the ratio of the cluster velocity and the gas velocity) was about 50 %.

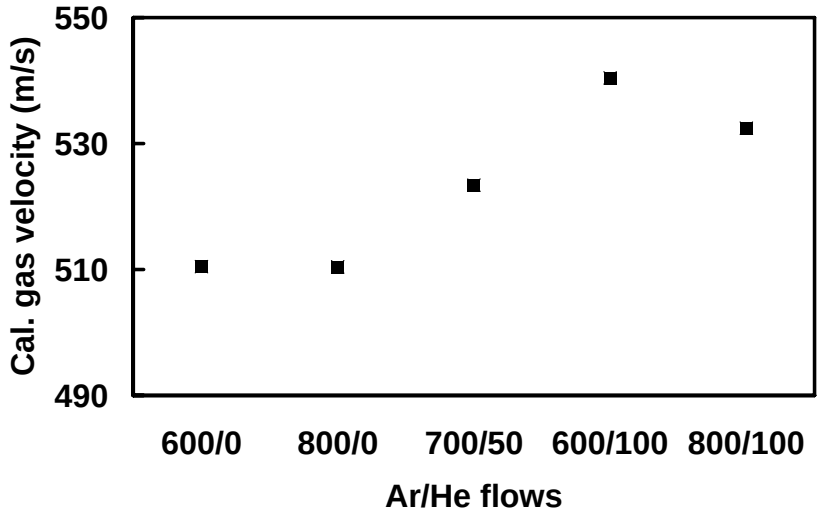

Figure 6-15: Calculated gas velocity as a function of gas flows, using *Eq. 6-1*.

6.3.3 Reflection of clusters on planar surfaces

In order to study the reflection of clusters on different surfaces, an experiment was conducted by placing four different substrates in close proximity. As illustrated in Figure 6-16, a Ru sample, a Cu sample and a SiO_2 sample were placed on each unpatterned TaN sample. SEM images were taken at the highlighted region so that the cluster distribution and the bouncing were not affected by any non-uniformity in the cluster beam. Using 800 sccm argon flow, the samples were deposited for different durations. Based on the coverage of the surfaces, the reflectivity of Cu clusters on these substrates followed this order: TaN > Cu > Ru > SiO_2, as shown in Figure 6-17. The clumping of clusters was observed on TaN and Cu samples, which was very similar to the bouncing Sb discussed in Section 4.3.2, indicating that the clusters bounced away from the substrate and only adhered to the surface defects or other clusters on the surface.

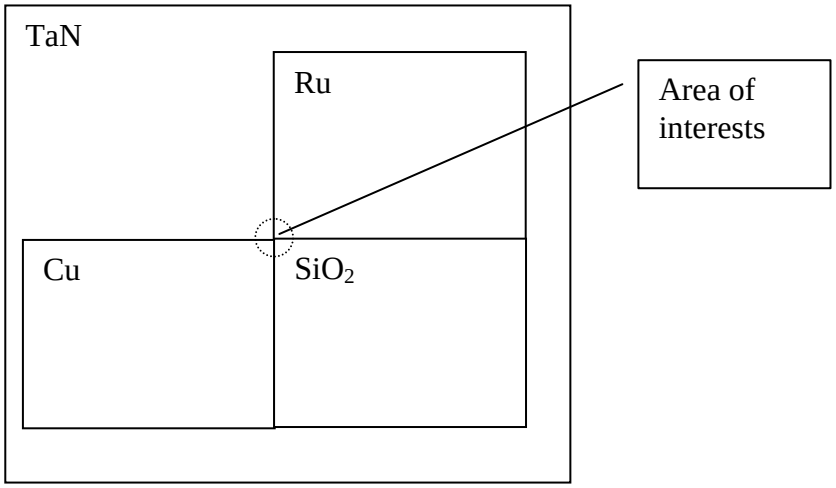

Figure 6-16: Schematic drawing of the reflectivity setup.

Another deposition was conducted by pre-annealing the sample in H_2 at 200ºC for 30 minutes before cluster deposition. As shown in Figure 6-18, there was not such significant clumping of clusters on TaN and Cu samples (compared to Figure 6-17). The order of the cluster-substrate reflectivity changed to: Ru > TaN > SiO_2 > Cu, with much smaller differences than in Figure 6-17. It was hypothesized that the change of reflectivity could be caused by the reduction of the surface defects or the reduction of water molecules on the surfaces; in the case of air-exposed metals, the ruthenium native oxide and copper native oxide could be reduced.

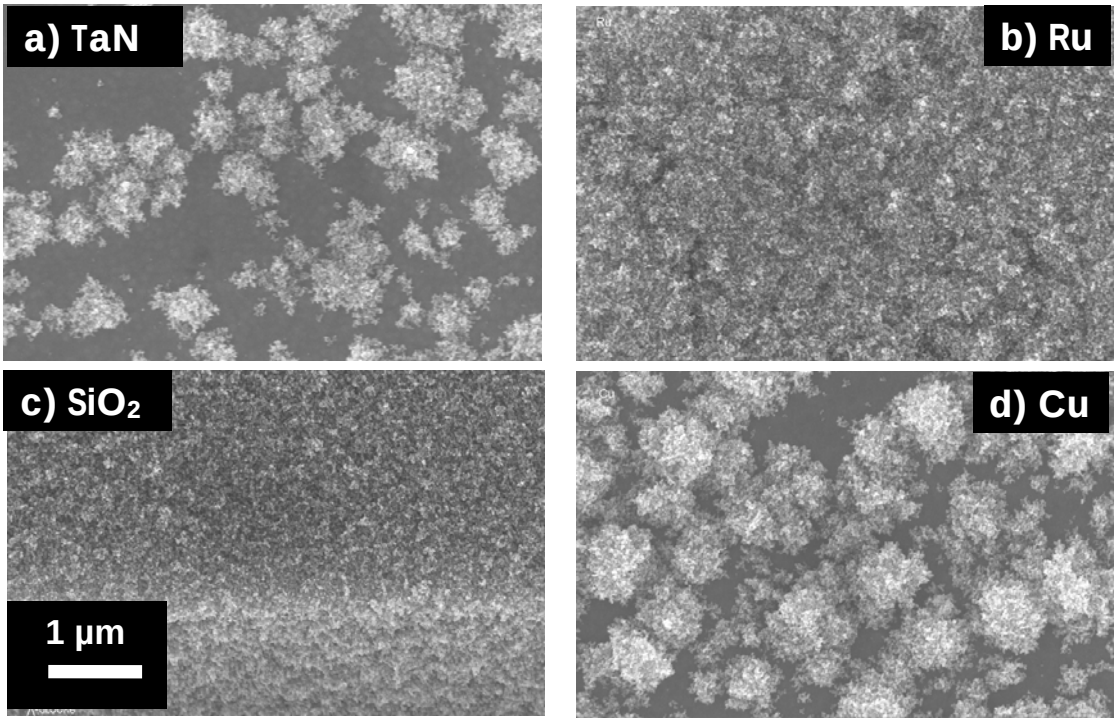

Figure 6-17: **Deposition of clusters on four different substrates: (a) TaN, (b) Ru, (c) SiO_2 and (d) Cu. The clusters were deposited at 800 sccm argon flow with 0.8 $Ås^{-1}$ deposition rate for 40 minutes. The order of cluster-substrate reflectivity is (from highest to lowest): TaN > Cu > Ru > SiO_2.**

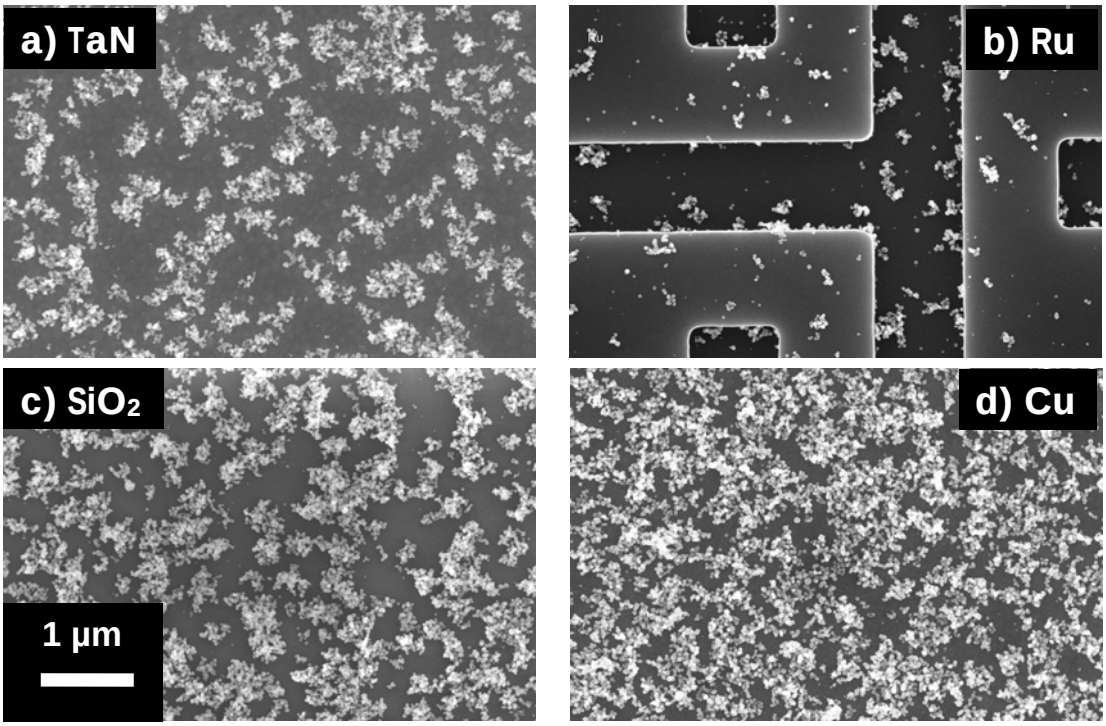

Figure 6-18: **Deposition of clusters on four different pre-annealed substrates: (a) TaN, (b) Ru, (c) SiO_2 and (d) Cu. The samples were subjected to hydrogen pre-annealing at 200°C for 30 minutes before the cluster deposition. The clusters were deposited at 800 sccm argon flow with 0.4 $Ås^{-1}$ deposition rate for 20 minutes. The order of cluster-substrate reflectivity is (from highest to lowest): Ru > TaN > SiO_2> Cu.**

6.3.4 Bouncing of clusters on oblique surfaces

Since the bouncing behaviour varies depending on the substrate, it would be interesting to examine the bouncing behaviour when the clusters are deposited at an angle to the substrate. This sub-section discusses the bouncing properties of clusters on two different oblique surfaces: a) V-grooves and b) TaN trenches.

As demonstrated by Partridge *et al*. [8], bismuth nanowires and antimony nanowires could be formed by using V-grooved Si substrates and a momentum driven assembly of bismuth and antimony clusters. In this work, an experiment was conducted to form copper nanowires similar to Ref. [8]. A sample was prepared with V-grooves of about 3.8 µm width. Figure 6-19 shows an excellent selectivity between the plateau and inside the V-groove, using 800/0 Ar/He flow ratio in the magnetron sputtering source. The selectivity is defined by the number of clusters in the V-groove compared to the number of clusters on the plateau. The clusters bounced away from the top SiO_2 surface but slid along the sidewall of the V-groove and collected at the apex of the V-groove. With 3 minutes of deposition at 1.1 $Å s^{-1}$, a 1.7 µm wide wire was formed.

An interesting experiment was conducted to deposit the clusters on a TaN sample at an angle. The sample was placed at an angle to the cluster beam by rotating the sample arm. Clusters were produced at 800 sccm argon flow. Figure 6-20 shows the oblique deposition of copper clusters when the sample was tilted at a 22.5±5º angle. There were four interesting observations: a) accumulation of clusters, b) shadowing, c) re-deposition after first bouncing and d) re-deposition after second bouncing. For the surfaces directly exposed to the cluster beam, the clusters accumulated on one side of the trenches. Because the sample was tilted, certain locations of the trenches were shadowed by the sidewalls, thus, there were no clusters in region (b). Although some regions should be shadowed by the sidewalls, clusters were deposited due to the bouncing from the sidewalls of the trenches (c-d). In the next section, the unique bouncing properties of clusters will be used for the trench filling application.

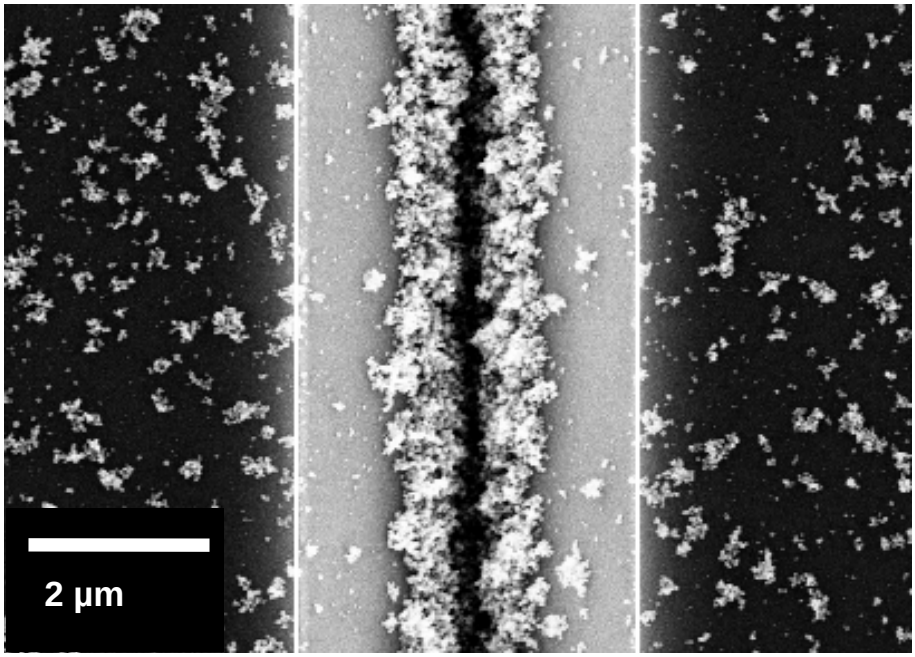

Figure 6-19: **Excellent selectivity between the plateau and in the V-groove, using 800/0 Ar/He flow ratio in the magnetron sputtering source. The sample was deposited at 1.1 Ås^{-1} for 3 minutes. The dark strip in the V-groove is an artefact of the SEM imaging.**

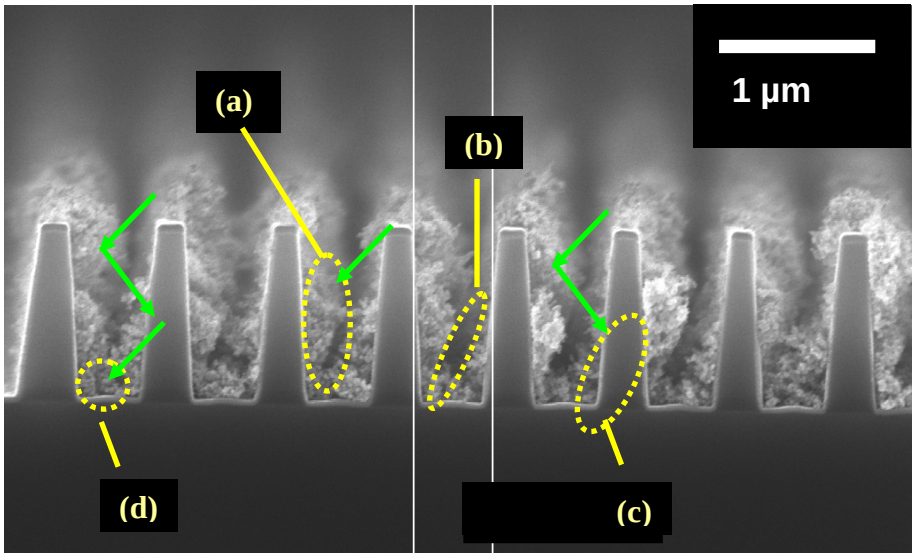

Figure 6-20: **Oblique deposition at 22.5º such that the clusters bounced along the side wall. Trench width of 496.8nm. Four different behaviours were observed: (a) accumulation, (b) shadowing, (c) re-deposition after first bouncing and (d) re-deposition after second bouncing. The green arrows indicate the directions of the cluster movement.**

6.4 Trench filling

This section presents the filling of copper clusters into various patterned samples. All the samples were deposited in the magnetron sputtering source unless otherwise stated. In this study, there were more than 50 TaN samples, 10 RU samples and 30 CU samples deposited with different gas flows, different DC power and different substrate temperatures. For simplicity, only some of the typical examples are presented in this chapter. The TaN samples had the highest aspect ratio and therefore were the most difficult structures for filling among the samples listed in Table 6-1.

Initially, the TaN samples were deposited with argon flow rate between 100 sccm and 600 sccm. The range of the DC power was varied between 25 and 100 W. A high DC power (> 100 W) was not obtainable because the sputtering source experienced some electric arcing problems. The effect of DC power on the filling performance was not significant compared to the gas flow. In order to have a reasonable deposition rate, a DC power of 100 W was used. Figure 6-21 shows copper clusters deposited at 400 sccm argon flow. It was obvious that the clusters did not fill the trenches with both 800 nm and 300 nm widths. In fact, the way the clusters adhered on the sidewalls of the trenches or to the other clusters and formed a Christmas-tree-like structure was very similar to the “sticky ball” model proposed by Haberland *et al.* [1]. The filling or the sintering for most of the TaN, RU or CU samples was not successful because the optimum conditions for the flow rates, deposition time and the sintering temperature were not met.

Figure 6-22 shows that the filling of the trenches was improved compared to Figure 6-21, when the argon flow was increased to 600 sccm. The clusters did not adhere to the sidewall. However, the accumulation of the clusters on the top plateau caused a closure of the top openings. The top closure was likely to prevent further deposition into the trenches.

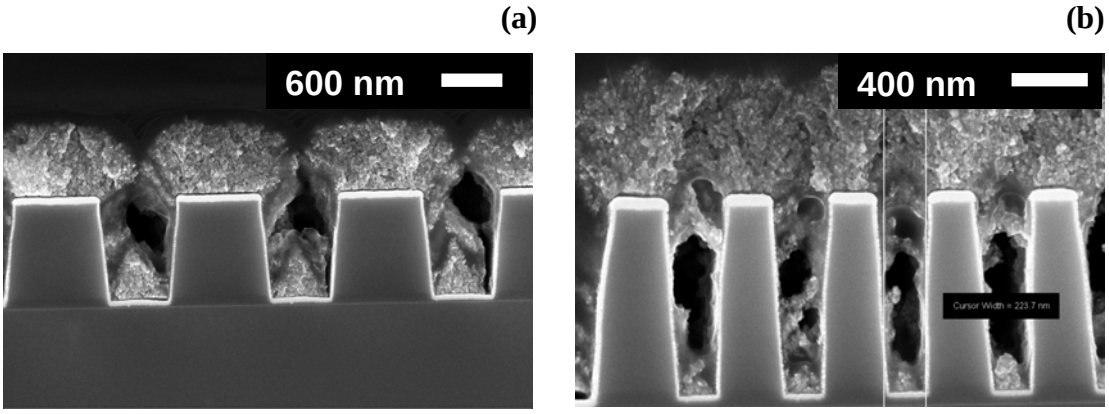

Figure 6-21: **XSEM images for clusters produced at 400 sccm argon flow in the magnetron sputtering source using trenches with two different widths: (a) 800 nm and (b) 300 nm.**

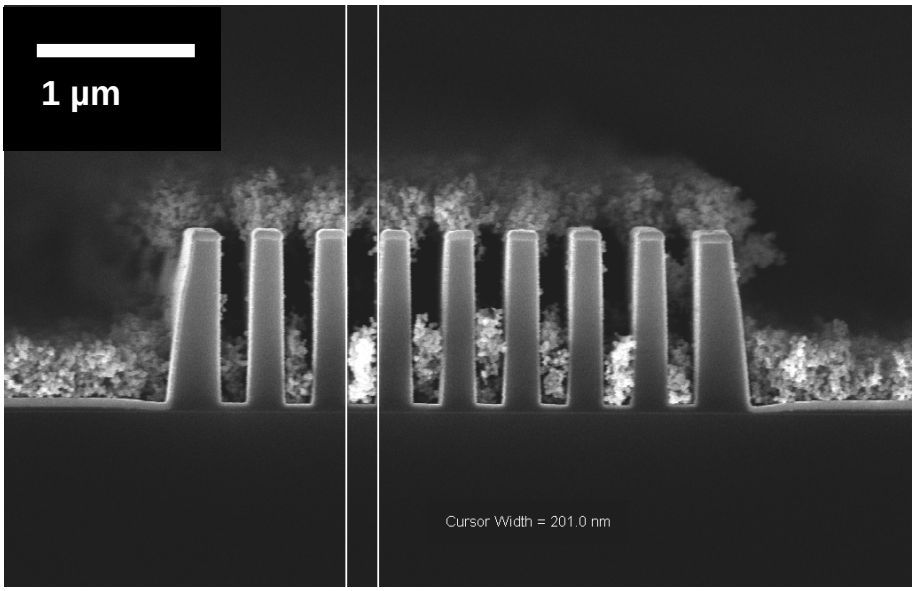

Figure 6-22: **At 600 sccm argon flow, the filling of the TaN trenches was affected by the closure of the top openings. The deposition was carried out at 0.9 $Ås^{-1}$ for 15 minutes.**

Figure 6-23 shows excellent filling of clusters into trenches with different widths. The clusters were produced at 800 sccm argon flow. The filling of the trenches for width starting from (a) 400 nm down to (d) 195 nm is a strong evidence showing that the filling does not occur just for trenches with a fixed aspect ratio. In an IC chip, the metal lines in the interconnects have different widths and depths depending on the design. Thus, the filling of clusters with different dimensions in this study meets the industry requirements in filling metal 1 trenches with less than 2:1 aspect ratio, as stated in ITRS roadmap 2007 [3].

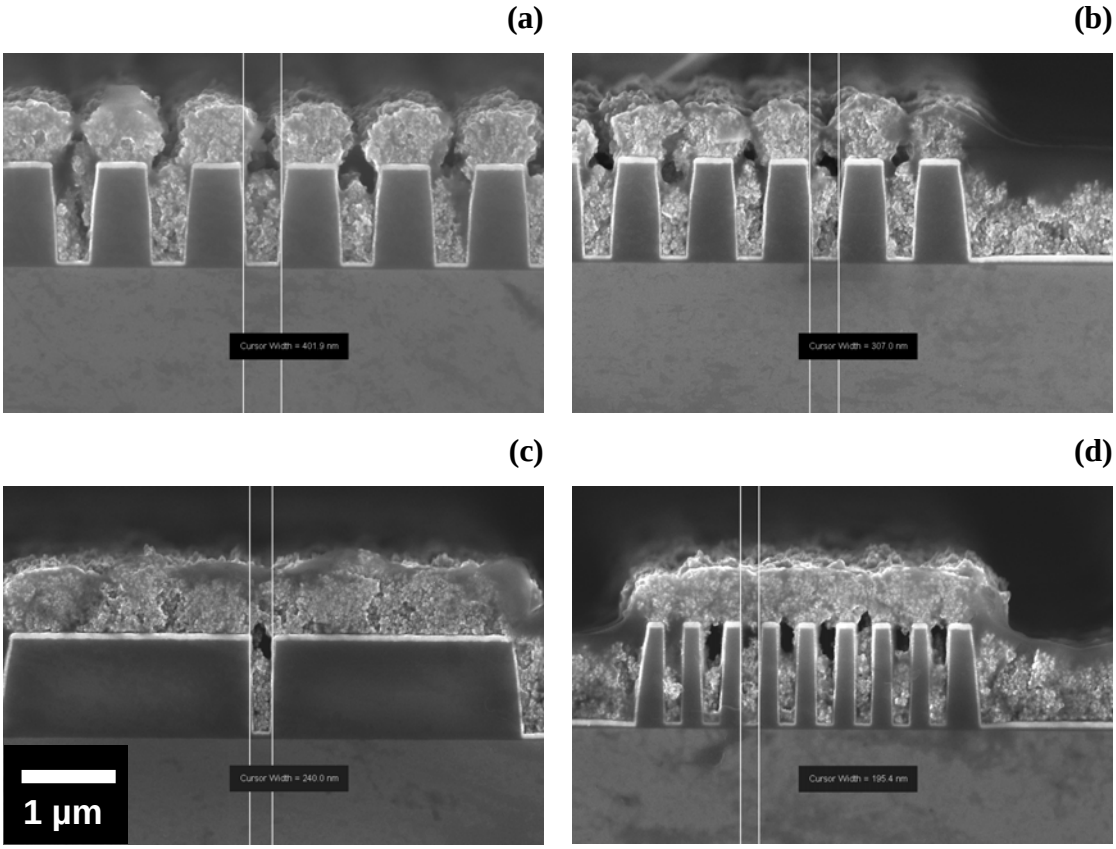

Figure 6-23: **XSEM images of copper clusters filling 1µm deep TaN trenches of different widths: (a) 400nm, (b) 300nm, (c) 240nm and (d) 195nm. The copper clusters were produced in the magnetron sputtering source at 800 sccm argon flow. All images had the same magnification.**

Figure 6-24 shows XSEM image of clusters deposited at 800/100 Ar/He flows. It was ambiguous whether the trenches were filled. It was speculated that the trenches were filled but the clusters fell off during cleaving. Therefore, a focused ion beam analysis should be used to cut the trenches without affecting the clusters and give a clear image. However, the facility was not available during the study.

Figure 6-25 shows the excellent filling of sub-100 nm trenches coated with TaN/Ru diffusion barrier layers. In this case the trenches had an aspect ratio of 3.5:1, but the selectivity was not apparent because the deposition time was longer than necessary, resulting in clusters spilling out of the trenches and spreading across the neighbouring plateaus. This explanation is supported by top view SEM images of large planar regions of the same sample which had clean plateaus, as depicted in Figure 6-26.

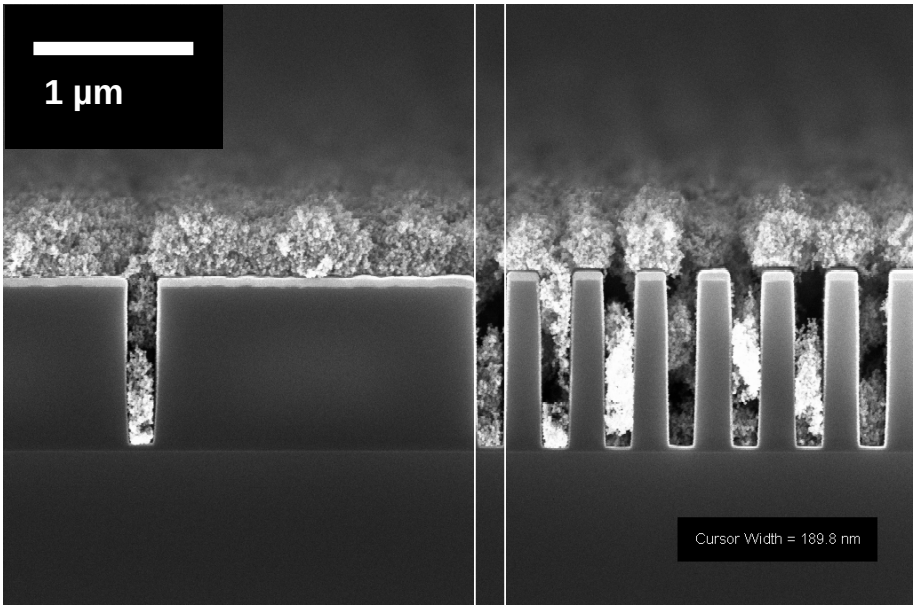

Figure 6-24: XSEM of a TaN sample deposited with clusters at 800/100 Ar/He flows.

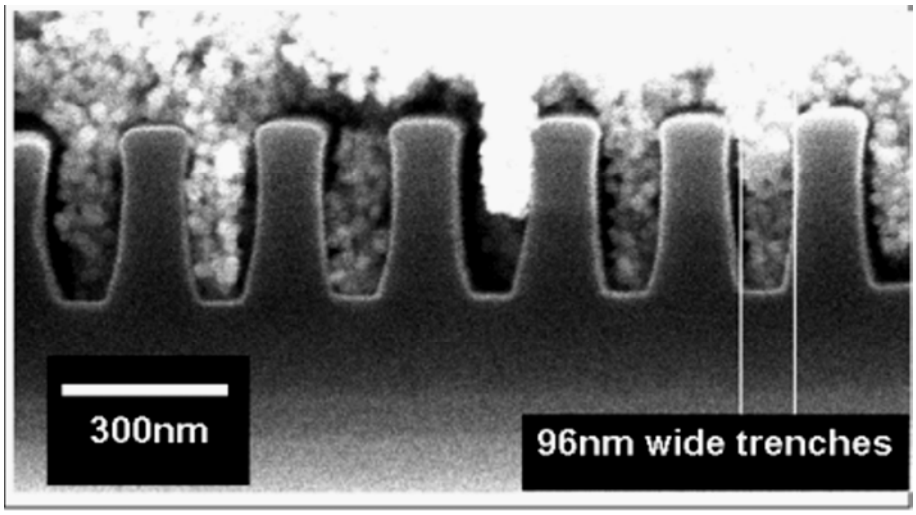

Figure 6-25: XSEM of clusters filling 96 nm wide Ru-coated trenches. The low-k dielectric in the Ru coated sample has deformed during the SEM imaging.

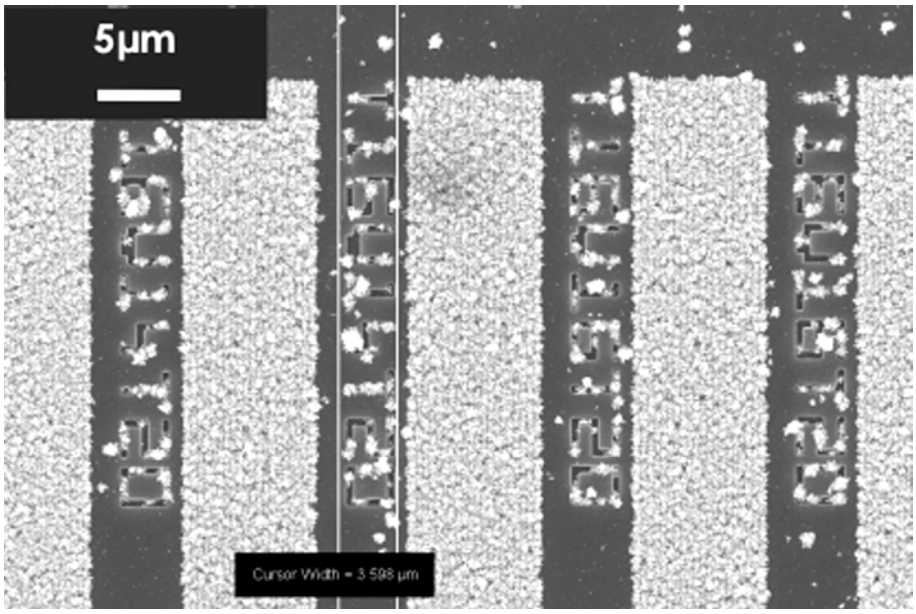

Figure 6-26: Large scale top view SEM image of the sample shown in Figure 6-25, highlighting the selectivity of the deposition.

To further prove the selectivity, an experiment was carried out with a shorter deposition time. Figure 6-27 shows excellent selectivity on a Ru-coated sample, with accumulation in trenches and clean plateaus between them. From the relative cluster coverage on the plateaus and trenches in Figure 6-27, a selectivity of at least 500:1 was estimated. The selectivity was calculated by estimating the number of clusters in the trenches divided by the number of clusters on the plateau.

The surfaces of the samples studied were oxidized after being exposed to air and it was clear that the surface state might play an important role in determining the selectivity (see Section 6.3.3). However, excellent selectivity (similar to Figure 6-26) was also observed on a RU sample pre-annealed in 5 Torr H_2 at 200ºC for 30 minutes prior to deposition. After the pre-annealing, the ruthenium oxide should be reduced to a pure ruthenium [19], and yet the selectivity was not degraded. Therefore, the selectivity was not limited to oxidized metal surfaces.

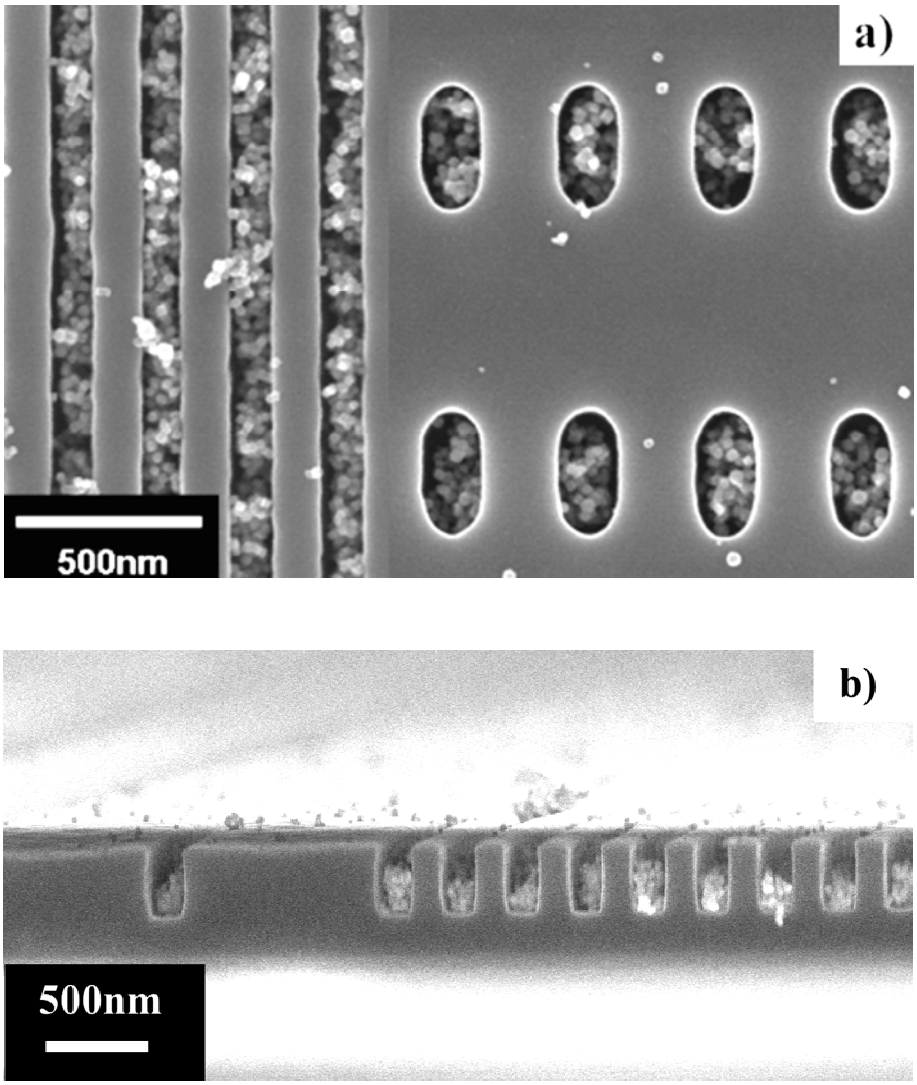

Figure 6-27: **SEM images of selectively filling sub-200 nm Ru coated trenches and holes from (a) top-view and (b) cross-sectional view. Very few clusters adhere to the top planar surface, while the trenches and holes are filled.**

The results indicate that the cluster-based deposition technique has some desirable and unique characteristics. For example, it has the same high purity and directional deposition as ionized physical vapour deposition (iPVD) [20], as well as the selective filling capability of electro-chemical deposition (ECD) [21], as described in Chapter 5. It is generally accepted in the cluster community that clusters generated in similar sources are free from oxidation or other contamination, as shown in the mass and photoelectron spectra in Ref. [22]. Hence, the purity of the Cu clusters which can in principle be at least as good as in iPVD processes, is in strong contrast with the significant level of impurities that are incorporated into interconnect structures by ECD processes [23, 24]. Although selective filling has been demonstrated in electro-

deposition and a Chemical Vapour Deposition (CVD) process [25], this is the first time it has been achieved with a technique which intrinsically produced high purity metal.

The mechanism for the selective accumulation of clusters at the bottom of the trenches in this experiment is proposed to be as follows. Due to the high kinetic energy (at least 2 keV/cluster), clusters bounced off the planar surfaces which were perpendicular to the cluster beam but slid along (or glanced off) the side walls to the bottom of the trenches. The clusters did not stick where they landed because their energy was large enough to overcome the adhesion energy to the surface. The relatively rough or disordered morphology of barrier/seed at the bottom of the trenches might have also facilitated the adhesion of clusters. After the arrival of the first clusters at the bottom of the trenches, the accumulation was enhanced because clusters adhered to other clusters efficiently. Figure 6-28 shows an SEM image of copper clusters deposited on a planar sample with double the deposition time compared to the patterned sample in Figure 6-27. From the distribution of the clusters, this demonstrated that the clusters adhered to other clusters better than to the substrate (c.f. antimony clusters described in Chapter 4).

The selectivity was better for larger clusters because of their high kinetic energy, as described in Ref. [8]; however, the filling of narrow trenches with small (10-15 nm diameter) clusters in this experiment was achieved, showing that the technique was

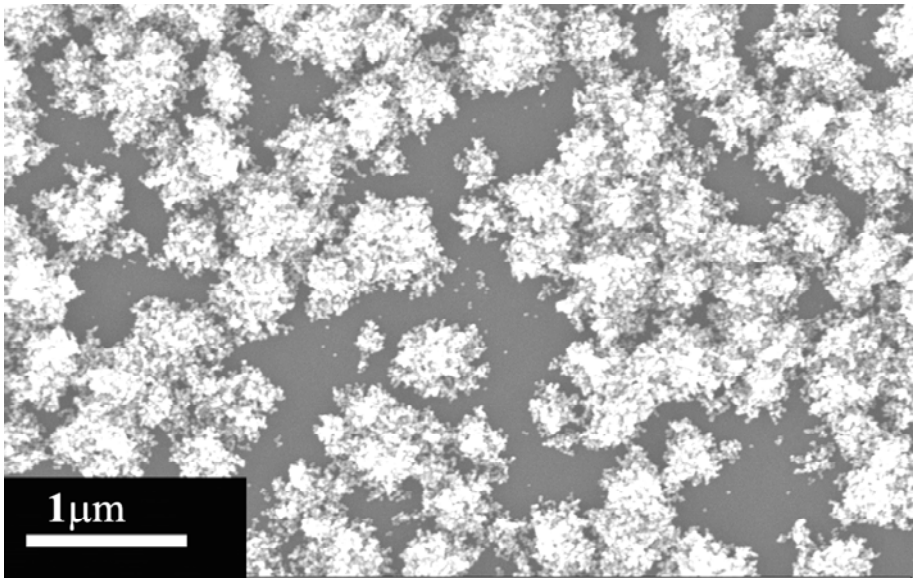

Figure 6-28: With a long deposition time on a planar Ru sample, more clusters have been collected on the plateau. From the distribution of the clusters, this demonstrates that the clusters stick to other clusters better than to the Ru substrate.

compatible with the requirement of current and future ultra-large-scale integrated (ULSI) technology. More generally the probability of sticking or bouncing was a complex function of the substrate and cluster materials, and the cluster size and velocity [26]. The bouncing behaviour observed in this experiment was not observed in Ref. [1], most likely due to differences in substrate materials and the kinetic energy/atom of the clusters: in the present case the kinetic energy/atom was very small (~ 0.02 eV/atom), and so the deposition was within what was usually considered the "soft-landing" regime, but the total energy/cluster was very high (> 2keV).

In Ref. [27], Denby *et al.* reported the size selection of cobalt clusters and gold clusters using a parallel-plate electrostatic separator. Therefore, an experiment was conducted to deposit ionised clusters on a TaN sample using a similar set up (see the deflector section in Chapter 2). The sample was placed on top of the Faraday cup. The positively charged clusters were selected by biasing 500 V to the deflector. After 30 minutes, there were no clusters observed at the bottom of the trenches. The low coverage of the samples could be due to two reasons: (a) by biasing a fixed voltage, only clusters with certain diameter could reach the Faraday cup. Therefore, the flux of the ionised beam could be quite low. In this case, a longer deposition time was needed; (b) as the clusters were hitting the surface with an angle because of the deflection, the adhesion could be less compared to the clusters landing at a 90º angle. Certainly, the clusters could be aligned normally to the sample surface by using a mass filter (see the mass filter section in Chapter 2), but the flux from the mass filter was even lower, because of the pulsed voltages used.

In this section, trenches in samples with different coatings including a reduced RU sample and different aspect ratios were filled by copper clusters using the magnetron sputtering source. Similar filling could also be achieved by using the IGA source, as illustrated in Figure 6-29. The TaN sample was deposited with the IGA source at 200 sccm argon flow and was filled with copper clusters. Therefore the cluster deposition either with an IGA source or a magnetron sputtering source is capable of filling the 5:1 aspect ratio trenches. The next section will discuss the sintering results of the filled samples.

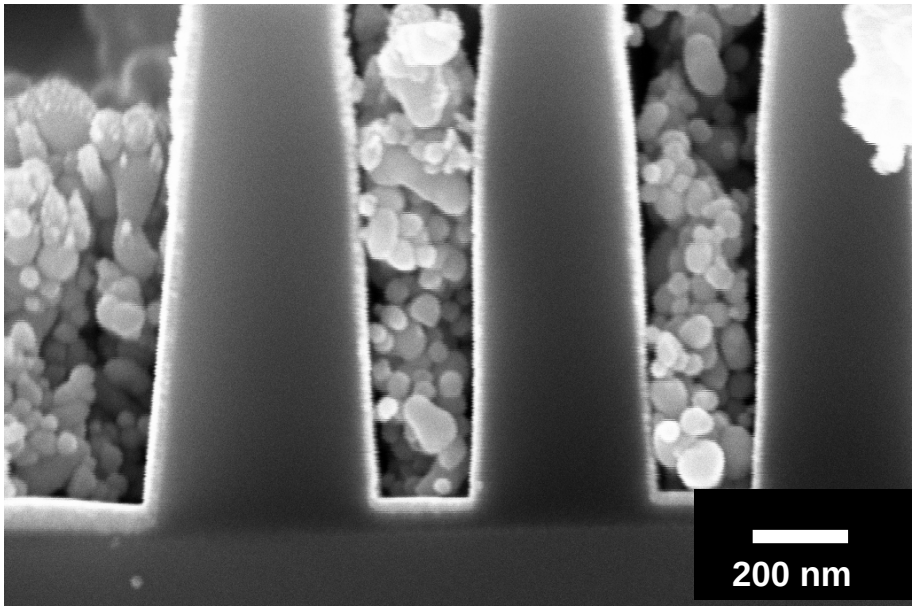

Figure 6-29: Excellent filling in the high aspect ratio trenches using IGA source at 200 sccm argon flow.

6.5 Sintering

Clearly the cluster-filled trenches shown in Section 6.4 have many voids and will have a low electrical conductivity. Therefore, a sintering process [22] was required. Sintering could be achieved by a vacuum annealing or molecular hydrogen annealing without the need to apply other advanced annealing techniques [28, 29]. This section discusses three ways of cluster sintering: a) sintering during deposition at an elevated substrate temperature; b) sintering in hydrogen and c) sintering in a vacuum.

In Ref. [1], Haberland *et al.* suggested the use of a substrate temperature higher than 500 K (equivalent to 227ºC) to improve the filling of the trenches. In order to study the effect of substrate temperature during deposition, a RU sample (labelled as RU#90) was deposited at an elevated substrate temperature. Figure 6-30 shows the XSEM images of the sample deposited at 400ºC using 800 sccm argon flow and annealed in vacuum at the same temperature for one hour. The cluster diameter was 41 ± 4 nm, estimated from 20 clusters in the image. The results indicate that the clusters were larger with a high substrate temperature, but the sintering was not complete.

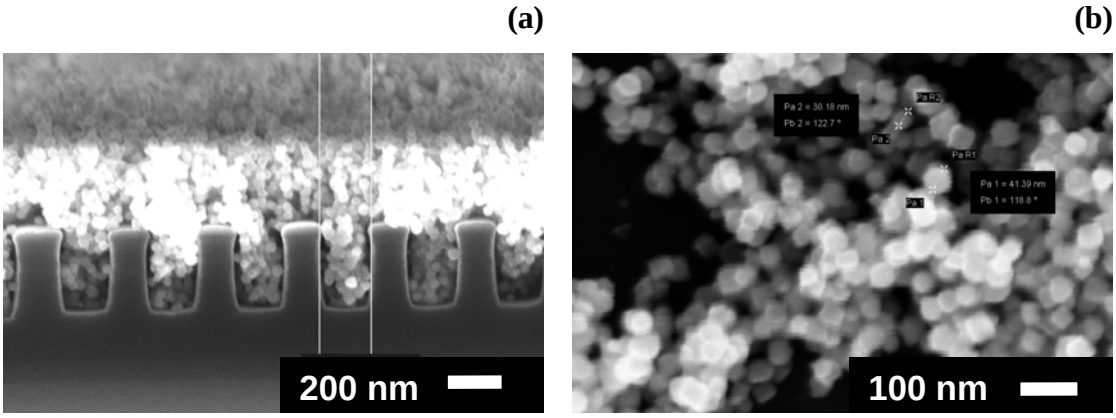

Figure 6-30: **(a) XSEM and (b) Top view SEM of a RU sample. The sample was deposited at 400ºC using and continued to hold at the same temperature for one hour. The cluster diameter was 41 ± 4 nm (calculated from 20 clusters).**

After the SEM imaging for Figure 6-30, the same sample (RU#90) was transferred to an annealing stage and annealed in 5 Torr H_2 at 400ºC for one hour. Figure 6-31 shows that using the same annealing temperature and the same annealing time as the vacuum annealing performed previously, the clusters had grown to much larger grains. It could be due to a capillary effect that made the clusters within the trenches move toward the top surface. From the SEM images, it was speculated that the sintering was more effective in the hydrogen environment compared to in a vacuum.

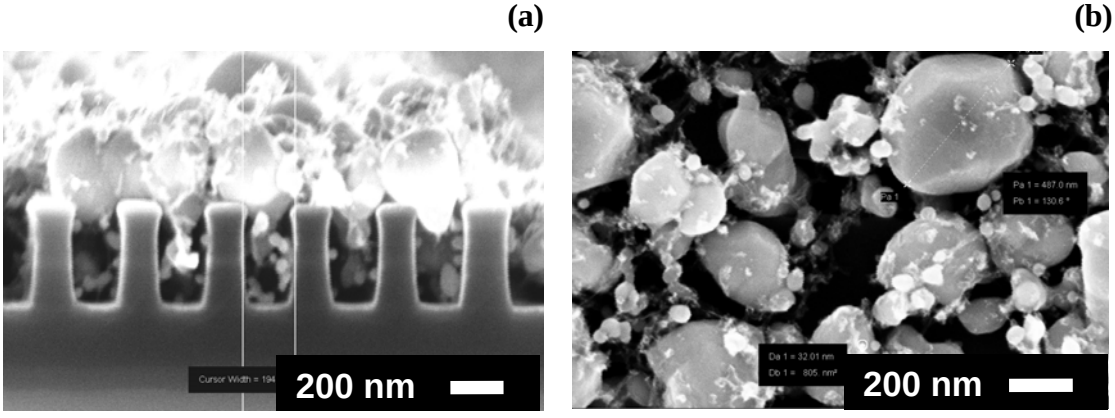

Figure 6-31: **(a) XSEM and (b) Top view SEM of a RU sample (RU#90) deposited at 400ºC, annealed at the same temperature for one hour, exposed to air and annealed in 5 Torr H_2 at 400ºC for another one hour. The sample illustrates the post H_2 annealed clusters for the sample shown in Figure 6-30.**

In order to verify that Figure 6-31 was not caused by the combination effect of the vacuum annealing and the hydrogen effect or the excessive clusters on the top plateau, a control experiment was conducted. Figure 6-32 shows an XSEM of a RU sample, deposited using 800 sccm argon flow and annealed in 5 Torr H_2 at 350ºC for one hour. It was evident that the Cu clusters did not wet the Ru diffusion barrier layer after the annealing. The annealing experiments on Ru seed layers were not successful because the copper clusters failed to adhere to the seed. A similar result was observed in the TaN sample. Therefore, the subsequent sintering experiments focused on the trenches with a Cu seed.

Figure 6-33 shows a CU sample annealed at 400ºC in 5 Torr H_2 for one hour after deposited at 800 sccm argon flow and exposed to air. The reason of using a CU sample was that the copper seed layer on the sample could facilitate the sintering. Although the sintering in H_2 could be more effective than in vacuum, the temperature was not high enough to sinter the clusters completely into the copper seed layer.

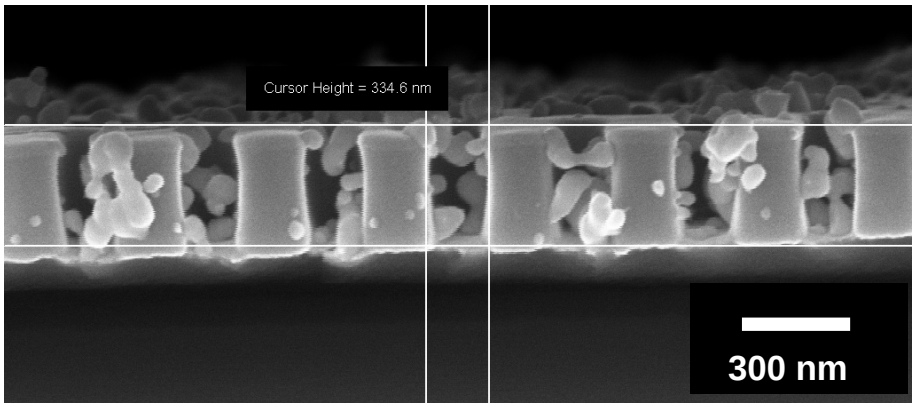

Figure 6-32: Poor wetting of the copper clusters on the air-exposed Ru layer after H_2 annealing at 350ºC for one hour.

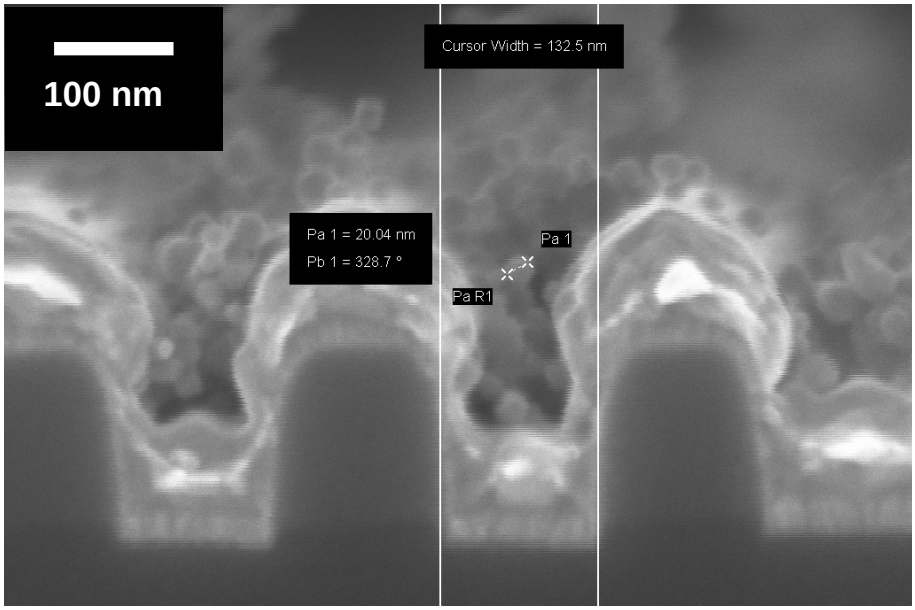

Figure 6-33: A CU sample deposited at 800 sccm argon flow, exposed to air, moved to annealing stage and annealing in H_2 at 400°C for one hour.

Figure 6-34 shows the results of a hydrogen annealing experiment with a CU sample at 450ºC. The XSEM images of the cleaved samples before and after deposition are shown in Figure 6-34 (a-b). Since these structures were relatively shallow, it was difficult to optimize the deposition time and the clusters overflowed from the trenches onto the plateaus (as per discussion in Section 6.4). The cleaved sample was subjected to annealing at 450ºC in a ~5 Torr ultra high purity hydrogen environment for 2 hours. Higher annealing temperatures were expected to cause decomposition of the low-k dielectric. Figure 6-34 (c) shows the copper clusters effectively sintered after the annealing. Since the clusters on the cleaved surface were directly exposed to hydrogen gas during annealing, the wafer was re-cleaved to demonstrate the same effect of sintering within the trenches. Figure 6-34 (d) shows that while there was some roughness/damage caused by the cleaving process, the trenches were indeed densely filled with copper.

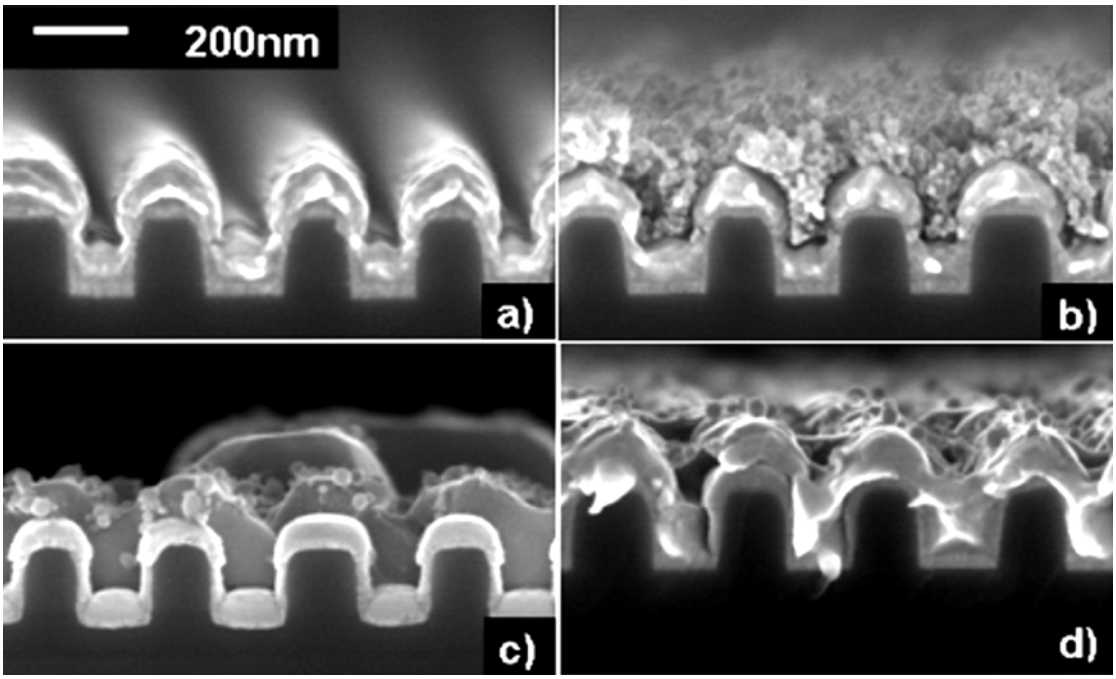

Figure 6-34: **Results of annealing experiment in ~5 Torr hydrogen at 450ºC for 2 hours.**
(a) after cleaving but before cluster deposition;
(b) after deposition but prior to annealing;
(c) after annealing. The cluster material appears to be darker than the diffusion barrier and copper seed layer; and
(d) after annealing and after additional cleaving
All images showing XSEM of Ta/Cu coated trenches are with the same magnification.

Since the annealing at 450ºC in a hydrogen environment could effectively sinter the copper clusters, the effect of vacuum annealing at 450ºC was studied. To avoid the oxidation of the copper clusters, a sample was annealed in a vacuum (~10^{-6} Torr) at 450ºC immediately after the completion of the deposition. Figure 6-35 shows an excellent sintering using a vacuum annealing. Thus, as long as the copper cluster films were not exposed to air, vacuum annealing at 450ºC for two hours could be applied. However, the deposition time for sample in Figure 6-35 was too short; thus, an experiment was carried out with a long deposition time. Figure 6-36 shows the XSEM images of a sample deposited at 600/100 Ar/He flows for 30 minutes at 0.5 $Å s^{-1}$ and subsequently annealed in a vacuum for 10 hours. A complete sintering was observed for trenches with widths of 145 nm and 270 nm.

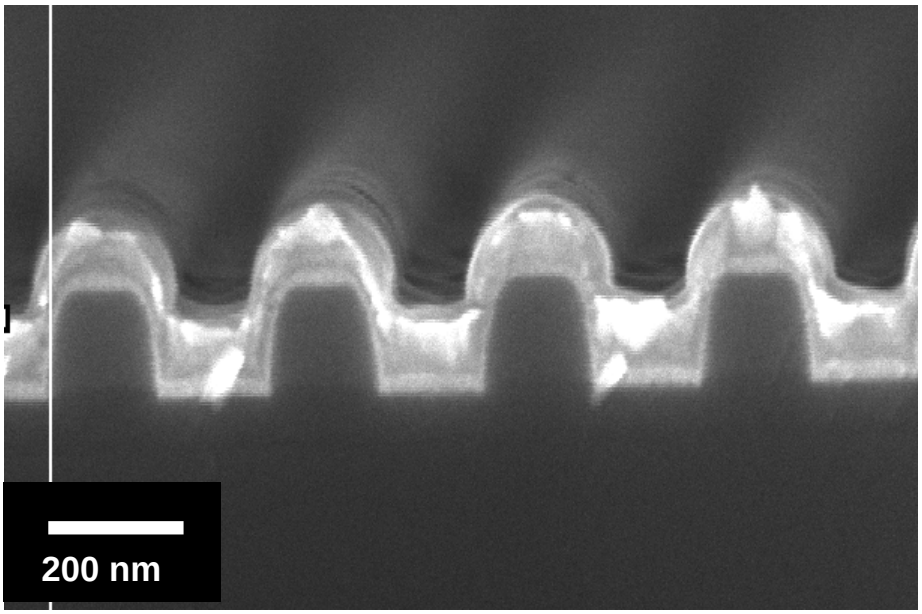

Figure 6-35: XSEM of a CU sample deposited with copper clusters and immediately annealed in vacuum at 450ºC for 2 hours. The clusters have completely sintered into the seed layer, because the copper has now filled the trenches.

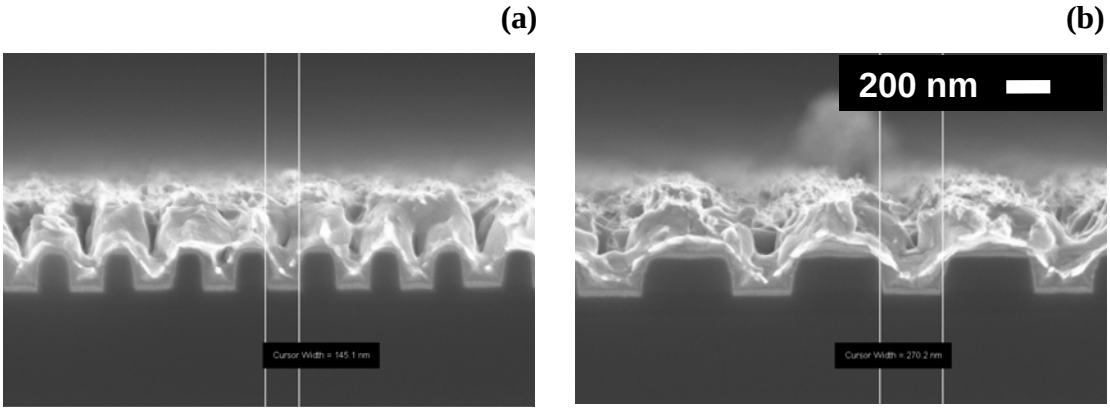

Figure 6-36: Vacuum annealing at 450ºC for 10 hour was carried out immediately after the cluster deposition at room temperature using 600/100 Ar/He flows for 30 minutes at 0.5 $Å s^{-1}$. The widths of the trenches are: (a) 145 nm and (b) 270 nm respectively. Both figures had the same scale.

Other than the one step deposition followed by annealing, an experiment was conducted to deposit and anneal the high-aspect-ratio samples in a repetitive manner. Two TaN samples were deposited with 10 minute duration and 15 minute duration. The deposition and annealing cycles were repeated once for each sample. Therefore, the total deposition times were 20 minutes and 30 minutes respectively. Figure 6-37 shows a typical XSEM from the second sample. The sample was deposited at room temperature using 800 sccm argon flow for 15 minutes, annealed at 450ºC for 30 minutes, deposited again for the same duration at 450ºC and then stayed at the same

temperature for 30 minutes before cooled down to room temperature. Unfortunately, the clusters clumped together during the sintering. Thus, the filling and the sintering using step deposition and annealing were not successful with the TaN samples. Unfortunately, the high aspect ratio CU sample was not available. It would be interesting to investigate the effect of step deposition/annealing on a high aspect ratio CU sample.

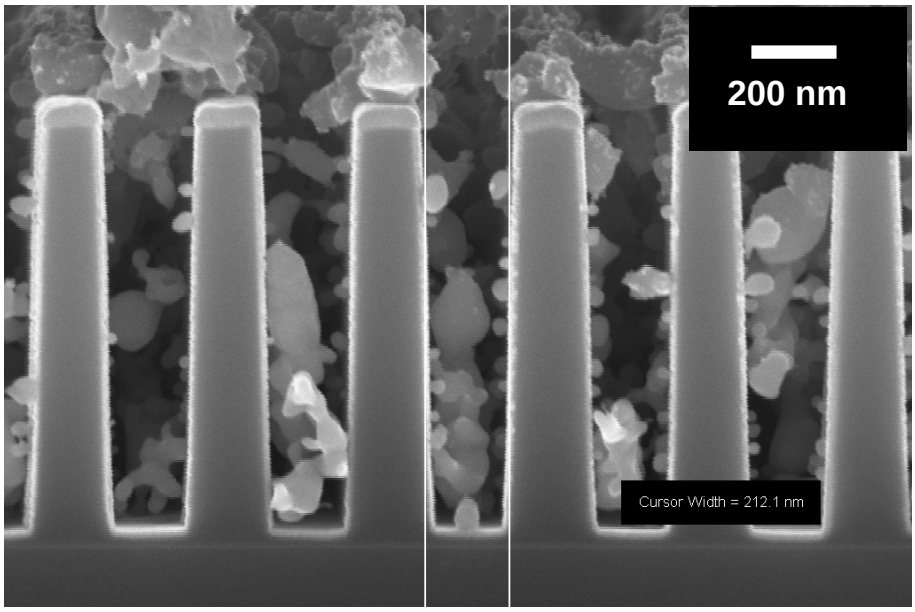

Figure 6-37: A typical XSEM of a TaN sample deposited and annealed repeatedly. The sample was deposited at room temperature using 800 sccm argon flow, annealed at 450ºC for 30 minutes, deposited again at 450ºC and stayed at the same temperature for 30 minutes before cooled down to room temperature.

6.6 Summary and future work

This chapter describes the characterisation of copper clusters from an IGA source and a magnetron sputtering source. Various samples with different dimensions and coatings were used. Some of the coatings such as the tantalum based diffusion barrier layer and the copper seed layer were prepared by the semiconductor manufacturers using a state-of-the-art processing. Even more exciting, samples with Ru coating which represents the diffusion barrier for future technology nodes were tested. V-groove samples were also prepared to examine the bouncing behaviour in order to compare the bouncing properties of copper clusters to the bouncing of other materials.

In the magnetron sputtering source, the diameters of the clusters were measured by using the mass filter. For a lower argon flow rate, the cluster diameter was smaller. The diameter of the clusters was reduced when 100 sccm helium flow was added.

The velocity of the clusters was measured by using a deflector. The dominating factor for the cluster velocity was the helium flow, followed by the argon flow. The relation between the cluster velocity and the gas flows could be explained by the gas acceleration within the de Laval nozzle. The slip between the cluster velocity and the gas velocity was about 50 %.

Reflection of clusters was studied on various planar surfaces. By placing the samples in close proximity, the effect of a non-uniform cluster beam was eliminated. At 800 sccm argon flow, it was found that the clusters bounced the most on a TaN surface without pre-annealing and on a Ru surface with H_2 pre-annealing.

It was demonstrated that the reflection of clusters could be employed to achieve selective filling of high aspect ratio (5:1) damascene trenches with copper. The filling was also shown in RU samples and CU samples. As the deposition could be made selectively, the amount of copper left for CMP could be greatly reduced. In this case, the CMP issues such as dishing or erosion would be minimized, thus leading to better process integration. Annealing in either hydrogen or in a vacuum drastically improved the quality of the deposited material. This technique has great potential to meet the requirements for ULSI interconnect metallization.

In this work, the aspect ratio of the CU samples was small and the copper seed layer was relative thick. Thus, it would be interesting to deposit the copper clusters in high aspect ratio trenches with a thin copper thin layer. As the reflection of clusters on copper seed layer is different from the reflection of clusters on TaN surfaces, the process condition may be different. The other advantage of deep trenches is that the clusters would be confined within the trenches during sintering, thus, it is important to verify the sintering of the clusters within those trenches with the appropriate seed used by the industry. The repetitive deposition and annealing could also be tried out with high aspect ratio trenches coated with a copper seed layer. The next chapter will discuss the resistivity measurement for annealed cluster films.

References

[1] H. Haberland, M. Mall, M. Moseler, Y. Qiang, T. Reiners, and Y. Thurner, "Filling of micron-sized contact holes with copper by energetic cluster impact," *Journal of Vacuum Science & Technology A: Vacuum, Surfaces, and Films*, vol. 12, pp. 2925-2930, 1994.

[2] P. Gatz and O. F. Hagena, "Cluster beams for metallization of microstructured surfaces," *Applied Surface Science*, vol. 91, pp. 169-174, Oct 1995.

[3] *International Technology Roadmap for Semiconductors, 2007*, http://public.itrs.net.

[4] U. S. Chen, W. J. Hsieh, H. C. Shih, Y. S. Chang, K. W. Weng, and D. Y. Wang, "Nanostructure and adhesion of electroless-plated Cu film on the self-catalyzed Cu using metal-plasma ion implanter," *Nuclear Instruments & Methods in Physics Research Section B-Beam Interactions with Materials and Atoms*, vol. 237, pp. 470-476, 2005.

[5] B. Cui, W. Wu, C. Keimel, and S. Y. Chou, "Filling of nano-via holes by laser-assisted direct imprint," *Microelectronic Engineering*, vol. 83, pp. 1547-1550, Apr-Sep 2006.

[6] E. Kondoh and H. Kato, "Characteristics of copper deposition in a supercritical CO_2 fluid," *Microelectronic Engineering*, vol. 64, pp. 495-499, 2002.

[7] C. H. Seah, S. Mridha, and L. H. Chan, "DC/pulse plating of copper for trench/via filling," *Journal of Materials Processing Technology*, vol. 114, pp. 233-239, 2001.

[8] J. G. Partridge, S. A. Brown, A. D. F. Dunbar, R. Reichel, M. Kaufmann, C. Siegert, S. Scott, and R. J. Blaikie, "Templated-assembly of conducting antimony cluster wires," *Nanotechnology*, vol. 15, pp. 1382-1387, 2004.

[9] A. Ayesh, "Device fabrication using Bi nanoclusters," *PhD thesis, University of Canterbury*, 2007.

[10] H. Gong, H. Gong, K. M. Chooi, and C. K. Ong, "Charging of deformed semicrystalline polymers observed with a scanning electron microscope," *IEEE Transactions on Dielectrics and Electrical Insulation [see also IEEE Transactions on Electrical Insulation]*, vol. 2, pp. 1123-1131, 1995.

[11] T. C. Jen, L. Li, Q. Chen, W. Cui, and X. Zhang, "The acceleration of micro- and nano-particles in supersonic de-Laval-type nozzle," Washington, DC., United States, 2003, pp. 281-287.

[12] S. V. Falkovich and M. Tech, "On theory of Laval nozzle," National Advisory Committee for Aeronautics, Washington, DC, United States 1949.

[13] H. Haberland, M. Karrais, M. Mall, and Y. Thurner, "Thin-films from energetic cluster impact - a feasibility study," *Journal of Vacuum Science & Technology a-Vacuum Surfaces and Films*, vol. 10, pp. 3266-3271, Sep-Oct 1992.

[14] D. R. Lide, *CRC handbook of Chemistry and physics*, 84th ed. New York: CRC Press, 2004.

[15] P. G. Hill and C. R. Peterson, *Mechanics and thermodynamics of propulsion*, 2nd ed.: Addison-Wesley, 1992.

[16] http://www.braeunig.us/space/propuls.htm#intro.

[17] *http://members.aol.com/ricnakk/th_nozz.html*.
[18] *http://farside.ph.utexas.edu/teaching/sm1/lectures/node51.html#tab1*.
[19] M. Hiratani, Y. Matsui, K. Imagawa, and S. Kimura, "Hydrogen reduction properties of RuO_2 electrodes," *Japanese Journal of Applied Physics Part 2-Letters,* vol. 38, pp. L1275-L1277, Nov 1999.
[20] C. A. Nichols, S. M. Rossnagel, and S. Hamaguchi, "Ionized physical vapor deposition of Cu for high aspect ratio damascene trench fill applications," *Journal of Vacuum Science and Technology B,* vol. 14, p. 3270, 1996.
[21] D. Josell, D. Wheeler, C. Witt, and T. P. Moffat, "Seedless superfill: Copper electrodeposition in trenches with ruthenium barriers," *Electrochemical and Solid State Letters,* vol. 6, pp. C143-C145, Oct 2003.
[22] W. A. de Heer, "The physics of simple metal clusters: experimental aspects and simple models," *Reviews of Modern Physics,* vol. 65, p. 611, 1993.
[23] M. Stangl, V. Dittel, J. Acker, V. Hoffmann, W. Gruner, S. Strehle, and K. Wetzig, "Investigation of organic impurities adsorbed on and incorporated into electroplated copper layers," *Applied Surface Science,* vol. 252, pp. 158-161, 2005.
[24] B. Gang, C. Chien, N. Cox, F. Sychyi, D. S. Gardner, A. Mack, T. Marieb, M. Xiao-Chun, V. Ochoa, R. Villasol, and Y. Jick, "Copper interconnection deposition techniques and integration," Honolulu, HI, USA, 1996, pp. 48-9.
[25] P. Hyungsang, K. Wonyong, C. Seung-Man, P. Ki-Chul, K. Ho-Kyu, M. Joo-Tae, S. Kyuchan, L. Hyunbae, K. Ohgyum, and K. Sangwon, "Superfilling CVD of copper using a catalytic surfactant," in *International Interconnect Technology Conference*, Burlingame, CA, USA, 2001, pp. 12-14.
[26] A. Awasthi, S. C. Hendy, P. Zoontjens, and S. A. Brown, "Reentrant Adhesion Behavior in Nanocluster Deposition," *Physical Review Letters,* vol. 97, p. 186103, 2006.
[27] P. M. Denby and D. A. Eastham, "Efficient technique for producing high-brightness, size-selected cluster beams," *Applied Physics Letters,* vol. 79, pp. 2477-2479, Oct 2001.
[28] T. Miyake, H. Petek, K. Takeda, and K. Hinode, "Atomic hydrogen enhanced reflow of copper," *Applied Physics Letters,* vol. 70, pp. 1239-1241, 1997.
[29] K. K. Choi, J. H. Yun, and S. W. Rhee, "Effect of hydrogen remote plasma annealing on the characteristics of copper film," *Thin Solid Films,* vol. 429, pp. 255-260, Apr 2003.

Chapter 7

Resistivity of annealed copper cluster films

As described in Chapter 5, copper has been the main on-chip conductor for all deep-submicron integrated circuits (ICs) since 1997. Yet, filling the high aspect ratio trenches in the copper damascene structures remains challenging. In Chapter 6, selective filling and sintering of copper clusters has been demonstrated in those trenches. Although the annealed cluster films were dense in the cross-sectional scanning electron micrographs (XSEM), there was no quantitative analysis of the films, such as studying micro- (or even nano-) voids in the films after sintering. A straight-forward method to investigate the film properties is to measure the resistivity of the annealed films. A truly dense copper film should have low resistivity. Thus, in order for the cluster technology to be applied to interconnect applications, the resistivity of the annealed films should at least meet the requirement of the industry (2.2×10^{-8} Ω.m) [1] (the resistivity of bulk copper is 1.68×10^{-8} Ω.m).

This chapter describes the examination of the resistivity of annealed cluster films. The sample preparation is illustrated in Section 7.1. The deposition conditions are described in Section 7.2. Then the equipment setup is described in Section 7.3. In Section 7.4, the methodology is described in detail. The evolution of the film morphology is discussed in Section 7.5, with emphasis on the variation of morphology with increasing thickness. The resistivity of the films is calculated based on the measurements of the annealed films in Section 7.6. The chapter concludes with a summary and some recommendations for future work.

7.1 Sample preparation

This section describes the samples used for the resistivity characterisation. An 8 inch wafer was supplied by Texas Instruments. The wafer had a Ta-based diffusion barrier and a copper seed layer. As opposed to the samples demonstrated in Chapter 6, there was pre-textured surface on the wafer. The resistivity of the diffusion barrier layer and the copper seed layer were not disclosed due to confidentiality. The wafer was cleaved into square samples for experiments. Figure 7-1 shows a cross-sectional scanning electron micrograph (XSEM) of a typical part of the wafer. The XSEM sample was prepared by cleaving the sample and then sticking it to a SEM stud with the cleaved surface facing the incident electron beam at a 90º angle.

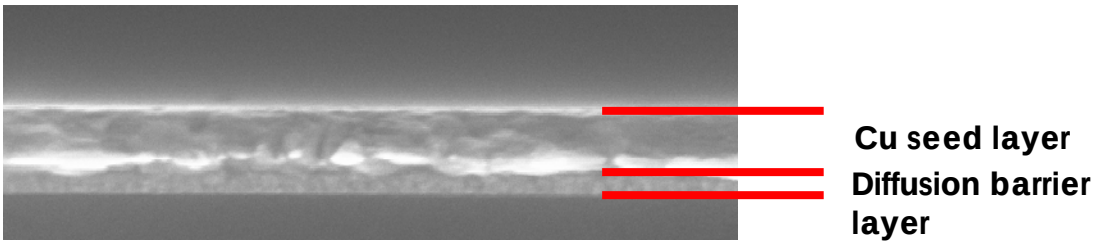

Figure 7-1: Cross-sectional SEM for wafer supplied by Texas Instruments.

Table 7-1 lists the samples used in the experiments. The width and the length of the samples were measured using a digital vernier. There was no cluster deposition for the reference sample #R1. For all other samples (#27 to #60), the clusters were produced in either 200/100 or 200/200 argon/helium flow ratio. The thickness was registered by a film thickness monitor (FTM). Except for sample #60, none of the samples underwent any lithographic process.

For sample #60, a series of process steps was carried out to form a wire. First, photo-resist was spun on the sample. Then the sample was soft-baked at 95ºC for two minutes. Subsequently, the sample was exposed to ultra-violet light through a reticle for ten seconds. After developing the photo-resist, the sample was etched by a mixture of (60%) HNO_3: (40%) HF: H_2O (volume ratio = 1:1:1). The copper seed layer and the tantalum, which were not protected by the photo-resist, were removed. Lastly, the photo-resist was removed by acetone/IPA, leaving an “I” shape pattern on the sample.

Table 7-1: **List of the samples, the width and length of the samples, the gas flow ratio and the thickness registered by film thickness monitor (FTM). There was no cluster deposited on Reference sample #R1. Samples with * were not used for resistivity evaluation.**

Sample no.	Width (mm)	Length (mm)	Ar/He ratio	FTM Thickness (nm)
#R1	19.94	20.7	-	-
#27	15.95	15.39	200/100	54
#29	15.33	15.68	200/200	36
#42	20.32	20.61	200/100	150
#46	18.85	19.66	200/100	122
#48	19.07	19.87	200/100	110
#50	23.30	20.20	200/100	86
#30*	22.82	15.46	200/200	144
#34*	18.62	18.73	200/200	207
#36*	18.63	18.24	200/200	66
#37*	21.58	18.68	200/200	106
#60*	-	-	200/200	36

Figure 7-2 shows the layout design of sample #60 and an optical image of a part of the sample. This structure enabled a four-terminal resistance measurement over a narrow line with a design aspect ratio (*L/W*) of 41.4. The next section describes the details of the process.

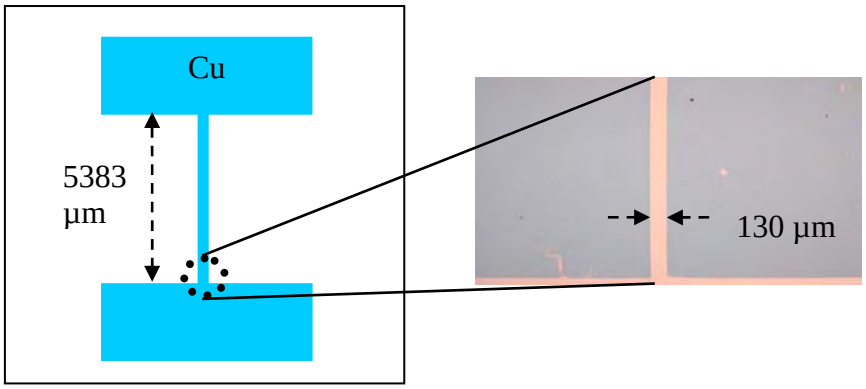

Figure 7-2: **Layout of sample #60 (left) and the optical photo of a part of the sample (right). The width and the length of the wire were 130 µm and 5383 µm, respectively.**

7.2 Experimental Description

This section describes the process of producing the clusters and sintering the films. Copper clusters were deposited on the samples described in Section 7.1. Then the samples were unloaded and underwent a visual inspection. After judging film uniformity from the colour of the samples, only the most uniform samples were selected for subsequent annealing. The details of the experimental description are presented in the following two sub-sections.

7.2.1 Cluster deposition

The clusters were generated in the inert gas aggregation (IGA) source. The details of this system were described in Chapter 2. In this system, the diameter of the clusters was controlled by changing the flow rate of the argon and helium gases. Figure 7-3 shows the SEM images of samples #27 and #29. At Ar/He ratios of 200/100 and 200/200, copper clusters with the diameters of 30 nm and 15 nm were produced, respectively. More than ten samples have been deposited using each Ar/He ratio. However, only five samples from the 200/100 and one sample from the 200/200 Ar/He ratios passed the visual inspection, as listed in Table 7-1. The rest of the samples failed the visual inspection. The failure was caused by the inhomogeneous deposition of the clusters (only some parts of the failed samples were covered by clusters).

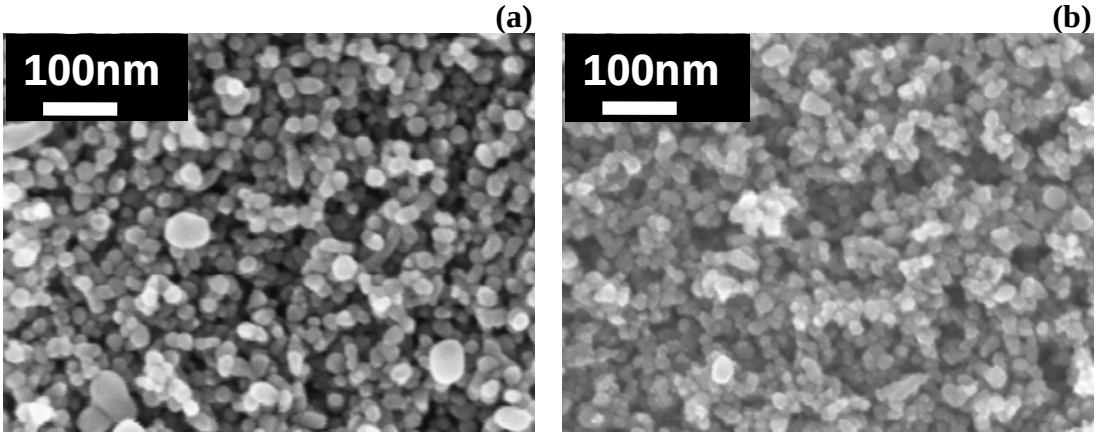

Figure 7-3: **SEM measurements from samples #27 and #29 show that the diameters of the copper clusters are around (a) 30 nm and (b) 15 nm, respectively.**

7.2.2 Annealing condition

The annealing conditions were identical to the conditions described in Chapter 6. After deposition, the copper clusters were exposed to air for visual inspection. Only the samples with uniform coverage were loaded onto the annealing stage. The design of the annealing stage was described in Chapter 2. For annealing, the deposition chamber was pumped to a vacuum (~10^{-6} Torr range) to remove moisture and oxygen. Subsequently, the chamber was isolated from the turbo pump using a gate valve, and filled with ~5 Torr of H_2. For annealing, the temperature was held at 450ºC for 2 hours. When the samples were cooled below 50ºC, the hydrogen gas was pumped out by a rotary pump. Finally, the system was vented with nitrogen before unloading the samples.

7.3 Measurement setup

This section describes the instrument used to measure the sheet resistance of the samples. Samples were tested in a probe station (micromanipulator model 1800) in combination with a HP 4155A Parameter Analyzer. Figure 7-4 shows the photos of the probe station which consists of a microscope and four manual manipulators, an illuminating light source and a sample stage with x-y-z controls. With light illumination, the position of the probe tips could be viewed under the microscope. The probe pins were mounted on manual manipulators which had x-y-z controls. Electrical connections between the probe pins and the source-measure unit (SMU) of the parameter analyzer were made through soldered wires and tri-axial cables. The measurement voltages were all in the mV range at the SMU which has a resolution of 20μV [2].

7.4 Methodology

This section describes the methodology for the resistivity measurement of the annealed copper cluster films. First, the concept of sheet resistance is reviewed. Second, the correction factors needed for the sheet resistance calculation are described. Then, the

electrical measurement conditions are presented, followed by the discussion of the parallel model used. The thickness measurement method is briefly described, and lastly, the calculations of the resistivity and the uncertainty analysis are presented.

7.4.1 Sheet resistance

From Ohm's law, the resistivity is defined as:

$$R = \rho \frac{L}{Wd} \qquad (Eq.\ 7\text{-}1)$$

where R is the resistance; ρ is the resistivity; L, W and d are the length, width and thickness of a rectangular conductor.

There are two parts in *Eq. 7-1*, namely the design aspect ratio (L/W) and the process parameters (ρ/d). In IC applications, the metals vary in thickness at the different levels of the interconnects, allowing different designs in the circuits [1]. Thus, the concept of sheet resistance is widely used in the industry for calculating the resistance of metal wires with different dimensions.

The sheet resistance is defined as the resistance for a wire with an aspect ratio (L/W) of unity:

$$R_{sh} = \frac{\rho}{d} \qquad (Eq.\ 7\text{-}2)$$

When the aspect ratio is equal to one, the resistance is essentially the resistance of a square. Thus, the unit of the sheet resistance is Ω/square. There are two ways to measure the sheet resistance of a material, either on a wire or on a thin film. Figure 7-5 and Figure 7-6 show the schematic of a four-point resistance measurement on a wire and on a thin film respectively. The four-point probe technique forces a current through the sample, using pins 1 and 4, and measures the resulting voltage between pins 2 and 3. The advantage of this arrangement over a two-point measurement is that the effect of contact resistance between the sample and the probes is eliminated.

(a)

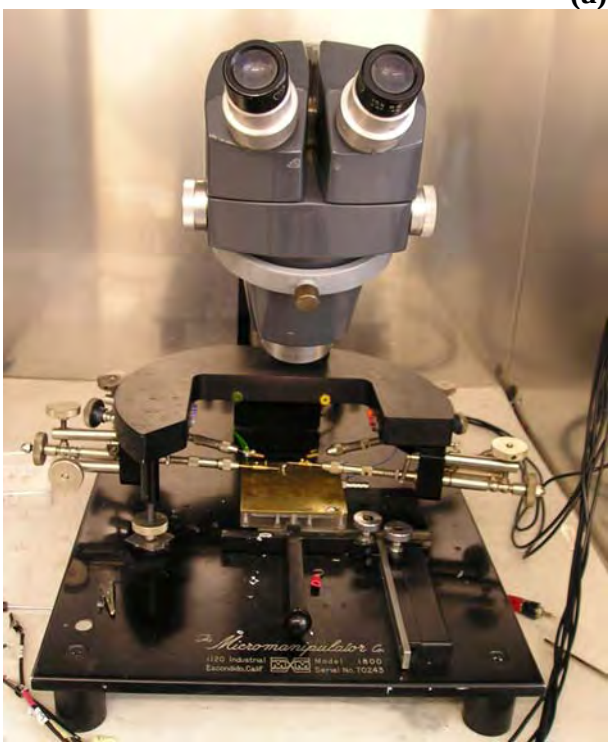

(b)

(c)

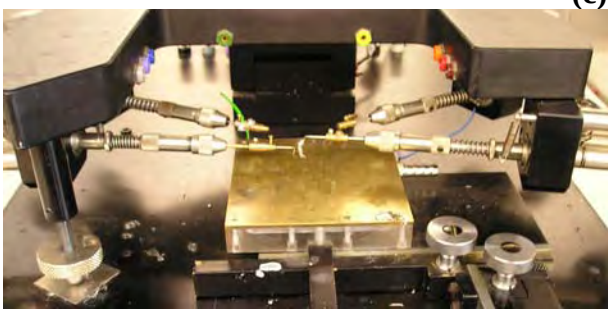

Figure 7-4: **Probe station for electrical measurement consists of (a) microscope, light illumination, (b) stage control, and (c) probe manipulators.**

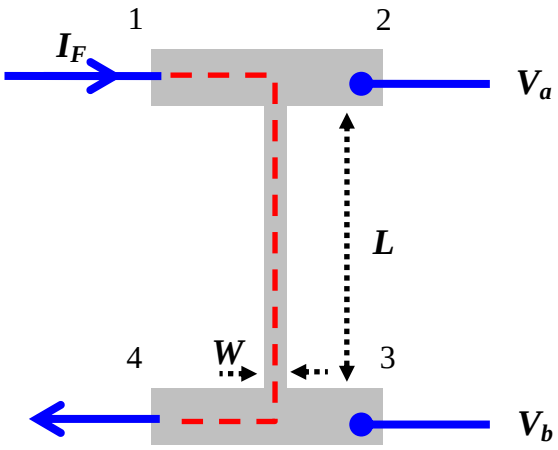

Figure 7-5: **Top view schematic of a four-point probe resistance measurement on a wire. A current is forced from pin 1 to pin 4. Voltage is measured in between pin 2 and pin 3. The length and width of the wire are denoted as *L* and *W*.**

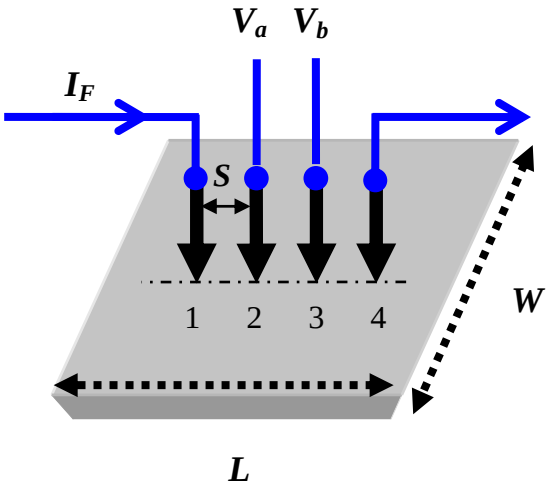

Figure 7-6: **Schematic of a four-point probe resistance measurement on a thin film. A current is forced from pin 1 to pin 4. The voltage is measured in between pin 2 and pin 3. The spacing between the pins is denoted as *S*. The length and width of the samples (except sample #60) are denoted as *L* and *W*.**

In order to measure the sheet resistance in a wire, the wire must have uniform thickness and well-defined width and length. With a uniform thickness, the sheet resistance is given by:

$$R_{sh} = \frac{V}{I} / (\frac{L}{W}) \qquad (Eq.\ 7\text{-}3)$$

where V and I are the voltage and the current measured in the four-point measurement and the L/W is the design aspect ratio.

The sheet resistance of a thin film is simply the four-point probe resistance multiplied by a correction factor (ξ).

$$R_{sh} = \xi \frac{V}{I} \qquad (Eq.\ 7\text{-}4)$$

The calculation of ξ will be described in Section 7.4.2.

There are two advantages in employing the sheet resistance measurement on narrow wires. The first advantage is that the sheet resistance of wires indicates the resistance of the interconnects of the actual circuitry. The second advantage is that the variation of the sheet resistance of a narrow wire reflects the variation in the critical dimension of the circuitry within a wafer. As embedding test structures in the scribe-lines (empty silicon areas between chips within a wafer) is a common practice, the measurement of the narrow wires in the test structures could be effectively used in the real product monitoring [3].

However, it is costly for industry to apply the sheet resistance measurement on wires as a routine calibration technique to a thin film process or at the initial research and development phase. Firstly, because of the additional lithographic process required, the cost of the lithographic processing must be added into the cost of the testing. Secondly, in order to obtain the resistivity, the thickness of the wire can only be measured by destructive methods such as an XSEM or a focused-ion-beam (FIB). Thus, the industry normally applies the sheet resistance measurement on wires for product monitoring. In research and development, the sheet resistance measurement on a thin film is often used.

Compared to the measurement of the sheet resistance on wires, the measurements on a thin film are more straight-forward. Firstly, the sample does not have to undergo any wafer processing, other than thin film deposition. Secondly, the industry often employs a non-destructive thin film measurement tool such as an ellipsometer, to obtain the thickness. Thirdly, the wafers can be recycled by removing the films with wet chemicals. Thus, the measurement of sheet resistance is the preferred method for characterisation of a thin film in a research and development phase and for routine process monitoring. The resistivity of the film can simply be calculated from the product of the sheet resistance and the thickness, as shown in *Eq. 7-2*. In this work, the resistivity of the annealed cluster films was calculated from the measurements on thin films. The measurement of the cluster film on a narrow wire (sample #60) was not successful because clusters were deposited on the wire and outside the wire.

7.4.2 Correction factor

This sub-section describes the correction factor used in the sheet resistance calculation for a four-point measurement on a thin film.

Within a wire, the current flux is parallel and uniformly distributed, thus, the sheet resistance is simply the measured resistance multiplied by the design aspect ratio (*L/W*) (*Eq. 7-4*). However, in a thin film, the current flux is not parallel but spread in curves across the thin film. Thus, a correction factor has to be applied to the measured resistance in order to obtain the sheet resistance. Yamashita *et al.* [4] derived the correction factor from the solution of Poisson's equation for a system consisting of a rectangular parallelepiped sample and a four point probe array. In an infinite sample with thickness *d*, the correction factor is given by:

$$\zeta_{\infty}^{-1} = \frac{1}{2\pi} \times \ln \frac{(S_{12} + S_{23} - \delta)(S_{23} + S_{34} - \delta)}{(S_{12} - \delta)(S_{34} - \delta)} \qquad (Eq.\ 7\text{-}5)$$

where S_{12}, S_{23}, S_{34} are the spacings between pins 1-2, pins 2-3 and pins 3-4 respectively. δ is the diameter of the probe tips. When the diameter of the probe tips is much smaller than the probe spacing, and the probes have equal distance *S*, the correction factor ξ is $\pi/\ln(2)$.

When the sample is of finite size (especially for $W/S<40$), the correction factor is not only a function of probe separation and the diameter of the probe tip, but also a function of sample geometry, sample size, the position of probes relative to the sample and film thickness [5]. In 1958, Smits derived the correction factor of different types of samples using the method of images [6]. The values of the correction factors can be found in any standards for sheet resistance measurement. In this work, the correction factors were obtained from the ASTM standard [5]. In this standard, the correction factors are comprised of a lateral correction factor and a thickness correction factor.

Figure 7-7 shows the lateral correction factor for two rectangular thin films as a function of the ratio of the sample width (W) to probe spacing (S), and the ratio of sample length (l) to the width (W). When W decreases, the electrical current is more confined; forcing the resistances measured to be higher and closer to the sheet resistance value. Thus, less correction is needed for smaller W/S. The data points are obtained from Ref. [5]. In this work, the correction factors were found by interpolating of these data points.

Figure 7-8 shows the thickness correction factor for a rectangular thin film as a function of the film thickness (d) to probe spacing (S) [5]. When the W/S ratio is smaller than 0.4, the thickness correction factor approaches one. In this work, the thickness of the cluster film was in the sub-µm region and the probe spacing was in the mm range. Because the ratio of d/S was very small, the thickness correction factor was not required.

Since the W/S of the electrical characterised samples listed in Table 7-1 ranged from 10 to 15.5 and the L/W ratios were close to one, the correction factor was approximated by:

$$\xi = 0.0335 \times W/S + 3.8862 \qquad (Eq.\ 7\text{-}6)$$

which is the equation obtained by interpolation of Figure 7-7 for L/W between 10 and 15.

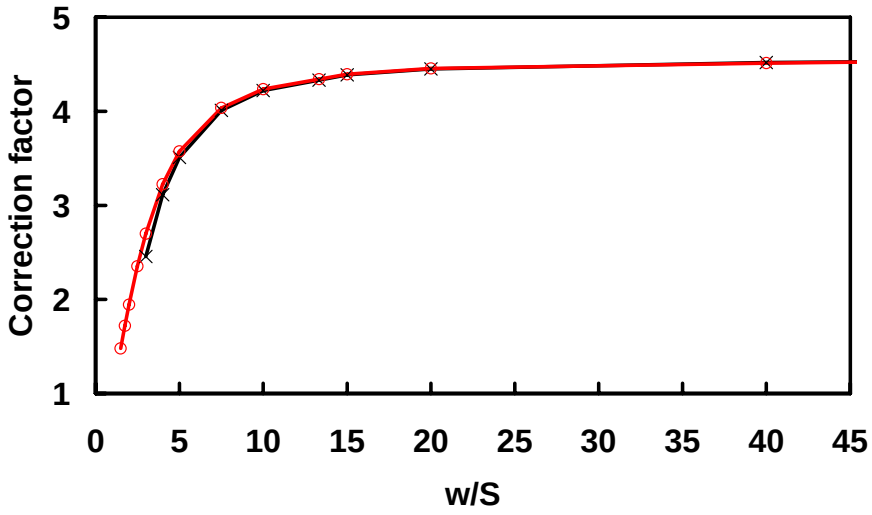

Figure 7-7: **Lateral Correction factor for two rectangular thin films as a function of *W/S*. The geometry of the films are *L/W*=1 (cross symbols) and *L/W*=2 (circles). Data points are taken from Ref. [5].**

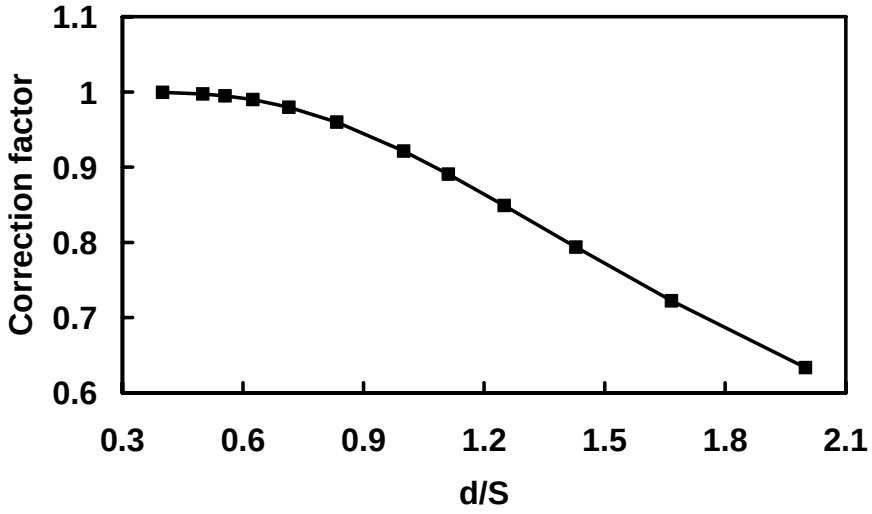

Figure 7-8: **Thickness correction factor as a function of *d/S*.**

7.4.3 *I*(*V*) curves of the reference sample

This subsection describes the procedure for extracting the conductance from current-voltage *I*(*V*) curves. A four-point probe measurement was performed with 1.5mm probe spacing. Figure 7-9 shows that the *I*(*V*) curves of sample #R1 were linear when a current was applied from -100 mA to 100 mA and back to -100 mA. However, there were some outliers at either end of the *I*(*V*) curve. When the current changed direction, some capacitance-related fluctuations were likely to be induced because of instrumental errors. Thus, to eliminate the errors, the data range from -75 mA to 75 mA was selected for the fitting of *I*(*V*) curves.

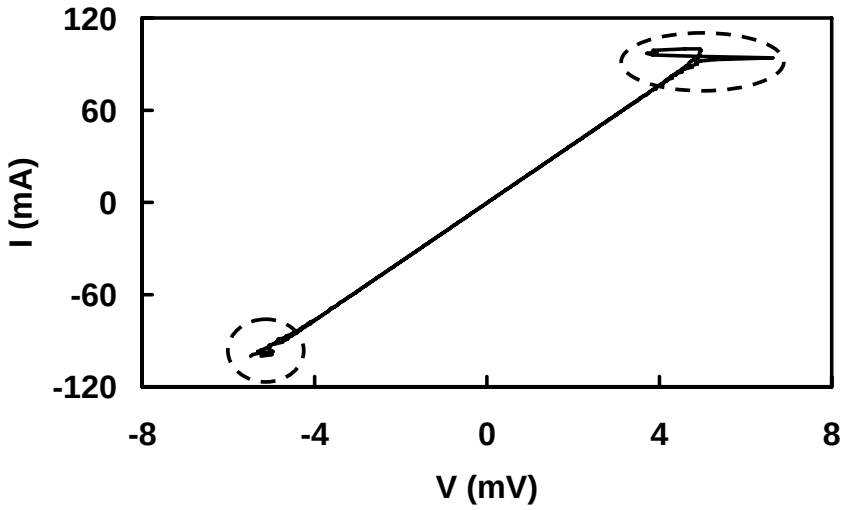

Figure 7-9: ***I*(*V*) curve of sample #R1 was linear over the range of -100 mA to 100 mA. There are some outliers at one or both ends (circled in dashed ovals).**

The linearity of the *I*(*V*) curve in Figure 7-9 suggested that there was no Joule heating (local heating) in the thin film. If there was any Joule heating (I^2R) due to the applied current, the *I*(*V*) curves would be non linear because the resistance would change as the temperature increased. Thus, Joule heating could be ruled out.

An experiment was conducted by measuring the resistances in the dark and after illumination by a light source shown in Figure 7-4 (b). The resistances of $0.299 \pm 0.002\Omega$ (without illumination) and $0.300 \pm 0.001\Omega$ (with illumination) were

stable over the range of 30 mA to 100 mA. Since the measurement was insensitive to light, it could be safely assumed that the probe pins did not punch through the film and collect current from the silicon substrate.

After establishing a reliable procedure for obtaining the $I(V)$ curves, the resistance of the film was calculated from the slope of the $I(V)$ curves. In order to obtain the sheet resistance, a correction factor calculated from *Eq. 7-6* was applied. The sheet resistances measured from a wire (sample #60) and a thin film (sample #R1) were compared. The sheet resistance of the wire was calculated using *Eq. 7-3* and the sheet resistance of the thin film was calculated using *Eq. 7-4*. The sheet resistances of the diffusion barrier/seed layers were 0.31 Ω/square and 0.32 Ω/square respectively. Thus, since the two sheet resistances were about the same, the correction factor applied was accurate. When clusters were deposited on the sample, the sheet resistance measured were the combined resistance from the cluster film and the copper seed layer, thus, a parallel resistance model was used.

7.4.4 Parallel resistor model

As described in Chapter 6, a copper seed layer was required for the sintering of the cluster film. However, the electrical measurements on the samples would naturally include resistance contributed by the copper seed layer and tantalum-based diffusion barrier. Therefore, a method of separating the resistance of the annealed cluster films from the resistance of the barrier/seed layers was developed. This sub-section describes the parallel resistor model used to extract the resistance of the annealed cluster films from the measured resistance.

Figure 7-10 shows a schematic of a parallel resistor model. R_{sh0} and R_{sh1} are the sheet resistances of the diffusion barrier/seed layer and the total resistance of the film after cluster deposition and sintering. R_{cf} is the sheet resistance of the annealed cluster film alone. In a parallel resistor configuration, the sheet resistance of the annealed cluster film is given by:

$$R_{cf}^{-1} = R_{sh1}^{-1} - R_{sh0}^{-1} \qquad (Eq.\ 7\text{-}7)$$

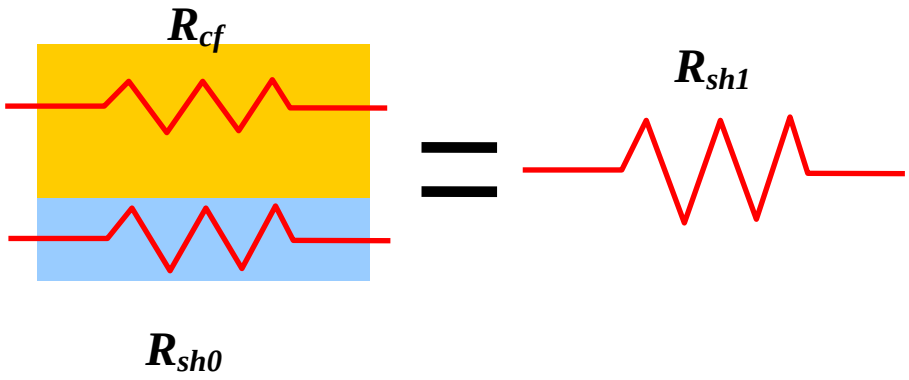

Figure 7-10: **Schematic of a parallel resistor model. R_{sh0} and R_{cf} are the sheet resistance of the diffusion barrier/copper seed layer and the sheet resistance of the annealed clusters film respectively. R_{sh1} is the effective sheet resistance from the measured data. The relation of these resistances was shown in *Eq. 7-7*.**

Using the parallel resistor model, the sheet resistance of the annealed cluster film could be obtained. In order to calculate the resistivity, both the sheet resistance and the thickness of the cluster film have to be measured. The next section describes the procedure for measuring the film thickness.

7.4.5 Thickness measurement of the reference sample

This sub-section examines the uncertainty of the thickness measurements. In this work, the film thickness of the reference sample #R1 was measured from XSEM images. XSEM was performed in a Raith 150 FE-SEM system. The samples were cleaved into two halves. One half of the sample was mounted on a SEM stud which was made of aluminium. The cleaved surface of the samples was facing the incident electron beam at a 90^o angle. As shown in Figure 7-1, the copper seed layer and the diffusion barrier layer were visible, but the boundary between them was vague. In the thickness measurement, the total thickness of the diffusion barrier/copper seed layers was denoted as d_o, and the total thickness of the diffusion barrier/copper seed/annealed cluster film layers was denoted as d_1. The thickness of the annealed cluster film, d_{cf}, could then be obtained:

$$d_{cf}=d_1-d_o \qquad (Eq.\ 7\text{-}8)$$

Figure 7-11 shows the thickness of the barrier/seed layers (d_o) at different magnifications (50 kX, 100 kX, 150 kX) of reference sample #R1. Depending on the final thickness of the cluster film, different magnifications were used. The total thickness (d_o) was found to be 117±5 nm. The uncertainty of the thickness with different magnification was meant to calculate the uncertainty of the XSEM measurement technique.

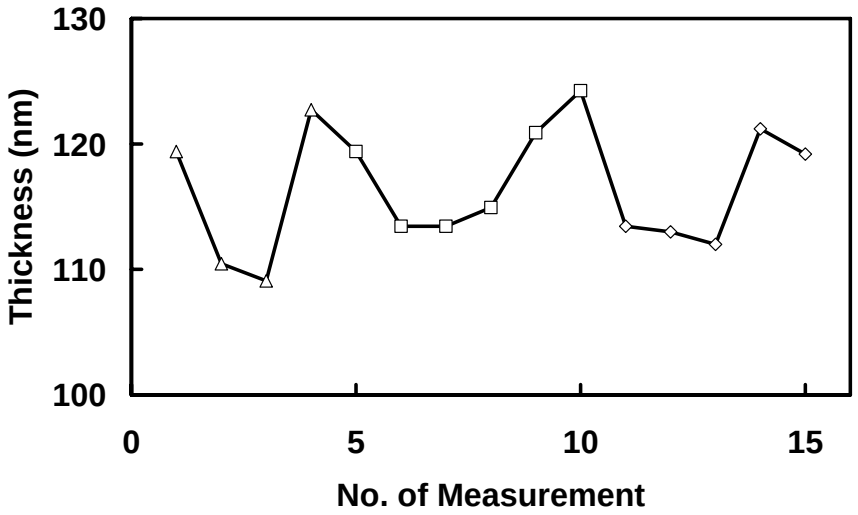

Figure 7-11: Total film thickness of the diffusion barrier and the copper seed layer at 50 kX (triangles), 100 kX (squares) and 150 kX (diamonds) magnifications.

7.4.6 Resistivity calculation and uncertainty analysis

This sub-section describes the methodology for calculating of the resistivity and uncertainty analysis. Assuming the sheet resistance and the thickness are known using the methods described previously, the resistivity could be calculated using (*Eq. 7-2*). To calculate the sheet resistance of a thin film, the correction factors must be acquired. However, since the samples had multiple layers, the sheet resistance of the cluster film was obtained by using a parallel resistor model. The thickness of the cluster film was measured by taking the difference between the total film thickness of the annealed sample and the film thickness of diffusion barrier/seed layers of the reference sample.

When the sheet resistance and the thickness are obtained, the resistivity of the annealed cluster film ρ_{cf} can be calculated as follows:

$$\rho_{cf} = \xi R d \qquad (Eq.\ 7\text{-}9)$$

where R is the resistance obtained in the four-point measurement.

Figure 7-12 shows the block diagram of the sources of uncertainties and the calculation of the uncertainty of the resistivity due to these uncertainties. As depicted in Figure 7-12, the resistivity has a relative uncertainty given by [7]:

$$\frac{s_\rho}{\rho_{cf}} = \sqrt{\frac{s_\xi^2}{\xi^2} + \frac{s_R^2}{R^2} + \frac{s_d^2}{d^2}} \qquad (Eq.\ 7\text{-}10)$$

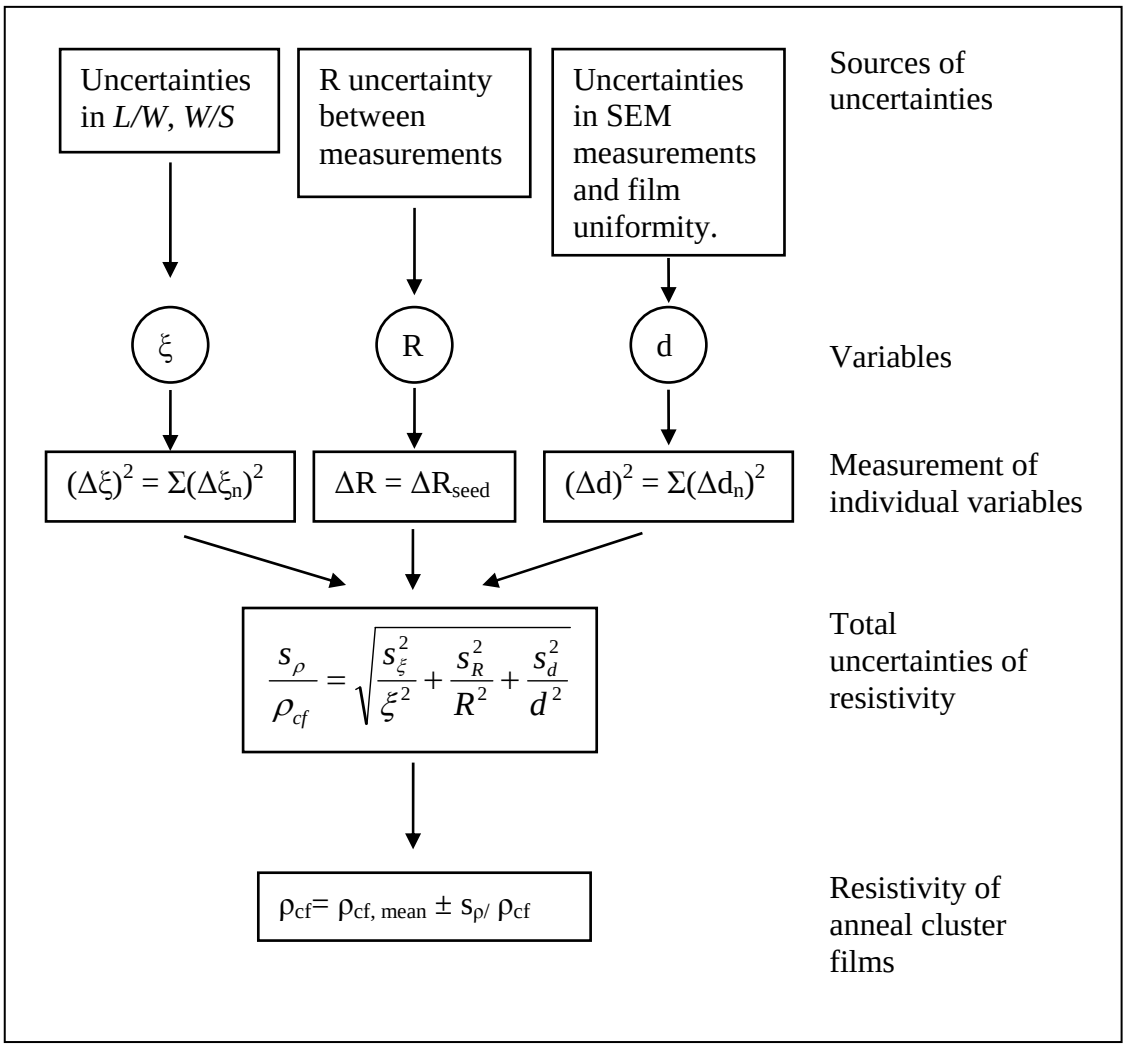

Figure 7-12: Block diagram for the estimation of resistivity

In this work, the sources of relative uncertainty in the extraction of the resistivity consisted of the relative uncertainties of the correction factors (s_ξ/ξ), the relative uncertainties of the $I(V)$ measurements from sample to sample (s_R/R) and the relative uncertainties of the thickness measurement (s_d/d).

The uncertainty in the correction factor comes from the uncertainties of probe spacing (S) and sample geometry. When the samples are in contact with the probe pins, the spacing of the probes could be slightly different in each measurement. Furthermore, the small differences in the sample geometry could affect the correction factor as well. Thus, the deviation in the correction factor was evaluated from the uncertainties in W/S and L/W.

As the probe spacing was 1.5 mm, the design aspect ratio L/W ratios were close to one and the W/S ratios ranged from 10 to 15.5 for sample listed in Table 7-1. The relative uncertainty of correction factors due to the uncertainty of width and probe spacing (W/S) could be estimated from the slope in Figure 7-7 at $L/W = 1$. For the W/S range of 10 to 15.5, the slope was 0.034. The uncertainty of correction factor was equal to the uncertainty of W/S multiplied by 0.034.

Assuming W was 20 ± 3 mm, and S was 1.5 ± 0.3 mm, the W/S ratio could change by 12 %. Therefore, the relative uncertainty of the correction factors due to the relative uncertainty of W/S was equal to:

$$s_\xi/\xi = W/S \times 0.12 \times 0.034$$

$$s_\xi/\xi = 0.004\ W/S \qquad (Eq.\ 7\text{-}11)$$

Since W/S ranged from 10 to 15.5, the relative uncertainty of the correction factors s_ξ/ξ changed from 4 % to 6 %.

Assuming the L/W ratio of the sample varies by 10 %, the correction factor only changes by < 0.1 %. Thus, the uncertainty of the correction factors due to the uncertainty of L/W was insignificant compared to the uncertainty of correction factors due to the uncertainty of W/S.

As for the uncertainties of the resistance measurements from run to run, sample #R1 was used as a reference. Before measuring each of the annealed films, sample #R1 was measured, and plotted in Figure 7-13. The mean and the relative uncertainty of the resistance measurement were 70.76 mΩ and 7 %. The uncertainty (7 %) in the measurements of sample #R1 was assumed to be the same as the uncertainty in the resistance measurements from sample to sample.

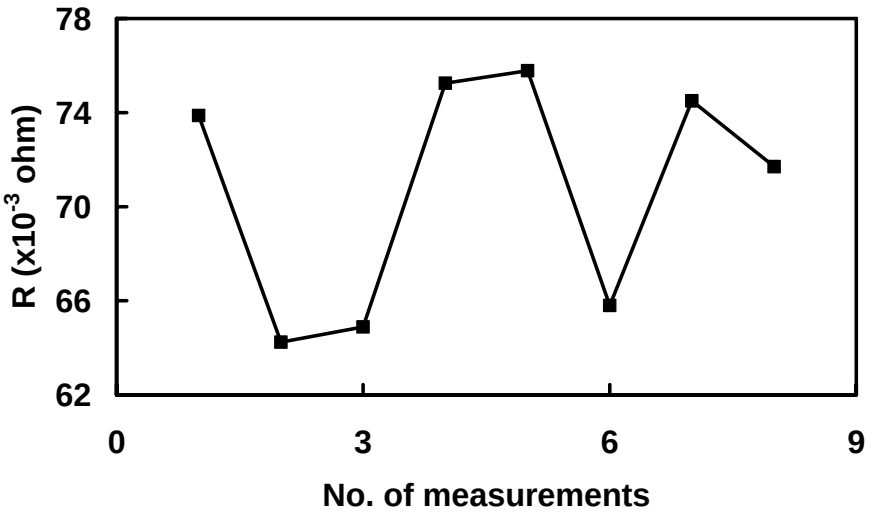

Figure 7-13: Resistance measurements of reference sample #R1 before each measurement of the cluster samples

The uncertainties of thickness measurements come from the uncertainty in film thickness across the probing area and the uncertainty in an XSEM measurement. The total uncertainty in the thickness measurement can be calculated from the statistical sum of individual uncertainties, as follows:

$$(\Delta d)^2 = \Sigma(\Delta d_n)^2 \qquad (Eq.\ 7\text{-}12)$$

where

Δd_1 is the non-uniformity in barrier and seed thickness for original samples. (~5 nm)

Δd_2 is the variation in thickness across the annealed samples. This is calculated from the standard deviation of the thickness within ± 1 mm from the centre of each sample.

Δd_3 is the uncertainty in measurement of final thickness. (~5 nm)

Δd_4 is the uncertainty in measurement due to the angle of cross section. The uncertainty in the thickness measurement due to the tilt angle (assumed to be 10^o at maximum) was less than 1.52 %, which is negligible.

This completes the review of the required methodology for the resistivity calculation and the uncertainty analysis. The next two sections present the results from the XSEM measurements and the resistivity calculation of the annealed cluster films.

7.5 Result: Film morphology

The previous section described the methodology for measuring the film thickness and the resistivity. The reference sample was used for setting up the measurement procedure and analysing the uncertainties. This section presents the morphology of the annealed cluster films and the results of their film thickness. Due to the difference in the cluster diameter (30 nm versus 15 nm) for the 200/100 Ar/He process and the 200/200 Ar/He process, the film morphologies of the samples with the two processes were studied. In this section, the film morphology of the films made of 30 nm clusters, followed by the film morphology of the films made of 15 nm clusters, will be presented.

Figure 7-14 shows the film morphologies of sample #27 after cluster deposition and H_2 annealing. The clusters were produced at 200/100 Ar/He flows. As the cluster films were quite uniform and the boundary between the barrier and the dielectric was clearly visible, the total thicknesses of the diffusion barrier/Cu seed/annealed cluster films were found to be 189 nm. As described in Section 7.4.5, the thickness of the diffusion barrier and Cu seed layers was 117 ± 5 nm. Thus, the thickness of the annealed cluster film (d_{cf}) was 72 ± 5 nm.

Figure 7-15 shows the XSEM images for samples #42, #46, #48 and #50 deposited in the 200/100 Ar/He process. The annealed cluster thicknesses (excluding the barrier and seed layers) are 155± 5 nm, 141± 5 nm, 121± 5 nm and 61± 5 nm respectively. Except for sample #50 (Figure 7-15d) which had the thinnest film, the three other samples had quite a rough surface. In fact, there was a tendency towards a rougher surface as the thickness increased.

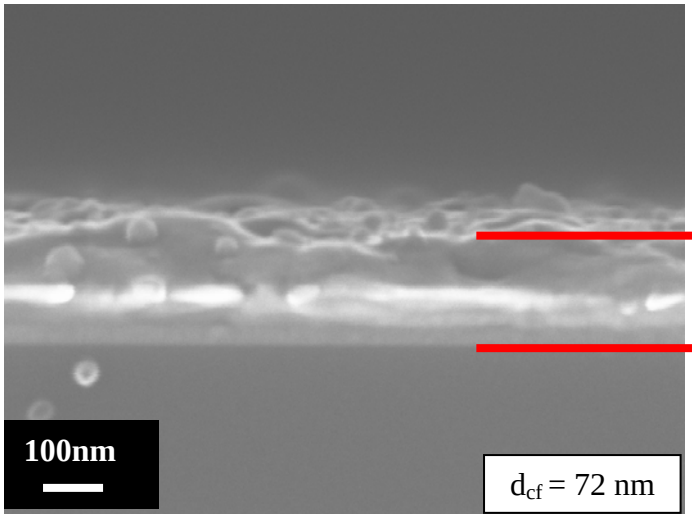

Figure 7-14: **XSEM of sample #27 after H_2 annealing. The image shows that the film is uniform locally. The boundary between the barrier and the dielectric is clearly visible. The total thicknesses of the stacks were 189 nm.**

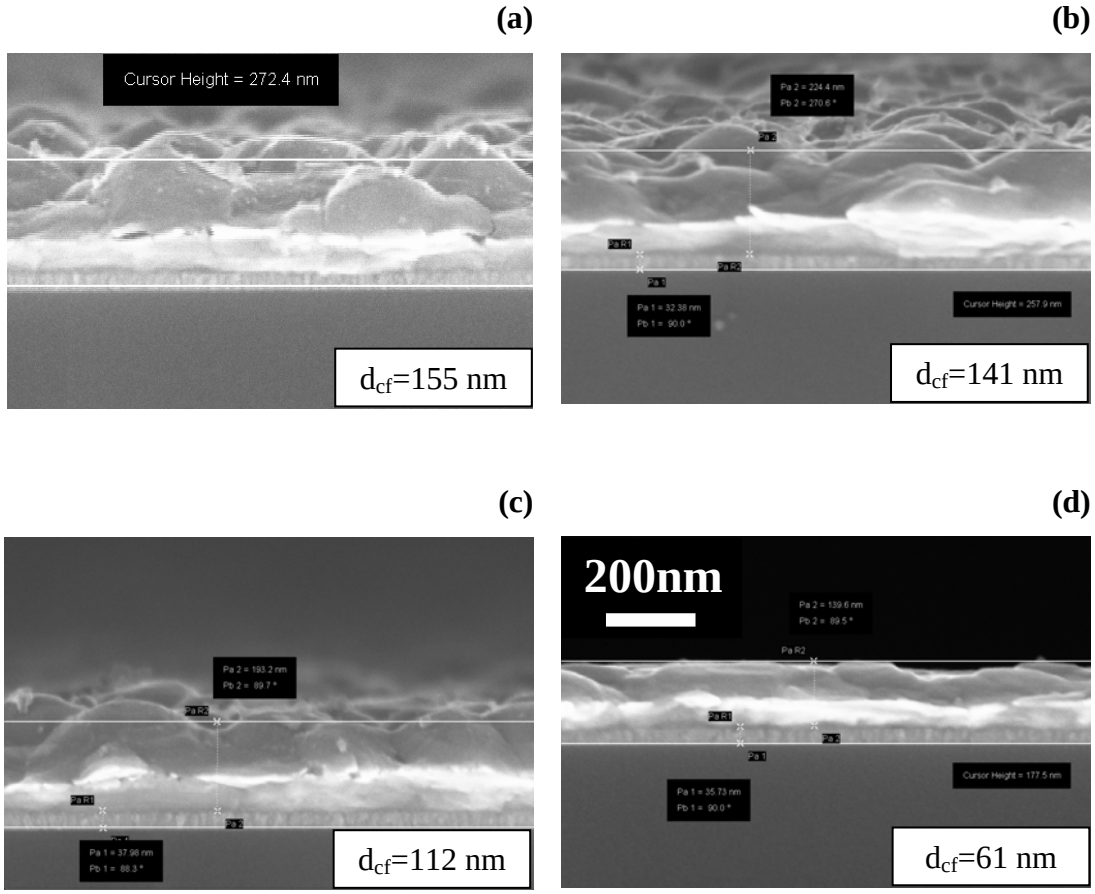

Figure 7-15: **XSEM images for samples (a) #42, (b) #46, (c) #48 and (d) #50. All figures have the same scale.**

Figure 7-16 shows the XSEM images of sample #42 at three different locations. Due to the non-uniform deposition across sample #42, the tendency toward a rougher surface as the thickness increased was observed within the same sample. This observation was consistent with the trend of different samples in Figure 7-15.

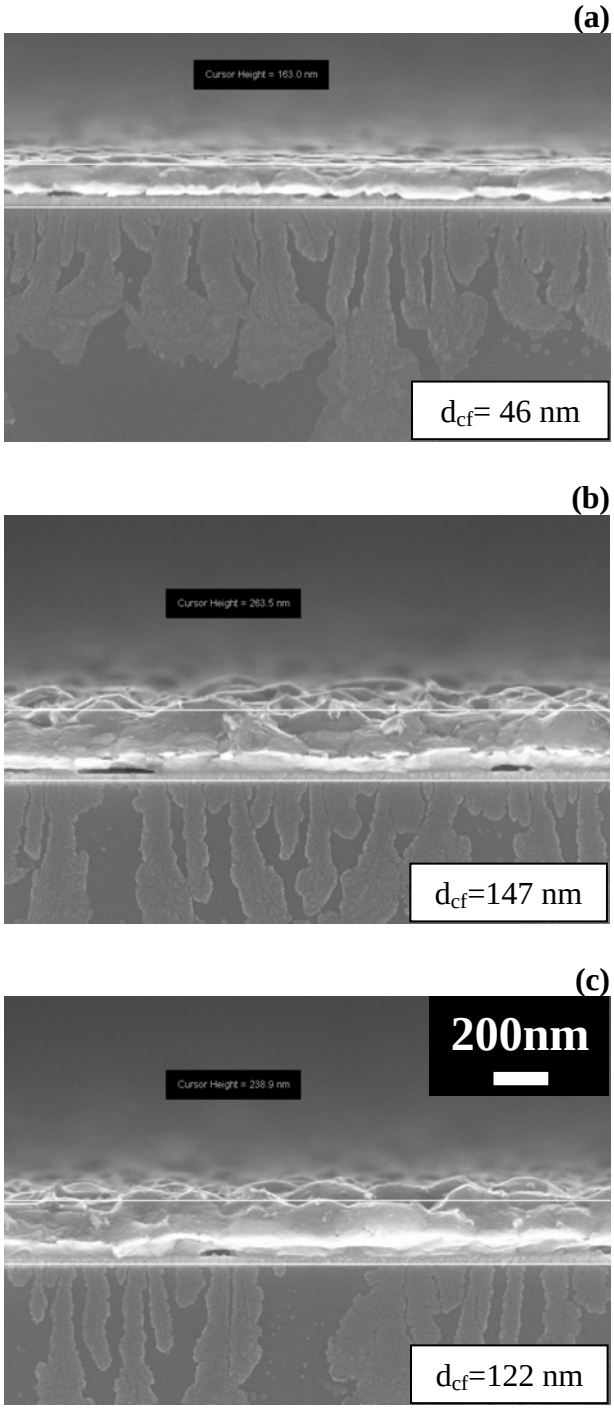

Figure 7-16: **XSEM of sample #42 at different locations:- (a) top, (b) centre and (c) bottom. The annealed cluster thicknesses (excluding the barrier and seed layers) are 46±5 nm, 147± 5 nm and 122± 5 nm respectively. All figures have the same scale.**

On the other hand, the sintering of the thick films which were made of small clusters (<15 nm) were studied. These clusters were generated with 200 Ar/ 200 He flow ratios. Figure 7-17 shows the XSEM images for sample #37 at three different locations. As the thickness increased across the sample, the quality of the annealed films changed from smooth to rough surface, to granular film and eventually became three dimensional (3-D) porous films. The resistivity of the granular films and porous films was not measured because the thickness of the films was not uniform throughout the samples.

As discussed previously, from the XSEM of the films made of small clusters or large clusters, the quality of the annealed films could be categorised in either of these features: a smooth surface, a rough surface, a granular film and a three dimension (3-D) porous film. Figure 7-18 shows the relationship of the film thicknesses to film categories for 15 nm cluster films and 30 nm cluster films. The thickness of the porous film were not shown (thickness in the range of 675 nm to 1.1 μm), but were included as a comparison. Resistivity for samples for cluster films less than 200 nm was calculated (see Section 7.6). As the thickness of the films increased, the film morphology changed from smooth surfaces, to granular surfaces and eventually to a porous film for films with clusters of 30 nm diameter. As for the films made of small clusters, the film morphology changed from smooth surfaces to rough surfaces when the thickness was more than 100 nm.

In order to quantify the roughness, an atomic force microscope (AFM) (Dimension 3100) [8] was used. Two samples (samples #30 and #48) were selected. Figure 7-19 shows the AFM images of the sample #30 which had a very rough surface. The height of the AFM measurements can be transformed into a root-mean-square (rms) value for the roughness. For the roughness calculation, an area of 10 μm by 10 μm was selected. The scan rate was 0.5 Hz. Table 7-2 shows the relationship between the measured roughness and the estimated film thickness of the two samples. The reason the exact film thickness could not be compared was that it was difficult to find the exact XSEM locations for measuring the roughness using AFM. Nevertheless, a relative comparison could be made. It was found that the roughness increased as the film morphology changed from smooth, to rough and to granular structures. The porous films had a relative smooth top surface. This observation was consistent with the XSEM images.

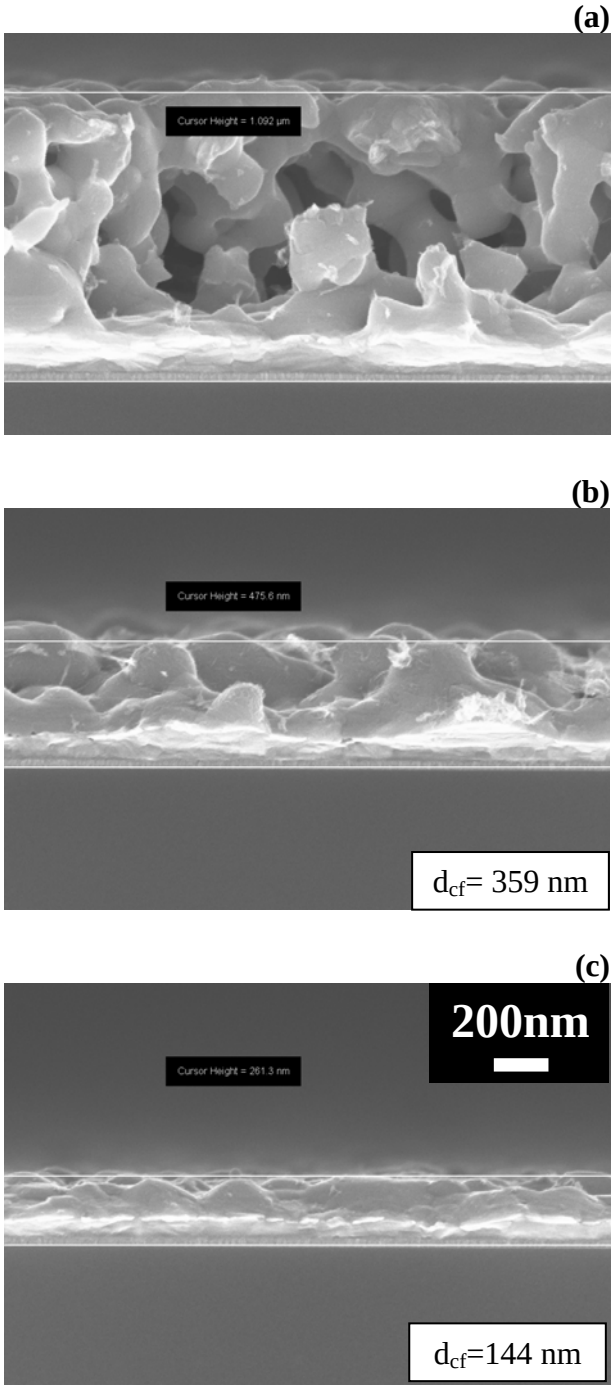

Figure 7-17: **XSEM of sample #37 at different locations:- (a) top, (b) centre and (c) bottom. The original cluster size was around 15 nm. The film morphologies can be grouped into three categories: smooth surface (c), rough surface (b) and porous film (a). All figures have the same scale.**

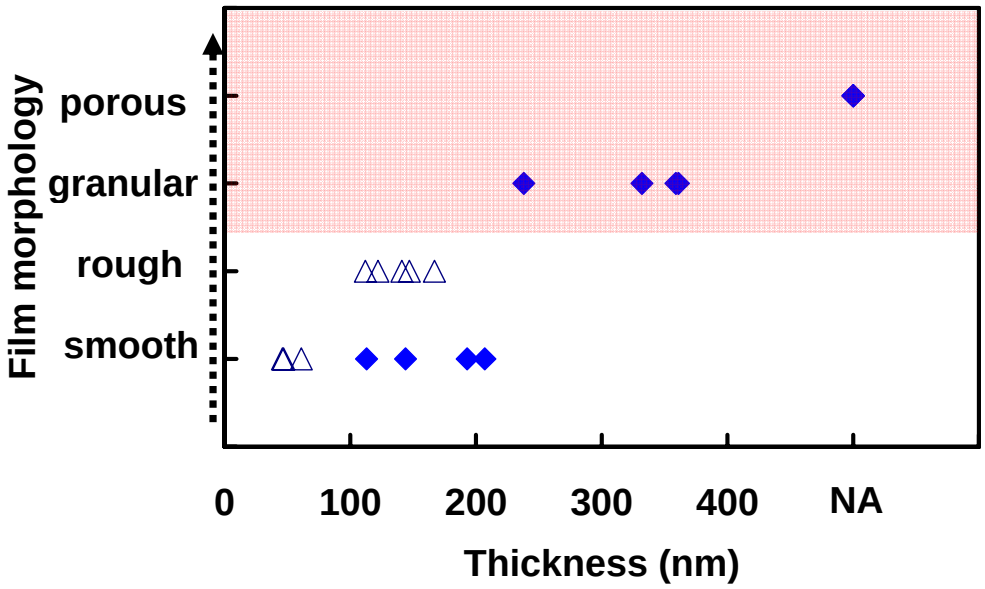

Figure 7-18: **Relationship of film thickness to film categories for 15 nm clusters (closed diamonds) and 30 nm clusters (open triangles). The data were measured from individual locations of the samples. The thickness of the porous film was not shown (in the range of 675 nm to 1.1 µm). Resistivity was calculated for samples with smooth and rough surfaces (white region), but not for samples with granular and porous films (shaded region).**

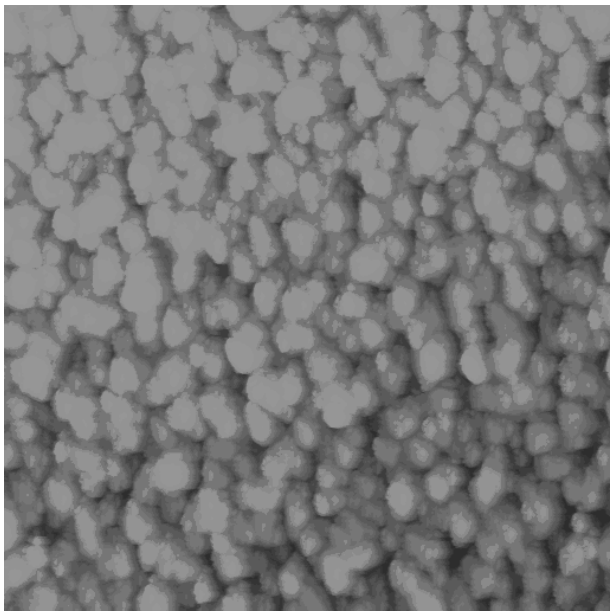

Figure 7-19: **An AFM image of sample #30.**

Table 7-2: Relationship between the measured rms roughness and the estimated film thickness.

Sample	Cluster diameter (nm)	Location	Estimated film thickness (nm)	Category	Measured rms roughness (nm)
30	15	A	~110	Smooth	13
30	15	B	~240	Rough	29
48	30	A	~300	Granular	33
48	30	B	~400	Porous	11

Figure 7-20 shows the surface of the film annealed from 30 nm clusters is rougher than the surface of the film annealed from 15 nm clusters. The thicknesses of the films at these particular locations were both 145 nm. Although 3-D porous films have not yet been observed in the film deposited with the 30 nm clusters, it could be inferred from Table 7-2 that granular structure and 3-D porous film would form for a thicker cluster film made of 15 nm clusters.

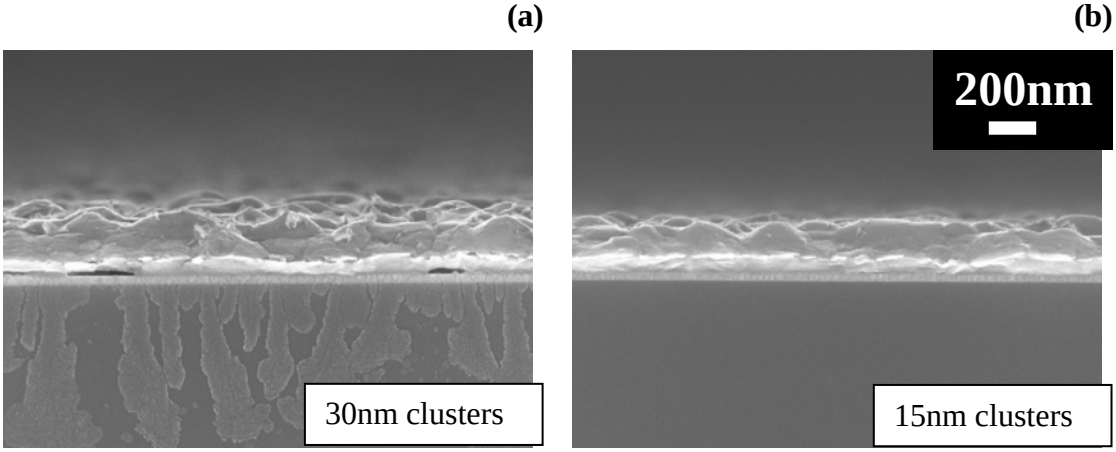

Figure 7-20: The surface of (a) the film annealed from 30 nm clusters (sample #42) is rougher than the surface of the film annealed from 15 nm clusters (sample #37). The cluster films were both 145 nm thick at these locations. Both figures have the same scale.

Due to the non-uniform cluster beam, the thickness of the cluster film varied from location to location. Therefore, it was essential to prepare many cross section images at several locations distributed over the length of the samples. Figure 7-21 shows the film thickness at different locations within the samples measured from the XSEM images. The locations within ±1 mm from location 10 were the possible points that the sensing probes could have landed. Therefore, the mean and the standard deviation of the thickness at this region were used for the resistivity calculation.

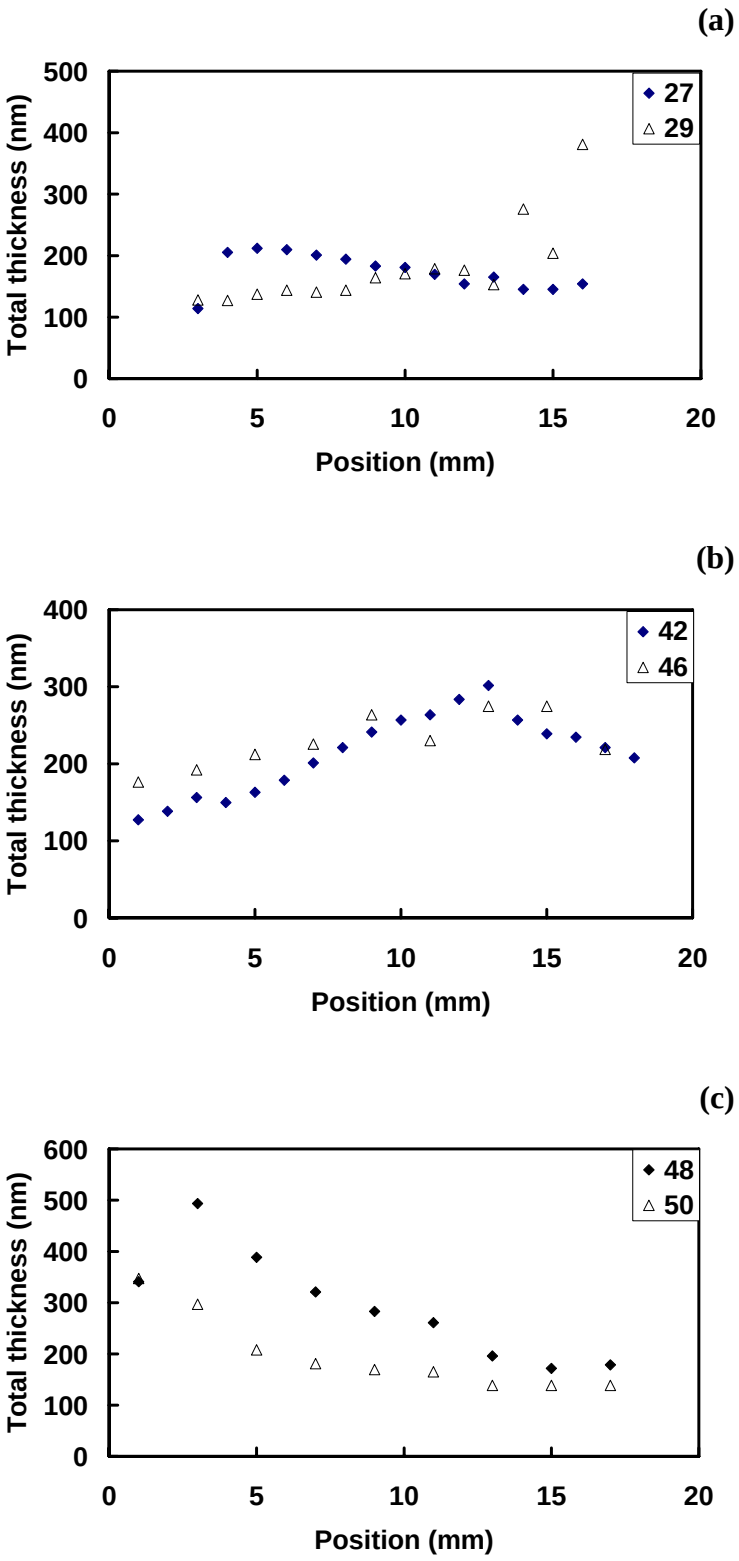

Figure 7-21: **Thickness profile across six samples (#27, #29, #43, #46, #48 and #50). Position at 10 mm is the centre point which is about where the probes landed. Numbers in the legend (right) are the sample numbers.**

7.6 Results: Resistivity of the annealed cluster films

With the thickness information from previous section, the resistivity can now be calculated. The section describes the calculation of the resistivity of the annealed cluster films based on the methodology described in Section 7.4. Samples #27 and #29 were used as the examples.

Figure 7-22 shows an example of $I(V)$ curves with the selected data range (from 0 to ±75 mA) for samples #27, #29 and #R1. Samples #27 and #29 were deposited with clusters while sample #R1 was a reference sample without any cluster deposited. The gradient of the fitting lines was the R^{-1} of the samples. As only one measurement was performed at the centre of each sample, the non-uniformity of the film could not be addressed by the electrical measurements. Even for a film with a very uneven surface between the probes, the resistance measurement only reflected an equivalent electrical resistance. The resistance measured for samples #27 and sample #29 were around 38 mΩ and 41 mΩ respectively, compared with the resistance of 74 mΩ for the diffusion barrier and Cu seed layer of the reference sample.

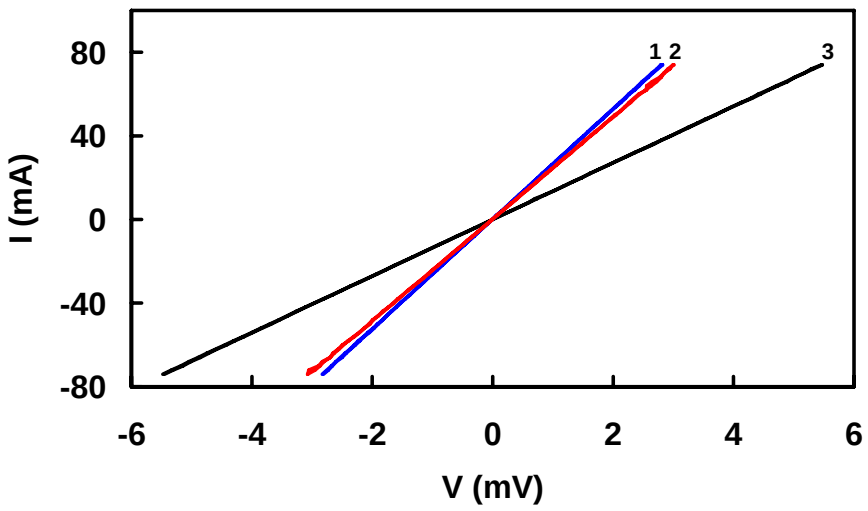

Figure 7-22: ***I*(*V*) measurements for samples #27 (line 1) and #29 (line 2) and #R1 (3) with data between -75 mA and 75 mA.**

On the other hand, the average thickness of samples #27 and #29 were 185 ± 17 nm and 161 ± 20 nm. As the average barrier/seed thickness was 117 nm, the thicknesses of annealed cluster film were 68 ± 17 nm (sample #27) and 44 ± 20 nm (sample #29) respectively.

In previous section, the thickness of the samples was measured. In order to calculate the resistivity, both the thickness and the sheet resistance need to be known. To calculate the sheet resistances, the correction factors (ξ) were applied according to individual sample geometry. Using the parallel model described in Section 7.4.4, the sheet resistance of the annealed cluster film R_{cf} could be separated out. The average thickness of the annealed cluster film was calculated from the thickness within ± 1 mm from the centre of each sample. Table 7-3 summarises the sheet resistances and the thickness of the samples.

Table 7-3: The sheet resistances R_{sh1}, R_{sh0} , R_{cf} and the average cluster thickness.

Sample	R_{sh1}	R_{sh0}	R_{cf}	Cluster thickness
	Ω/square	Ω/square	Ω/square	nm
#27	0.161	0.320	0.325	68
#29	0.173	0.320	0.378	44
#42	0.123	0.326	0.197	123
#46	0.123	0.278	0.220	135
#48	0.126	0.278	0.231	169
#50	0.168	0.278	0.427	54

Figure 7-23 shows the resistivity as a function of the thickness of annealed cluster films. One sample was deposited with 15 nm clusters in the 200/200 Ar/He process and five samples were deposited with 30 nm clusters in the 200/100 Ar/He process. In the case of the 30 nm clusters, the mean of the resistivity was $2.3\pm 0.28 \times 10^{-8}$ Ωm for thin films (<120 nm). In the case of the 15 nm clusters, the mean of the resistivity was $1.63\pm 0.22 \times 10^{-8}$ Ωm. Since the roughness increased with the thickness, the resistivity increased as well. For the advanced interconnects, it is known that the surface roughness will be the primary factor to the increase in the resistivity [9]. Nevertheless, these two values should be the resistivity of the dense cluster film in the trenches discussed in Chapter 6. Within those trenches, the films were dense and the surfaces were smooth.

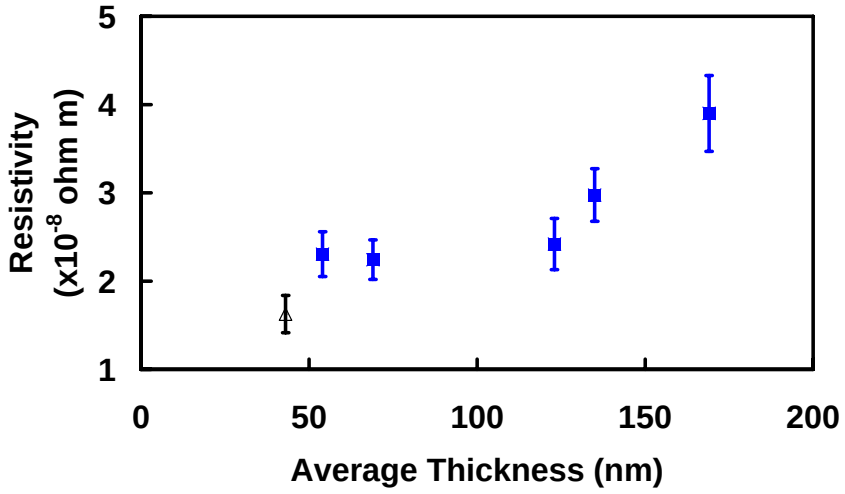

Figure 7-23: **The resistivity as a function of average thickness of annealed cluster films for 15 nm clusters (open black triangle) and 30 nm clusters (closed blue squares).**

It was hypothesized that the small clusters should sinter into the seed layer more easily than the large clusters, therefore a film with a cluster diameter ≤ 15 nm should have a lower resistivity. This argument was supported by the mean resistivity of $1.63 \pm 0.22 \times 10^{-8}$ Ωm for the thin 15 nm cluster film. Even if the coalescence rate was enhanced by the cluster size effect, the resulting clusters in the process of coalescence are still small compared to 30 nm clusters. It takes eight clusters of 15 nm in diameter to have the same volume as one cluster of 30 nm diameter. Thus, the sintering process in the 15 nm clusters should be better than the 30 nm clusters. In this work, the resistivity of a thicker film made of 15 nm clusters could not be obtained due to the formation of the 3-D porous networks, as discuss previously.

An attempt has been made to deposit cluster selectively on sample #60 with the 200/200 Ar/He flows. The copper seed layer of sample #60 was patterned through etching, leaving a narrow line for electrical measurement. The purpose of the selective deposition was to deposit copper clusters only on the pre-patterned copper seed layer and not on the SiO_2. However, the clusters adhered to both the patterned copper seed layer and SiO_2. Thus, the electrical measurement solely on the pre-patterned region was not possible as the clusters covered the whole sample. The low selectivity of the cluster deposition on the patterned sample was probably due to the damaged surface on the dielectric promoting the adhesion of copper clusters. In order to measure the line

resistance of the copper clusters, a damascene structure and a chemical-mechanical process (CMP) are required for measuring the line resistance.

7.7 Summary and recommendation

In this chapter, the resistivity of the annealed cluster film was calculated. Cu clusters of different diameters (15, 30 nm) were generated in an IGA source. These clusters are then deposited on unpatterned samples with a diffusion barrier and a copper seed layer. After annealing in H_2 at 450ºC for two hours, the conductance and the thickness of the film were measured. From the XSEM images, a transition from smooth surfaces, to rough surfaces, to granular film and eventually to 3-D porous networks was observed with increasing the film thickness. Using a parallel resistor model, the resistivity of the cluster films was found to be $2.3 \pm 0.28 \times 10^{-8}$ Ω.m (for films < 120 nm thick) in the 30 nm cluster film and $1.63 \pm 0.22 \times 10^{-8}$ Ω.m (for film < 50 nm thick) in the 15 nm cluster film. These values were the resistivity anticipated for the trenches discussed in Chapter 6 and they were close to the bulk resistivity (1.6×10^{-8} Ωm) and the value required by industry (2.2×10^{-8} Ωm).

For the technology to be applied to the IC application, the line resistivity (the resistivity of copper in the trenches) and the reliability (such as electro-migration and stress migration) needs to be studied. These tests require a more complete integration of the process. Subsequent processing of the samples is needed: (1) to remove the parasitic resistance of the barrier/seed on the top surface, (2) to passivate the samples (to prevent oxidation) and (3) to open the pads for electrical contacts. In addition, dual damascene structures are needed for a stress migration test. These tests will be feasible when there is more collaboration with the semiconductor industry.

References

[1] "International Technology Roadmap for Semiconductors, 2006 (Update), *http://public.itrs.net.*"

[2] *Manual for HP 4155A parametric analyzer*.

[3] N. S. Nagaraj, M. Kulkarni, T. Bonifield, N. Usha, I. Hossain, and C. Zabierek, "A systematic approach to interconnect modeling and process monitoring," Burlingame, CA, USA, 2003, pp. 114-16.

[4] M. Yamashita, "Resistivity correction factor for the four-probe method," *Journal of Physics E: Scientific Instruments*, vol. 20, pp. 1454-1456, 1987.

[5] *ASTM standard: Standard Test Method for Sheet Resistance of Thin Metallic Films With a Collinear Four-Probe Array (F390-98)*.

[6] F. M. Smit, "Measurements of Sheet Resistivity with the Four-Point Probe," *Bell System Technical Journal*, vol. 37, p. 371, 1958.

[7] S. Bell, "A beginner's guide to uncertainty of measurement," *Measurement Good Practice Guide*, vol. 11, 1999.

[8] *http://www.veeco.com/*.

[9] S. M. Rossnagel and T. S. Kuan, "Alteration of Cu conductivity in the size effect regime," *Journal of Vacuum Science & Technology B: Microelectronics Processing and Phenomena*, vol. 22, pp. 240-247, 2004.

Chapter 8 Conclusions and outlook

The thesis consists of two parts: In the first part, uniform antimony cluster films were characterised. In the second part, the application of the copper clusters in the ULSI interconnects were presented. As conclusions and recommendations were presented in each chapter, this chapter summarises the conclusions and gives a brief description for future work.

8.1 Sb clusters

Using a first stage nozzle and a tantalum plate, the deposition process produced uniform cluster films that were suitable for electrical measurements. The diameter of the clusters was ~ 15 nm. A consistent percolation exponent for conduction (1.85) was found. After the deposition, the resistance of the films continued to increase because of coalescence. All the $I(V)$ curves from the resultant films were linear. It was found that the temperature coefficient of resistance at room temperature was in the order of 10^{-4} K^{-1}, while the temperature coefficient of resistance of other semiconductors was in the order of 10^{-2} K^{-1} at room temperature. The resistance and the temperature coefficient of resistance did not change significantly after annealing up to 450 K. Furthermore, there was no gate effect observed when the gate was biased up to ± 10V at both room temperature and liquid nitrogen temperature. Thus, it was concluded that there was no semiconducting behaviour in these films, possibly due to the coalescence.

8.2 Cu clusters

After understanding the damascene process and the needs for future interconnect application, various copper filling and reflow techniques were studied. Previously, there is no technique that has both the high purity and selective filling required by the industry. We have demonstrated that the unique properties of clusters such as bouncing and melting behaviours could be utilised for the interconnect application.

XSEM was used to study the filling in nanoscale trenches. Various coatings representing present and future diffusion barrier and copper seed layers were provided by semiconductor manufacturers. It was demonstrated that copper clusters filled the high aspect ratio (5:1) trenches with TaN coating and medium aspect ratio (3.5:1) trenches with TaN/Ru coatings.

Excellent films were formed after sintering the copper clusters into the copper seed layers in both hydrogen and vacuum environment at 450ºC. The resistivity measured by a four-point probe technique was close to the industry's requirement. An attempt to measure the line resistivity of the cluster films was not successful because clusters were deposited on the whole sample instead of the pre-patterned copper line. Nevertheless, the cluster deposition was proved to have a great potential in the interconnect application.

8.3 Outlook

In the amorphous antimony experiments, coalescence appears to have modified the semiconducting behavior of the cluster films. Thus, in order to prevent the coalescence, a different substrate or different materials for the metal contacts could be tried. In the configuration used, the clusters were small. It would be interesting to examine the electrical properties of the films made of large clusters, provided the clusters do not bounce on the substrate and produce non-uniform films. If the velocity of the large clusters could be further reduced, it might be possible to make a uniform film. The

reduction of the cluster velocity could be achieved by ionizing clusters and then applying an electric field to slow the clusters down. Since the coalescence could be more pronounced in small clusters, the semiconducting behaviours might be preserved in a uniform film consisting of larger clusters.

For future work on the copper clusters, more support from the industry is needed. For example, since the bouncing behaviour is different on different substrates, it is necessary to demonstrate the filling in the high aspect ratio trenches coated with a copper seed layer. Other tests on the copper cluster technology such as line resistance measurement, electro-migration and stress migration would involve a more integrated process, which are only feasible with the collaboration with the semiconductor industry.

Acknowledgments

I wish to express sincere appreciation to my supervisors, Professor Richard Blaikie and Associate Professor Simon Brown for their assistance and patience in the preparation of this thesis. It has been my pleasure to work with my former NCD colleagues: Dr. Andreas Lassesson, Dr. Joris van Lith, Monica Schulze, Dr. Ganesh Kumar, Mark Darvill, Shannon Kopp and Lyn Dawson. I want to thank them for all their help, support and encouragement. I am thankful for the sponsorship from Foundation for Research Science and Technology (FRST) under Technology in Industry Fellowship (TIF). I would like to acknowledge the resource provided by The MacDiarmid Institute for Advanced Materials and Nanotechnology, and by the University of Canterbury.

In this project, there have been a strong support and encouragements from our post-doc team and our fellow students: Dr. Jim Partridge, Dr. Franck Natali, Dr. Pierre Convers and Dr. Euan Boyd, Dr. Shelley Scott, Dr. Martin Kaufmann, Dr. René Reichel, Dr. Ahmad Ayesh, David McCarthy and David Mackenzie.

I would like to thank Dr. Richard Tilley at Victoria University and Dr. Kevin Stevens from Industrial Research Limited (IRL) for performing the high resolution TEM.

I would like to express my gratitude to every technician in Physics and Chemistry Departments, who has provided me the best support I can ever ask for. In particular, I

would like to thank Owen Caughley, Stephen Hemmingsen, Graeme Kershaw, Danny Leonard, Wayne Mackay for making the IGA components and the annealing stage, Ross Ritchie, Graeme MacDonald for fixing the turbo pump controller and replacing the filament for the electron gun, Wayne Smith for fixing the gate valve and Russell Gillard for arranging the workshop requests. I would like to thank Dr. Orlon Petterson for the computer support. The assistance from Gary Turner and Helen Devereux from Electrical Engineering Department is also greatly appreciated. I am grateful for the help from my English teachers from Learning Skills Centre, Mdm. Val Melhop and Mdm. Frieda Looser.

Finally, I would like to express my greatest appreciation for my mother, my brother, my sisters, my wife Woon li, my two sons, Rayner and Ivan, as well as my in-law family for supporting me all these years to fulfil my dream.

List of Figures

List of Tables